CARBONIC ANHYDRASE MODULATORS FOR DETECTION AND TREATMENT OF HUMAN DISEASES

A Dissertation
Submitted to
the Temple University Graduate Board

In Partial Fulfillment
of the Requirement for the Degree
DOCTOR OF PHILOSOPHY

By
Utpal Kumar Mondal
May 2019

Examining Committee Members:

Dr. Marc A. Ilies, Advisory Chair, Department of Pharmaceutical Sciences
Dr. Daniel J. Canney, Department of Pharmaceutical Sciences
Dr. Ellen A Walker, Department of Pharmaceutical Sciences
Dr. Eugen F. Mesaros, External Member, Arbutus Biopharma

ABSTRACT

Carbonic anhydrases (*CAs, EC 4.2.1.1*) are a class of metalloenzymes that catalyze the hydration of CO_2 under physiologic conditions and are involved in many physiological and pathological processes. Modulation of CA activity, particularly CA inhibition is exploited pharmacologically for the treatment of many diseases such as cancer, glaucoma, edemas, mountain sickness. CA activation has been less frequently investigated till recently. Genetic deficiencies of several CA isozymes are reported in the literature and reflect the important role of carbonic anhydrases in human physiology and homeostasis. Activation of CA isozymes in brain have been correlated recently with spatial learning and memory. Based on these premises, activators of CA isozymes have the potential to alleviate mild dementias and to act as potential nootropic agents.

In chapter 3, continuing our long-term interests towards the development of potent and selective CAAs, we carried out X-ray crystallographic studies with a small series of pyridinium histamine derivatives, previously developed as CAAs by our group. This study revealed important insights into the binding of this class of activators into the active site of CA II isozyme. A potent pyridinium histamine CAA **25i** was successfully crystallized with CA II isozyme and was found to bind into the hydrophobic region of the active site, with two binding conformations being observed. This is one of the very few X-ray crystal structures of a CAA available. Based on the findings of this X-ray crystallographic study and building on our previously developed ethylene bis-imidazole CAAs, we advanced a novel series of lipophilic bis-imidazoles. Enzymatic assays carried out on purified human CA isozymes revealed several low nanomolar potent activators against various brain-relevant CA isozymes. Bis-imidazole **30e** was found to be a

nanomolar potent activator for CA IV, CA VA and CA IX. Due to their conjugated structure, these CAAs were also fluorescent and therefore were fully characterized in terms of photophysical properties, with several representatives proving to display very good fluorophores. The very good activation profile against several different CA isozymes, along with excellent fluorescence properties recommend these compounds as great molecular tools for elucidation of role of CA isozymes in brain physiology, as well as towards improvement of memory and learning.

Focusing on inhibition of CA isozymes, it must be stressed that over the last decade a clear connection had been established between the expression of CA IX and CA XII and cancer. Since cancer is the second most common cause of death in the world, we explored the possibility to kill cancer cells via inhibition of different CA isozymes present in cancer cells. The membrane bound carbonic anhydrase IX (CA IX) isozyme represents a particularly interesting anticancer target as it is significantly overexpressed in many solid tumors as compared to normal tissues. In malign tissues this CA isozyme was found to play important role in pH homeostasis and promotes tumor cell survival, progression and metastasis. Thus, CA IX represents a potential biomarker and an appealing therapeutic target for the detection and treatment of cancer. CA IX can be targeted either through the development of small or large molecular weight, potent, and selective inhibitors or through the development of CA IX targeted drug delivery systems for selective delivery of potent chemotherapeutic agents. Building on these premises, in this dissertation, we also revealed our continuing efforts towards the development of potent and selective CA IX inhibitors along with their translation into the development of CA IX targeted drug delivery systems.

In chapter 4, we designed a series of small molecular weight (MW) ureido 1,3,4-thiadiazole sulfonamide derivatives employing the "tail approach", through the decoration of established sulfonamide CA inhibitor warheads with different tail moieties via ureido linker. The generated CAIs were tested against tumor associated CA IX and CA XII isozymes and off-target cytosolic isozymes CA I and CA II, and were revealed to be moderate to highly selective and nanomolar, even sub-nanomolar, potent CA IX inhibitors. Several potent pan-inhibitors were also identified in this section. We assessed these CAIs for their *in vitro* cell killing ability using MDA-MB 231 breast cancer cell line expressing CA IX and CA XII. The most efficient CAI proved to be ureido-1,3,4-thiadiazole-2-sulfonamide **69**, which showed subnanomolar potency against purified human CA IX and CA XII isozymes, with good selectivity against CA I and CA II, and consistent, statistically significant cancer cell killing.

In Chapter 5, continuing our efforts towards the development of potent and selective CA IX inhibitors, we designed, synthesized, characterized and evaluated a new series of PEGylated 1,3,4-thiadiazole-2-sulfonamide CAIs, bearing different PEG backbone length. We increased the PEG size from 1K to 20K, in order to better understand the impact of the PEG linker length on the *in vitro* cell killing ability against CA IX expressing cancer cell lines and also against a CA IX negative cell line. In vitro cell viability assays revealed the optimum PEG linker length for this type of bifunctional bis-sulfonamide CAIs in killing the tumor cells. The most efficient PEGylated CAI was found to bis-sulfonamide DTP1K **91**, which showed consistent and significant cancer cell killing at concentrations of 10−100 μM across different CA IX and CA XII expressing

cancer cell lines. DTP1K **91** did not affect the cell viability of CA IX negative NCI-H23 tumor cells, thus revealing a CA IX mediated cell killing for these inhibitors.

In chapter 6, we decided to further explore the possibility of using CA IX as a targeting epitome for the development of a gold nanoparticle-based drug delivery system. We translated the oligoEG- and PEGylated CAI conjugates into efficient targeting ligands for gold nanoparticle decoration along with chemotherapeutic agent doxorubicin (Dox), in a novel multi-ligand gold nanoplatform designed to selectively release the drug intracellularly, in order to enhance the selective tumor drug uptake and tumor killing. We were successful in developing compatible CAI- and Dox- ligands for efficient dual functionalization of gold nanoparticles. Our optimized, CA IX targeted gold nanoplatform was found to be very efficient towards killing HT-29 tumor cells especially under hypoxic conditions, reducing the hypoxia-induced chemoresistance, thus confirmed the potentiating role of CA IX as a targeting epitome.

DEDICATION

This dissertation is dedicated

to my beloved mother,

Shandha Rani Mondal

ACKNOWLEDGMENTS

Starting my Ph.D. studies in US at Temple University was a dream to come true for me, while finishing the Ph.D. studies is the fulfillment of the dream. I am truly grateful to Temple University School of Pharmacy for giving me this opportunity to pursue the Ph.D. studies with full funding and appropriate resources. I cherished each and every moment of this beautiful journey. At this important point of my life, I would like to thank all those wonderful people who inspired me, supported me and encouraged me to finish this degree requirements.

First and foremost, I would like to express my gratitude and appreciation towards my advisor Dr. Marc A. Ilies. Just after joining the school, I promptly joined Dr. Ilies lab. Dr. Ilies provided me with excellent training in his interdisciplinary lab during my five and half years of Ph.D. studies. He pushed me to the limit for learning different aspects of the projects I worked with. He taught me to think freely, come up with ideas, trouble shoot problems and work more independently. Thank you, Dr. Ilies, for allowing me to work in the interface of medicinal chemistry, material chemistry and drug delivery. I learned diverse skill sets in different aspects of pharmaceutical sciences. Without your constant support that was not possible. Besides science, you are like local guardian to me at Philadelphia. I am really grateful to you for many things. It was a great pleasure for me to be part of your excellent lab, Dr. Ilies.

I would like to express my sincere gratitude towards the members of my dissertation advisory committee, Dr. Daniel Canney, Dr. Ellen Walker and Dr. Eugen F. Mesaros - without their positive inputs, motivation and encouragement, this thesis would

not have been complete. I would like to specially thank Dr. Canney for providing the opportunity to work as a teaching assistant for consecutive five years.

I would like to express my appreciation to Almira and Sophon Din, administrative assistants, for smooth and timely processing of our paperwork so that I concentrate on my study and research.

I would also like to acknowledge our collaborators in US and across the globe for their contributions towards finishing different projects. I want to specially thank Dr. Claudiu T. Supuran (University of Florence), Dr. Daniela Vullo (University of Florence), Dr. Robert McKenna (University of Florida).

I would like to acknowledge Temple University Graduate School for a doctoral dissertation completion grant. The research completed in this dissertation is financed in part by NIH through a grant (R03EB026189).

I am very thankful to all my lab mates and friends Ahmed, Uttam, and Rajesh. Thank you, guys, for encouraging me, motivating me and for always being there for me. It was a pleasure for me to share memories with you all which will be remembered forever. I would like to address my special thanks to my former lab mate Dr. Bogdan Draghici for teaching me in different aspects of organic synthesis in the very beginning my Ph.D. studies. I am also grateful to my former lab mates Dr. Vishnu Sharma, Dr. Suleyman Akocak and Dr. Ozlem Karakus.

I would also like to acknowledge and thank all the undergraduate students (Joe, Ronit, Elizabeth, Kate and Dave) who worked with me in different projects. Their contributions and hard works for moving the projects forward are really appreciated.

I would like to thank Dr. Robert Stanley (Temple University, College of Science and Technology) for allowing me to run my samples in UV-Vis and fluorescence spectrophotometers.

I would like to thank my intimate friends from Bangladesh for their encouragement, love and continuous supports during my Ph.D. studies. I want to specially thank Sujan and Uttam for motivating me during my hard times through my Ph.D. studies. I would also like to thank my cousin Khokan for taking care of many things on behalf of me in Bangladesh.

I would like to give special thanks to my wife Shikha for her unconditional love, constant support and sacrifices during my Ph.D. study. Without your love and support, I might not able to finish my Ph.D. studies. Above all, thank you for being my best friend. I am indebted to you for everything. Along with my wife, I would like to acknowledge my son Siddhartha. You have fulfilled my life and made my life joyful than ever. Your smile helped me to relive the stresses and gave me extra strength to get things done.

Lastly, I would like to express my profound and sincere gratitude to my late father, my mother and all my family members for their unconditional love, support and encouragement throughout my education life. Thank you all for encouraging me, believing in me and allowing me to follow my dreams.

TABLE OF CONTENTS

Page

LIST OF TABLES

Table Page

LIST OF FIGURES

Figure Page

LIST OF SCHEMES

LIST OF CHARTS

ABBREVIATIONS

Au NPs: Gold nanoparticles

ATP: Adenosine triphosphate

AAZ: Acetazolamide

BCA: Bicinchoninic acid assay

BZA: Benzolamide

CA: Carbonic anhydrase

CAA: Carbonic anhydrase activator

CAI: Carbonic anhydrase inhibitor

CARP: Carbonic anhydrase related proteins

DCM: Dichloromethane

DCP: Dichlorphenamide

DDS: Drug delivery systems

DMEM: Dulbecco's modified eagle medium

DMF: Dimethylformamide

DMSO: Dimethyl sulfoxide

DOX: Doxorubicin

DSC: Differential scanning colorimetry

DTDP: Dithiodipropionic acid

9,10-DPA: 9,10-Diphenylanthracene

EG: Ethylene glycol

ETZ: Ethoxzolamide

FBS: Fetal Bovine Serum

HIF: Hypoxia inducible factor

FIH: Factor inhibiting HIF

ICP-OES: Inductively coupled plasma optical emission spectroscopy

GLUT: Glucose transporter

HPLC: High performance liquid chromatography

HR-MS: High resolution mass spectrometry

LC-MS: Liquid chromatography-mass spectrometry

LTP: Long term potentiation

LA: Lipoic acid

LOX: Lysyl oxidase

MALDI: Matrix Assisted Laser Desorption/Ionization

MCI: Mild cognitive impairment

MCT: Monocarboxylate transporters

MMPs: Matrix metalloproteinases

MTT: Methyl thiazolyl tetrazolium

MW: Molecular Weight

NAD: Nicotinamide adenine dinucleotide

NBS: N-Bromosuccinimide

NMM: N-methylmopholine

NMR: Nucleic Magnetic Resonance

PBS: Phosphate buffer saline

PHD: Prolyl hydroxylase domain

PEG: Polyethylene glycol

PDB: Protein Data Bank

PDK-1: Pyruvate dehydrogenase kinase 1

PFK 1: Phosphofructokinase 1

QD: Quantum dots

RES: Reticulo-endothelial system

SA: Sulfonamide

SAR: Structure activity relationship

SDS-PAGE: Sodium dodecyl sulfate polyacrylamide gel electrophoresis

TDA: Thiadiazole

THF: Tetrahydrofuran

TLC: Thin Layer Chromatography

TPM: Topiramate

TFA: Trifluoroacetic acid

UV-Vis: Ultraviolet-visible spectroscopy

VEGF: Vascular endothelial growth factor

VHL: Von Hippel–Lindau

ZNP: Zonisamide

CHAPTER 1

OVERVIEW AND MAIN RESEARCH GOALS

The reversible hydration of carbon dioxide to bicarbonate ion and a proton ($CO_2 + H_2O \rightleftharpoons HCO_3^- + H^+$) is a simple but very important reaction for most organisms. Under physiologic conditions, this reaction is catalyzed by a class of ubiquitous zinc metalloenzymes, known as ***Carbonic anhydrases*** (CAs, EC 4.2.1.1), present in both prokaryotes and eukaryotes. Six distinct, evolutionary unrelated, gene families encode the structure of different classes of CA enzymes such as α-, β-, γ-, δ-, ζ-CAs and η-CA. In mammals, 15 α-CA isozymes or CA-related proteins (CARPs) have been reported to date, with different catalytic activity, sub-cellular localization, and tissue distribution. They play very important roles in many physiological and pathological processes, including respiration and CO_2 transport between metabolizing tissues and lungs, pH and CO_2 homeostasis, electrolyte secretion, aqueous humor secretion. In addition, CAs modulate biosynthetic reactions such as gluconeogenesis, lipogenesis, and ureagenesis, bone resorption, and calcification. Therefore, they represent potential targets for many therapeutic interventions owing to their diverse functions and to their association with different disease states such as edemas, glaucoma, osteoporosis, obesity, cancer and several neurological disorders [1-3].

Modulation of CA enzymatic activity, i.e. through the use of CA activators and inhibitors, have been reported long ago in the literature [4]. Activation of CA isozymes in brain have been correlated with spatial learning and memory [5] and in this context, may alleviate mild dementias or enhance cognition. On the other hand, several inhibitors are already in clinical use such as acetazolamide, methazolamide, ethoxzolamide, and

dichlorphenamide, for the treatment of glaucoma, epilepsy and hypertension [6]. Over the last decade, researchers discovered a connection between cancer and the expression of certain carbonic anhydrase isozymes, notably CA IX and CA XII. Recent studies have shown that many fast-growing solid tumors become hypoxic and that hypoxia triggers the expression of hundreds of genes, including carbonic anhydrase IX. Consequently, CA IX is over-expressed in many tumor cells and associated with various types of cancers. Thus, CA IX represents a promising target for early detection and treatment of hypoxic tumors, which could be explored either directly, with the development of CA IX selective inhibitors or indirectly, with the development of CA IX targeted drug delivery systems aimed to deliver various theranostic agents selectively to the hypoxic tumors [2].

Our **long term goal** is to treat mild dementias and cancer by modulating the activity of CA isozymes associated with these disease states. The **objective** of this thesis is to design, synthesize and characterize a set of CA activators and inhibitors, and to establish structure-activity relationships in order to identify the most efficient scaffolds and substituents for development as lead compounds in subsequent libraries.

Our **central hypothesis** is that we can generate potent carbonic anhydrase modulators (activators/inhibitors), selective for specific CA isozymes, with the potential to be developed as molecular tools for elucidating the role of CA isozymes and anti-cancer agents. The rationale is that CA activators can be employed for elucidating the role of CA isozymes in brain and also in memory and learning processes, while CA inhibitors can be developed as anti-cancer agents since CA IX is a key isozyme required by hypoxic tumors to thrive.

We decided to test our central hypothesis, and to accomplish the objectives of this thesis by pursuing the following specific aims:

Specific aim 1: To design, synthesize and characterize CA activators with specific physicochemical and activation properties for brain CAs and to establish structure-activity. In this aim, two series of CA activators was synthesized and characterized in terms of physicochemical and biological properties (CA activation potency, isozyme selectivity).

Specific aim 2: To design, synthesize and characterize potent carbonic anhydrase inhibitors of tumor overexpressed CA isozymes CA IX and to translate these carbonic anhydrase inhibitors towards the development and optimization of a gold nanoplatform targeting carbonic anhydrase IX (CA IX) epitope. This aim is proposed to be achieved through three subaims:

Specific aim 2.1 Small MW CAIs. To rationally design, synthesize and characterize small MW CAIs that will efficiently inhibit CA IX and to establish their selectivity against other CA isozymes, drawing structure-activity relationships

Specific aim 2.2 PEGylated bis-sulfonamide CAIs. To design, synthesize, characterize, and evaluate the impact of the PEG linker length within a new series of PEGylated CAIs with different PEG backbone length, using the 1,3,4-thiadiazole-2-sulfonamide warhead and succinyl linker, on in vitro cell killing ability against CA IX expressing cnacer cell lines and CA IX negative cell line.

Specific Aim 2.3 CA IX targeted nanoplatform. To design, synthesize and characterize CA inhibitor conjugates and doxorubicin conjugates required towards the development and optimization of a gold nanoplatform targeting carbonic anhydrase IX (CA IX) epitope, which is overexpressed in many hypoxic tumor cells versus normal tissues.

Based on these specific aims, this dissertation is divided into 6 different chapters. The introduction which details the background and significance of this dissertation is described in Chapter 2. Chapter 3 deals with the development of carbonic anhydrase activators (CAAs), while Chapters 4 details the development and biological evalauation of small MW carbonic anhydrase inhibitors (CAIs). The design, synthesis, characterization and biological evaluation of PEGylated bis-sulfonamides as CAIs are described in Chapter 5. Chapter 6 provides the transalation of PEGylated bis-sulfonamides towards the development and optimization of a gold nanoplatform targeting carbonic anhydrase IX (CA IX) epitope. The working hypothesis and the rationale for each project are described in the first part of the respective chapter.

Chapter 7 of the dissertation presents a summary of the above-mentioned projects and suggests future studies that could further advance the research described in this dissertation.

CHAPTER 2

INTRODUCTION

Carbonic anhydrase: overview, distribution, physiologic roles, structure

Carbon dioxide is the end product of cellular respiration in living organisms and its rapid transport and elimination are very important for achieving faster metabolic rates [7]. Carbonic anhydrases (CAs, E.C. 4.2.1.1) are ubiquitous metalloenzymes that catalyze the reversible hydration of CO_2 under physiologic conditions to produce bicarbonate ion (HCO_3^-) and proton (H^+) (equation 1)[2, 8].

$$CO_2 + H_2O \rightleftharpoons HCO_3^- + H^+ \qquad (1)$$

The uncatalyzed reaction has a kinetic rate that is too slow for physiologic needs, hence unlines the importance of CAs. Through the activity of different CAs present in the body, carbon dioxide can be rapidly hydrated and transported from mitochondria though cytoplasm to the exterior of the cells (Figure 2.1) [2]. It was determined that about 85% of total CO_2 produced in human body is transported as bicarbonate from tissues to lungs, where is excreted. CA and its isozymes are particularly important for the brain hemostasis, because the brain is a major CO_2 producer in the body.

The enzymatic activity of carbonic anhydrase was first observed in the late 1920s in an experiment performed with hemolyzed blood samples, which revealed that the rate of carbon dioxide release from the hemolyzed blood was higher than expected, indicating the presence of a catalyst in blood, which is increasing the rate of reaction [9]. In 1933, Meldrum and Roughton first extracted carbonic anhydrase (CA) from erythrocytes [10]. CA is also found to be ubiquitously in plants [11], where it plays a key role in CO_2

fixation [12] and in almost all living organisms, from unicellular organisms to human. Six evolutionary unrelated gene families encoded their structure, and led to the generation of the α-, β-, γ-, δ-, ζ-CAs and η-CA [13-15]. Only the α-CAs are present in vertebrates and human α-CAs are also present in some algae, bacteria, protozoa, cytoplasm of green plants. Fourteen different α-class CA isozymes were discovered in human body (hCAs) till now [2, 13, 16]. These hCAs have a wide tissue and organ distribution, subcellular localization and possess diverse catalytic activities [2, 17], maintaining the equilibrium of CO_2/HCO_3^- pools in the interior and exterior of cells [17]. Based on the subcellular localization, one can distinguish four subgroups of CA isozymes [18, 19]:

- Cytosolic hCAs (CA I, CA II, CA III, CA VII, CA VIII, CA X, CA XI, and CA XIII).
- Membrane-bound hCAs (CA IV, CA IX, CA XII, and CA XIV).
- Mitochondrial hCAs (CA VA and CA VB).
- Secreted hCAs (CA VI).

In terms of kinetic properties, CA isozymes have turnover numbers for catalysis that range from 10^4 to 10^6 molecules per second. On the basis of catalysis rate, they can be broadly divided into two categories: fast isozymes, such as CA II, CA IV, CA VII, CA IX, CA XII, CA XIII, and slow isozymes such as CA I, CA III, CA V, CA VI and CA XIV [5, 17]. Non-catalytic CA isozymes (CA VIII, CA X and CA XI) - known as carbonic anhydrase-related proteins (CARPs) are structurally related with CAs but do not

possess catalytic activity. Their subcellular localizations and relative enzymatic activity are illustrated in Figure 2.1 [1, 2, 20].

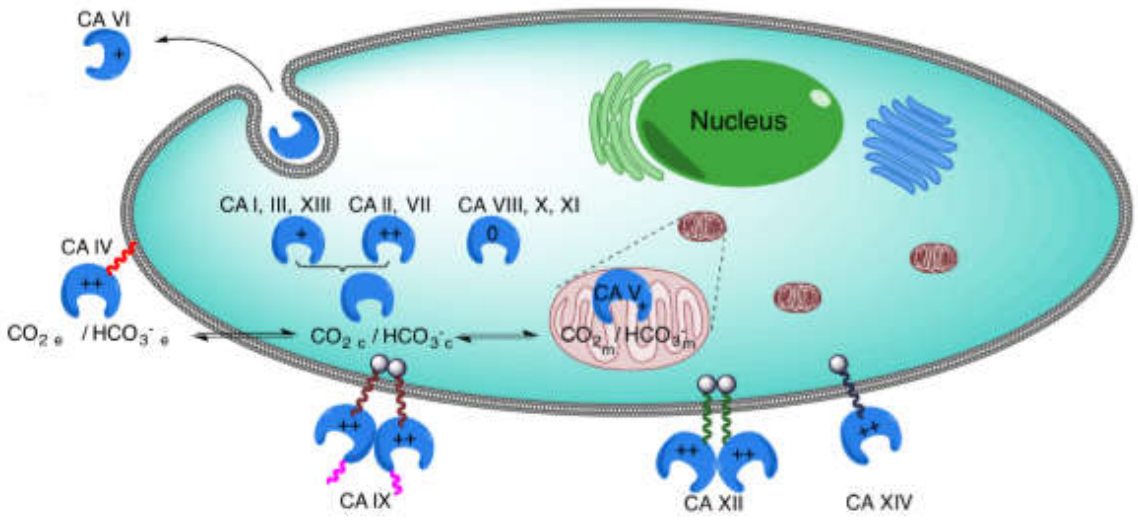

Figure 2.1 Schematic representation of subcellular localization and enzymatic activity of human CAs (devoid of catalytic properties (0), low activity (+), high activity (++)) [18]. The cytosolic CAs, secreted and the mitochondrial CA VA and VB consist only of the CA domain; the membrane-associated CA IV, IX, XII and XIV have a membrane anchor and, except for CA IV, also a cytoplasmic tail, while CA IX is the only isozyme with a N-terminal proteoglycan-like domain. (e, c, m = extracellular, cytosolic and mitochondrial) [2].

Table 2.1 The human CA isozymes discovered to date, with their subcellular localization, catalytic activity, tissue/organ localization/distribution, and physiologic roles [2].

Human CA isozyme	Subcellular localization	Catalytic activity/ Kcat(s-1)	Tissue/organ localization	Dysfunction disease
hCA I	cytosol	moderate /2.0 x 10^5	erythrocytes, GI tract, eye	respiratory, circulatory
hCA II	cytosol	high /1.4x10^6	erythrocytes, GI tract, eye, bone, osteoclasts, kidney, lung, testis, CNS (oligodendrocytes, astrocytes, dorsal root ganglia and neurons)	glaucoma, edema, altitude sickness epilepsy, osteoporosis, gastric ulcer, diabetes, cerebral edema, idiopathic intracranial hypertension.
hCA III	cytosol	low/3.0 x 10^5	skeletal muscle, adipocytes, liver	oxidative stress
hCA IV	membrane-attached	high/1.1 x 10^6	kidney, eye, heart muscle, lung, pancreas, brain capillaries, colon	glaucoma, retinitis pigmentosa stroke
hCA VA	mitochondria	moderate/2.9 x 10^5	liver, mitochondria of neuronal and glial cells	obesity
hCA VB	mitochondria	high/9.5 x 10^5	pancreas, kidney, GI tract, spinal cord, mitochondria of neuronal and glial cells	obesity
hCA VI	secreted (saliva, milk)	moderate /3.4 x 10^5	salivary and mammary glands	cariogenesis
hCA VII	cytosol	high/9.5 x 10^5	CNS, colon, liver, skeletal muscle, duodenum, stomach	epilepsy
hCA-related protein VIII	cytosol	acatalytic (0)	CNS	neurogenerative cancer
hCA IX	trans membrane	high/3.8 x 10^5	tumors, GI mucosa, brain	cancer
hCA-related protein X	cytosol	acatalytic(0)	CNS	ND
hCA-related protein XI	cytosol	acatalytic(0)	CNS	ND
hCA XII	trans membrane	high/4.2 x 10^5	renal, intestinal, eye, tumors, reproductive epithelia, brain	cancer, glaucoma
hCA XIII	cytosol	moderate /1.5x 10^5	kidney, brain, lung, gut, reproductive tract	sterility
hCA XIV	trans membrane	moderate/3.1 x 10^5	kidney, liver, eye, neurons, axons, medulla oblongata, pons, corpus callosum, pyramidal tract, hippocampus, choroid plexus and cerebral white matter.	retinopathy, epilepsy

Focusing on CA structure, the sequence length of CA isozymes ranges from 260 to 459 amino acid residues. There are slight differences in the secondary structures of different CA isoforms. They have approximately 15% α-helices (nine helices and 41 amino acid residues) and 29% β-sheets (18 strands and 77 residues)[21]. Many of these amino acids are conserved across different CA isoforms and this translates into a high degree of structural homology between different isozymes, making the design of isozyme selective modulators a challenging task [22]. The active site of the catalytically able α-CAs contains a zinc ion as a cofactor, which is essential for catalytic activity. The zinc ion is located at the bottom of conical shaped active site (15 Å deep, Figure. 2.2) [2]. It is coordinated by three histidine residues (His-94, His-96 and His-119 in CA II numbering), with the fourth ligand being either a water molecule or a hydroxyl ion in the enzymatic inactive and enzymatically active forms correspondingly. Half of the amino acid residues in active site are hydrophilic, while the other half are hydrophobic residues [2, 13]. The imidazole ring of His-64 amino acid acts a proton shuttling unit for the enzyme. It is involved in the deprotonation of zinc bound water, via a proton wire, to form the zinc-hydroxyl ion. The proton is then transferred to the buffer molecules in the environment, a process that is assisted by a histidine cluster His-4, His-3, His-17, His-15 and His-10 in CA II. This deprotonation process of the Zn-bound water transforms the inactive form of the enzyme ($Zn\text{-}OH_2$) into its active form (Zn-OH).

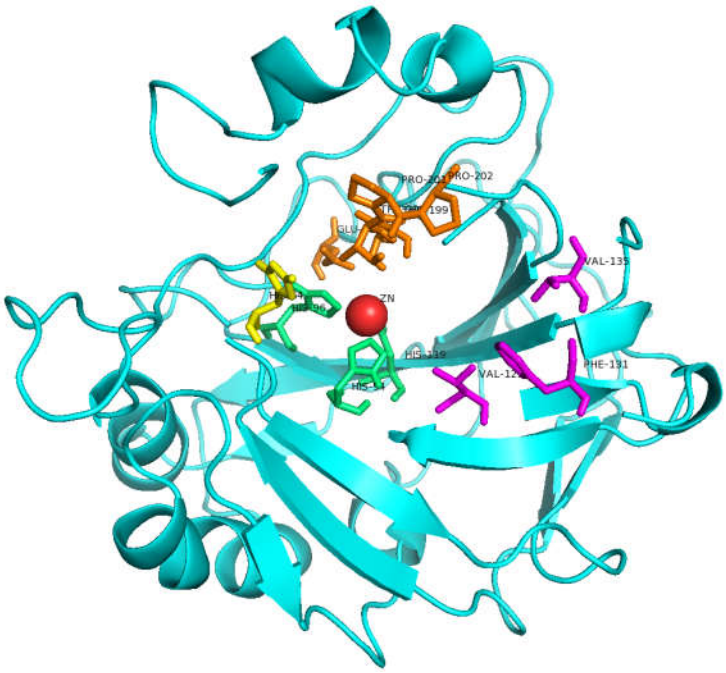

Figure 2.2 X-ray crystal structure of human CA II (PDB: 4RN4), revealing the main features and residues important to catalysis. The hydrophobic amino acids are depicted in magenta, the hydrophilic residues in orange, Zn ion is in red and the proton shuttle His-64 in yellow. Figure made by using PyMol (DeLano Scientific).

As mentioned above, human CA enzymes use Zn^{2+} ion as a cofactor to decrease the pKa of water from 15.7 to 7 in order to facilitate its deprotonation to a hydroxide ion. In the active form of the enzyme, the hydroxide ion bound to the Zn (II), is a very strong nucleophile (Fig 2.3a) [13, 23-29]. The HO^- nucleophile attacks the CO_2 molecule, bound in a hydrophobic pocket comprising residues Val-121, Val-143, and Leu-198 in hCA II (Fig. 2.3b), leading to the formation of bicarbonate coordinated to Zn(II) (Fig. 2.3c). The bicarbonate ion is then displaced by a water molecule and liberated into solution, leading to the inactive acidic form of the enzyme, with water coordinated to Zn(II) (Fig. 2.3d). Deprotonation of the zinc bound water is required to regenerate the active form of the

enzyme. This is the rate limiting step of the catalytic mechanism. Deprotonation is assisted intra-molecularly by the proton shuttle of the enzyme (BH^+ in below figure). In CA II, His-64 acts as a proton shuttle via a proton wire consisting of two water molecules, thus rapidly moving the proton from the active site to the external milieu [30, 31].

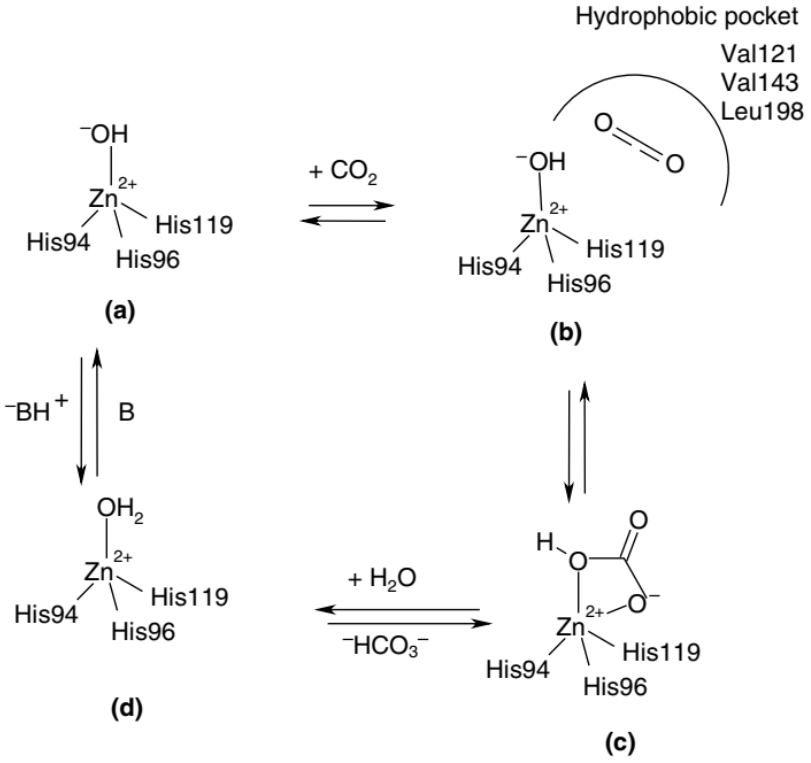

Figure 2.3 Schematic representation of the catalytic mechanism of α-carbonic anhydrases [22].

CA isozymes in central nervous system

While examining Table 2.1 one may observe that certain CA isozymes are present in different parts of the CNS. Some of the CA isozymes-enriched CNS regions are cerebellum, spinal cord, hippocampus, medulla, the brain stem, cerebellum, the choroid

plexus, the luminal surface of cerebral capillaries, and axon's myelin sheath [32]. At the level of choroid plexus, CAs was found to be directly involved in cerebrospinal fluid (CSF) secretion and thus maintain the volume, buffereing capacities and turnover rate of CSF through the production of bicarbonate ion from CO_2 and water [33-35]. Among these CNS parts, hippocampal CA1 pyramidal cells play an essential role in spatial learning in mammals, where the high expression of mitochondrial isoform CA V, cytosolic CA II, CA VII isozymes and the membrane-bound isoforms CA IV and CA XIV, has been reported. While examining the cellular distribution of CA isozymes, it was observed that most CA isozymes are mainly present in neurons, astrocytes and glial cells, in the epithelial cells of the choroid plexus, and in the Purkinje cells of the brain [36-38].

Overall, CAs play a very important role in brain homeostasis and normal cerebral function, which is emphasized in CA deficiency syndrome [39, 40], a distinct genetic disorder characterized by severe pathological modifications of the lungs, kidney, brain and bone metabolism [39]. Human clinical data showed that absence of CA II in these organs and in red blood cells is associated with mental retardation, cerebral calcification, respiratory and renal tubular acidosis, and inherited osteoporosis [39]. It was also found that the level of CA was significantly diminished in Alzheimer's disease compared to healthy adults [41]. In another study, a reduced level of CA was observed in 20-month old rats compared to young rats [1], being associated with a reduced resistance to dehydration, alteration in choroidal control of brain homeostasis, and reduced cerebrospinal fluid production [42]. In several recent redox proteomics studies, the isoforms CA I and CA II found to be oxidized or nitrosylated in the frontal cortex and hippocampus of Alzheimer patients, thus having reduced catalytic activity [43-45],

indicationg a direct connection between reduced CA activity with impaired brain function.

CAs in learning and memory

Although the exact mechanisms of learning and memory are not fully understood, it is believed that hippocampal CA1 pyramidal cells play an essential role in spatial learning in mammals [5, 46, 47]. Sun and Alkon first suggested that carbonic anhydrase activators (CAAs) can enhance learning and memory [5, 48], having the potential to treat/control dementias. In the hidden-platform water maze, rats injected with the CAAs phenylalanine or imidazole had significantly higher latencies to escape. In further support of a CA role in this learning animal model, the CA inhibitor acetazolamide impaired memory and prevented the improvements in learning observed after injection of both phenylalanine and imidazole [5, 49]. Along similar lines, the inhibitor methazolamide infused nasally increased the CO_2 detection threshold and impaired CO_2 discrimination in a discrimination test in rats. The effect of the nasally infused methazolamide lasted 6 h but was reversed by 24 hours [50]. These data support the hypothesis that olfactory neurons exhibit CA activity and suggest a role for this enzyme in the transduction mechanism of CO_2 chemoreceptors. Memory improvements in rodents have also been suggested through CA activation with the dipeptide carnosine [51]. With our team's experience in designing CAAs and high throughput models for evaluating learning and memory in mice, a novel set of compounds was developed (described below in Chaper 3), with the potential to be developed as nootropics in order to help millions of people with mild dementias where memory and learning is impaired.

Carbonic anhydrase inhibition

Carbonic anhydrase inhibition and CA inhibitors (CAIs) were discovered almost immediately after the enzyme was characterized [10]. CA inhibitors can be divided into two main classes: metal complexing inorganic anions and organic ligands [2, 19]. The metal complexing small anions include CN^-, HS^-, SCN^-, CNO^-, N_3^-, X^- (X = F, Cl, Br, I), NO_3^-, HSO_3^-, SO_4^{2-}, ClO_4^-, R-COO^-, etc. These anions bind with different affinities to the Zn^{2+} ion, leading to the formation of trigonal bipyramidal and other related adducts, thus interfering with the catalytic mechanism of the enzyme. Organic CAI ligands include sulfonamides, sulfamates, sulfamides, hydroxamates, and the very recently introduced xanthates, polyamines, and phenol derivatives. Among these various classes of inhibitors, sulfonamides are the most investigated and used CAIs in physiological and pharmacological studies, as well as in clinical use. They bind in a tetrahedral geometry of the Zn(II) ion (Figure 2.4), in deprotonated state, with the nitrogen atom of the sulfonamide moiety coordinated to Zn(II), also forming an extended network of hydrogen bonds, involving residues Thr199 and Glu106. The aromatic/heterocyclic part of the inhibitor (R) interacts with hydrophilic and hydrophobic residues of the cavity. Early inhibition studies established that only the aromatic and heteroaryl primary sulfonamides (R-SO_2NH_2, R = Aryl, Hetaryl) are efficient CA inhibitors.

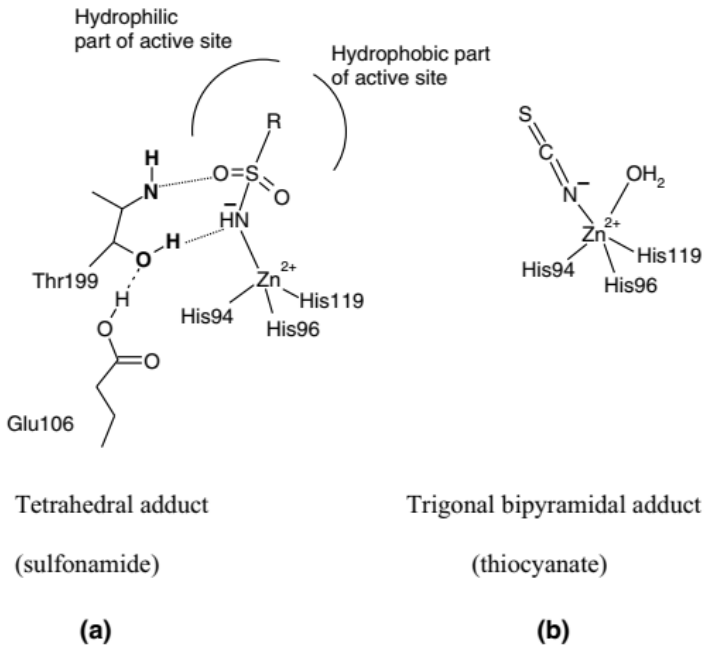

Figure 2.4 Human CA inhibition mechanism by a) organic ligands such as sulfonamide and by b) anionic ligands such as thiocyanate [2, 22].

CAIs in disease states and in cancer detection and treatment

After the initial discovery of sulfonamides as CAIs, a large number of sulfonamide, sulfate or sulfamide derivatives were designed, synthesized and investigated as CAIs through a rational drug design processes. Currently, there are over 30 clinically used drugs or chemical entities in clinical development reported to possess significant CA inhibitory properties. Some of the clinically used compounds such as acetazolamide **1**, methazolamide **2**, ethoxzolamide **3**, dichlorphenamide **4**, were initially developed in the search of novel diuretics or antiepileptics in the 1950s and 1960s [22]. They were subsequently employed for systemic treatment of glaucoma and are still in use in ophthalmology [2, 52]. However, further physicochemical optimization for topical administration while preserving the CA inhibition potency led to the development of two

novel derivatives dorzolamide **5**, brinzolamide **6** as topical antiglaucoma agents (Chart 2.1). Since very diverse inhibition profiles were obtained with different series of carbonic anhydrase inhibitors, these agents are used clinically as diuretics, antiglaucoma agents and antiepileptics [6]. They are also used in the management of mountain sickness, osteoporosis, gastric and duodenal ulcers [53, 54]. Two other drugs, zonisamide **7** and topiramate **8**, approved by FDA in 2003 and 1996 respectively as antiepileptic agents and ad anti-obesity agents, also possess significant CA inhibitory potency [2, 22, 55, 56]. Recently, the inhibitory effects against different over expressed CA isozymes have been investigated in various disease states such as cancer. Over the last decade, a connection has been established between cancer and the expression of two transmembrane CA isozymes, namely CA IX and CA XII. These isozymes were found to be overexpressed in tumors, where they are involved in pH regulation and tumor progression [57, 58].

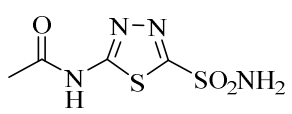

1 Acetazolamide (AAZ)

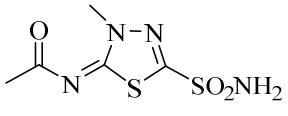

2 Methazolamide (MZA)

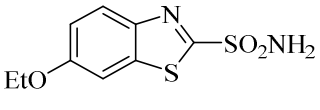

3 Ethoxzolamide (EZA)

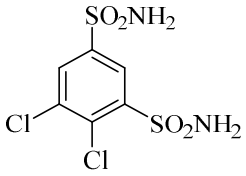

4 Dichlorophenamide (DCP)

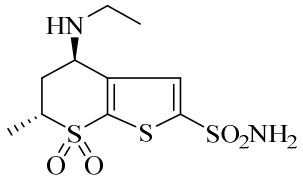

5 Dorzolamide (DZA)

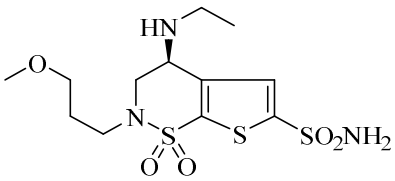

6 Brinzolamide (BRA)

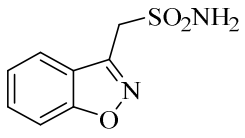

7 Zonisamide (ZNP)

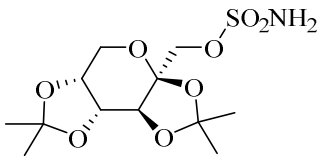

8 Topiramate (TPM)

Chart 2.1 CA inhibitors in clinical use, designed either for systemic use or for topical administration [2].

Cancer is the second most common cause of death in the US, accounting for 25% of deaths [59]. It is a complex group of diseases characterized by abnormal growth of cells with possibility to spread and invade other organs in the body. Multiple factors lead to the development of cancer such as genetic and epigenetic mutations as well as chromosomal abnormalities that result in activation of the oncogenes and suppression of the tumor suppressor genes such as p53 [60, 61]. As a result, normal cells metamorphose into malignant cells and lose their normal functions.

The process of cancer cell proliferation, differentiation, survival and metastasis is governed by various features. One of these hallmark features is characterized by their upregulated glucose metabolism [62, 63]. This feature was first observed by Otto Warburg, hence it is called Warburg's effect [64]. In normal cells glucose is metabolized via glycolysis to pyruvate, which is subsequently oxidized in the mitochondria through the citric acid cycle and oxidative phosphorylation to form carbon dioxide and water, producing 38 moles of ATP per molecule of glucose (Figure 2.5). Uncontrolled cell growth and lack of adequate vasculature make the tumor cells hypoxic due to lack of enough oxygen [2, 65, 66]. Oxidative phosphorylation cannot occur in hypoxic tumor cells. Consequently, in order to cope up with the energy needs, hypoxic tumor cells shift their regular metabolism towards glycolysis, and consequently convert most of the pyruvate to lactate (anaerobic glycolysis) in order to generate $NAD^{+,}$ required for the glycolysis to continue. Glycolysis is a very energy-inefficient process and produces only 2 moles of ATP per single mole of glucose (Figure 2.5) [64]. Moreover, it was found that tumor cells favor the glycolysis process even upon reoxygenation as they obtain metabolic intermediates like lactate and pyruvate that are used for the biosynthesis of

nucleotides, amino acids and lipids. This gives the cancer cells a selective advantages against the normal cells, which leads to the rapid proliferation of these cells to form tumors, with the possibility to invade adjacent normal structures [64].

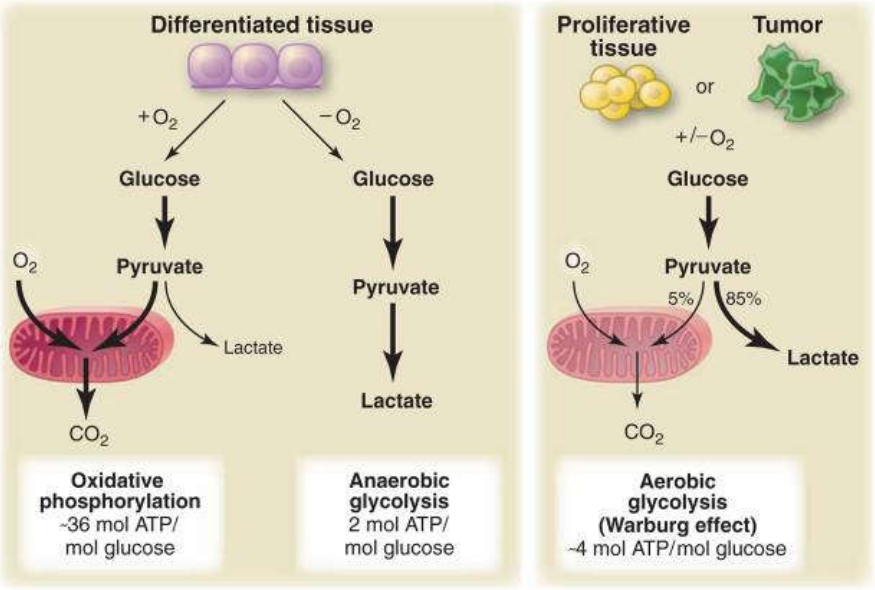

Figure 2.5 Schematic representation of the differences between oxidative phosphorylation, anaerobic glycolysis, and aerobic glycolysis (Warburg effect). Normal cells mainly undertake oxidative phosphorylation in presence of oxygen, while tumor cells, irrespective of the presence of oxygen, overexpress glycolysis for their energetic and biosynthetic needs [64].

Hypoxia further induces the overexpression of several transcription factors, out of which the most important one is the Hypoxia Inducible Factor-1 (HIF-1). HIF-1 expression in turn triggers the expression of nearly 500 genes [2, 65, 66]. Under normal O_2 level, this HIF-α is rapidly degraded in the cytoplasm through hydroxylation by prolyl hydroxylase domain (PHD) and factor inhibiting HIF (FIH), followed by binding and

ubiquitination by von-Hippel Lindau tumor suppressor protein (VHL) (Figure 2.6) [67, 68].

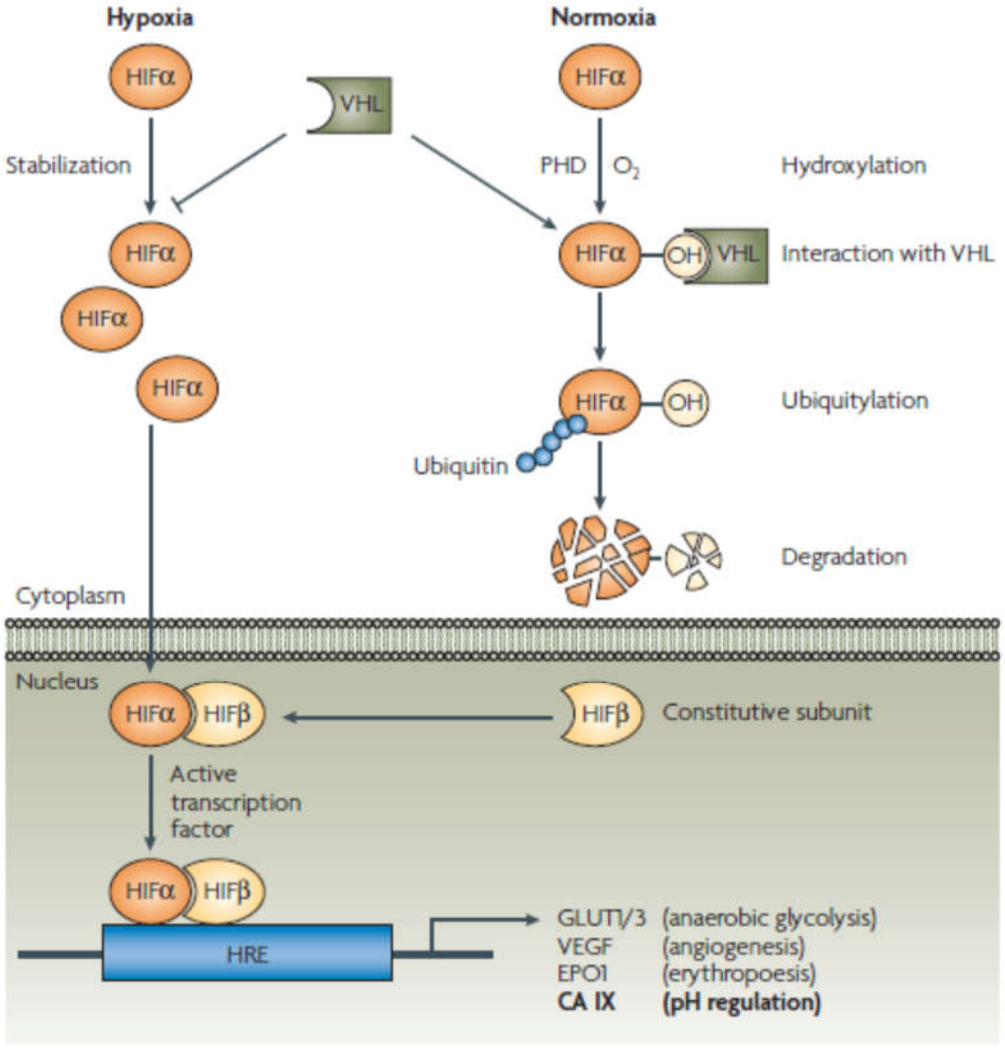

Figure 2.6 Mechanism of hypoxia-induced gene expression mediated by the HIF transcription factor [2].

However, under hypoxic conditions both PHD and FIH lose their activity which results in the stabilization of HIF-α that accumulates into cytoplasm and relocates to the nucleus. In the nucleus, it binds transcription factor HIF-β and their association triggers the expression of genes that encode proteins such as vascular endothelial growth factor

(VEGF) and matrix metalloproteinases (MMPs) for angiogenesis and tissue remodeling, carbonic anhydrase IX (CA IX), lysyl oxidase (LOX) that support metastasis as well as glucose transporters (GLUT-1), mono carboxylate transporter 4 (MCT 4) and pyruvate dehydrogenase kinase 1 (PDK-1), which are essential for survival of cancer cells under hypoxic conditions (Figure 2.6) [69, 70].

Among these proteins that are necessary for cancer cell proliferation and survival is the membrane bound carbonic anhydrase CA IX (Figure 2.7). CA IX is a dimeric membrane-bound CA isozyme, attached on the outer surface of plasma membrane, where it regulates the extracellular pH and CO_2/HCO_3^- pools [57, 71, 72]. Importantly, its role becomes critical in hypoxic tumors, where glycolysis is upregulated to supply the fast dividing cancer cells with ATP and cellular building blocks [73, 74]. Here, CA IX works in tandem with cytosolic isozymes, especially CA II, to facilitate the efficient transport of glycolytic protons from cytoplasm to exterior of the cell (Figure 2.7) [57, 72, 75], while maintaining the internal pH within normal limits (around 7.2). Consequently, proton export leads to a reduction in the extracellular pH (pHe = 6.8) [2, 65, 66]. This is a salient feature of the tumor microenvironment and gives a substantial Darwinian growth advantage to cancer cells over normal cells, as normal cells undergo apoptosis in response to continuous exposure to such acidic environment (Figure 2.7).

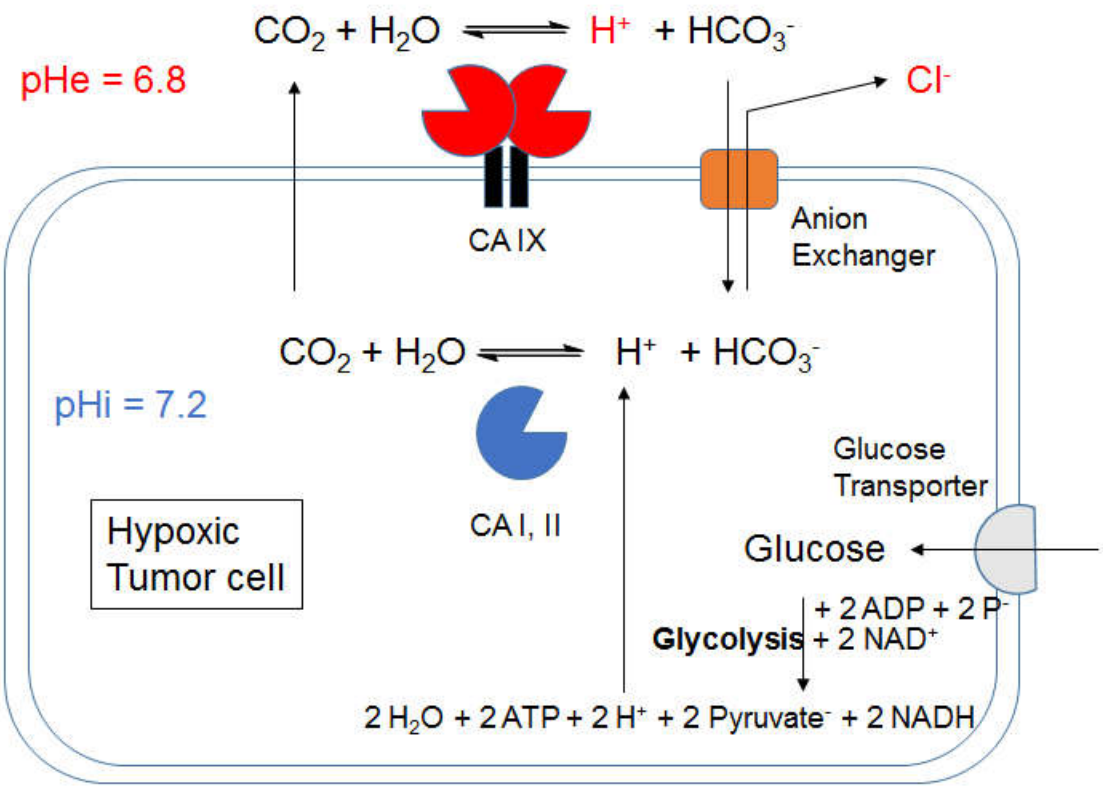

Figure 2.7 The role played by isozyme CA IX in pH homeostasis of cytoplasm of hypoxic tumor cells. Protons produced in glycolysis react with HCO_3^- (catalyzed by cytosolic CA I, CA II) and the CO_2 formed permeates the plasma membrane, leaving the cell. In the extracellular space CO_2 is rehydrated to H^+ and HCO_3^- by membrane-bound CA IX, and HCO_3^- is exchanged for Cl^-, entering the cell. The net effect is H^+ transport from cytoplasm (that remains at pH = 7.2) to extracellular space, which becomes acidic [57, 72].

Thus, CA IX is over-expressed in many tumor cells, and was associated with poor prognosis in breast [76-78], colorectal, [79-81], ovarian [82, 83], bladder [84], head and neck [85], cervical [86, 87], brain [88], pancreatic [89] and renal cancer [90]. The expression of CA IX and CA XII in normal tissues and in tumors is shown in Figure 2.8.

However, normal expression of CA IX in the human body is restricted to the epithelium of stomach, duodenum and upper small intestine [57, 91]. On the other hand, CA XII was found to be co-expressed with CA IX in several tumor tissues but was also found in a wide range of normal tissues. As CA IX is overexpressed in a large variety of cancer cells, chemical entities that can selectively inhibit overexpressed CA IX may have therapeutic value for detection, imaging and treatment of a large variety of hypoxic tumors.

Consequently, inhibition of CA IX was exploited for detection, imaging and killing of hypoxic solid tumors [57, 72, 92, 93]. Unfortunately, the CA IX active site(s) share(s) a high structural homology to other CA isozymes, all being efficiently inhibited by (unselective) classical CA inhibitors such as aromatic and heterocyclic sulfonamides, and their sulfamide and sulfamates isosteres [57, 58, 93]. Despite this fact, our team has shown that it is possible to obtain selective inhibitors for membrane CA isozymes, including CA IX, by making the CA inhibitors membrane-impermeant, either though attached charged moieties [94-96] or via oligoethyleneglycol- and polyethyleneglycol (PEG) conjugation [92]. The PEG-ylated CA IX inhibitors from the last category recently proved able to control the growth of several hypoxic carcinomas over-expressing CA IX [92]. One of the goals of this thesis was to continue the development of CA IX potent inhibitors and to attempt to enhance their selectivity against the other CA isozymes.

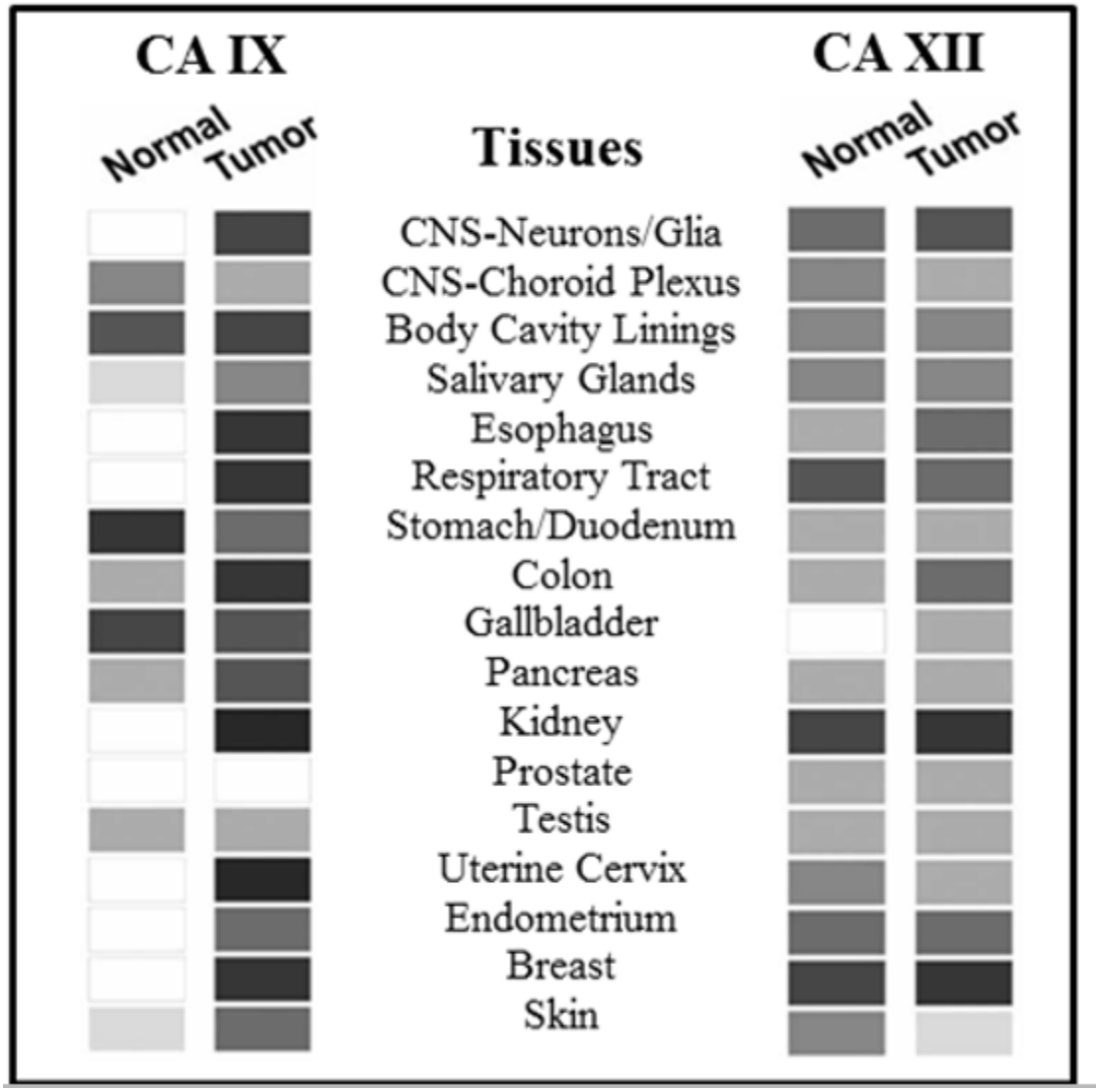

Figure 2.8 Distribution of CA IX and CA XII in human normal tissues and corresponding tumor tissues. The intensity of the gray color represents the level and frequency of expression. Adapted with permission from [97].

Drug delivery system in cancer treatment

Focusing on cancer treatment, one may emphasize that the success of conventional cancer therapy is limited due to the non-specific biodistribution of chemotherapeutic drugs. As a result, high doses of drugs are required to obtain the

therapeutic effects, posing a vicious cycle of massive doses and subsequent toxicities to normal cells. This narrowed down the therapeutic index of the chemotherapeutic drugs with increased risk of developing multiple drug resistance [98]. The development of efficient drug delivery systems able to deliver the drugs specifically to the cancer cells offers a possible solution to this problem.

Consequently, nanotechnology-based drug delivery systems emerged over the past two decades and represent a promising platform technology for safe and efficient delivery of chemotherapeutic drugs and diagnostic agents [99, 100]. Nanosystem-based drug delivery systems (DDSs) offer several advantages over conventional cancer treatments such as 1) better delivery efficiency owing to unique physicochemical properties with size in the nano domain, which allow them to overcome delivery barriers and selectively deliver the cytotoxic cargo to the tumor site, minimizing the systemic toxic side effects [101]; 2) high drug loading capacity; 3) enhanced intratumoral accumulation and intracellular uptake owing to their small size, which ranges from 1 nm-100 nm; 4) longer circulation time in the blood, as compared to free drugs which are rapidly cleared from the body, due to their optimal size and surface modification with hydrophilic polymers such as polyethylene glycol (PEG); and, 5) co-delivery of different types of drugs and/or diagnostic agents in combination therapy [100].

Apart from therapeutic applications, various nanosystems such as quantum dots (QD), gold nanoparticles (GNPs), superparamagnetic iron oxide nanoparticles have been applied in the field of tumor imaging and diagnosis, owing to their unique optical, magnetic, and acoustic properties [102-105].

Different nanosystem based DDSs mainly employed two distinct strategies for targeting the tumor microenvironment, namely passive targeting and active targeting [106]. Passive targeting mainly works through enhanced permeation and retention phenomenon (EPR effect) in which the nanoparticle based drugs enter into the tumor interstitium through the leaky vasculature of tumor having fenestrations [107]. However, in order to get significant benefit from the EPR effect, the nanoparticles should have long circulation time [108], which can be achieved by surface modification of nanoparticles with water soluble polymers such as polyethylene glycol (PEG) [109]. Passive targeting proved to be less efficacious therapeutically, due to limited uptake of the nanoparticles by the tumor, unwanted uptake by scavenging organs such as liver and spleen, slow release of the encapsulated drug, non-uniform distribution of the nanoparticles within the tumor microenvironment owing to heterogeneous nature of the tumor growth [110].

On the other hand, active targeting was found to be an effective strategy for enhancing uptake of chemotherapeutics in various tumor tissues. In this strategy, nanoparticles are functionalized with target specific-ligands, which have high binding affinity towards specific receptors overexpressed in the tumor tissue. Some of the targeting ligands help in cellular uptake by receptor mediated endocytosis process [111]. Various targeting ligands such as antibodies, proteins, peptides and small molecules, have been employed in cancer research so far [112-114].They can be conjugated directly to nanoparticle surfaces or coupled to PEG backbone in case of PEGylated “stealth” systems [115].

Several classes of nano DDSs with different characteristics have been developed so far to deliver different classes of drugs (Figure 2.9). The most common nanoparticles

based DDSs in cancer therapy are drug conjugates such as protein drug conjugates, lipid drug conjugates, polymeric nanoparticles, solid nanoparticles (carbon nanotube, metal particle), liposomes and other solid-lipid hybrid particles [116-119].

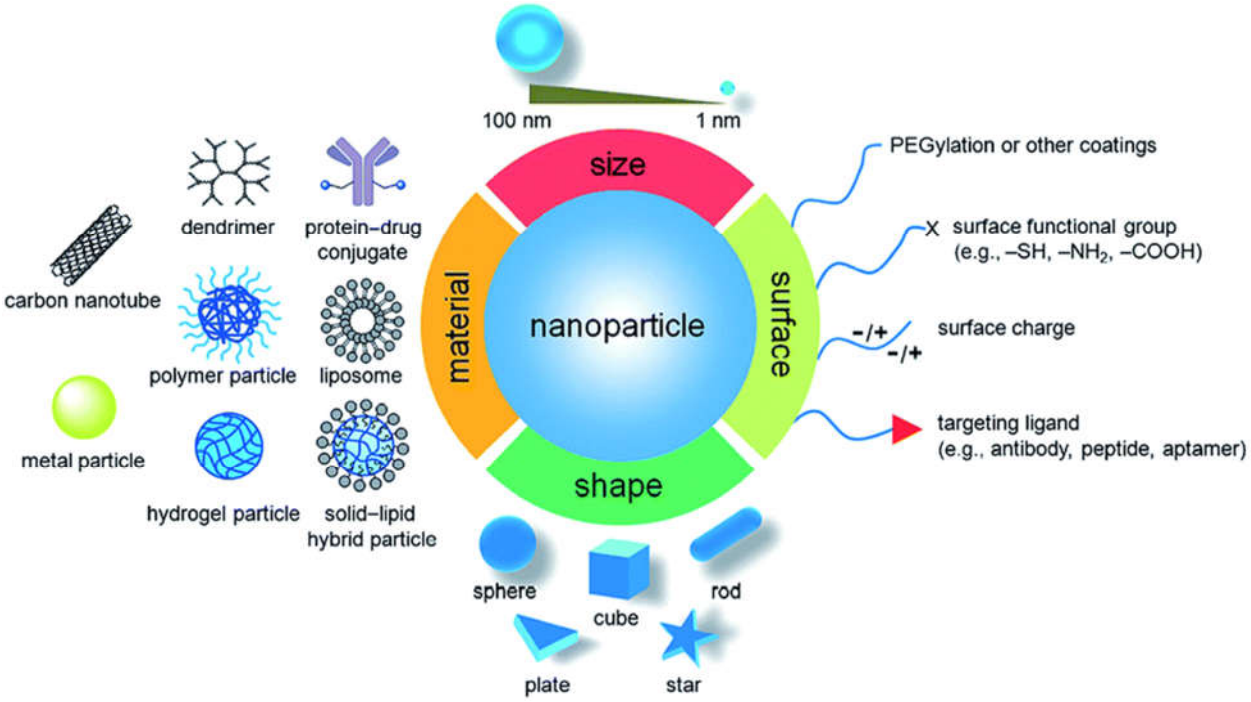

Figure 2.9 Schematic overview of different nanotherapeutic platforms. Adapted with permission from [100].

Gold nanoparticles (Au NPs) have emerged as a robust and versatile platform technology for diagnostic and delivery purposes during recent years, due to their unique physicochemical and optical properties and excellent biocompatibility [120-124]. Examples of biological applications include delivery of enzyme inhibitors [125], activators [126], various drugs[127-129], oligonucleotides [130] and nucleic acids[123, 131]. Au NPs can be synthesized reliably in a variety of sizes and shapes and can be functionalized with a plethora of ligands in order to achieve optimum ligand

concentrations and the desired functional designs [120-123, 132, 133]. Using ligands strategically designed against epitopes expressed on cells in different pathological states, along with various drug conjugates, Au NPs can act as targeted delivery systems in the treatment and detection of various dysfunctions and diseases, including cancer [129, 134, 135]. It must be emphasized that solid tumors are very heterogenous and hypoxic in nature, witih plastic metabolism and fast mutation rate. These make them resistant to many chemotherapeutic agents and thus very difficult to treat by conventioal dosage forms [62, 73].

Building on these studies, our goal is to transform CAI and their conjugates into targeting ligands for DDSs such as gold nanoparticles, in an attempt to focus their action to hypoxic tumor cells. Moreover, another goal of our research is to combine the CA IX inhibition by CAI-decorated AuNPs with co-delivery of chemotherapeutic agent doxorubicin to hypoxic cancer cells in order to enhance the cytotoxic effect and tumor killing.

Focusing on the drug cargo, it must be emphasized that doxorubicin is considered to be one of the most effective chemotherapeutic drugs, making it a first line treatment to cure many types of cancer such as lung, breast, ovaries and multiple myeloma [136, 137]. It acts through intercalation in between DNA base pairs and also inhibits topoisomerase II, responsible for relaxing of supercoiled DNA, thus preventing DNA transcription and translation. Doxorubicin was also found to promote free radical formations, resulting oxidative damage to DNA, proteins and cell membrane lipids [138]. The drug is very toxic for normal cells due to the combined effect from multiple mechanism of actions. The IV administration of free doxorubicin associated with severe side effects such as

dose-dependent cardiotoxicity, myelosuppression, mucocutaneous reactions, nausea, vomiting and hyperpigmentation of the skin [139, 140]. These premises raise the demand to deliver the drug to the tumor cells in a selective manner, which we believe it could be ensured by our designed Dox-loaded Au NPs targeted against CA IX epitope over-expressed in hypoxic tumors.

In this context, we highlight that Supuran et al. showed that efficient CA inhibition can be achieved with gold nanoparticles decorated with short CAI inhibitors [125]. Supuran and Winum also proved that these CAI decorated Au NPs can enhance the CA IX binding through cooperativity and bivalent binding with CA IX [125]. More recently, Ratto showed that gold nanorods decorated with CAI could be targeted to hypoxic cells, where they are actively endocytosed and can elicit tumor killing through thermal effects [141]. Also, importantly, CA IX inhibition was recently shown to prevent resistance of tumors to chemotherapeutic drugs such as melphalan and doxorubicin [142, 143], which makes our proposed dual technology particularly appealing. Thus, another goal of this dissertation was to design, synthesize and characterize a series of CAI conjugates and doxorubicin conjugates in order to dual functionalize the gold nanoparticles for the selective delivery of doxorubicin.

CHAPTER 3

DESIGN, SYNTHESIS AND CHARACTERIZATION OF CARBONIC ANHYDRASE ACTIVATORS

In this chapter, our goal was to design, synthesize and characterize CA activators employing structure based drug design approach, with specific physicochemical and activation properties, targeting the brain CAs and to establish structure-activity relationships.

Our working hypothesis is that X-ray crystallographic study of potent and selective histamine pyridium CAAs (previously developed by our lab) will reveal important drug design insights on the binding of these activators into the CA active site cavity. This allows subsequent relevant design modification of the existing histamine pyridium CAAs and ethylene bis-imidazoles CAAs, based on these X-ray findings, to develop a new series of CAAs with improved potency and selectivity towards brain relevant CA isozymes. The rationale behind the hypothesis is described below.

Background and design approach

CA activators (CAAs) remained largely unexplored for a long time, although activation of CA was reported simultaneously with CA inhibition[144]. The exploration of CAAs was re-ignited two decades after, when Ho and Sturtevant first reported the activation of CA with EDTA in 1960 [145]. Silverman et al. identified several small molecules as CA activators such as histamine [146], imidazole, histidine [147-149], which are closely related structures to the proton shuttling group His-64 of the enzyme.

Coleman et al. also investigated the CA activation with lysine, polylysine, imidazole, glycine, and histamine in 1989 [150]. Despite all these studies the field did not develop much, especially due to lack of applications for CAAs.

As mentioned in the significance section, the rate-limiting step of the CA catalytic cycle is the deprotonation of zinc-bound water to form a zinc-hydroxide species, which constitutes the active form of the enzyme (equation (2) in the catalytic mechanism). It was hypothesized that CA activators bind within the enzyme active site with the formation of enzyme-activator complexes and act by speeding up the deprotonation of zinc bound water in the rate-determining step [31], with generation of the active form of the enzyme [147]: (see equations 3 below)

$$EZn^{2+}\text{-}OH^- + CO_2 \rightleftharpoons EZn^{2+}\text{-}HCO_3^- \overset{+H_2O}{\rightleftharpoons} EZn^{2+}\text{-}OH_2 + HCO_3^- \quad (1)$$

$$EZn^{2+}\text{-}OH_2 \rightleftharpoons EZn^{2+}\text{-}OH^- + H^+ \quad \text{-rate determining step-} \quad (2)$$

In the presence of an activator '**A'**, equation (2) becomes (3):

$$\mathbf{EZn^{2+} - OH_2 + A \rightleftharpoons \left[EZn^{2+} - OH_2 \text{------} A \rightleftharpoons EZn^{2+} - OH^- \text{------} AH^+ \right] \rightleftharpoons EZn^{2+} - OH^- + AH^+} \quad \mathbf{(3)}$$

enzyme-activator complex

Kinetic and crystallographic studies revealed that the activator does not influence the K_M (the affinity of the enzyme for the substrate) and only increases the k_{cat} of the enzyme-catalyzed reaction [151, 152]. Studies of Co(II)-substituted CAs with CA activators histamine and dopamine further proved that the activator does not interact with the metal ion and that the activator binds far away from metal ion within the active site cavity [151, 152]. Several X-ray crystal structures of CA with amines and amino acid activators such as histamine **11**, L- and D-His **22**, **23** (Chart **3.2**), L- and D-Phe, and D-

Trp proved again that activator binding site is located far away from the zinc ion, toward the edge of the active site cavity, in the opposite part of active site region where His-64 is found (Figure 3.1a)[152-155]. All these activators except D-Trp bind to the same site, believed to be one of the possible main activator binding sites (Figure 3.1a).

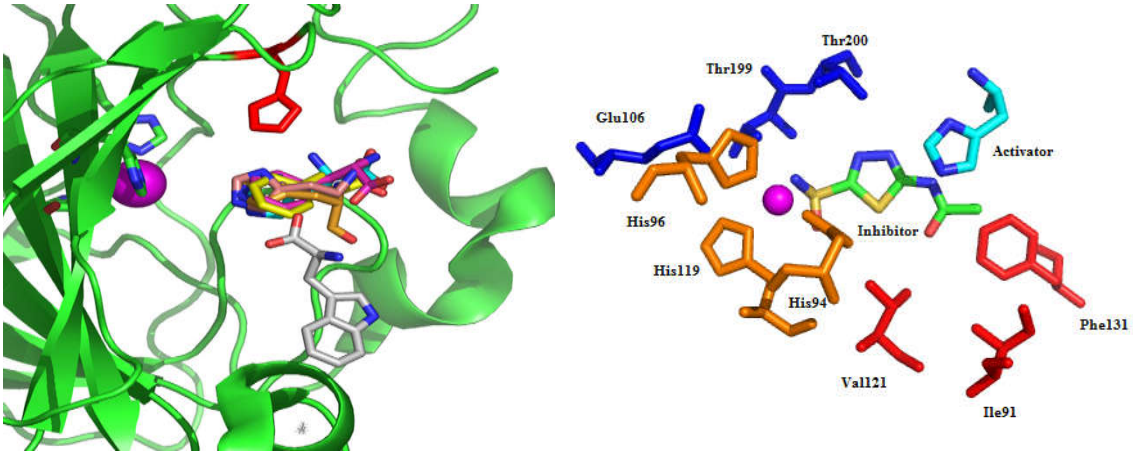

Figure 3.1 a) Superposition of the X-ray crystal structures of hCA II complexed with several activators: histamine (pink, PDB: 1AVN), L-His (gold, PDB: 2ABE), D His (blue, PDB: 2EZ7), L-Phe (magenta, PDB: 2FMG), D-Phe (yellow, PDB: 2FMZ), D-Trp (grey, PDB: 3EFI), His 64 (red). The zinc ion is shown as violet sphere. b) Binding of inhibitor acetazolamide **AAZ 1** (green, PDB: 2HOC) and activator L-histidine **22** (cyan) in the active site of CA II isozyme, revealing that activator binds far away from metal, in a site different from the inhibitor binding site [152-155].

In contrast, X-ray crystal structure of sulfonamide inhibitor acetazolamide **1** showed that the inhibitor binding site is different from the activator binding site (Figure 3.1b). The crystal structure of histamine- CA II adduct confirmed the mechanism of CA

activation (Figure 3.2). Thus, as mentioned earlier, histamine binds into the activator-binding site and participates in favorable interactions with active site amino acids and water molecules. Through a network of water molecules the imidazole moiety of histamine tranfers the proton from zinc bound-water to the external buffers, in a similar fashion as the natural proton shuttle residue His-64, and facilitates the formation of the zinc hydroxide active form of the enzyme (Figure 3.2).

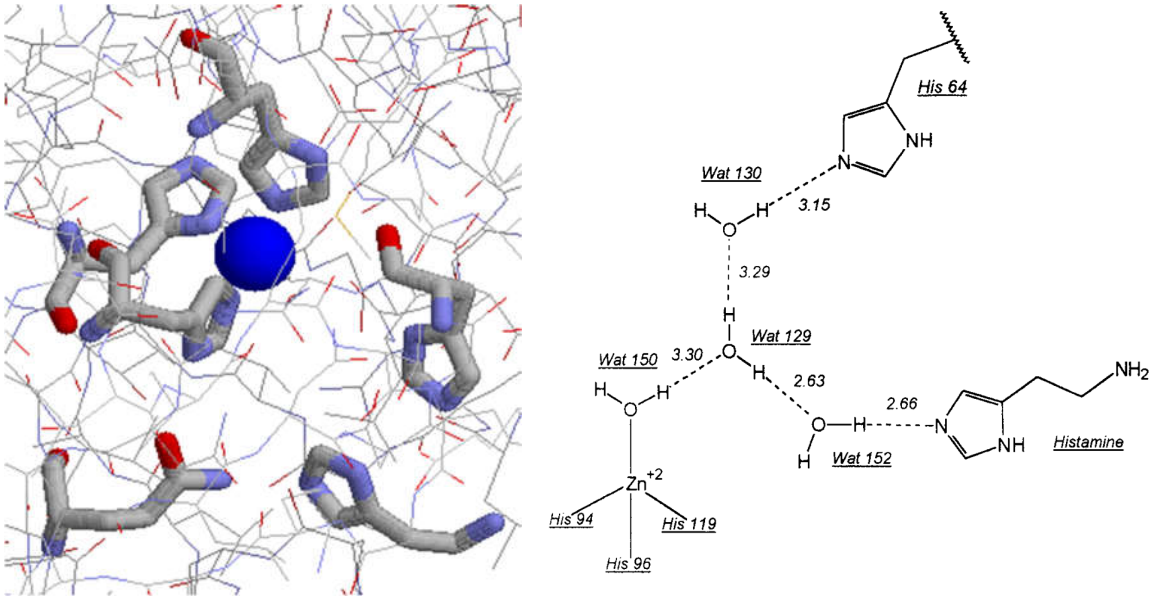

Figure 3.2 Schematic of proton shuttling in histamine-CA II adduct, showing the proton shuttle residue His-64 of the enzyme and the main proton wire (Wat 130, Wat 129) and the CAA histamine **11** acting as a secondary proton shuttle through Wat 152 [152].

Towards the generation of potent and selective CAAs, our group designed and synthesized several series of CA activator molecules [17, 77, 146, 156]. A comprehensive structure-activity relationship (SAR) studies done by our team identified that efficient CA activators (CAAs) possess a proton-shuttling group attached to a

hydrophobic/amphiphilic aromatic/heterocyclic anchor via a short, flexible linker (Chart 3.1) [157].

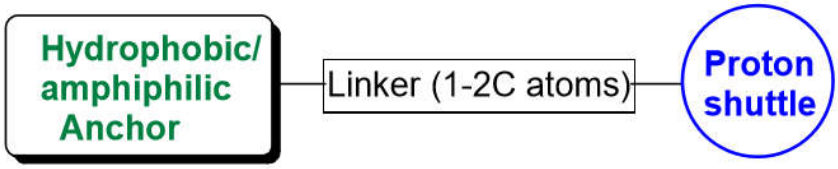

Chart 3.1 General structure of a carbonic anhydrase activator, involving a proton shuttling moiety (blue), attached to a hydrophobic/amphiphilic anchor via a short (1-2 C atoms) linker.

Therefore, CAAs with different proton-shuttling moieties and anchors have been explored by our team and by others over the last two decades (Chart 3.2). From various proton shuttling moieties assessed, we identified imidazole and primary amines as efficient shuttling moieties, in combination with various anchors. In the early design of CAAs, a primary amine was employed as main proton shuttling unit. Thus, the first generation of CAAs tested proved that phenylalanine **9**, tyrosine **10**, and histamine **11** (Chart 3.2), and other amino acids and biogenic amines, all bearing a primary amine, can act as potent CAAs for both isozyme CA I and CA II. Within this design, serotonin **12** displayed moderate efficiency in activating CA isozyme [158]. In the design of second generation of CAAs **13-15**, the primary amine was retained as proton shutting unit and was attached to different heterocyclic amphiphilic anchors. Among these compounds, CAA **15**, having the pyridinium moiety as anchor, proved to be particularly efficient. Activation of CA with bis-(N1)-azoles such as bis-(N1)-imidazole **16** was also reported almost simultaneously with histamine **11**, in which one imidazole moiety acts as

hydrophobic amphiphilic anchor and another one acts as proton shuttle (Chart 3.2) [159, 160]. These findings prompted the reinvestigation of the mechanism of CA activation by histamine **11**, which posesses two moieties that can shuttle protons.

An analysis of the X-ray crystal structure of CA II adduct with histamine **11**, done by Briganti et al.[152], revealed that the activator histamine is anchored at the entrance of the active site cavity through its imidazole moiety, which shuttles the protons from the active site to the bulk solvent, and acts as a second proton shuttle of the enzyme, in addition to His-64 (Figure 13). The amino group does not shuttle protons and thus can be derivatized to enhance the anchoring of the CAA into the active site of the enzyme. Consequently, various azoles have been employed as proton shuttling moieties in combination with different hydrophobic/amphiphilic anchors in the subsequent designs, yielding powerful CAAs such as 1,2,4-triazole pyridinium derivative **17** and 4-imidazole-pyridinium derivative **18** [146]. Several key SAR studies from our team [146, 161], supported by X-ray crystallography studies [89, 152, 153, 162-166], clearly established imidazole moiety as one of the most efficient proton-shuttling groups available. In fact, the imidazole moiety (pKa = 6–7) is a superior proton-shuttling group as compared to the primary amino moiety (pKa = 9–10), because its pKa is very close to the pKa of Zn-bound water of ~ 7, thus facilitating deprotonation and transfer of H^+ to the external buffers [89, 152, 153, 162-166].

The design was further exploited in the generation of several series of activators bearing imidazole as main proton shuttling units in combination with various anchors such as pyridinium [77, 161], peptidyl [167] and other anchors (Chart 3.2). Subsequently, other groups also reported carbonic anhydrase activators bearing imidazole moiety, such

as 4-bromoethylimidazole (4-BEI, **19**), 2-chloromethyl-imidazole (2-CMI, **20**) [164, 168].

These studies reconfirmed the reliability of imidazole moiety in CA activation. Our team also reported several series of CA activators utilizing imidazole as proton shuttling unit in combination with various anchors such as (4-methylimidazole **21**, L- and D-histidine (**22** and **23**), carnosine **24** and congeners), and, more recently, 4-(pyridinium-ethyl)imidazoles **25a-z**.

One problem foreseen with the pyridinium imidazole CAAs **18** and their congeners was the reduced mobility of the azole ring, which is directly attached to the pyridinium moiety. This direct connection between the two heterocyclic systems has a significant influence on the electronic properties of both aromatic systems and on their relative conformations. The positively-charged pyridinium group diminishes the pKa of the imidazole moiety and reduces its proton shuttling capabilities due to a strong electron-withdrawing effect. To overcome this problem, our group developed a new series of pyridinium imidazoles represented by CAAs **25a-z** based on the crystal structure of CA II-hitamine **11** adduct. The amino group of histamine **11** was replaced with a bulkier amphiphilic pyridinium anchor, separated from the imidazole ring via a short ethylene linker [169].

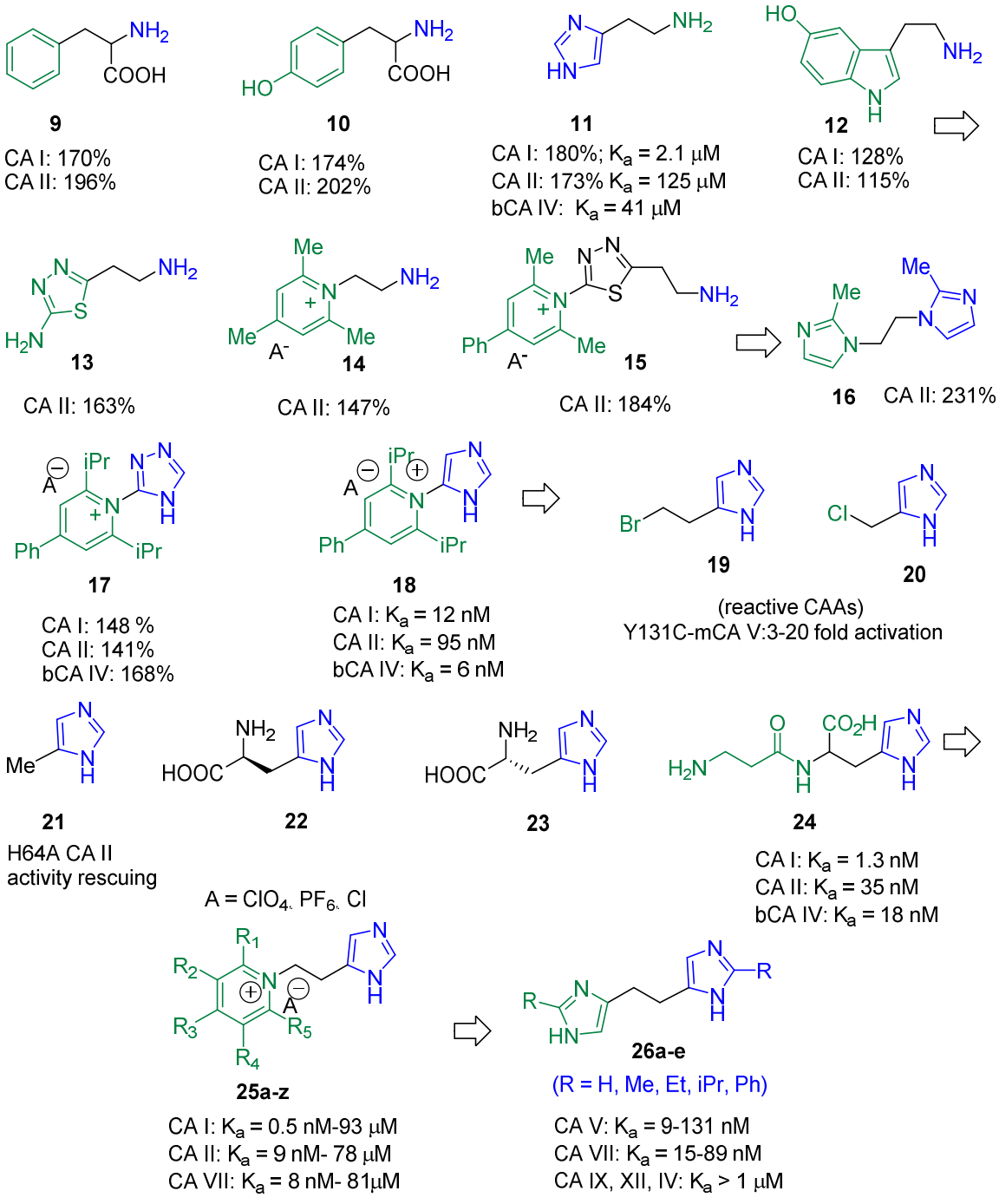

Chart 3.2 Evolution of CA activators design and the activation potency of representtive CAAs **9-26** developed previously [77, 159, 161, 167, 170-172].

Table 3.1 hCA I, II and VII activation with histamine pyridinium derivatives **25a-25z** and histamine, assessed by a stopped-flow, CO_2 hydration assay [77, 173].

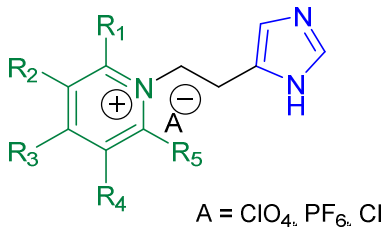

25a-z

No.	R1	R2	R3	R4	R5	K_A (μM)		
						hCA I	hCA II	hCA VII
Histamine						2	125	37.5
25a	Me	H	Ph	H	Me	58	4.76	2.15
25b	Et	H	Ph	H	Et	56	3.18	0.014
25c	*n*-Pr	H	Ph	H	*n*-Pr	0.95	23	19
25d	*i*-Pr	H	Ph	H	*i*-Pr	0.74	78	65
25e	*n*-Bu	H	Ph	H	*n*-Bu	4.53	21	23
25f	Me	H	Me	H	Me	3.15	18	7.71
25g	Et	H	Me	H	Et	0.0005	43	1.15
25h	*n*-Pr	H	Me	H	*n*-Pr	7.13	66	52
25i	*i*-Pr	H	Me	H	*i*-Pr	0.63	0.009	0.13
25j	*n*-Bu	H	Me	H	*n*-Bu	0.089	19	24
25k	Me	H	Me	H	Et	37	45	1.12
25m	Me	H	Me	H	*n*-Pr	43	31	1.16
25n	Me	H	Me	H	*i*-Pr	24	0.043	7.53
25o	Me	H	Me	H	*n*-Bu	7.88	0.13	8.16
25p	Me	Me	Me	H	Me	0.24	0.11	0.008
25q	Me	H	Ph	H	Ph	79	44	67
25r	Et	H	Ph	H	Ph	84	31	75
25s	*n*-Pr	H	Ph	H	Ph	93	0.018	81
25t	*i*-Pr	H	Ph	H	Ph	65	0.127	46
25u	*n*-Bu	H	Ph	H	Ph	60	51	74
25v	Ph	H	Me	H	Me	34	0.92	53
25x	Ph	H	Me	H	Ph	58	0.97	79
25y	Me	3,5-$(CH_2)_9$-			Me	29	1.15	0.073
25z	*i*-Pr	H	Me_2N-styryl	H	*i*-Pr	77	0.99	12.5

All these pyridinium histamine derivatives were tested for their ability to activate cytosolic isoforms, hCA I, II and VII and were found to be subnanomolar to micromolar potent, with K_a in the range of 0.5 nM-93 μM for CA I, 9 nM-78 μM for CA II and 8 nM-81 μM for CA VII (Table 3.1).

The substitution pattern at the pyridinium ring was the main factor influencing activity, and the three isozymes showed different requirements for good activation potency, in terms of both the number and the nature of substituent groups at the pyridinium ring, among a large number of alkyl, aryl and styryl moieties assessed. This study further revealed that the small differences in the structure of activators **25a-z** could trigger dramatic changes in the activation profile of these compounds through the exploitation of the differences in the amino acids lining the active site of various CA isozymes. Within this series, our group successfully identified nanomolar potent and selective activators for each isozyme (e.g. **25g** for CA I, **25s** for CA II, **25b** for CA VII) and also activators with a relatively good activity for all isozymes tested such as **25i** and **25p**, valuable tools for future biological and x-ray crystallographic studies for designing next generation CA activators (Table 3.1).

Inspired by the very promising results obtained with CAAs of type **25a-z**, our group also generated a series of compact bis-imidazoles **26a-e** in which two imidazole moieties were C-linked via a flexible ethylene linker, attached to the 4(5)-position of the imidazole ring. In these compounds one imidazole moiety as the proton-shuttling moiety, while the other one acts as the anchoring unit [17]. The activators are structurally related to their congeners **16** but possess a free imidazole NH that confers them superior proton shuttling capabilities. To facilitate the anchoring of the activator on the rim of the

different isozymes of CA, different hydrophobic substituents of increased steric bulk were introduced in the 2-position of the imidazole ring.

Table 3.2 Activation profile of human CA isozymes (hCAs) with bis-imidazoles **26a–e** [17].

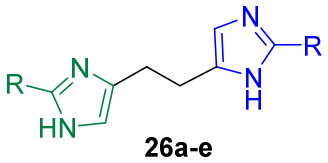

26a-e

(R = H, Me, Et, iPr, Ph)

	K_A (μM)							
No.	**CA I**	**CA II**	**CA IV**	**CA VA**	**CA VII**	**CA IX**	**CA XII**	**CA XIV**
Histamine	2.1	125			37.5			
26a	16.4	68.5	1.25	0.021	0.015	9.51	8.63	13.9
26b	23.5	69.3	4.51	0.009	0.020	13.1	5.40	10.2
26c	1.13	76.8	2.37	0.037	0.071	24.7	6.13	18.5
26d	4.81	80.4	9.50	0.131	0.054	20.1	9.85	24.6
26e	5.96	78.7	12.4	0.052	0.089	18.5	12.6	25.9

The new series of CAAs **26** showed an excellent activation profile against most isozymes and were more potent than histamine **11**, which has further validated our design. We were able to generate activators with nanomolar potency for hCA VA and hCA VII (Table 3.2). The most potent activators were **26a** (R = H), with a K_A= 21 nM for hCA VA, K_A= 15 nM for hCA VII, **26b** (R = CH_3) with a K_A= 9 nM for hCA VA and K_A= 20 nM for hCA VII [17]. However, these bis-imidazoles **26a-e** displayed only micromolar potency against membrane-bound hCA IV, hCA XII, hCA IX and hCA XIV and against cytosolic isozymes hCA I and hCA II.

Results and discussion

The excellent results obtained with the pyridinium histamine **25a-z** prompted us to reinvestigate the most potent CAAs from this series by x-ray crystallography in order to better understand the binding of these activators within the active site of CA isozyme and to design next generation CAAs. We resynthesized a set of five compounds following the previously published procedures (Scheme 3.1) [77]. Briefly, pyrylium salts having different aliphatic/aromatic sustituents, were reacted with histamine **11** to yield the pyridinium derivatives, as outlined in Scheme 3.1 below.

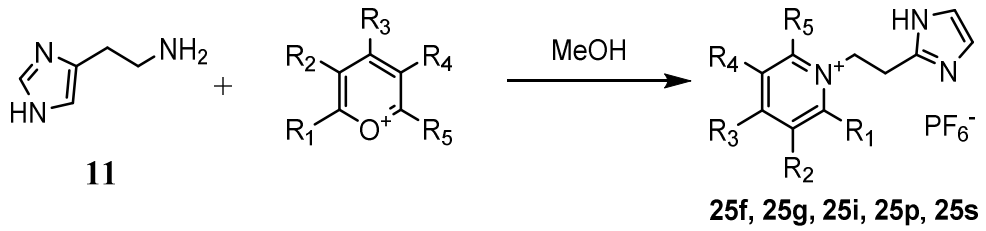

Scheme 3.1 Synthesis of pyridinium imidazole derivative CAAs **25f, 25g, 25i, 25p** and **25s**

All these five compounds were purified following previously published procedures [77] and characterized by NMR and LC-MS to confirm their structures and consequently were sent to our collaborator Dr. McKenna, at University of Florida to obtain the X-ray crystal structures. From these five pyridinium derivatives, only CAA **25i** successfully crystallized with CA II isozyme. In the crystal structure of **25i**/CA II adduct (PDB: 5W8B), CAA **25i** was found to bind in the active site of the enzyme along together with its PF_6^- counter ion, which stabilizes the activator within CA active cavity.

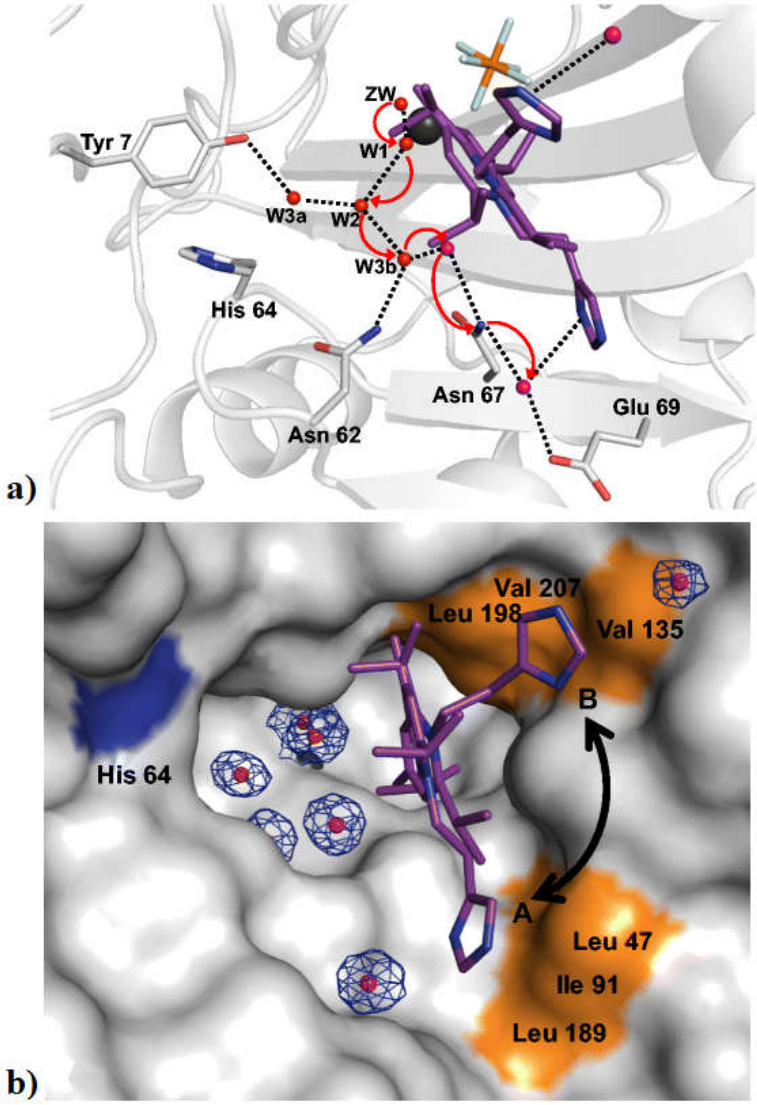

Figure 3.3 a) Crystal structure of CA II in complexed with **25i** (purple) together with its PF_6^- counterion (orange/blue, PDB: 5W8B). Active site waters are shown as red spheres, with black dottted lines representing the network of H-bond interactions and with red arrows indicating postulated proton transfer mechanism b) Surface representation of CA II-**25i** adduct. Activator **25i** is shown in its two conformations, A and B, detected in the X-ray crystal structure. Conformation A has the imidazole tail moiety within the van der Waals interactions with Leu 47, Ile 91, Leu 189 (orange) and conformation B has the tail moiety interacting with Val 135, Val 207, Leu 198 (orange).

Only one molecule of **25i** was observed to be bound, indicating that this ligand has a single, unique binding site (Figure 3.3). The x-ray structure of CA II -**25i** adduct was superimposed over the wildtype CA II isozyme structure and compared. Superposition did not reveal any significant changes in protein conformation upon CAA binding. CAA **25i** was found to be anchored via the pyridinium group on the hydrophobic side of the active site (Figure 3.3), which did not play any direct role in the proton transfer mechanism.

Interestingly, the imidazole tail moiety of CAA **25i** displayed two conformations, denoted conformation A and B. The activator was found to bind into the hydrophobic side of the CA II active site, with the imidazole ring positioned in two different regions of the hydrophobic pocket that are separated by residue Phe 131 (Figure 3.3b). Conformation A was bound to the hydrophobic region delimited by residues Leu 189, Ile 91 and Leu 47, whereas conformation B was bound to a pocket delimited by residues Leu 198, Val 207 and 135. Two water molecules were found to locate within 2.5 Å of the imidazole moiety, one near the imidazole in conformation A and the other near the imidazole in position B. Thus, imidazole moiety through a network of water molecules shuttles the proton from the zinc bound water and creates a secondary proton transfer site (Figure 3.3b) for CA II isozyme, and thereby activates the enzyme.

These findings revealed important insights for designing the next generation CAAs with better activation potency and selectivity. The ethylene linker makes the activator molecule very flexible and thus the activator can addopt several different conformations within this active site cavity. Some of these conformations might be useful for proton shuttling, others may not help it at all. We hypothesized that restricting a

specific conformation within a rigid linker might stabilize the imidazole rings in the specific 3D orietation useful for proton shuttling and consequently improve the potency of this class of activators.

A key finding emerged from the above-mentioned X-ray structure of CA II -**25i** adduct is that this class of activators mainly bind onto the hydrophobic side of the active site cavity, indicating that a certain lipophilicity of CAAs is required for efficient binding the activators into these CAA binding area. The increased lipophilicity is benefic for any CNS-centered applications, ensuring the penetration of the CAA through the blood-brain barrier (BBB).

Building on these premises we decided to develop a new series of CAAs by replacing the ethylene linker of CAAs **26a-e** with a more lipophilic and rigid phenylene linker. The linker substitution was chosen to be either 1,4-phenylene or 1,3-phenylene, in order to mimick the two possible positions/conformations of the two imidazole moities relative to the ethylene moiety, namely anti (mimicked by the 1,4-phenylene linker, series **30** in Chart 3.3) and sin (mimicked by the 1,3-phenylene linker, series **34**, Chart 3.3). A consequence of this design is an improvement of the lipophilicity of the activators, with potential beneficial effects on their activity. In order to preserve/increase the lipophilicity of the CAAs we used aliphatic and aromatic/heterocyclic R groups at the 2-position of both imidazole moieties, gradually increasing their steric bulk and hydrophobicity from H- to Ph- (Chart 3.3).

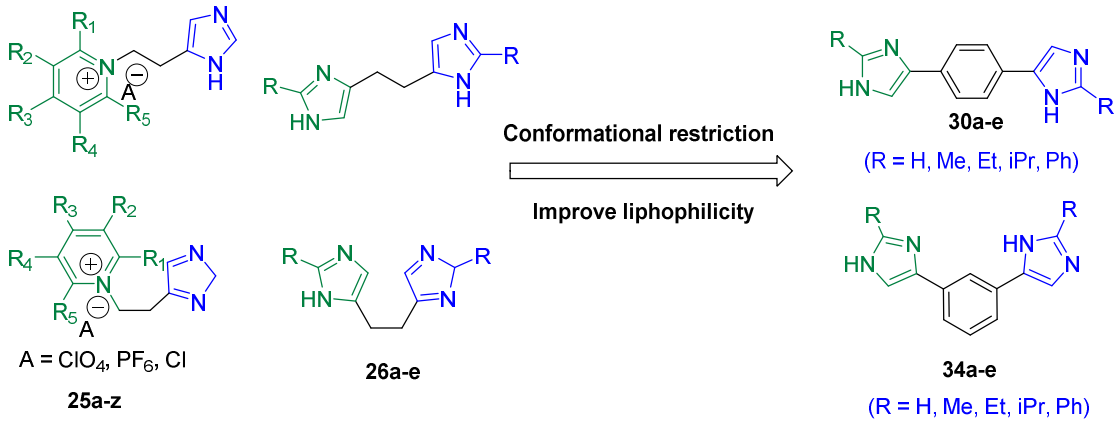

Chart 3.3 Working hypothesis for the generation of new series of bis-imidazoles **30a-e** and **34a-e** by mimicking the two possible conformations anti and sin of the imidazole rings relative to the ethylene unit of CAAs series **25** and **26** by the 1,4-phenylene and 1,3-phenylene linkers respectively.

Synthesis of phenylene-bis-imidazoles

Based on the reported literature and research conducted by our group, bis-imidazoles can be generated by a variety of methods including: i) condensation of amidines with α-haloketones [174] or α-ester ketones [175]; ii) condensation of α-haloketones with formamide via Bredereck cyclization [176]; iii) conversion of bis-oxazoles to bis-imidazoles using formamide [177]. These methods often required elevated temperature and prolonged reaction times and generate low to moderate yields. In the Bredereck cyclization method, the two α-keto units in the molecule must be separated by four to eight C atoms, with longer spacer groups producing higher yields.

Previously, we have prepared bisimidazoles **26a-e**, substituted at position 2 of the imidazole ring, from 1,6-dibromohexane-2,5-dione [178] and corresponding alkylamidines [179] in the presence of ammonia solution in methanol following modified Leschke

method [17, 174]. We employed a microwave-mediated procedure in order to decrease the reaction time and to improve the yield of this synthetic strategy to generate the desired bis-imidazoles **26a-e** [17]. However, we quickly discovered that this procedure produced low to moderate yields and that the separation of the pure compounds from side products was quite tedious, with several normal and reverse phase chromatographic separation steps being required for each compound.

In order to synthesize the new series of bis-imidazoles **30a-e** and **34a-e** bearing 1,4-phenylene and 1,3-phenylene spacers, we followed the same Leschke method [175] through the condensation of substrate 1,4-diacetylbenzene **27** with corresponding alkylamidines. However, we did not obtain the corresponding bisimidazoles with any separable yield. Therefore, in an effort to improve the cyclization efficiency, we have investigated the cyclization of α-ester ketones, generated from α-dihaloalkyldione in the presence of ammonium acetate under microwave irradiation (Scheme 3.2) [180]. Briefly, 1,4-diacetylbenzene **27** was brominated by Br_2 in acetic acid to form the corresponding 1,1'-(1,4-phenylene)-bis-(2-bromoethanone) **28**, which was subsequently condensed with different carboxylic acids having various R groups to yield corresponding α-ester ketone derivatives **29a-e**. Cyclization of α-ester ketone derivatives **29a-e** with ammonium acetate [175] under conventional reflux or microwave irradiation yielded the desired bis-imidazoles **30a-e**. The meta-congeners were synthesized following the same synthetic strategy, with only one exception. Thus, bromination of 1,3-diacetylbenzene **31** was carried out using N-bromosuccinamide instead of Br_2 in acetic acid, which improved the yield of desired product by 10%. This cyclization of α-ester ketone is universal and is not

so sensitive to the electronic effect of different substituents on the 4-position of the phenyl ring.

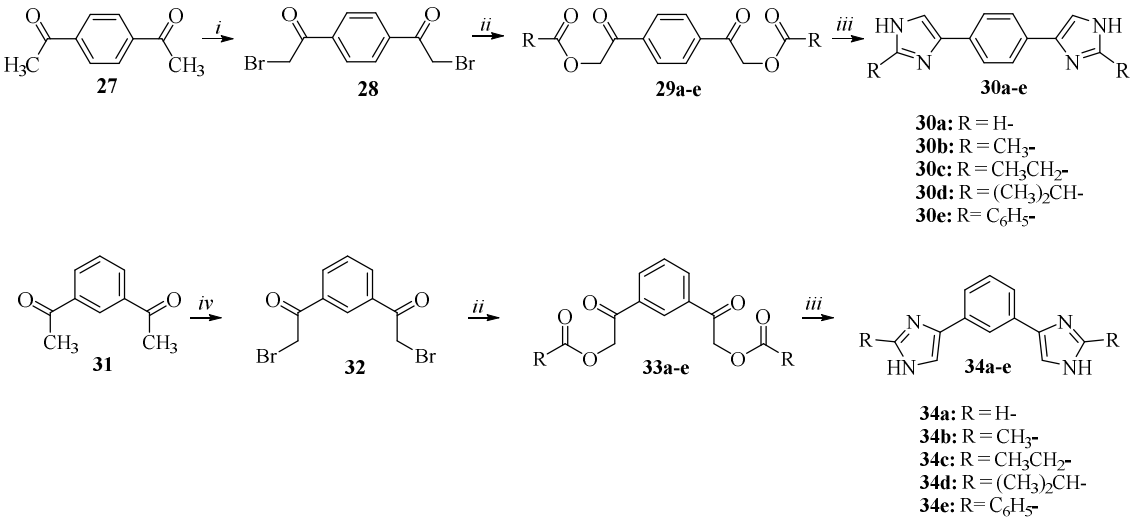

Scheme 3.2 Synthesis of phenylene-bis-imidazoles **30a-e** and **34a-e**. Reaction conditions: *i)* Br_2, AcOH, 2h *ii)* RCO_2H, NEt_3, ACN, r.t. overnight or RCO_2H, NEt_3, ACN reflux 8h. *iii)* NH_4OAc, p-Xylene MW 200W, 140ºC, 90 min), iv) NBS, TsOH, CH_3CN, reflux 5h.

This method produced bis-imidazoles with low to moderate yield and separation of the purified products proved again to be very tedious, with several purification steps required for each compound. To increase the yield and to avoid lengthy separation procedures, we tested another synthetic route for the preparation bis-imidazoles, through the Suzuki-Miyaura cross- coupling reaction of 4 (5) -bromo-2-arylimidazoles with 1,4-phenylenediboronic acid [181]. We successfully scaled up the synthesis for bis-imidazole **30e**, having phenyl substituent at 2-imidazole position and we also synthesized two para-phenylene bis-imidazole congeners **47-48**, having 4-pyridyl and 3-pyridyl substituents at the 2-position of the imidazole ring respectively. These two representatives were synthesized in order to assess the effect of increasing the polarity of the end aromatic

groups in **30e**, via replacement of the phenyl groups with 3- and 4-pyridyl, on the activation properties of these amphiphilic imidazoles.

The procedure started by synthesizing imidazoles **37-38** having 4-pyridyl and 3-pyridyl substituents at 2-position, from the corresponding aldehyde derivatives **35-36** through condensation with glyoxal and NH_4OH (Scheme 3.3, Method A) [182]. Once again, this method for synthesizing imidazoles proved relatively inefficient, produced imidazoles **37-38** at only 25-30% final yield. After a comprehensive survey of available literature, we found a new method for synthesizing imidazole starting form nitrile derivatives [183]. In this method, nitrile derivatives **39-40** were treated with NaOMe to form the corresponding imidates. Subsequent nucleophilic substitution of imidates with aminoacetaldehyde dimethyl acetal, followed by acid deprotection and cyclization resulted in imidazoles **37-38** as hydrochloride salts. Basic workup wih K_2CO_3 yielded the neutral imidazoles **37-38** at 99% yield and excellent purity, with no chromatographic separation being required for further purification. Conseqently, imidazoles **37-38** and **41** (2-phenyl imidazole) were subsequently brominated with N-bromosuccinamide to form the dibromo-imidazole derivatives **42-44**. Reductive debromination of dibromo-imidazole derivatives **42-44** was achieved with sodium sulfite under reflux and produced mono-bromo-imidazole derivatives **45-47**, which were subsequently coupled with 1,4-phenylenediboronic acid through Suzuki-Miyaura cross coupling reaction using $Pd(OAc)_2$, A-^{ta}Phos as the catalysts and K_2CO_3 as the base, either under conventional reflux or microwave irradiation, yielded bis-imidazoles, **48-49** and **30e** [181]. This synthetic route produced bis-imidazoles with 90% yield and the separation of pure

compounds was very easy, with a single normal phase flash chromatography being sufficient for purifying the bis-imidazoles **48-49** and **30e** to a purity > 96% (Scheme 3.3).

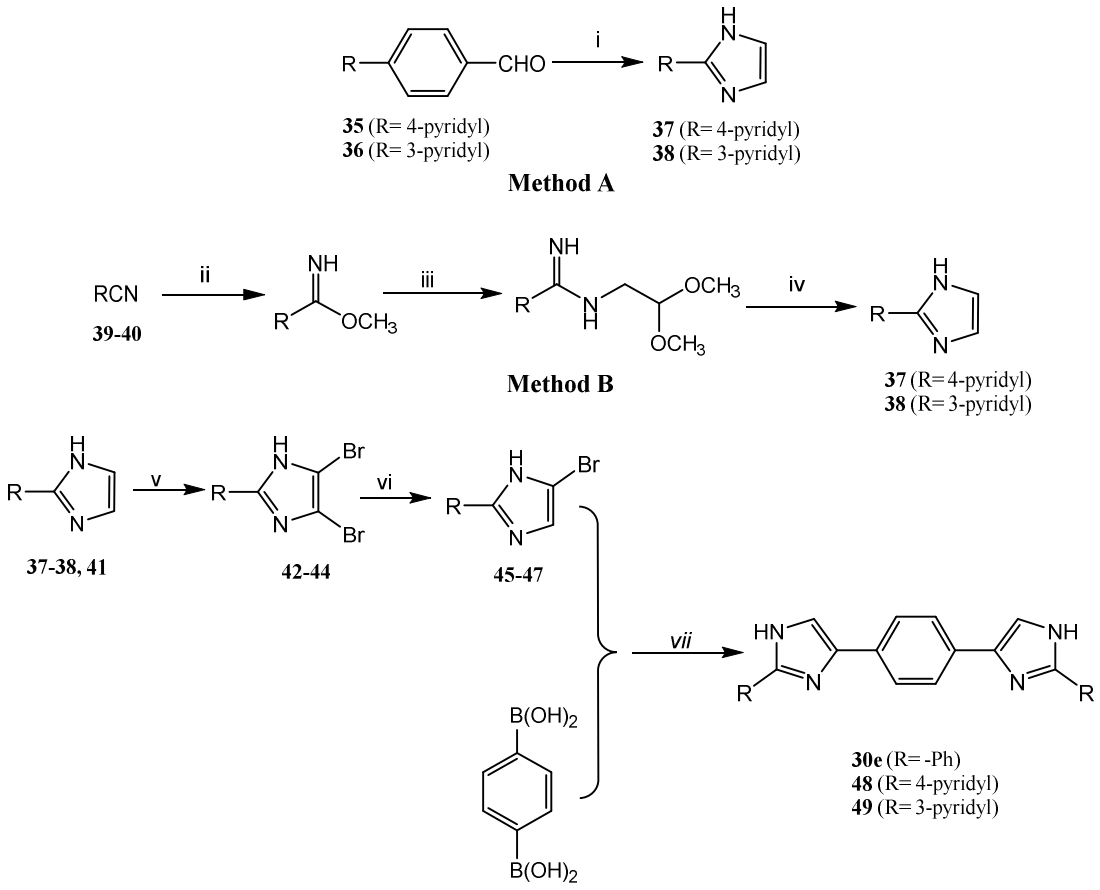

Scheme 3.3 Synthesis of CAAs **30e**, **48**, **49** through Suzuki-Miyaura cross-coupling**.** The required starting imidazoles were synthesized through different procedures (Methods A and B). Reagents and conditions: (i) NH_4OH, glyoxal, ethanol, rt for 2-3 days, ii) 30% NaOMe for 1-5 hrs, iii) aminoacetaldehyde dimethyl acetal, acetic acid, reflux for 30 min/ 50°C for 1h iv) 6N aqueous HCl, reflux for 5-6 hrs v) NBS, THF, 0ºC for 15 mins, then r.t 1h vi) Na_2SO_3, EtOH, H_2O, r.t for 2-3 days vii) $Pd(OAc)_2$, A-^{ta}Phos, dioxane or THF, K_2CO_3, H_2O, 140°C reflux for 48 hrs or MW irradiation at 120°C for 1h.

CA activation study

The novel bis-imidazoles **30a-e** and **34a-e** were tested for their ability to activate eight of the CA isozymes involved in brain homeostasis, namely the mitochondrial hCA VA, the cytosolic hCA I, hCA II, hCA VII and the membrane-bound hCA IV, hCA IX, hCA XII and hCA XIV, using the CO_2 hydration assay method [156, 173], by Dr. Supuran at University of Florence. Results are presented in Table 3.3.

Table 3.3 Activation profile of human CA isozymes (hCAs) with bis-imidazoles **30a-e and 34a-e**, using the CO_2 hydration assay method [156, 173].

No.	**K_A (µM)**							
	hCA I	**hCA II**	**hCA IV**	**hCA VA**	**hCA VII**	**hCA IX**	**hCA XII**	**hCA XIV**
Histamine	2	125			37.5			
30a (R= -H)	12.5	42.3	0.09	0.098	18.5	1.02	7.81	6.54
30b (R= -Me)	34.2	44.5	0.14	0.007	23.4	0.84	6.23	14.1
30c (R= -Et)	8.1	50.2	0.061	0.005	20.7	0.79	9.5	10.2
30d (R= -iPr)	6.42	49.3	0.04	0.013	21.9	0.013	9.21	18.5
30e (R= -Ph)	5.5	51.7	0.029	0.01	30.5	0.01	12.4	24.6
34a (R= -H)	1.13	36.8	7.58	0.004	24.6	0.009	10.5	13.9
34b (R= -Me)	1.42	38	12.3	0.002	26.8	0.005	10.7	14.1
34c (R= -Et)	3.21	35.3	5.04	0.027	20.4	0.012	14.4	10.2
34d (R= -iPr)	4.97	27.1	8.93	0.013	31.7	0.031	21.5	18.5
34e (R= -Ph)	6.2	40.2	15.6	0.009	25.1	0.028	28.7	24.6

Data from Table 3.3 showed an excellent activation profile for the new series of bis-imidazoles **30a-e and 34a-e**. We were able to further increase the potency of the compounds compared to the previous series of bis-imidazoles **26**, generating compounds that displayed low nanomolar activation potency for several CA isoforms. CA VA was the best activated isozyme by these novel phenylene bis-imidazoles, followed by isozyme CA IX, followed by CA IV. All these compounds displayed micromolar activation

potency for all other isozymes CA I, CA II, CA VII, CA XII and CA XIV. Bis-imidazoles **30a-e, 34a-e** were nanomolar potent against hCA VA and hCA IX.

Focusing on activation of CA VA, one can observe that all CAAs **30a-e** and **34a-e** were very potent, with both series having low nanomolar potent compounds. The potency of CAAs was found to depend on both the type of substituents and linker used. For the 1,4-phenylene congeners **30a-e** the CA VA activation potency increased abruptly while increasing the steric bulk and lipophilicity of the substituents in 2- position of the imidazole ring from H to Me, then stayed consistently high while substituting Me with Et, iPr or Ph. For the 1,3-phenylene congeners **34a-e** the activation potency against CA VA isozyme was maximum when R substituents were either very small (R = H, Me in **34a**, **34b**) or very large (R = Ph, **34e**), with a small decrease observe for intermediate size substituents (R = Et, iPr in **34c**, **34d**). The best activator for CA VA proved to be **34b**, with a K_A of 2 nM for this isozyme, although both series displayed many low nanomolar potent compounds.

In respect with CA IX activation, 1,3-phenylene CAAs **34a-c** proved generally more potent than their corresponding 1,4-phenylene congeners **30a-c**. Within 1,4-phenylene bis-imidazoles **30** series, the potency against CA IX was found to increase monotonously with the increase of steric bulk of substituents on the imidazole ring, from H to Ph. The most potent CAA bearing a 1,4-phenylene linker proved to be **30e**, with a Ka value of 10 nM. An opposite trend was observed for 1,3-phenylene bis-imidazoles **34a-e** where the potency decreased while increasing the steric bulk of substituent in the 2- position of the imidazole ring. CAA **34b** was the best activator for CA IX, followed by **34a**, with Ka values of 5 nM and 9 nM respectively. While CA VA and CA VII activation

did not prove to be very sensitive to the nature of the linker, CA IV activation with 1,4-phenylene bis-imidazoles **30a-e** was far more efficient as compared with the 1,3-phenylene congeners **34a-e**. All the 1,4-phenylene bis-imidazoles **30a-e** were nanomolar potent for CA IV, having K_A values in range of 29 nM to 140 nM, while 1,3-phenylene bis-imidazoles **34a-e** were only micromolar potent. Within 1,4-phenylene bis-imidazoles **30a-e** series, the potency was found to increase with the increase of steric bulk of substituent in the 2-position of the imidazole ring. The best activator for CA IV was bis-imidazole **30e,** bearing phenyl R groups, with a K_A value of 29 nM.

Notably, the 1,4-phenylene bis-imidazole **30e** proved to be best activator for three of the isozymes tested, with a K_A value of 29 nM for CA IV, and a K_A value of 10 nM for both CA VA and CA IX.

The final bis-imidazoles **48-49**, as well as all intermediate compounds **37, 38** and **41-47** synthesized following Scheme 3.3 are all amphiphilic imidazoles that comply with the general structure of a carbonic anhydrase activator (Chart 3.1). Consequently, these imidazoles are expected to be able to shuttle protons within CA active site, while their R groups and bulkier bromine substituents are expected to access different pockets within the CA structure. Therefore, we assessed these intermediate imidazoles **37, 38** and **41-47** as well as the final bis-imidazoles **48-49** for their ability to activate mitochondrial hCA VA, the cytosolic hCA I, hCA II, hCA VII and the membrane-bound hCA IV, hCA IX, hCA XII and hCA XIV, using the CO_2 hydration assay method. [156, 173] The results obtained with compounds **37, 38** and **41-47** are tabulated in Table 3.4, while activation profile obtained with bisimidazoles **48-49** are shown Table 3.5.

Table 3.4 Activation profile of human CA isozymes (hCAs) with 2-arylimidazoles **37, 38** and **41**, corresponding dibromo derivatives **42-44** and monobromo derivatives **45-47**, using the CO_2 hydration assay method [156, 173].

No.	**K_A (µM)**							
	hCA I	**hCA II**	**hCA IV**	**hCA VA**	**hCA VII**	**hCA IX**	**hCA XII**	**hCA XIV**
Histamine	2	>50			37.5			
37 (R= 4-pyridyl)	0.47	>50	1.37	3.19	>50	13.7	>50	0.52
38 (R= 3-pyridyl)	0.018	>50	0.92	4.07	>50	1.58	2.36	1.03
41 (R= -Ph)	0.674	>50	10.1	0.041	>50	>50	>50	>50
42 (R= 4-pyridyl)	0.073	>50	9.72	0.22	>50	8.70	0.046	0.26
43 (R= 3-pyridyl)	0.002	>50	14.3	0.78	>50	0.054	13.2	0.005
44 (R= -Ph)	0.001	>50	2.40	0.104	>50	7.12	1.69	0.12
45 (R= 4-pyridyl)	0.38	>50	7.21	4.38	>50	>50	31.8	1.85
46 (R= 3-pyridyl)	0.086	>50	14.8	1.03	>50	28. 3	>50	0.062
47 (R= -Ph)	0.024	>50	>50	0.27	>50	1.12	27.9	2.12
48 (R= 4-pyridyl)	0.16	>50	>50	8.34	>50	10.4	7.29	0.10
49 (R= 3-pyridyl)	0.042	>50	10.5	4.91	>50	36.9	41.8	0.002

Activation profile obtained from Table 3.4 revealed that 2-arylimidazoles **37**, **38** and **41**, and their corresponding dibromo **42-44** and mono bromo derivative **45-47**, were particularly potent activators for CA I and CA XIV.

CA I was the best activated isozyme by these compounds **37, 38** and **41-47**, followed by isozyme CA XIV, with low nanomolar activation potency obtained with several representative compounds. However, all these compounds displayed only micromolar activation potency for all other isozymes CA II, CA IV, CA VA, CA VII, CA IX, and CA XII. Few exceptions were observed such as dibromo-imidazole derivative **42** was 46 nM potent for CA XII and dibromo-imidazole derivative **43** was 54 nM potent for CA IX, while compound **41** (2-phenyl imidazole) was found to be 41 nM potent for CA VA.

All the compounds **37-38** and **41-47** displayed nanomolar potency against CA I, with the strongest activation obtained with dibromo imidazole derivatives **42-44**. Dibromo imidazole derivatives **42-44** were more potent than their corresponding imidazole derivatives **37-38** and **41**, and also more potent than their corresponding mono brominated congeners **45-47**. Dibromo imidazole CAA **44** was found to be the best activator for CA I with 1 nM activation potency, followed by dibromo imidazole **43** with 2 nM activation potency. We postulate that bulkier bromine groups of imidazole ring are binding with the CA I active site residues. Mono bromo-imidazoles **45-47** were less potent than dibromo derivatives but found to be more potent that their corresponding imidazoles, except mono bromo imidazole **46**, which was less potent than its corresponding imidazole **38**. Overall, dibromo imidazole derivative **43** having 4-pyridyl R groups was the best activator for three of the isozymes tested, with Ka value of 2 nM for CA I, 54 nM for CA IX and 5 nM for CA XIV.

Table 3.5 Activation profile of human CA isozymes (hCAs) with bis-imidazoles **48-49**, using the CO_2 hydration assay method [156, 173]. The activation profile of histamine **11** and bis-imidazole **30e** are also included in the table.

No.	**K_A (µM)**							
	hCA I	**hCA II**	**hCA IV**	**hCA VA**	**hCA VII**	**hCA IX**	**hCA XII**	**hCA XIV**
Histamine	2	>50			37.5			
30e (R= -Ph)	5.5	51.7	0.029	0.01	30.5	0.01	12.4	24.6
48 (R= 4-pyridyl)	0.16	>50	>50	8.34	>50	10.4	7.29	0.10
49 (R= 3-pyridyl)	0.042	>50	10.5	4.91	>50	36.9	41.8	0.002

Similar to the precursor imidazole derivatives, these novel bis-imidazoles **48-49**, having 4-pyridyl and 3-pyridyl group at the 2-position, displayed nanomolar potency against CA I and CA XIV, while only micromolar activation potency for all other isozymes CA II, CA IV, CA VA, CA VII, CA IX, and CA XII.

In respect with CA IX activation, bis-imidazole **49** was 42 nM potent for CA I, while bis-imidazole **48** was 160 nM potent against CA I. Interestingly, bis-imidazole **49** having 3-pyridyl was 42 nM potent against CA I and proved to be ~4-times more potent compared to the bis-imidazole **48** for CA I. In case of CA XIV activation, both bis-imidazoles **48-49** also displayed nanomolar potency against CA XIV, with Ka value of 100 nM and 2 nM respectively. Bis-imidazole **49** was proved to be ~50-times more potent for CA XIV compared to bis-imidazole **48**. Thus, change in the position of –N

atom on pyridyl group had huge impact on the potency of these against CA I and CA XIV.

Comparing the activation profile obtained with these two bis-imidazoles **48-49** having 4-pyridyl and 3-pyridyl, with bis-imidazole **30e** bearing a phenyl R group (Table 3.5), one can observe that bis-imidazoles **30e** were selectively potent for CA IV, CA VA and CA IX, while bisimidazoles **48-49** were selectively potent for CA I and CA XIV. Thus, the activation potency is dictated to very great extent by the substituents of these bis-imidazoles.

Determination of optical properties for bis-imidazoles CAAs 30a-e, 34a-e and 48-49

During the synthesis and purification steps, we observed that bis-imidazoles CAAs **30a-e, 34a-e** and **48-49** are very bright fluorescent compounds. These bisimidazoles are terphenyl-like structures, and a literature survey in this direction revealed that terphenyls have good photophysical properties such as absorption and fluorescence properties due to extensive electron delocalization over the three aromatic rings [184]. As fluorescence properties of molecules are very useful for tracking and quantifying these compounds in vivo by means of fluorescence based assays, we decided to assess photophysical properties of these bis-imidazoles CAAs **30a-e, 34a-e** and **48-49**. Good fluorescence properties can make these CAAs appealing biomolecular tools for labelling, imaging and quantifying the CA isozymes in different organs. These fluorescent CAAs expected to equip us for fluorescence-based technologies to reveal new biochemical and biological roles played by different CA isozymes. Important parameters

of photophysical properties are absorption maximum (λ_{max}), emission maxium λ_{em}, molar extinction co-efficient (ε), and fluorescent quantum yield (Φ) [185].

Briefly, a plot of absorbance of a compound versus wavelength is called absorption spectrum and the wavelength of maximum absorbance is a characteristic value of each compound, called absorption maxima and designated λ_{max}. Similarly, one can record the emission spectrum of the same compound when excited with a radiation with a wavelength corresponding to λ_{max}. The wavelength of maximum fluorescence intensity is a characteristic value, called emission maxima and designated as $\lambda_{em.}$ The emission maximum wavelength (λ_{em}) occurs at higher wavelengths (i.e., at lower energy) than λ_{max} due to energy losses by solvent reorganization or other non-radiative energy transfer processes. The difference between λ_{max} and λ_{em} is termed the "Stokes shift". Fluorophores with small Stokes shifts are susceptible to self-quenching via energy transfer, which limits their use for fluorescence quantification and imaging [185].

The fluorescence output of a given compound depends on the efficiency with which it absorbs and emits photons. Absorption and emission efficiencies are most usefully quantified in terms of the molar extinction coefficient (ε) for absorption and the quantum yield (Φ) for fluorescence. Both are constants under specific environmental conditions. Molar extinction coefficient (ε) is a measure of how strongly a compound absorbs light at a particular wavelength. Fluorescence quantum yield (Φ) is a critical property of a fluorophore and defined as the ratio of the photons fluoresced to those absorbed. The value of ε is specified at a single wavelength, usually the absorption maximum λ_{max}, whereas Φ is a measure of the total photon emission over the entire fluorescence spectral profile. Another simple parameter for making meaningful

comparisons between different fluorescent molecules is the product of the extinction coefficient and the quantum yield (ε × Φ). This term is directly proportional to the brightness of the dye, accounting for both the amount of light absorbed and the quantum efficiency of the fluorophore. Accurate comparisons between dye molecules must include both of these parameters [185].

All bis-imidazoles **30a-e, 34a-e** and **48-49** were assessed for their photophysical properties. Absorption maximum (λ_{max}), emission maxium λ_{em}, Stokes shift, molar extinction co-efficient (ε), fluorescent quantum yield (Φ) and the brightness (ε x Φ) were determined in methanol following standard literature procedures using UV-Vis and fluorescence spectrophotometers [186-188]. The relative fluorescent quantum yield (Φ) was measured by comparing with 9,10-diphenylanthracene (9,10-DPA) in cyclohexane. The absorption and emission spectra are shown in Figure 3.4 and Figure 3.5, and the obtained photophysical properties are tabulated in Table 3.6.

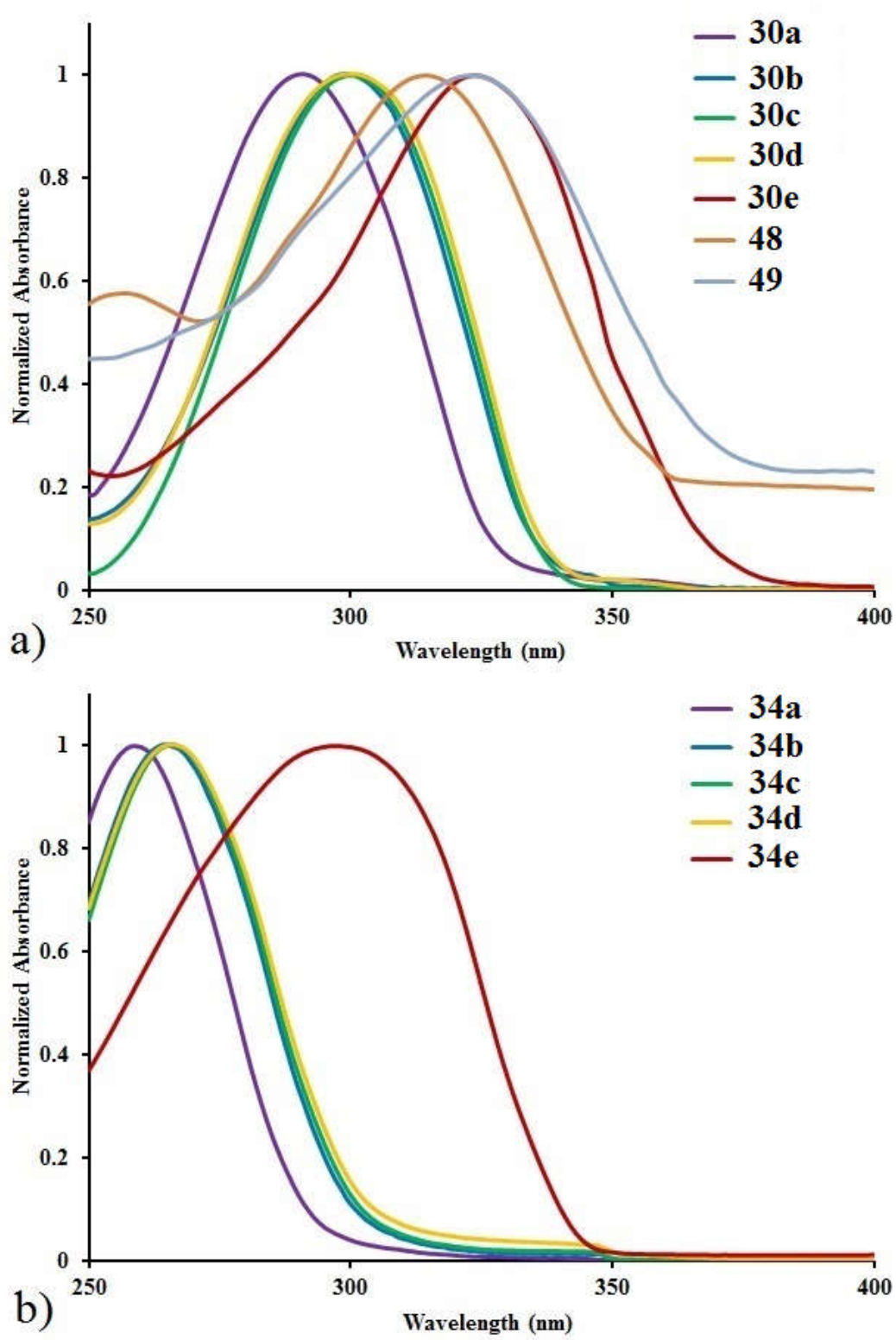

Figure 3.4 a) Normalized absorption spectra of 1,4-phenylene bis-imidazoles **30a-e** and **48-49** b) normalized absorption spectra of 1,3-phenylene bis-imidazoles **34a-e.**

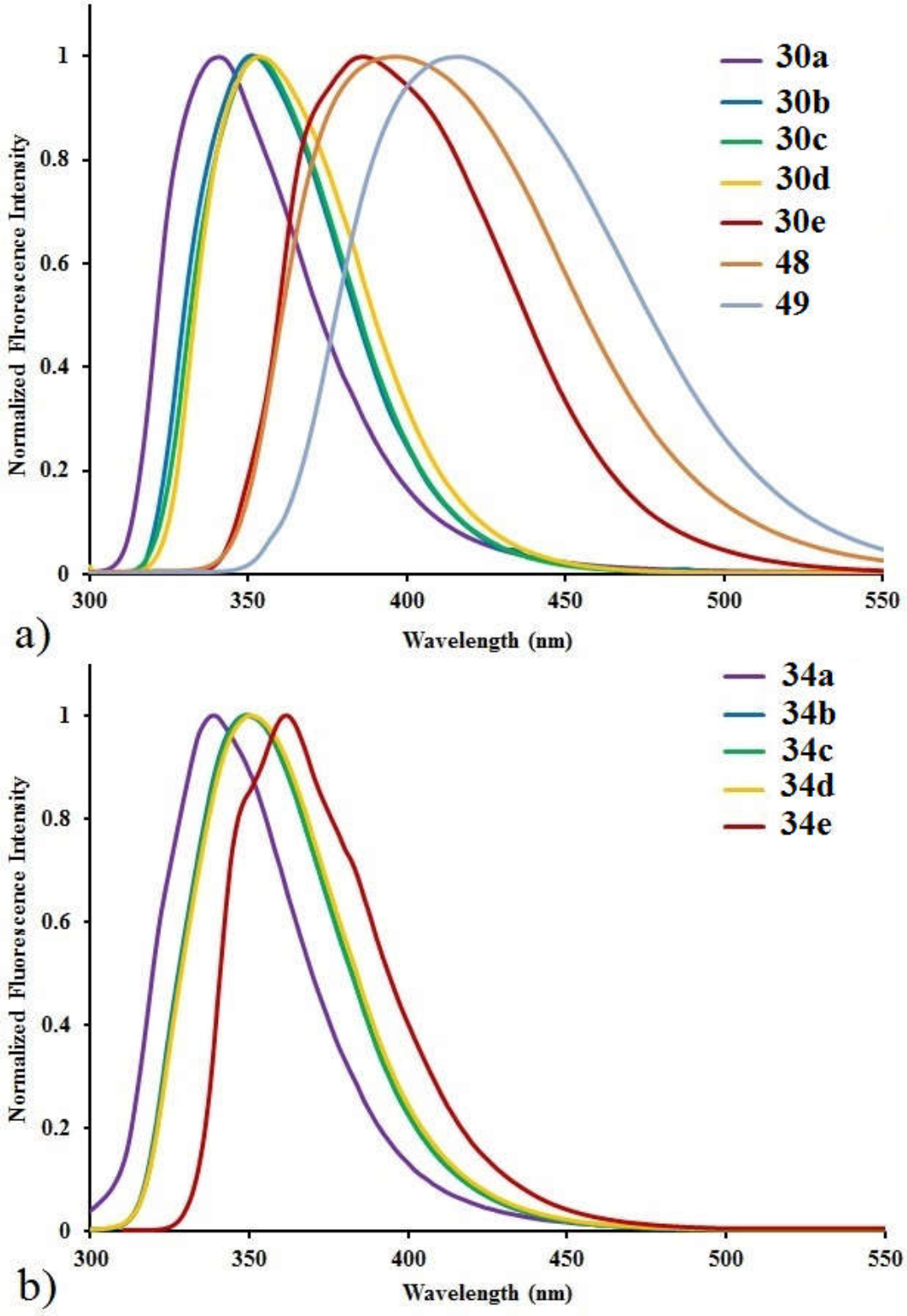

Figure 3.5 a) Normalized emission spectra of 1,4-phenylene bis-imidazoles **30a-e** and **48-49** b) normalized emission spectra of 1,3-phenylene bis-imidazoles **34a-e.**

Table 3.6 Optical properties of bis-imidazoles **30a-e, 34a-e** and **48-49**.

No.	Absorption maximum (nm)	Emission miximam (nm)	Stokes shifts (nm)	Quantum yield	ε $M^{-1} \times cm^{-1}$	Brightness ε × Φ $(M^{-1} \times cm^{-1})$
30a	291	340	49	0.13	13080	1700.4
30b	299	352	53	0.13	13477	1752.01
30c	300	352	52	0.15	7972	1195.8
30d	301	354	53	0.17	19325	3285.25
30e	324	386	62	0.55	11071	6089.05
34a	264	338	74	0.03	8498	254.94
34b	265	348	83	0.03	18266	547.98
34c	266	350	84	0.05	16291	814.55
34d	266	350	84	0.04	19365	774.6
34e	297	362	65	0.16	24273	3883.68
48	315	395	80	0.44	37566	16529.04
49	323	415	92	0.1	40424	4042.4

Data from Figure 3.4 and Figure 3.5 and Table 3.6 revealed that all these bis-imidazoles **30a-e, 34a-e** and **48-49** displayed absorption maximum in the range of 264 nm to 324 nm, with emission maxima in the range of 338 nm to 415 nm. Bis-imidazole **30e** having phenyl R group on imidazole 2-position, showed the highest absorption maximum of 324 nm, followed by bis-imidazole **49** bearing 3-pyridyl R group with an absorption maximum at 323 nm. All the 1,4-phenylene bisimidazoles **30a-e** and **48-49**

showed higher absorption maximum compared to the corresponding 1,3-phenylene congeners **34a-e**.

In terms of emission maximum, a similar trend was observed as well, with 1,4-phenylene bisimidazoles **30a-e** and **48-49** showing higher emission maximum compared to the corresponding 1,3-phenylene congeners **34a-e**. Among these compounds, bis-imidazole CAA **49** showed the highest maximum emission at 415 nm, while the corresponding 4-pyridyl analog **48** showed absorption maxima at 395 nm. Bis-imidazole **30e**, showed the second highest maximum emission at 386 nm.

Stokes shifts were determined by subtracting absorption maximum (λ_{max}) from emission maximum emission maxium ($\lambda_{em)}$, revealed all these bis-imidazoles being have Stokes shift in the range of 49 nm to 92 nm. Interestingly, 1,3-phenylene bis-imidazoles **34a-e** showed longer Stokes shifts compared to their corresponding 1,4-phenylene derivatives **30a-e**. The 3-pyridyl bis-imidazole **49** displayed the highest Stokes shift of 92 nm, while the corresponding 4-pyridyl analog showed an 80 nm Stokes shift, quite favorable for biological applications.

In terms of quantum yield, 1,4-phenylene bis-imidazoles **30a-e** and **48-49** showed higher quantum yield compared to their 1,3-phenylene congeners **34a-e.** Bisimidazole **30e** having the phenyl R group showed highest relative quantum yield of 0.55 compared to 9,10-DPA (Φ= 0.9). The 4-pyridyl bis-imidazole **48** showed second best quantum yield of 0.44, whereas the corresponding 3-pyridyl analog **49** was significantly less fluorescent with quantum yield of only 0.1.

In terms of molar extinction co-efficient (**ε**), all these bis-imidazoles showed molar extinction co-efficient in the range of 7972 $M^{-1} \times cm^{-1}$ to 40424 $M^{-1} \times cm^{-1}$. The 3-

pyridyl bis-imidazole **49** showed the highest maximum molar extinction co-efficient of 40424 $M^{-1} \times cm^{-1}$, while the corresponding 4-pyridyl bis-imidazole **48** displayed second best molar extinction co-efficient of 40424 $M^{-1} \times cm^{-1}$.

We determined the brightness of the multiplying the molar extinction co-efficient with the relative quantum yield, revealed bis-imidazole **48** having the 4-pyridyl R group is the brightest compound with the value of 16529.04 $M^{-1} \times cm^{-1}$, whereas bisimidazole **30e** bearing phenyl R group is the second brightest compound with the value of 6089.05 $M^{-1} \times cm^{-1}$. Excellent fluorescence properties recommend these bis-imidazole CAAs as compelling fluorescent probes for labelling and imaging of different CA isozymes in brain and other organs.

Conclusions

A set of pyridinium histamine derivatives CAAs previously developed by our group were resynthesized and used to study the binding of this class activators into the active site CA II isozyme by X-ray crystallography. From a set of five pyridinium histamine derivatives, CAA **25i** was successfully crystallized with cytosolic isozyme CA II. Activator **25i** was found to bind into the hydrophobic region of active site, with two binding conformations being observed. Based on these X-ray findings and building on our previous ethylene bis-imidazole CAAs, we designed two new series of bis-imidazoles **30a-e**, **34a-e** and **48-49**, by replacing the flexible ethylene linker with either 1,4-phenylene or 1,3-phenylene rigid linker, in order to restrict the conformations and also to further increase the lipophilicity of the activators. All new bismidazoles **30a-e**, **34a-e** and **48-49**, together with their precursors were tested for their activation potency against CNS-relevant CA isozymes. We were able to identify potent activators for CA I, CA IV, CA VA, CA IX and CA XIV. Bis-imidazole **30e** was found to be the best activator for CA IV, CA VA and CA IX. These compounds were also assessed for the photophysical properties such as absorption maximum (λ_{max}), emission maxium λ_{em}, Stokes shift, molar extinction co-efficient (ε), fluorescent quantum yield (Φ) and the brightness (ε x Φ). Bis-imidazole **48** showed the highest brightness with a quantum yield of 0.44 and Stokes shift of 80 nm, while bis-imidazole **30e** was found to be second best fluorophore with a quantum yield of 0.55 and Stokes shift of 62 nm. The very good activation profile against several different CA isozymes, along with excellent fluorescence properties recommend these compounds as great molecular tools for elucidation of role of CA isozymes in brain physiology, and as tools to test in assays of memory and learning.

Experimental Section

Materials and Methods

Materials: The following materials were used as received: bromine, (Acros, Pittsburgh, PA), 1,4-diacetylbenzene (TCI America, Portland, OR), trimethylamine (Fisher Scientific, Fair Lawn, NJ), ammonium acetate (EM Science, Gibbstown, NJ), sodium bicarbonate (Fisher Scientific, Fair Lawn, NJ), hydrochloric acid (BDH-VWR International, Radnor, PA), Sodium sulfite (VWR, Solon, OH), 2-phenyl-imidazole (Acros Organics, NJ), Benzoic acids (TCI America, Portland, OR), glyoxal (Alfa Aesar, Great Britain) A-taPhos (Sigma-Aldrich, St. Louis, MO), 1,4-phenylene dibornic acid and Palldium acetate (Oxchem corporation, Irwindale, CA).

Organic solvents (HPLC quality) were purchased from Fisher Scientific (Pittsburgh, PA), EMD (Gibbstown, NJ), and VWR International (West Chester, PA), p-dioxane (J.T. Baker, Center Valley, PA), p-xylene (Alfa Aesar, Ward Hill, MA).
For quantum yields: the following materials were used as standards: Quinine (Aldrich, Milwaukee, WI), 9,10 diphenyl anthracene (Aldrich, Milwaukee, WI), sulfuric acid (Fisher, Pittsburg, PA).

Techniques:

The microwave synthesis was performed into a CEM Discover Microwave (Matthews, NC) equipped with an Explorer PLS autosampler.

The purity and the structure identity of the intermediary and final products were assessed by thin-layer chromatography (TLC), HPLC-MS, ^{1}H-, ^{13}C- and ^{19}F-NMR, high resolution mass spectrometry (HR-MS) and melting points. TLC was carried out on SiO_2-

precoated aluminum plates (ALGURAM® SIL G/UV_{254} 20×20 cm with F254 indicator; layer thickness 0.20 nm; pore size 60 Å) from Macherey-Nagel, Bethlehem, PA. Flash chromatography was performed using a Isco Combiflash RF (Teledyne Isco, Lincoln, NE) and Isco prepacked silica columns. The purity of compounds was also assessed via LC-MS using an Agilent 1200 HPLC DAD-MS system (Santa Clara, CA) equipped with a G1315A DAD and a 6130 Quadrupole MS via a ZORBAX SB-C18 column eluted with H_2O (0.1% HCOOH)/MeCN (0.1% HCOOH) 95/5 to 0/100 linear gradient. Preparative reverse phase chromatography was performed on GILSON GX-281 system (Middleton, WI) using a GEMINI 5µ C18 110 A AXIA 50×150 mm reverse phase column, a flow rate of 40 mL/min and gradient of 15/85 to 10/90 ACN/Water over 15 min.

NMR spectra were recorded at T = 300 K with a Bruker Avance III 400 Plus spectrometer equipped with a 5 mm indirect detection probe, operating at 400 MHz for ^{1}H NMR, at 100 MHz for ^{13}C NMR, and at 376 MHz for ^{19}F NMR. Chemical shifts are reported as δ values, using tetramethylsilane (TMS) as internal standard for proton spectra and the solvent resonance for carbon and fluorine spectra. ^{19}F NMR were carbon decoupled. Assignments were made based on chemical shifts, signal intensity, COSY, HMQC, and HMBC sequences. High resolution mass spectrometry (HR-MS) was performed on a LTQ Orbitrap XL hybrid ion trap-orbitrap mass spectrometer (ThermoScientific, Waltham, MA). The melting points were determined via Thermolyne heating stage microscope (Dubuque, IA), equipped with an Olympus 5X objective, at heating/cooling rate of ~ 4 ^{o}C/min and were uncorrected.

General Procedure for the Preparation of Compounds 25 [77]

Histamine dihydrochloride (0.92 g, 5 mmol) was dissolved in minimum amount of water (200 μL) and was treated with a methanolic solution of sodium methoxide generated by reacting 115 mg Na metal with 10 mL of MeOH. The NaCl precipitate was filtered off and the methanolic filtrate containing the histamine free base was added dropwise, under stirring, over a suspension of pyrylium hexafluorophosphate (6 mmol) in 10 mL MeOH. The homogenous mixture was refluxed for 5 min, and then was treated with 0.9 mL (15 mmol) glacial acetic acid and refluxed for another 1-2 h. Aqueous ammonium hydroxide 25% (0.5 mL) was added to the reaction mixture to convert any unreacted pyrylium salt into the corresponding pyridine. The solvent was evaporated to dryness and the residue was washed with ethyl ether, and then crystallized from MeOH or iPrOH. Advanced purification was achieved by column chromatography on SiO_2, using MeOH/CH_2Cl_2 gradient elution. Useful fractions were grouped, evaporated to dryness, and the purified product was crystallized from MeOH or iPrOH.

1-[2-(1H-Imidazol-4-yl)-ethyl]-2,4,6-trimethylpyridinium hexafluorophosphate 25f

White crystals, mp. 227-229 ºC, Yield 33%; ^{1}H-NMR (dmso-d^6), δ, ppm: 9.14 (s, 1H, NH Im), 7.82 (s, 2H, H-3,5 Py), 7.68 (s, 1H, H-5 Im), 4.76 (t, *J* = 8.2 Hz, 2H, Py-$\underline{CH_2}$), 3.32 (t, *J* = 8.2 Hz, 2H, Im-$\underline{CH_2}$), 2.89 (s, 6H, 2CH_3 α-Py), 2.54 (s, 3H, CH_3 γ-Py); ^{13}C-NMR (dmso-d^6), δ, ppm: 157.6 (C-4 Py), 154.6 (2C, C-2,6 Py), 134.0 (C-2 Im), 128.23 (C-4 Im), 128.20 (2C, C-3,5 Py), 117.3 (C-5 Im), 50.4 (Py-$\underline{C}H_2$-), 22.5 (Im-$\underline{C}H_2$-), 20.8 (CH_3 γ-Py), 20.6 (2C, 2CH_3 α-Py).

1-[2-(1H-Imidazol-4-yl)-ethyl]-2,6-diethyl-4-methylpyridinium hexafluorophosphate 25g

White crystals, mp. 238-241 ºC, Yield 58%; ^{1}H-NMR (dmso-d^{6}), δ, ppm: 9.07 (s, 1H, NH Im), 7.80 (s, 2H, H-3,5 Py), 7.66 (s, 1H, H-5 Im), 4.70 (t, *J* = 8.2 Hz, 2H, Py-$\underline{CH_2}$), 3.27 (t, *J* = 8.2 Hz, 2H, Im-$\underline{CH_2}$), 3.14 (q, *J* = 7.3 Hz, 4H, 2$\underline{CH_2}CH_3$ α-Py), 2.60 (s, 3H, CH_3 γ-Py), 1.39 (t, *J* = 7.3 Hz, 6H, 2$CH_2\underline{CH_3}$ α-Py) ; ^{13}C-NMR (dmso-d^{6}), δ, ppm: 158.7 (2C, C-2,6 Py), 158.3 (C-4 Py), 134.5 (C-2 Im), 128.1 (C-4 Im), 126.1 (2C, C-3,5 Py), 117.4 (C-5 Im), 48.8 (Py-$\underline{C}H_2$-), 25.7 (2C, 2$\underline{C}H_2CH_3$ α-Py), 23.7 (Im-$\underline{C}H_2$-), 21.2 (CH_3 γ-Py), 12.6 (2C, 2$CH_2\underline{C}H_3$ α-Py).

1-[2-(1H-Imidazol-4-yl)-ethyl]-2,6-di-*iso*-propyl-4-methylpyridinium hexafluorophosphate 25i

White crystals, mp. 214-217 ºC, Yield 72%; ^{1}H-NMR (dmso-d^{6}), δ, ppm: 9.08 (s, 1H, NH Im), 7.92 (s, 2H, H-3,5 Py), 7.68 (s, 1H, H-5 Im), 4.76 (t, *J* = 7.9 Hz, 2H, Py-$\underline{CH_2}$), 3.49 (hept, *J* = 6.6 Hz, 2H, 2$\underline{CH}(CH_3)_2$ α-Py), 3.24 (t, *J* = 7.8 Hz, 2H, Im-$\underline{CH_2}$), 2.62 (s, 3H, CH_3 γ-Py), 1.40 (d, *J* = 6.5 Hz, 12H, 2CH($\underline{CH_3}$)$_2$ α-Py) ; ^{13}C-NMR (dmso-d^{6}), δ, ppm: 163.8 (2C, C-2,6 Py), 159.5 (C-4 Py), 135.4 (C-2 Im), 128.8 (C-4 Im), 125.6 (2C, C-3,5 Py), 118.5 (C-5 Im), 49.4 (Py-$\underline{C}H_2$-), 31.3 (2C, 2$\underline{C}H(CH_3)_2$ α-Py), 26.1 (Im-$\underline{C}H_2$-), 23.5 (bs, 4C, 2CH($\underline{C}H_3$)$_2$ α-Py), 22.1 (CH_3 γ-Py).

1-[2-(1H-Imidazol-4-yl)-ethyl]-2,3,4,6-tetramethylpyridinium hexafluorophosphate 25p

White crystals, mp. 203-206 ºC, Yield 78%; ^{1}H-NMR (dmso-d^{6}), δ, ppm: 9.03 (s, 1H, NH Im), 7.76 (s, 1H, H-5 Py), 7.62 (s, 1H, H-5 Im), 4.70 (t, *J* = 8.3 Hz, 2H, Py-$\underline{CH_2}$), 3.28 (t, *J* = 8.3 Hz, 2H, Im-$\underline{CH_2}$), 2.87 (s, 3H, 6-CH_3 α-Py), 2.83 (s, 3H, 2-CH_3 α-Py), 2.81 (s, 3H, CH_3 β-Py); 2.40 (s, 3H, CH_3 γ-Py); ^{13}C-NMR (dmso-d^{6}), δ, ppm: 157.6 (C-4 Py), 155.7 (C-6 Py), 153.9 (C-2 Py), 135.4 (C-2 Im), 129.2 (C-4 Im), 129.0 (C-5 Py), 128.0 (2C, C-3,5 Py), 118.3 (C-5 Im), 51.8 (Py-$\underline{C}H_2$-), 23.7 (Im-$\underline{C}H_2$-), 21.6 (CH_3 γ-Py), 21.4 (CH_3 β-Py), 18.5 (6-CH_3 α-Py), 16.6 (2-CH_3 α-Py).

1-[2-(1H-Imidazol-4-yl)-ethyl]-2-*n*-propyl-4,6-diphenylpyridinium hexafluorophosphate 25s

White crystals, mp. 132-135 ºC, Yield 47%; ^{1}H-NMR (dmso-d^{6}), δ, ppm: 8.89 (s, 1H, NH Im), 8.51 (bs, 1H, H-5 Py), 8.28 (bs, 1H, H-3 Py), 8.23 (m, 2H, H_{ortho} 4-Ph), 7.69 (m, 8H, H_{meta}, H_{para} 4,6-diPh, H_{ortho} 6-Ph), 7.19 (s, 1H, H-5 Im), 4.73 (t, *J* = 7.1 Hz, 2H, Py-$\underline{CH_2}$), 3.21 (t, *J* = 7.7 Hz, 2H, $\underline{CH_2}CH_2CH_3$ α-Py), 3.02 (t, *J* = 7.1 Hz, 2H, Im-$\underline{CH_2}$), 1.97 (sext, *J* = 7.2 Hz, 2H, $CH_2\underline{CH_2}CH_3$ α-Py), 1.15 (t, *J* = 7.2 Hz, 3H, $CH_2CH_2\underline{CH_3}$ α-Py) ; ^{13}C-NMR (dmso-d^{6}), δ, ppm: 160.1 (C-6 Py), 156.8 (C-2 Py), 154.8 (C-4 Py), 135.8 (4-Ph), 134.2 (C-2 Im), 133.9, 133.1, 131.5, 130.5 (2C), 129.9 (4C), 129.3 (2C), 128.9 (C-4 Im), 125.7 (C-5 Py), 125.6 (C-3 Py), 116.8 (C-5 Im), 52.7 (Py-$\underline{C}H_2$-), 35.6 ($\underline{C}H_2CH_2CH_3$ α-Py), 26.8 (Im-$\underline{C}H_2$-), 23.0 ($CH_2\underline{C}H_2CH_3$ α-Py), 14.6 ($CH_2CH_2\underline{C}H_3$ α-Py).

Preparation of 1,1'-(1,4-phenylene)-bis-(2-bromoethanone) 28 and **1,1'-(1,3-phenylene)-bis(2-bromoethan-1-one) 32**

To a solution of 1,4-diacetylbenzene **27** (5.028 g, 31.00 mmol) in acetic acid (120 mL), bromine (3.20 mL, 62 mmol) was added dropwise over 10 min. The reaction mixture turned dark once all the bromide was added, then gradually lightens within 40 min to yield a colorless final solution from which the product was precipitated off. The suspension was stirred for additional 2 h, after which the precipitate was filtered off, washed with AcOH and dried under vacuum to give colorless microcrystals of 1,1'-(1,4-phenylene)bis(2-bromoethanone) **28** (7.41 g, yield 70 %). The product was used in the next step without any further purification.

1,1'-(1,4-phenylene)-bis-(2-bromoethanone) 28. ^{1}H NMR (500 MHz, DMSO-d_6, δ): 8.14 (s, 4H), 5.02 (s, 4H). ^{13}C NMR (100 MHz, DMSO-d_6, δ): 191.9, 138.1, 129.5, 34.9. mp. 180.0–182.0. ºC, mp. lit.[189] 168.0 ºC.

1,1'-(1,3-phenylene)bis(2-bromoethan-1-one) 32 was prepared according to the procedure of Wang et al. [190]. To a solution of 1,3-diacetylbenzene (5.00 g, 30.82 mmol) in 120 mL MeCN, p-toluene sulfonic acid was added in small portions (15.92 g, 90.94 mmol). The resulting reaction mixture was stirred at r.t. for 10 min, then n-bromosuccinimide (10.97g, 61.64 mmol) was added and the resulting reaction mixture was heated under reflux for 3.5 h. Solvent was removed under reduced pressure, dichloromethane was added (300 mL) and was washed with water 2 × 200 mL). The organic layer was dried over MgSO4. Solvent was removed under reduced pressure to

give the crude product as a pale white precipitate colorless microcrystals were obtained after slow recrystallization from EtOH. Yield (80%). ^{1}H NMR (500 MHz, $CDCl_3$, δ): 8.58 (t, *J* = 1.4 Hz, 1H), 8.23 (dd, *J* = 7.8, 1.6 Hz, 2H), 7.66 (t, *J* = 7.8 Hz, 1H), 4.49 (s, 4H). ^{13}C NMR (100 MHz, $CDCl_3$, δ): 190.4, 134.5, 133.8, 129.6, 129.3, 30.3. mp found 88.0-89.0 ºC.

General procedure for the preparation of bis-esters 29a-e and 33a-e

To a stirred solution of carboxylic acid (6.6 mmol) in acetonitrile (10 mL) triethyl amine (920 mL, 6.6 mmol) was added dropwise and the resulting reaction mixture was stirred for 15 min to generate the corresponding carboxylate. The solution was treated with a suspension of dihaloketone **28** or **32** (0.960 g, 3 mmol) in acetonitrile (10 mL), which was added in small portions under vigorous stirring. The resulting reaction mixture was stirred at room temperature (25ºC) overnight. The reaction was monitored by TLC (EtOAc/hexanes 1/3 vol.). In the case of compound **29e** the reaction was brought to reflux for 8 h. Solvent was removed under reduced pressure to give the bis-α-ketoester **29a-e** or **33a-e**, which was purified by recrystallization from ethanol.

General procedure for the preparation of bis-imidazoles 30a-e and 34a-e

The corresponding bis-ester (**29a-e, 33a-e**) (1 equiv.) was suspended in p-xylene (2 mL) in a microwave mini reactor, then NH_4OAc (20 equiv.) was added in small portions under vigorous stirring, followed by an additional volume of 2 mL xylene. In the case of **29a** dimethylformamide (1 mL) was added to enhance the solubility. The resulting reaction

mixture was subjected to microwave irradiation (150W, 140ºC, 90 min). Solvent was removed under reduced pressure to give a brown oil which was suspended in water, then HCl 3N (pH = 1), followed by $NaHCO_3$ saturated (pH 8). The resulting yellow precipitate was filtered off, washed with a cold water and dried under vacuum overnight.

For compound **30a**, the microwave reaction gave self-condensation byproducts that were not soluble in water under acidic or basic media and were filtered off. The aqueous media was concentrated, and the resulting precipitate was further purified. Therefore, Bredereck cyclization under microwave was used (75% isolated as TFA salt).

The crude bis-imidazoles were adsorbed on silicagel and purified via flash chromatography using linear gradient DCM to DCM: MeOH 3:1 over 15 min. The useful fractions were identified via TLC and LC-MS, were grouped and evaporated to dryness yielding pre-purified products that were subjected to reverse phase purification with water (0.1% TFA): acetonitrile (0.1% TFA) gradients (90:10 to 40:60). The bis-imidazoles were isolated as TFA salts, (> 99% purity by HPLC).

1,4-Phenylenebis(2-oxoethane-2,1-diyl) diformate, 29a. Colorless crystals, 0.67 g, Yield 90%. mp 158.0-160.0 ºC.^{1}H NMR (500 MHz, $CDCl_3$, δ): 8.26 (s, 2H), 8.05(s, 4H), 5.45(s, 4H).^{13}C NMR (100 MHz, $CDCl_3$, δ): 190.6, 159.9, 137.8, 128.4, 65.4. HRMS-FAB (*m/z*): $[M+H]^+$ calcd. for $C_{12}H_{11}O_6$ 251.0550; found: 251.0554.

1,4-Phenylenebis(2-oxoethane-2,1-diyl) diacetate, 29b. Colorless microcrystals, 0.80g, Yield 97% yield. Mp 150.0-151.0 ºC; lit.[191] mp 146.0–147.0 ºC ^{1}H NMR (500 MHz, $CDCl_3$, δ): 8.02(s, 4H), 5.34 (s, 4H), 2.24 (s, 6H). ^{13}C NMR (100 MHz, $CDCl_3$, δ):

191.72, 170.4, 138.0, 128.3, 66.1, 20.5. HRMS-FAB (*m/z*): $[M+H]^+$ calcd. for $C_{14}H_{15}O_6$ 279.0863; found: 279.0871.

1,4-Phenylenebis(2-oxoethane-2,1-diyl) dipropionate, **29c.** Colorless microcrystals, 0.78g, Yield 83%. Mp 137.0-130.0 ºC.^{1}H NMR (500 MHz, $CDCl_3$, δ): 8.02(s, 4H), 5.34 (s, 4H), 2.53 (q, *J* = 7.6 Hz, 4H), 1.22 (t, *J* = 7.6 Hz, 6H). ^{13}C NMR (100 MHz, $CDCl_3$, δ): 191.9, 174.0, 128.2, 66.0, 27.2, 9.0). HRMS-FAB (*m/z*): $[M+H]^+$ calcd. for $C_{16}H_{19}O_6$ 307.1176; found 307.1182.

1,4-Phenylenebis(2-oxoethane-2,1-diyl)-bis(2-methylpropanoate), 29d. Colorless microcrystals, 0.75g, Yield 73 %. mp. 121.0-122.0 ºC.^{1}H NMR (500 MHz, $CDCl_3$, δ): 8.01 (s, 4H), 5.32 (s, 4H), 2.74 (sep, *J* = 7.0 Hz, 2H), 1.27 (d, *J* = 7.0 Hz, 12H). ^{13}C NMR (100 MHz, $CDCl_3$, δ): 192.0, 176.5, 138.0, 128.2, 65.9, 33.8, 19.0. HRMS-FAB (*m/z*): $[M+H]^+$ calcd. for $C_{18}H_{23}O_6$ 335.1489; found 335.1491.

1,4-Phenylenebis(2-oxoethane-2,1-diyl) dibenzoate 29e, colorless microcrystals, 0.71g, Yield 60%. mp. 238-239 ºC; mp. lit.[192] 214.0-215.0 ºC. ^{1}H NMR (500 MHz, $CDCl_3$, δ):8.24 (s, 4H), 8.06 (dd, *J* = 6.8, 1.6 Hz, 4H), 7.75-7.71 (m, 2H), 7.61 – 7.58 (m, 4H), 5.83 (s, 4H). ^{13}C NMR (100 MHz, $CDCl_3$, δ): 192.7, 165.2, 137.6, 134.0, 129.4, 129.0, 128.9, 128.3, 67.4. HRMS-FAB (*m/z*): $[M+H]^+$ calcd. for $C_{24}H_{19}O_6$ 403.1176; found 403.1182.

1,3-Phenylenebis(2-oxoethane-2,1-diyl) diformate 33a, colorless microcrystals, 0.75g, Yield 96 %. mp. 129.0 – 130.0 ºC.. ^{1}H NMR (500 MHz, $CDCl_3$, δ): 8.45 (t, *J* = 1.4 Hz, 1H), 8.26 (s, 2H), 8.17 (dd, *J* = 7.8, 1.6 Hz, 2H), 7.68 (t, *J* = 7.8 Hz, 1H), 5.47 (s, 4H). ^{13}C NMR (100 MHz, $CDCl_3$, δ): 190.4, 159.9, 134.6, 132.8, 129.8, 127.0, 65.3. HRMS-FAB (*m/z*): $[M+H]^+$ calcd. for $C_{12}H_{11}O_6$ 251.0550; found 251.0556.

1,3-Phenylenebis(2-oxoethane-2,1-diyl) diacetate 33b, colorless microcrystals, 0.54g Yield 63%. mp found 125.0–126.0 ºC; mp lit.[193] 121.0–121.5 ºC.^{1}H NMR (500 MHz, $CDCl_3$, δ): 8.43 (s, 1H), 8.15 (dd, *J* = 7.8, 1.6 Hz, 2H), 7.65 (t, *J* = 7.8 Hz, 1H), 5.36 (s, 4H), 2.24 (s 6H). ^{13}C NMR (100 MHz, $CDCl_3$, δ): 191.4, 170.4, 134.8, 132.6, 129.7, 127.0, 66.0, 20.5. HRMS-FAB (*m/z*): $[M+H]^+$ calcd. for $C_{14}H_{15}O_6$ 279.0863; found 279.0869.

1,3-Phenylenebis(2-oxoethane-2,1-diyl) dipropionate 33c, colorless microcrystals. 0.70 g, Yield 75%. mp. found 78.0–80.0 ºC.^{1}H NMR (500 MHz, $CDCl_3$, δ): 8.43 (s, 1H), 8.15 (dd, *J* = 7.8, 1.7 Hz, 2H), 7.65 (t, *J* = 7.8 Hz, 1H), 5.36 (s, 4H), 2.53(q, *J* = 7.6 Hz, 4H), 1.23 (t, *J* = 7.5 Hz, 6H). ^{13}C NMR (100 MHz, $CDCl_3$, δ): 191.6, 173.9, 134.8, 132.6, 129.6, 127.0, 65.9, 27.2, 9.1 HRMS-FAB (*m/z*): $[M+H]^+$ calcd. for $C_{16}H_{19}O_6$ 307.1176; found 307.1180.

1,3-Phenylenebis(2-oxoethane-2,1-diyl) bis(2-methylpropanoate) 33d, colorless microcrystals 0.60g, Yield 60%. Mp 38.0–40.0 ºC.^{1}H NMR (500 MHz, $CDCl_3$, δ): 8.43 (t, *J* = 1.5 Hz, 1H), 8.14 (dd, *J* = 7.8, 1.7 Hz, 2H), 7.64 (t, *J* = 7.8 Hz, 1H), 5.34 (s, 4H),

2.73 (sep, J = 7.0 Hz, 2H), 1.26 (d, J = 7.0 Hz, 12H). ^{13}C NMR (100 MHz, $CDCl_3$, δ): 191.7, 176.5, 134.8, 132.6, 129.6, 127.0, 65.8, 33.8, 19.0. HRMS-FAB (*m/z*): $[M+H]^+$ calcd. for $C_{18}H_{23}O_6$ 335.1489; found 335.1493.

1,3-Phenylenebis(2-oxoethane-2,1-diyl) dibenzoate 33e, colorless microcrystals, 0.76g, Yield 63%. Mp 158.0 -160.0 ºC.^{1}H NMR (500 MHz, $CDCl_3$, δ): 8.54 (t, J = 1.4 Hz, 1H), 8.22 (dd, J = 7.8, 1.6 Hz, 2H), 8.15 – 8.13 (m, 4H), 7.68 (t, J = 7.8 Hz, 1H), 7.61 (tt, J = 5.7, 1.3 Hz, 2H), 7.48 (t, J = 7.9 Hz, 4H), 5.60 (s, 4H). ^{13}C NMR (100 MHz, $CDCl_3$, δ): 191.5, 166.0, 134.9, 133.5, 132.7, 130.0, 129.7, 129.2, 128.5, 127.2, 66.5. HRMS-FAB (*m/z*): $[M+H]^+$ calcd. for $C_{24}H_{19}O_6$ 403.1176; found 403.1178.

5-(4-(1H-Imidazol-5-yl)phenyl)-1H-imidazol-3-ium trifluoroacetate 30a, colorless microcrystals. [194], mp lit.[195] > 340 ºC. ^{1}H NMR (500 MHz, DMSO-d_6, δ): 9.10 (s, 2H), 8.21 (s, 2H), 7.97 (s, 4H). ^{13}C NMR (100 MHz, DMSO-d_6, δ): 158.5 (q, J = 32.3 Hz), 135.5, 132.5, 127.8, 125.8, 116.0, 116.0 (q, J = 241.3 Hz). ^{19}F NMR (376 MHz DMSO-d_6, δ): -73.9. LC-MS: calcd. for $C_{12}H_{11}N_4$ $[M+H]^+$ 211.0978; found 211.1 (t_R = 0.24 min, > 97% purity).

2-Methyl-5-(4-(2-methyl-1*H*-imidazol-5-yl)phenyl)-1*H*-imidazol-3-ium, trifluoroacetate salt 30b, colorless microcrystals mp > 340 ºC. ^{1}H NMR (500 MHz, DMSO-d_6, δ): 14.70 (br s, 2H), 8.10 (s, 2H), 7.93 (s, 4H), 2.65 (s, 6H). ^{13}C NMR (100 MHz, DMSO-d_6, δ): 158.6 (q, J = 32.4 Hz), 145.4, 131.2, 127.4, 125.5, 121.3, 116.8 (q, J

= 297.0 Hz), 115.3, 11.3. ^{19}F NMR (376 MHz DMSO-d_6, δ): -74.0.[196] LC-MS: $[M+H]^+$ calcd. for $C_{14}H_{15}N_4$ 239.1291; found 239.1 (t_R = 0.32 min, > 99% purity).

2-Ethyl-5-(4-(2-ethyl-1*H*-imidazol-5-yl)phenyl)-1*H*-imidazol-3-ium trifluoroacetate 30c, colorless microcrystals, mp > 340 ºC. ^{1}H NMR (500 MHz, DMSO-d_6, δ): 14.61 (brs, 4H), 8.15 (s, 2H),7.96 (s, 4H), 3.01 (q, *J* = 7.6 Hz, 4H), 1.35 (t, *J* = 7.6 Hz, 6H). ^{13}C NMR (100 MHz, DMSO-d_6, δ): 158.9 (q, J =34.6 Hz), 150.4, 131.7, 127.9, 126.1, 116.7 (q, J = 293.7 Hz), 115.9, 19.6, 11.9. ^{19}F NMR (376 MHz DMSO-d_6, δ) -74.4. LC-MS (*m/z*): $[M+H]^+$ calcd. for $C_{16}H_{19}N_4$ 267.1604; found 267.1 (t_R = 1.40 min, > 96% purity).

2-Isopropyl-5-(4-(2-isopropyl-1*H*-imidazol-5-yl)phenyl)-1*H*-imidazol-3-ium trifluoroacetate 30d, colorless microcrystals mp > 340 ºC. ^{1}H NMR (500 MHz, DMSO-d_6, δ): 14.68 (brs, 2H), 8.14 (s, 2H), 7.94 (s, 4H), 3.37 (sep, J = 6.9 Hz, 2H), 1.38 (m , 12H). ^{13}C NMR (100 MHz, DMSO-d_6, δ): 159.2 (q, *J* = 32.5 Hz), 153.8, 132.0, 127.9, 126.2, 117.3 (q, J = 297.3 Hz), 115.9, 26.9, 20.7. ^{19}F NMR (376 MHz DMSO-d_6, δ) -74.0. LC-MS (*m/z*): $[M+H]^+$ calcd. for $C_{18}H_{23}N_4$ 295.1917; found 295.1 (t_R = 1.50, > 98% purity).

2-Phenyl-5-(4-(2-phenyl-1*H*-imidazol-5-yl)phenyl)-1*H*-imidazol-3-ium trifluoroacetate, 30e, colorless microcrystals mp > 340 ºC. ^{1}H NMR (500 MHz, DMSO-d_6, δ): 8.25 (s, 2H), 8.12-8.10 (m, 3H), 8.07 (s, 4H), 7.69 – 7.58 (m, 6H). ^{13}C NMR (100 MHz, DMSO-d_6, δ): 158.4 (q, *J* = 33.7 Hz), 145.1, 134.9, 131.1, 129.2, 128.7,

126.6, 125.7, 125.1, 117.1, 116.5 (q, J = 295.8 Hz). ^{19}F NMR (376 MHz DMSO-d_6, δ) -74.2. LC-MS (*m/z*): $[M+H]^+$ calcd. for $C_{24}H_{19}N_4$ 363.1604; found 363.1 (t_R = 1.98 min, > 98% purity)

5,5'-(1,3-Phenylene)bis(1*H*-imidazol-3-ium) 34a, colorless microcrystals, mp found > 340 ºC. mp lit. [195] 287-288 °C. ^{1}H NMR (500 MHz, DMSO-d_6, δ): 9.16 (s, 2H), 8.32 (s 1H), 8.15 (s, 2H), 7.86 (dd, *J* = 8.0, 1.6 Hz, 2H) 7.68 (t, *J* = 8.0 Hz, 1H). ^{13}C NMR (100 MHz, DMSO-d_6, δ): 160.0 (q, *J* = 33.4 Hz), 137.2, 134.1, 131.7, 130.0, 126.9, 124.0, 118. 2 (q, *J* = 293.6Hz), 117.5. ^{19}F NMR (376 MHz DMSO-d_6, δ) -74.06. LC-MS (*m/z*): $[M+H]^+$ calcd. for $C_{12}H_{11}N_4$ 211.0978; found 211.1 (t_R = 0.21 min, > 97% purity).

5,5'-(1,3-Phenylene)bis(2-methyl-1*H*-imidazol-3-ium) trifluoroacetate 34b, colorless microcrystals Mp 244.0-245.0 ºC.. ^{1}H NMR (500 MHz, DMSO-d_6, δ): 14.7 (s, 4H), 8.24 (s, 1H), 8.04 (s, 2H), 7.80 (dd, *J* = 7.60 Hz, 2H), 7.68 (t, *J* = 7.32 Hz, 1H). ^{13}C NMR (100 MHz, DMSO-d_6, δ): 159.0 (q, *J* = 34.0 Hz), 146.0, 131.8, 130.8, 128.6, 125.4, 122.1, 116.9 (q, *J* = 295.4 Hz), 115.8, 11.8. ^{19}F NMR (376 MHz DMSO-d_6, δ) -74.27. LC-MS (*m/z*): $[M+H]^+$ calcd. for $C_{14}H_{15}N_4$ 239.1291; found 239.1 (t_R = 0.55 min, > 97% purity).

5,5'-(1,3-Phenylene)bis(2-ethyl-1*H*-imidazol-3-ium) trifluoroacetate salt 34c, colorless microcrystals. Mp 160ºC.. ^{1}H NMR (500 MHz, DMSO-d_6, δ): 14.68 (s, 3H), 8.26 (s, 1H), 8.06 (s, 2H), 7.82 (dd *J*= 7.72, 1.16 Hz, 2H), 7.66 (t, *J* = 7.80 Hz, 1H), 3.00 (q, *J* = 7.60 Hz, 4H), 1.35 (t, *J* = 7.60 Hz, 6 H). ^{13}C NMR (100 MHz, DMSO-d_6, δ): 158.6 (q, *J* = 32.3 Hz), 149.9, 131.6, 130.1, 128.3, 125.1, 121.8, 116.7 (q, *J* = 313.2 Hz),

115.3, 19.2, 11.4. ^{19}F NMR (376 MHz DMSO-d_6, δ) -73.89. LC-MS (*m/z*): $[M+H]^+$ calcd. for $C_{16}H_{19}N_4$ 267.1604; found 267.1 (t_R = 1.44 min, > 96% purity).

5,5'-(1,3-Phenylene)bis(2-isopropyl-1*H*-imidazol-3-ium) trifluoroacetate salt 34d, colorless crystals. Mp 304- 305 ^{0}C. ^{1}H NMR (500 MHz, DMSO-d_6, δ): 14.6 (s, 3H), 8.27 (s, 1H), 8.06 (s, 2H), 7.86-7.84 (m, 2H), 7.65 (t, *J* = 8.0 Hz, 1H), 3.38 (sep, *J* = 6.8 Hz, 2H), 1.40 (d, *J* = 6.9 Hz, 12H). ^{13}C NMR (100 MHz, DMSO-d_6, δ): 158.6 (q, *J* = 32.12 Hz), 153.3, 131.8, 129.9, 128.4, 125.3, 122.1, 121.4, 116.93 (q, *J* = 297.9 Hz), 115.3, 20.3, 15.1. ^{19}F NMR (376 MHz DMSO-d_6, δ) -73.90. LC-MS (*m/z*): $[M+H]^+$ calcd. for $C_{18}H_{23}N_4$ 295.1917; found 295.1 (t_R = 1.45 min, > 98% purity).

5,5'-(1,3-Phenylene)bis(2-phenyl-1*H*-imidazol-3-ium) trifluoroacetate salt 34e, colorless microcrystals mp > 340 ºC. ^{1}H NMR (500 MHz, DMSO-d_6, δ): 8.44 (s, 1H), 8.21 (s, 2H), 8.12 (dd, *J* = 8.2, 1.6 Hz, 3H), 7.94 (dd, *J* = 7.8, 1.6 Hz, 2H), 7.68 – 7.61 (m, 5H). ^{13}C NMR (100 MHz, DMSO-d_6, δ): 159.2 (q, *J* = 34.4 Hz), 146.0, 136.1, 131.8, 130.7, 130.5, 130.1, 127.4, 126.2, 126.0, 123.1, 117.8, 117.1 (q, *J* = 294.1 Hz). ^{19}F NMR (376 MHz DMSO-d_6, δ) -74.34. LC-MS (*m/z*): $[M+H]^+$ calcd. for $C_{24}H_{19}N_4$ 363.1604; found 363.1 (t_R = 1.95 min, > 97% purity).

General procedure for the synthesis of 2-Aryl-imidazole 37-38

We utilized two methods namely Method A for the synthesis of 2-aryl or heteroaryl imidazole following reported procedure [182, 183].

In Method A [182], to a stirring solution of 2-aryl benzaldehyde (10 mmol) in ethanol (40 mL) at 0ºC was slowly added a solution of 40% oxalaldehyde in water (1.3 mL, 11 mmol) and a solution of 29% ammonium hydroxide in water (100 mmol, 14 mL). After 15 mins the ice bath was removed and the reaction mixture was allowed to stir at room temperature for 2-3 days. After completion of the reaction, the solvent was evaporated from the reaction mixture and the crude product was purified by flash chromatography using linear gradient DCM: Methanol 9:1 over 20 min. The maximum yield was 30% with this procedure. Thus we approached for Method B to maximize the yield [182].

In Method B [183], to a stirring solution of aryl nitrile (10 mmol) in methanol (20 ml) was slowly added 30% solution of NaOMe in MeOH (10 mmol) and the reaction mixture was allowed to stir for 1h. Then aminoacetaldehyde dimethyl acetal (10 mmol) followed by acetic acid (20 mmol) was added slowly. The reaction mixture was refluxed for 30 min. After that the reaction mixture was allowed to cool down, methanol (25 ml) followed by 6N HCl in H_2O (25 ml) was added. The reaction mixture was refluxed for 5h. After completion of the reaction, the solvent was evaporated to dryness to obtain crude product. To the crude product freshly prepared warm solution of K_2CO_3 (5.5 g) in H_2O (5.5 g) was added very slowly to bring pH to 8-10. The product precipitated out from solution which is then filtered or extracted, dried and further purified by recrystallization [183].

General procedure for synthesis of 4,5-dibromo-2-aryllimidazole 42-44 [181]

To a stirring solution of 2-arylimidazole or 2-heteroarylimidazole (34.68 mmol) in THF (100 mL) was treated with NBS (69.36 mmol) in small portions at 0°C. The ice bath was then removed and the reaction mixture was stirred at room temperature for the 1-2 hrs for completion of the reaction. The products were purified by normal phase flash chromatography using linear gradient DCM: methanol 4:1 over 20 min. TLC was done to identify the desired compounds, useful fractions were combined and evaporated to dryness, and the purified products were used for subsequent steps.

General procedure for synthesis of 4 (5) -bromo-2-aryl or heteroarylimidazole 45-47

A stirred solution of 2-aryl (heteroaryl)-4,5-dibromoimidazol (16.5 mmol) and sodium sulfite (33 mmol) in 50% aqueous ethanol (50 mL) was refluxed for 2-3 days. The reaction mixture was allowed to cool down and methanol (50 ml) was added. Excess sodium sulfite and sodium salt were filtered out. The solvent from the filtrate was evaporated under reduced pressure to give the crude product as a pale white precipitate. The crude precipitate was adsorbed on silicagel and purified via flash chromatography using linear gradient DCM: Methanol 5:1 over 15 min. The useful fractions were identified via TLC and LC-MS, were grouped and evaporated to dryness yielding purified product (50-60%) [181, 197].

General procedure for synthesis of Bisimidazole 30e and **48-49**

A solution of 4 (5) -bromo-2-arylimidazole (2 mmol) and 1,4-phenylenediboronic acid (01.25 mmol) was prepared in dioxane (5 mL) and placed in a flame dried two neck round bottom flask under nitrogen gas flow. A premixed solution of palldium (II) acetate (0.018 g, 0.08 mmol) and A-^{ta}Phos (0.008 g, 0.03 mmol) in dioxane (5 mL) was added dropwise over 5 mins and nitrogen gas was purged through the solution. Finally, aqueous K_2CO_3 solution (5 mL, 1.2 M) was added to the reaction mixture. Then the reaction vessel was sealed and refluxed at 140°C for 48 hrs.[181] Alternatively, this reaction can be carried out using microwave irradiation instead of conventional reflux. A solution of 4 (5) -bromo-2-arylimidazole (1 mmol) in dry THF (1 ml) was placed in microwave tube which was then sealed and purged with nitrogen gas. To the microwave tube, a premixed solution of palldium (II) acetate (0.009 g, 0.04 mmol) and A-taPhos (0.009 g, 0.04 mmol) in THF (1 mL) was added through a syringe and the reaction mixture was allowed to stir for 30 mins. A solution of 1,4-phenylenediboronic acid (0.6 mmol) in THF (1 mL) followed by aqueous K_2CO_3 solution (1 mL, 2 M) was injected to reaction mixture and stirred for 30 mins. The microwave tube was purged with nitrogen gas again and irradiate under microwave heat at 120°C for 1h. After reflux or microwave irradiation, the reaction mixture was allowed to cool down and solvent was evaporated to yield crude precipitate. The crude precipitate was adsorbed on silicagel and purified via flash chromatography using linear gradient $CHCl_3$: MeOH 5:1 over 15 min. The useful fractions were identified via TLC and LC-MS, were grouped and evaporated to dryness yielding purified product [181].

4-(1H-imidazol-2-yl)pyridine 37

The crude product was obtained via Method A and which was then purified by flash chromatography and by recrystallization with boiling water to yield to pure product as off white solid (25% yield).[183] mp 210-212 °C. ^{1}H NMR (400 MHz, DMSO-d_6) δ 12.9 (br s, 1H), 8.63 (dd, 2H, J=4.5, 1.6 Hz), 7.87 (dd, 2H, J=4.5, 1.6 Hz), 7.27 (br s, 2H); ^{13}C NMR (400 MHz, DMSO-d_6) δ 150.1, 143.1, 137.3, 129.8 (br s), 118.7; MS (ESI) m/z 146 (M+H), ret. time 0.2 min, > 99% purity).

3-(1H-imidazol-2-yl)pyridine 38

The crude product was obtained via Method B which was purified by recrystallization with boiling water to yield pure product as off white solid (99% yield).[183] mp 195-196 °C. ^{1}H NMR (400 MHz, DMSO-d_6) δ 12.72 (br s, 1H), 9.14 (d, 1H, J= 1.6 Hz), 8.54 (dd, 1H, J=4.8, 1.6 Hz), 8.26 (td, 1H, J=8.1, 1.8 Hz), 7.49-7.22 (m, 1H), 7.21 (br s, 2H), ^{13}C NMR (400 MHz, DMSO-d_6) δ 148.6, 146.0, 142.9, 131.9, 129.6, 126.6, 123.7, 118.2; (MS (ESI) m/z 146 (M+H), ret. time 0.18 min, > 99% purity).

4-(4,5-dibromo-1H-imidazol-2-yl)pyridine 42

After completion the reaction mixture was evaporated to dryness and resulting crude product was then purified by flash chromatography using linear gradient DCM: MeOH 9:1 over 15 min. Yield was 75% (orange solid). mp 280-282 °C. ^{1}H NMR (400 MHz, DMSO-d_6) δ 14.1 (br s, 1H), 8.66 (dd, 2H, J=4.6, 1.5 Hz), 7.83 (dd, 2H, J=4.6, 1.7

Hz); ^{13}C NMR (400 MHz, DMSO-d_6) δ 179.3, 149.9, 144.5, 136.0 118.4; MS (ESI) m/z 304 (M+H), ret. time 1.74 min, > 99% purity)

3-(4,5-dibromo-1H-imidazol-2-yl)pyridine 43

After completion the reaction mixture was evaporated to dryness and resulting crude product was then washed with hot water (50 ml) three times and then with hexane to give purified product as a yellowish solid (99% yield), mp 215-220 °C. ^{1}H NMR (400 MHz, DMSO-d_6) δ 14.2 (br s, 1H), 8.62 (s, 1H), 7.98-7.91 (m, 2H) 7.45-7.42 (m, 1H); ^{13}C NMR (400 MHz, DMSO-d_6) δ 148.4, 146.6, 145.9, 137.0 123.3, 118.84; (MS (ESI) m/z 304 (M+H), ret. time 2.73 min, > 99% purity). The experimental data of this product were consistent with the literature data.[198, 199]

4,5-dibromo-2-phenylimidazole 44

EtOAc (100 mL) was added and the mixture was washed with water three times and then with brine. The organic layer was dried over $MgSO_4$, filtered, and concentrated in vacuum. yield orange solid (99% yield).[181] mp 135-137 °C . ^{1}H NMR (400 MHz, DMSO-d_6) δ 13.62 (br s, 1H), 7.89 (dd, 2H, J=7.2, 1.5 Hz), 7.49-7.40 (m, 3H), ^{13}C NMR (400 MHz, DMSO-d_6) δ 146.9, 129.0, 128.9, 124.9, 124.7, (MS (ESI) m/z 303 (M+H), ret. time 4.16 min, > 99% purity). The experimental data of this product were consistent with the literature data [181, 197].

4-(5-bromo-1H-imidazol-2-yl)pyridine 45

The purified compound was obtained as orange solid. Yield is 55%. mp 249-250 °C ^{1}H NMR (400 MHz, DMSO-d_6) δ 13.3 (br s, 1H), 8.65 (dd, 2H, J=4.8, 1.4 Hz), 7.83 (dd, 2H, J=4.6, 1.6 Hz); ^{13}C NMR (400 MHz, DMSO-d_6) δ 150.1, 143.3, 136.1, 118.9, 118.4, 115.6; (MS (ESI) m/z 224 (M+H), ret. time 0.59 min, > 99% purity).

3-(5-bromo-1H-imidazol-2-yl)pyridine 46

Purified product was obtained as an off white solid. Yield 60%. mp 225-226 °C ^{1}H NMR (400 MHz, DMSO-d_6) δ 13.11 (br s, 1H), 9.1 (d, 1H, J= 4.6 Hz), 7.98 (d, 1H, J= 7.8 Hz), 7.9 (td, 1H, J= 7.6, 1.4 Hz), 7.41 (d, 1H, J= 5.04), 7.38 (br s, 1H), ^{13}C NMR (400 MHz, DMSO-d_6) δ 148.9, 147.6, 145.4, 137.4, 123.5, 119.51, 118.4, 114.9; (MS (ESI) m/z 224 (M+H), ret. time 1.88 min, > 99% purity).

4 (5) -bromo-2-phenylimidazole 47

Purified product was obtained as a white solid. Yield 52%. mp 233-235 °C.[197] ^{1}H NMR (400 MHz, DMSO-d_6) δ 12.89 (br s, 1H), 7.89 (dd, 2H, J=8.5, 1.3 Hz), 7.47-7.42 (m, 3H), 7.39 (t, 1H J=7.3) ; ^{13}C NMR (400 MHz, DMSO-d_6) δ 145.8, 129.6, 128.8, 128.5, 124.73, 124.4, 117.3, 114.8; (MS (ESI) m/z 223 (M+H), ret. time 2.1 min, > 99% purity). The experimental data of this product were consistent with the literature data [181, 197, 200].

1,4-bis(2-phenyl-1H-imidazol-4-yl)benzene 30e

The pure compound was obtained as an off-white solid. Yield 50%. mp higher than 360 °C. ^{1}H NMR (400 MHz, DMSO-d6) δ, 12.65 (brs, 1H), 8.03 – 7.78 (m, 10H),

7.46 (brs, 6H). ^{13}C NMR (400 MHz, DMSO-d_6) δ 145.1, 134.9, 131.1, 129.2, 128.7, 126.6, 125.7, 125.1, 117.1, 116.5; MS (ESI) m/z 363 (M+H), ret. time 1.89 min, > 99% purity).

1,4-bis(2-(pyridin-4-yl)-1H-imidazol-4-yl)benzene 48

The pure compound was obtained as an off-white solid. Yield 50%. mp higher than 360 °C. ^{1}H NMR (400 MHz, DMSO-d_6) δ 13.09 (br s, 2H), 8.65 (d, 4H, J= 5.8 Hz), 7.93-7.88 (m, 5H), 7.39 (t, 4H, J= 7.6 Hz), 7. 39 (t, 1H, J= 7.2 Hz) ^{13}C NMR (400 MHz, DMSO-d_6) δ 150.2, 143.4, 142.0, 137.1, 134.1, 128.5, 126.6, 124.5, 118.8, 115.8; MS (ESI) m/z 365 (M+H), ret. time 1.8 min, > 99% purity).

1,4-bis(2-(pyridin-3-yl)-1H-imidazol-4-yl)benzene 49

The pure compound was obtained as an off-white solid. Yield 60%. mp higher than 360 °C. ^{1}H NMR (400 MHz, DMSO-d_6) δ 12.88 (br s, 2H), 9.23 (s, 2H), 8.57 (dd, 2H, J= 4.5, 1 Hz), 8.35 (d, 2H, J= 7.6 Hz), 7.9 (s, 6H), 7.52 (dd, 2H, J= 7.8, 4.8 Hz), ^{13}C NMR (400 MHz, DMSO-d_6) δ 148.9, 146.2, 143.4, 132.1, 126.4, 125.0, 124.6, 123.8, 114.83; (MS (ESI) m/z 365 (M+H), ret. time 1.87 min, > 99% purity).

CA activation assay

An Applied Photophysics stopped-flow instrument was used for assaying the CA catalysed CO_2 hydration activity [158]. Phenol red (at a concentration of 0.2 mM) was used as indicator, working at the absorbance maximum of 557 nm, with 10 mM Hepes (pH 7.5) as buffer, 0.1 M Na_2SO_4 (for maintaining constant ionic strength), following the

CA-catalyzed CO_2 hydration reaction for a period of 10 s at 25°C. The CO_2 concentrations ranged from 1.7 to 17 mM for the determination of the kinetic parameters and activation constants. For each activator at least six traces of the initial 5-10% of the reaction have been used for determining the initial velocity. The uncatalyzed rates were determined in the same manner and subtracted from the total observed rates. Stock solutions of activators were prepared in distilled-deionized water and dilutions up to 0.001 μM were done thereafter with distilled-deionized water. Activator and enzyme solutions were preincubated together for 15 min (standard assay at room temperature, or for prolonged periods of 24-72 h, at 4 °C) prior to assay, in order to allow for the formation of the E-A complex. The activation constant (K_A), defined similarly with the inhibition constant K_I [156, 201], can be obtained by considering the classical Michaelis-Menten equation (equation *4*), which has been fitted by non-linear least squares by using PRISM 3:

$$v = v_{max} /\{1 + K_M /[S] (1 + [A]_f/K_A)\} \qquad (4)$$

where $[A]_f$ is the free concentration of activator.

Working at substrate concentrations considerably lower than K_M ($[S] << K_M$), and considering that $[A]_f$ can be represented in the form of the total concentration of the enzyme ($[E]_t$) and activator ($[A]_t$), the obtained competitive steady-state equation for determining the activation constant is given by eq. *5* [156, 201]:

$$v = v_0 \,.\, K_A /\{K_A + ([A]_t - 0.5\, \{([A]_t + [E]_t + K_A) - ([A]_t + [E]_t + K_A)^2 - 4[A]_t.[E]t)^{1/2}\}\}$$

(*5*)

where v_0 represents the initial velocity of the enzyme-catalyzed reaction in the absence of activator [156, 201].

Determination of absorption, emission, Stokes shifts and quantum yield

Dilute solutions of CAAs in methanol having concentration range from 10^{-5} M- 10^{-5} M were prepared for each compound. Atmospheric oxygen contained in the solutions was not removed. The excitation wavelength was at the absorption maxima for acquiring the fluorescence spectra. Absorption and fluorescence spectra were determined on a Jasco V-760 UV-visible spectrophotometer and FluoroMax-2 Spectrofluorometer respectively using 10 mm quartz cuvette. Absorption maximum, emission maximum and Stokes shifts were determined using Microsoft Excel.

For the determination of the relative fluorescence quantum yields (Φf), a series of dilute solutions of CAAs in methanol, having absorbance below 0.1 (concentration ranging from 10^{-7} M- 10^{-6} M) at the excitation wavelength λ_{ex}, were prepared for each compound. First absorption spectra of the solutions were acquired and the absorption maxima for excitation (λ_{ex}) were determined. The fluorescence spectra of the same solutions were determined using excitation wavelength at absorption maxima (λ_{ex}). The integrated fluorescence intensity was determined and plotted against the corresponding absorbance to determine the gradient. The relative fluorescence quantum yields (Φf) were determined by following equation using 9,10-diphenylanthracene in cyclohexane as the reference standard (Φf 0.9):

$$Q = Q_R\left(\frac{m}{m_R}\right)\left(\frac{n^2}{n^2_R}\right)$$

where m is the gradient obtained from the plot of the integrated fluorescence intensity vs. absorbance. n is the refractive index of solvent and the subscript R refers to the reference fluorophore of known quantum yield.

CHAPTER 4

DEVELOPMENT AND BIOLOGICAL EVALUATION OF UREIDO-1,3,4-THIADIAZOLE SULFONAMIDES AS CARBONIC ANHYDRASE INHIBITORS FOR POTENTIAL ANTI-CANCER AGENTS

In this chapter, our goal was to rationally design, synthesize and characterize small MW CAIs that can efficiently inhibit CA IX and to establish their selectivity against other CA isozymes, drawing structure-activity relationships, and to evaluate their *in vitro* cell killing ability against CA IX expressing cancer cell line.

Our working hypothesis is that thiadiazole sulfonamide warhead attached to aliphatic and aromatic moieties with different sizes via ureido linker will reliably orient their hydrophobic tails into hydrophobic pockets within the CA active site and thereby will generate CAIs with high potency against CA IX and CA XII along with improved selectivity against off-target sytosolic isozymes CA I and CA II.

Background and design approach

As discussed in the background and significance (Chapter 2), CA IX and CA XII were found to be overexpressed in many hypoxic tumors, where they are involved in pH regulation and tumor progression [57, 58]. Thus, inhition of CA IX and CA XII offer a promising strategy to kill hypoxic tumor cells through potent and selective small molecular weight carbonic anhydrase inhibitors. However, the use of classical inhibitors such as acetazolamide **1** and other CAIs in clinical use (Chart 2.1) for treatment of hypoxic tumors failed due to lack of potency and selectivity of these drugs towards the

CA IX target and suboptimal pharmacokinetics [2, 16]. These findings triggered a quest for potent and selective CA IX inhibitors [2, 16].

However, the development of CA IX selective inhibitors proved to be a difficult task due to significant similarities that exist between the active sites of different isozyme (Figure 4.1) [16].

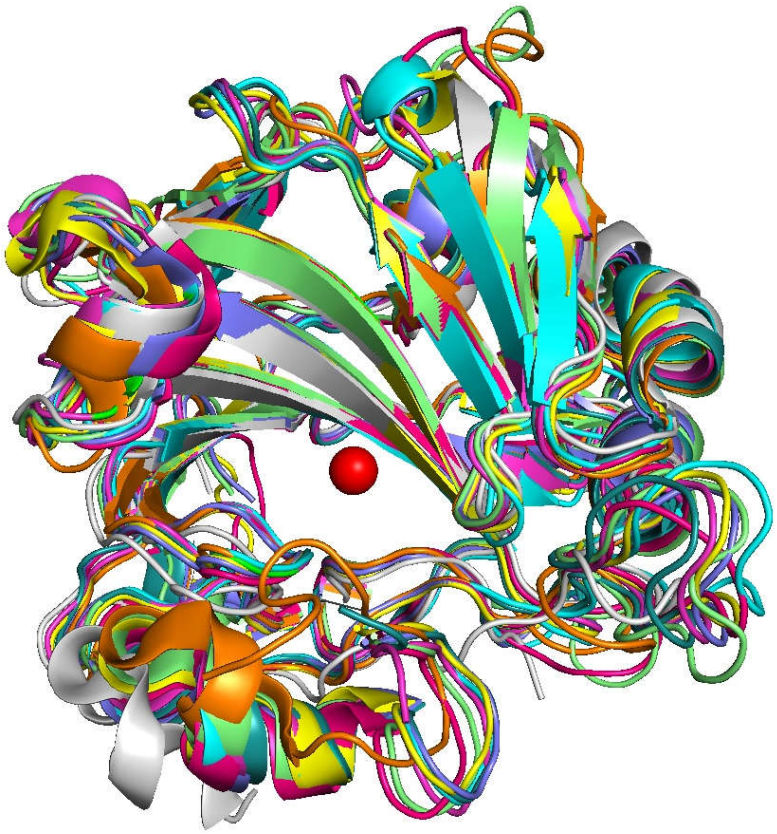

Figure 4.1 Overlay of hCA I (cyan, PDB: 3LXE), hCA II (magenta, PDB: 2HOC), hCA III (yellow, PDB: 1Z97), hCA VI (grey, PDB: 3FE4), hCA VII (blue, PDB: 6H36), hCA IX (orange, PDB: 3IAI), hCA XII (green, PDB: 4HT2), hCA XIII (red, PDB: 4HU1), hCA XIV (tint, PDB: 4LU3), showing the high structural similarity between different CA isozymes. The zinc ion is shown as red sphere.

Different research groups, including ours, came up with different design approaches to improve the potency and selectivity of the known CAI scaffolds against

CA IX. Even though CA isozymes possess high sequence homology and thus structural similarities, they are not identical. Various isozymes contain different small binding pockets within the active site due to the differences in their amino acid sequence.

Therefore, one of the most employed strategies to design isozyme selective inhibitors is through the use of classical aromatic/heterocyclic warheads found in clinically used CAIs (Chart 4.1), functionalized with different "tail" moieties that access regions of the active site, which are different among the isozymes (the "tail approach") [19, 202, 203]. All the structural elements of the inhibitor - warhead, linker, tail moiety – contribute to the potency and selectivity of the final CA inhibitor [204]. Their intrinsic physicochemical properties, such as length, polarity and rigidity, also impact the final characteristics of the CAI and determine its binding into the active site of different CAs.

Chart 4.1 Cartoon depicting the main structural elements essential for the design of selective CAIs via the "tail approach"

Our team showed that these mini pockets in the active sites of different CA isozymes can be exploited to induce CA IX isozyme selectivity through the derivatization of known CAI pharmacophores with halogens of increased steric bulk [205]. A series of 26 halogenated aromatic and heterocyclic sulfonamides were assessed through the decoration of sulfanilamide and aminobenzolamide with halogeno moieties (F, Cl, Br, I). The halogens were installed either through direct halogenation of the scaffolds or via sulfonylation of 2-amino-1,3,4-thiadiazole-5-sulfonamide with halogenated

benzenesulfonyl chlorides in an exemplification of the tail approach. The obtained CAIs were tested against tumor associated isozyme CA IX and CA XII, as well as on off-target isozymes CA I and CA II. We were able to generate potent CA inhibitors such as **50** and **51** (Chart 4.2) as the first CA inhibitors (CAIs) partially selective for CA IX [205].

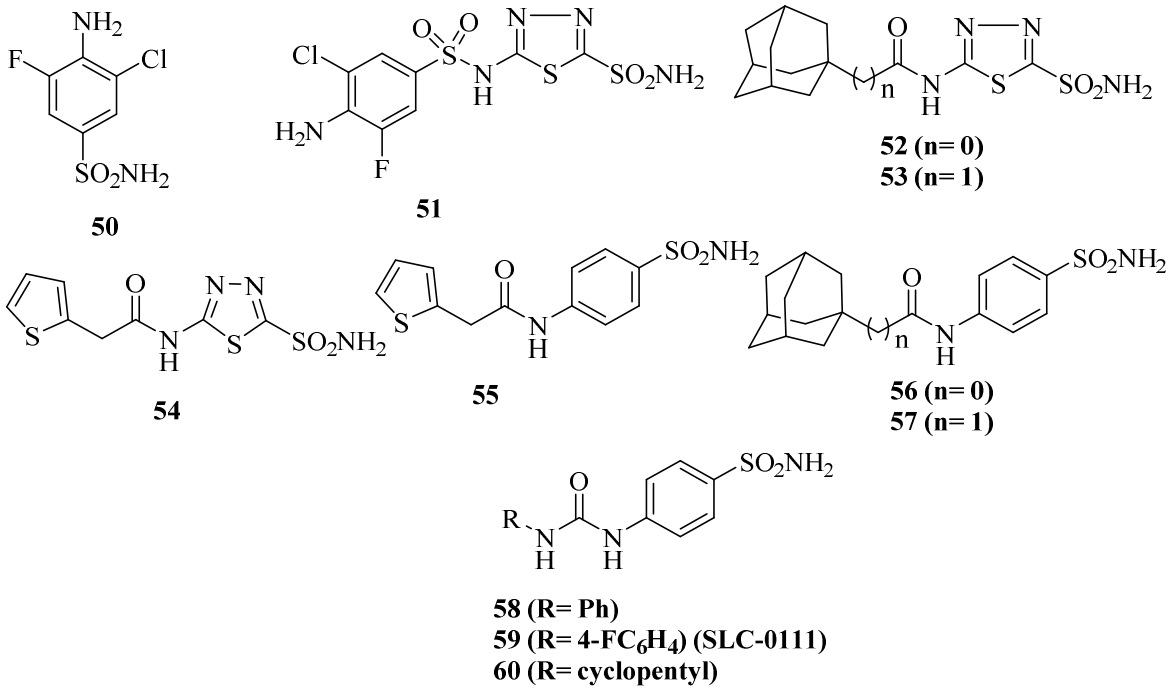

Chart 4.2 Representative lead CAIs developed in the quest of more potent and selective CA IX inhibitors [2, 22, 55].

X-ray crystallographic structure of human CA II isozyme with compound **51** (3-fluoro-5-chloroaminobenzolamide), done by Supuran and DeSimone's groups, revealed a bent conformation of the inhibitor **51** within the active site of the enzyme (Figure 4.2) [206]. In this adduct, the phenyl ring of the benzolamide scaffold was found to make an edge to face interaction with the Phe-131 and pointing towards the amphiphilic part of the

active site which is delimited with the residues Val-135, Leu-198, Pro 202 and Leu-204 [206].

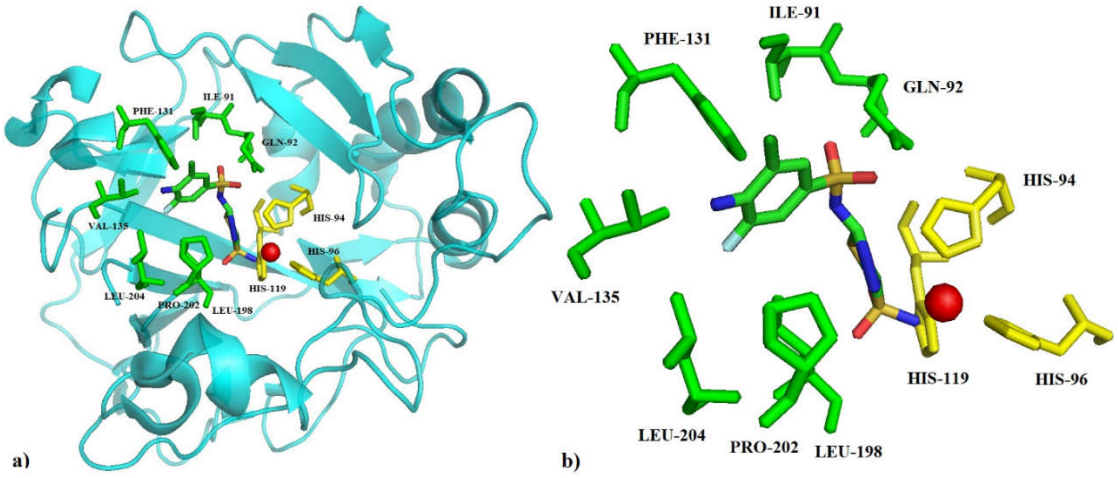

Figure 4.2 a) Ribbon diagram of hCA II/**51** adduct showing interactions with key residues within the hydrophobic part of the active site (PDB code: 2HOC) [206]. b) Diagram of CAI **51** binding within the active site of hCA II, revealing the bent conformation of the inhibitor with the edge-to-face interaction of phenyl moiety with residue Phe-131 and the accommodation of halogenated phenyl moiety within the hydrophobic pocket delimited by residues 131, 135, 198, 202 and 204.

Expanding this initial studies, our group, as well as other researchers, have generated inhibitors **52-60** [207-210], in which bulky, hydrophobic phenyl, substituted phenyl, cyclopentyl, thiophene and adamantane groups were attached to classical aromatic/heterocyclic sulfonamide warheads via amido, ureido and thioureido linkers in order to target different hydrophobic pockets present in CA IX. Among these congeners, adamantylamido 1,3,4-thiadiazole sulfonamide **52** was found be a very potent inhibitor of CA IX ($K_{I\ CA\ IX}$ = 6.4 nM, Table 4.1) [207, 210, 211]. However, its superior homolog **53**,

which contains an extra CH_2 group, was approximately seven times less potent against CA IX ($K_{I\ CA\ IX}$ = 49.5 nM, Table 4.1) [207, 210, 211]. However, when adamantane moiety was substituted with a smaller thiophene group in thiophenemethyleneamido-1,3,4-thiadiazole sulfonamide **54** the potency against CA IX was partially restored ($K_{I\ CA\ IX}$ = 11 nM, Table 4.1) [209]. Replacing the 1,3,4-thiadiazole-2-sulfonamide warhead with benzensulfonamide warhead in CAI **55** reduced the potency of the inhibitor ($K_{I\ CA\ IX}$ = 19 nM, Table 1) [209]. Likewise, adamantylamido-benzenesulfonamide congeners **56** and **57** showed a similarly reduced potency against CA IX as displayed by compound **53** ($K_{I\ CA\ IX}$ of 51.3 nM and 56.3 nM, Table 4.1) [210]. The same benzenesulfonamide warhead was used to generate ureido derivatives **58-60** and related congeners by Pacchiano et al. in order to further decrease the flexibility of the tail moieties connected with the warhead [208]. Some of these representatives showed improved potency against CA IX compared to acetazolamide **AAZ 1** ($K_{I\ CA\ IX}$ = 25 nM, Table 4.1) [208]. For example, congener **60**, bearing an cyclopentyl tail moiety, was found to be very potent against CA IX ($K_{I\ CA\ IX}$ = 7.3 nM, Table 4.1) [208]. The fluorinated derivative **59 (SLC-0111)** was moderately potent towards CA IX ($K_{I\ CA\ IX}$ = 45.1 nM), and was also approximately 300-times selective towards against CA IX compared to CA I and 2-times selective towards against CA IX compared to CA II (Table 4.1) [208]. Importantly, **59 SLC-0111** was advanced in phase I clinical trials for the treatment of hypoxic tumors that overexpress CA IX [212].

Table 4.1 Inhibition profile of selected representative CAIs **1 AAZ** and **50-60**, developed through the "tail approach" [207-210].

No.	Warhead	R	Linker	Ki (nM)			
				hCA I	hCA II	hCA IX	hCA XII
1 AAZ	1,3,4-TDA-2-SO_2NH_2	-	- (5-NH_2)	250	12	25	5.7
50	$PhSO_2NH_2$	-	- (4-NH_2)	3800	32	12	-
51	1,3,4-TDA-2-SO_2NH_2	3-F-5-Cl-4-NHPh-	5-sulfonamido	1.4	0.3	40	-
52	1,3,4-TDA-2-SO_2NH_2	Adamantyl-	5-amido	850	10.0	6.4	2.8
53	1,3,4-TDA-2-SO_2NH_2	Adamantyl-	5-amido	340	8.0	49.5	4.7
54	1,3,4-TDA-2-SO_2NH_2	Thiophene-	5-amido	72	51	11	12
55	$PhSO_2NH_2$	Thiophene-	4-amido	61	50	19	21
56	$PhSO_2NH_2$	Adamantyl-	4-amido	18600	265	53.1	7.1
57	$PhSO_2NH_2$	Adamantyl-	4-amido	15100	233	56.6	9.4
58	$PhSO_2NH_2$	Ph-	4-ureido	760	3750	575	67.3
59	$PhSO_2NH_2$	4-F-Ph-	4-ureido	5080	96	45.1	4.5
60	$PhSO_2NH_2$	Cyclopentyl-	4-ureido	470	226	7.3	6.0

The above-mentioned synthetic studies were mirrored by X-ray crystallographic investigations in order to support the discovery efforts and to improve understanding of the structural basis for potency and selectivity of CAIs [19, 204, 206, 209, 210, 213].

Two main hydrophobic/amphiphilic pockets were evidenced following these studies in CA isozymes, denominated pocket 1 (P1) and pocket 2 (P2) [204, 206, 209, 210, 213]. P1 is delimited by amino acids Phe 131, Val 135, Leu 198, Pro 202 and Leu

204 (CA II numbering) while P2 is delimited by residues Phe 131, Ile 91 and Gln 92 (CA II numbering) [204, 206, 209, 210, 213].

X-ray crystallography performed on CA II adducts with congeners **52** and **57** revealed the important role of 1,3,4-thiadiazole-2-sulfonamide and benzenesulfonamide warheads on the binding of these inhibitors into the CA II active site [210]. Both the benzenesulfonamide and 1,3,4-thiadiazole-2-sulfonamide warheads bind to the Zn^{2+} ion in similar fashion (Figure 4.3a). When bulky adamatane moiety was attached to the warheads via a rigid amide linker, one can observe that the 5-substituted-1,3,4-thiadiazole ring orients the adamantane moiety of CAI **52** into P2. The structure is very stable and translates into a potent CAI ($K_{I\ CA\ II}$ = 10 nM, Table 1) [210, 211]. On the other hand, the 4-substituted phenyl ring in connection with the amide linker (compound **56**) tends to move the adamantane moiety towards P1, clashing with Phe 131, thus diminishing the potency of CAI **56** ($K_{I\ CA\ II}$ = 265 nM, Table 4.1). Probably this is the reason for which the CA II/**56** adduct could not be crystallized. However, if a flexible CH_2 group was inserted in between the adamantane moiety and the amide linker as in CAI **57**, the adamantane moiety can reorient and fit well into P1, increasing the potency of **57** towards CA II ($K_{I\ CA\ II}$ = 233 nM, Table 4.1, Figure 4.3a). Therefore residue 131 plays a key role into orientation of this type of inhibitors in the active site of CA isozymes.

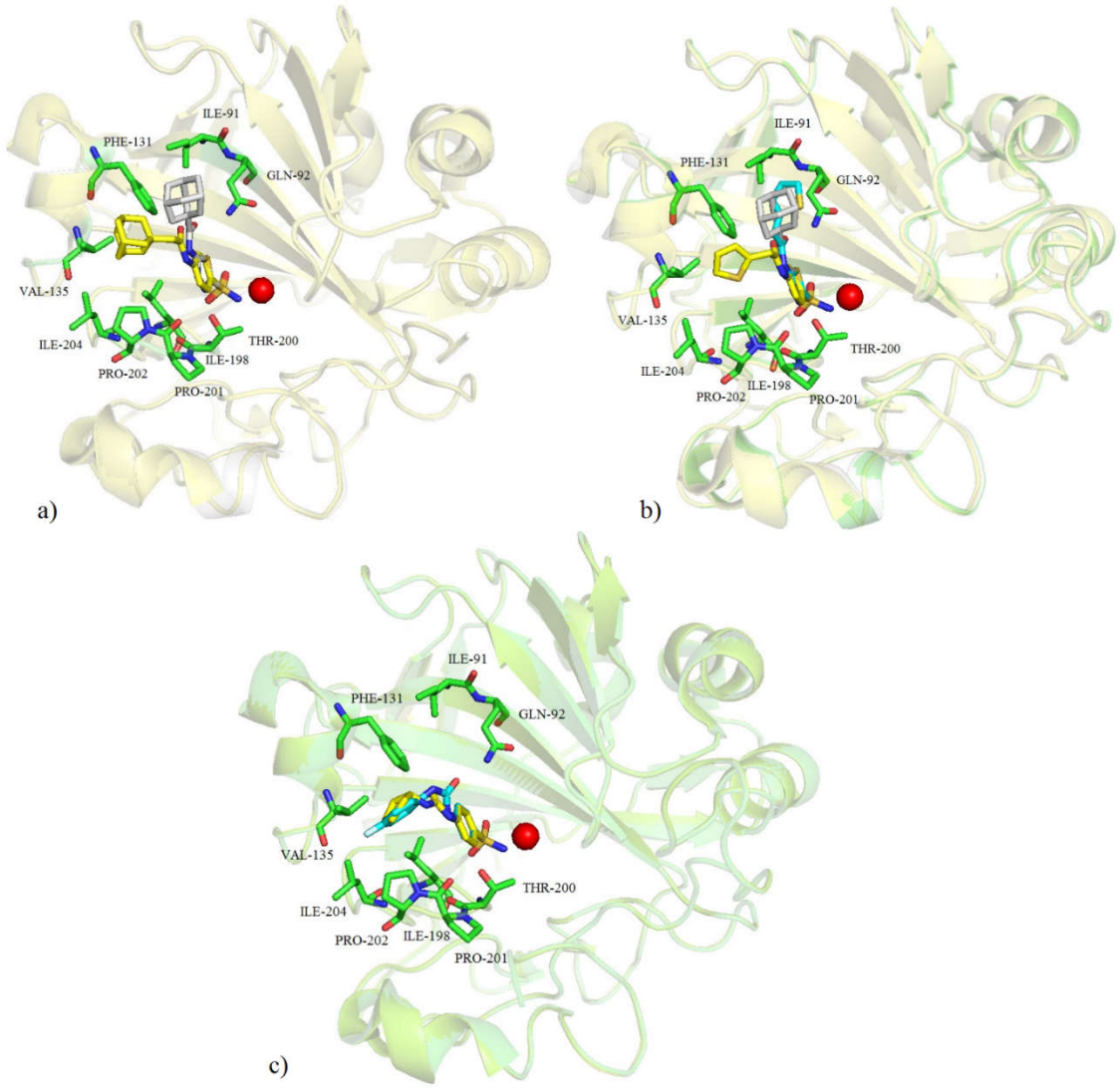

Figure 4.3 Superposition of a) hCA II-**52** (grey, PDB: 3MHC) and hCA II-**57** (yellow, PDB: 4ILX) b) hCA II-**52** (grey, PDB: 3MHC), hCA II-**54**, (cyan, PDB: 4IWZ) and hCA II-**55**, (yellow, PDB: 4IWZ) adducts c) hCA II-**59 (SLC-0111)** (cyan, PDB: 3N4B) and hCA II-**60** (yellow, PDB: 3MZC) adducts, revealing the orientation of the tail moieties as a function of warhead and linker type. Active site residues are labeled, and zinc ion is shown as a red sphere.

CA II has a Phe in position 131, with a medium steric bulk, while CA IX has a Val residue with a smaller steric bulk. The smallest steric bulk for residue 131 is found in CA XII, which has an Ala residue, while the highest steric bulk can be found in CA I, which has a Leu in position 131. The decrease in steric bulk for residue 131 from CA I to CA II, to CA IX and to CA XII is mirrored by the increase in potency of CAIs **52**, **56** and **57** against these CA isozymes, in the same order (Table 4.1) [210, 211].

This proposed interaction of this type of CAIs with different CA isozymes is supported by the observed inhibition profile for adamantane CAI **53**, the superior homolog of **52** (Table 4.1). In this case, the additional CH_2 moiety probably reorients the bulky adamantane moiety towards P1, increasing the affinity of the inhibitor towards CA II and CA I, and decreasing it towards CA IX and CA XII (Table 4.1) [210, 211].

Further proof of this mechanism is found by the observed binding of congener thiophene amidosulfonamides CAIs **54** and **55**, having the same warheads as CAIs **53** and **57** respectively, into the active site of CA II (Figure 4.3b). Thus, the thiophene tail of **54**, having the thiadiazole sulfonamide warhead, is again located into P2 in **5**/CA II adduct, similarly to the adamantane congener **52** bearing the same warhead (Figure 4.3b). Therefore, it is clear that the thiadiazole sulfonamide warhead can reliably orient hydrophobic tails connected via different linkers to P2 and induce high p otency against CA IX and CA XII with medium selectivity against CA I and CA II (Figure 4.3b and Table 4.1). On the other hand, one can observe that the benzenesulfonamide warhead orients the flexible thiophene tail of **55**, into P1 as observed in **55**/CA II adduct, reducing the potency and selectivity against CA IX and CA XII (Figure 4.3b and Table 4.1)[209]. Replacing the amido linker with an ureido linker does not change these orientation of

hydrophobic tail moieties, which continue to prefer P1, as exemplified by lipophilic ureidobenzenesulfonamides **58-60** (Figure 4.3c and Table 4.1). The inhibitory profile of these ureas depended heavily on the nature of the hydrophobic tail, its size and substitution [208, 213]. Thus, CAIs **58-60** display a variable potency against CA IX and CA XII, with K_Is ranging from 575 nM for 17 to 7.3 nM for **60** and a moderate selectivity towards CA I and CA II (Table 4.1) [208, 213].

Motivated by these premises and continuing our interest towards the development of CA IX potent and selective inhibitors, we designed a new series of compounds using thiadiazole sulfonamide as the warhead, ureido group as the linker with different hydrophobic tail moieties. We selected both aliphatic and aromatic moieties with different sizes in order to be able to draw structure-activity relationships. We also opted to generate a series of ureidobenzenesulfonamide congeners bearing the same linker and aliphatic/aromatic tail moieties, in order to expand our SAR and to better understand the impact of different warhead within ureido-based scaffolds towards the CA isozyme inhibition profile of this type of CAIs.

Results and discussion

Synthesis of ureido sulfonamide CAIs

The synthesis of ureido-sulfonamide CA inhibitors was carried out as outlined in Scheme 4.1. Briefly, 5-amino-1,3,4-thiadiazole-2-sulfonamide **61,** synthesized by acid deprotection of acetyl group of acetazolamide **1**, [214, 215] and sulfanilamide **71**, were subsequently reacted with a series of lipophilic/amphiphilic alkyl or aryl isocyanates, in dry THF, under conventional reflux conditions [207, 216], or via microwave irradiation, to yield alkyl/aryl ureido thiadiazole/benzene sulfonamides **62-70** and **72-77**. The crude reaction products were purified by flash chromatography followed by recrystallization from ethanol/water mixtures.

We assessed both synthetic strategies to access these compounds. Thus, microwave synthesis produced slightly better yields as compared with conventional reflux reaction for most ureido-sulfonamides and we were able to reduce the reaction time to less than 30 min for all condensations. Importantly, we were successful in synthesizing some of the ureido sulfonamide derivatives via microwave irradiation that were not possible to be generated through conventional refluxing of isocyanate with amino thiadiazole sulfonamides even at higher temperatures in various solvents as reported by Katritzky et al. [216].

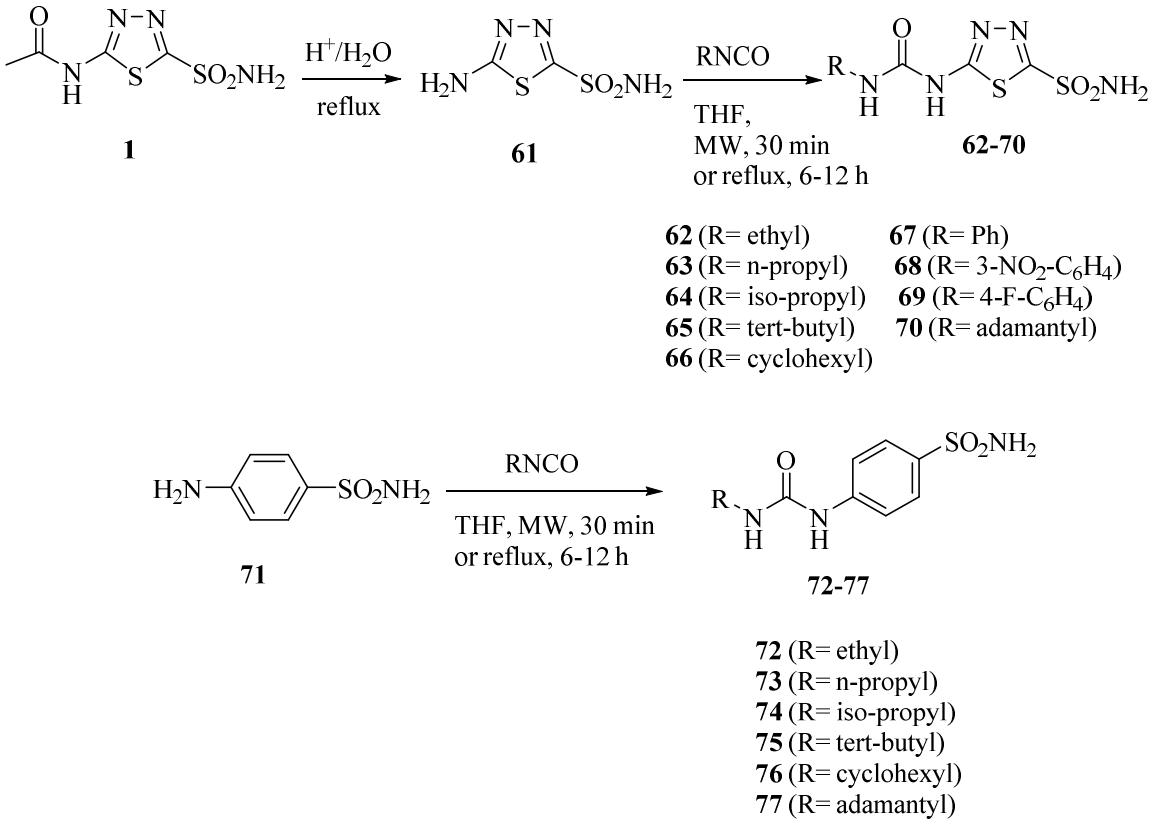

Scheme 4.1 Synthetic strategy for the generation of ureido sulfonamide CA inhibitors.

All ureido 1, 3, 4-thiadiazole/benzene sulfonamides **62-70** and **72-77** bearing aliphatic/aromatic/bulky tail moieties were tested for their ability to inhibit the transmembrane tumor-associated isozymes CA IX and CA XII, and against off-target cytosolic CA I and CA II, by a stopped-flow hydrase assay (Table 4.2). Acetazolamide (**AAZ**), a well-known sulfonamide CAI in clinical use, and **59 SLC-0111** which is currently in Phase I clinical trial for the treatment of metastatic breast cancer, were also included in these assays as reference compounds.

Table 4.2 Inhibition profile of human CA isoforms hCA I, II, IX and XII with new ureido sulfonamide derivatives **62-70** and **72-77** reported here, and the standard sulfonamide inhibitor **1** acetazolamide (**AAZ)** and **59 SLC-0111** by a stopped flow CO_2 hydrase assay [92].

No.			**K_I (nM)**			
	R	**Warhead**	**hCA I**	**hCA II**	**hCA IX**	**hCA XII**
62	5-Ethyl-	1,3,4-TDA-2-SO_2NH_2	547.2	8	5.9	6.5
63	5-n-Propyl-	1,3,4-TDA-2-SO_2NH_2	367.7	6.7	1.2	4.6
64	5-Isopropyl-	1,3,4-TDA-2-SO_2NH_2	453.7	5	3.9	6.3
65	5-tert-butyl-	1,3,4-TDA-2-SO_2NH_2	381.8	4.4	1.6	6.1
66	5-Cyclohexyl-	1,3,4-TDA-2-SO_2NH_2	665.1	6.1	0.78	2.9
67	5-Ph-	1,3,4-TDA-2-SO_2NH_2	164	0.44	0.075	0.62
68	5-(3-O_2NPh)-	1,3,4-TDA-2-SO_2NH_2	289.9	0.037	0.24	0.91
69	5-(4-F-Ph)-	1,3,4-TDA-2-SO_2NH_2	99.8	0.5	0.049	0.39
70	5-Adamantyl-	1,3,4-TDA-2-SO_2NH_2	729.7	9.3	0.45	5.3
72	4-Ethyl-	$PhSO_2NH_2$	83.7	63.8	45.6	25.7
73	4-n-Propyl-	$PhSO_2NH_2$	62.2	43.6	16.8	17
74	4-Isopropyl-	$PhSO_2NH_2$	95.2	28.5	29.6	29.2
75	4-tert-butyl-	$PhSO_2NH_2$	77.9	16.3	31.7	30.1
76	4-Cyclohexyl-	$PhSO_2NH_2$	492.3	65	6.2	8.8
77	4-Adamantly-	$PhSO_2NH_2$	649.2	230.1	23.2	28.9
1 AAZ	5-Acetamido	1,3,4-TDA-2-SO_2NH_2	250	12	25	5.7
59 SLC-0111	4-(4-F-Ph)-	$PhSO_2NH_2$	5080	96	45.1	4.5

Data from Table 4.2 revealed an excellent inhibitory profile of compounds **62-70** and **72-77** against both transmembrane isozymes CA IX and XII, and against cytosolic isozyme CA II, with nanomolar and even subnanomolar potency revealed for several representatives. Cytosolic CA I was the least susceptible to inhibition by compounds **62-70** and **72-77**, with inhibition potency in the range of 62.2-729.7 nM. Ureido-benzenesulfonamide derivative **73**, having an n-propyl tail moiety, was found to be the most potent inhibitor (Ki= 62.2 nM) against this CA I isozyme.

All the ureido-1, 3, 4-thiadiazole-2-sulfonamide CAIs **62-70** and **72-77** exhibited strongest inhibition potency against CA IX, with subnanomolar and nanomolar K_I values in the range of 0.049-5.9 nM, being significantly more potent inhibitors compared to both acetazolamide **AAZ 1** and the reference CA IX inhibitor **SLC-0111 59,** thus validating the rationale behind the proposed design. Within the 1,3,4-thiadiazole-2-sulfonamide CAIs **62-70**, potency of these CAIs increased against CA IX as the steric demand of the tail moiety increased, with highest potency observed with aromatic and bulky tail moieties. CAI **63**, having an n-propyl tail moiety, showed higher potency compared to its isomer CAI **64**, bearing an isopropyl tail group. CAIs **69** and **67**, bearing 4-fluorophenyl and phenyl tail moieties, were found to be the most efficient CA IX inhibitors, with low subnanomolar potency against CA IX having Ki value of 0.049 nM and 0.075 nM respectively. All the 1,3,4-thiadiazole-2-sulfonamide CAIs **62-70** were more potent than their corresponding benzenesulfonamide **72-77** analogs for inhibiting membrane-bound isozymes CA IX and CA XII. From these new ureido sulfonamide CAIs, inhibitor **69**, was found to be the most potent compound against tumor associated isozymes CA IX and CA XII, with Ki value of 0.049 nM and 0.39 nM respectively. CAI **69** was 920-times and

11-times more potent against CA IX and CA XII respectively, compared to its corresponding benzenesulfonamide analog CA IX inhibitor **SLC-0111 59**. From the benzenesulfonamides CAIs **72-77**, the best inhibitor for CA IX and CA IX was compound **76**, bearing a cyclohexyl tail moiety, with Ki value of 6.2 nM and 8.8 nM for CA IX and CA XII respectively.

Importantly, we were able to identify moderate to highly selective inhibitors for transmembrane isozymes versus cytosolic ones. Isozyme selectivity ratio for tumor-associated membrane-bound isozymes hCA IX and hCA XII versus off-target cytosolic isoforms hCA I and hCA II (i.e. I/IX, II/IX, I/XII and II/XII) with the most potent ureido-1,3,4-thiadiazole-2-sulfonamide CAIs **67-70** and acetazolamide **AAZ 1,** and the reference CA IX inhibitor **SLC-0111 59** is shown in Table 4.3. Higher I/IX, II/IX, I/XII and II/XII ratio are desirable for a compound to be developed as anticancer agent. The most efficient CA IX inhibitor **69** was found to be about 2000-times selective against CA IX compared to cytosolic isozyme CA I, and about 10-times selective for CA IX than isozyme CA II. The second-best CA IX inhibitor **67** showed approximately 2100-times and 6-times selectivity against CA IX compared to CA I and CA II respectively. Interestingly, thiadiazole sulfonamide **70** (Ki= 0.45 nM), bearing the bulky adamantly moiety, showed the best overall selectively against CA IX compared to both cytosolic isozymes CA I (1621 times) and CA II (20 times). Inhibitor **67**, **69** and **70** showed better overall selectivity profile for CA IX compared to the reference CA IX inhibitor **SLC-0111 59** which is approximately 100-times selective against CA IX compare to CA I and only 2-times more selective against CA II.

Table 4.3 Inhibition and isozyme selectivity ratio for tumor-associated membrane-bound isozymes hCA IX and hCA XII versus off-target cytosolic isoforms hCA I and hCA II with the most potent ureido 1,3,4-thiadiazole-2-sulfonamide CAIs **67-70**, acetazolamide **AAZ 1**, and the reference CA IX inhibitor **SLC-0111 59**.

Compound	**Ki (nM)**				**Selectivity Ratio**			
	hCA I	**hCA II**	**hCA IX**	**hCA XII**	**I/IX**	**II/IX**	**I/XII**	**II/XII**
67	164	0.44	0.075	0.62	2186	5	264	<1
68	289.9	0.037	0.24	0.91	1207	<1	318	<1
69	99.8	0.5	0.049	0.39	2036	10	255	1
70	729.7	9.3	0.45	5.3	1621	20	137	2
AAZ 1	250	12	25	5.7	10	<1	43	2
SLC-0111 59	5080	96	45.1	4.5	112	2	1128	21

In case of CA II inhibition, all ureido compounds having 1,3,4-thiadiazole-2-sulfonamide warhead **62-70** showed superior inhibition potency compared to both acetazolamide **AAZ** and **SLC-0111 59,** with subnanomolar and nanomolar K_I values of 0.037-9.3 nM. CAIs **67**, **68** and **69,** having phenyl, 3-nitrophenyl and 4-fluorophenyl tail moieties, showed subnanomolar inhibition potency with K_{Is} of 0.44 nM, 0.037 nm and 0.5 nM respectively, with CAI **68** being the most potent CAI for CA II. Ureido 1,3,4-thiadiazole-2-sulfonamide **70** bearing the bulky adamantyl moiety was found to be least potent compound against this CA II isozyme. However, ureido benzenesulfonamide CAIs **72-77** were less potent against CA II compared to acetazolamide **AAZ** but were more efficient than **59 SLC-0111**. Again, ureido benzenesulfonamide CAI **77,** having the bulky adamantly moiety, was the least efficient compound against CA II.

Considering the high potency and selectivity of these compounds against CA IX, it is expected that these compounds will efficiently kill the hypoxic tumor cells through a CA IX mediated cell killing mechanism. Therefore, we decided to test these inhibitors **62-70** and **72-77** along with acetazolamide **AAZ 1** and **SLC-0111 59** in 2D models of breast MDA-MB 231 cancer cell line that express CA IX and CA XII isozyme under normoxic and hypoxic conditions [74, 78, 92, 217, 218]. MDA-MB 231 cancer cells were grown subconfluent in 96 well plates in normal conditions (37^{o}C, 5% CO_2 in air). Subsequently, half of the well plates were incubated in normal (normoxic) conditions while the other half were subjected to hypoxic conditions (1% O_2, 5% CO_2 and 94% N_2) to induce the expression of CA IX isozyme.

CAIs stock solutions were prepared by dissolving the compounds in a 5 mM solution of hydroxypropyl-β-cyclodextrin in DMEM media, at 2.5 mM final concentration. All the well plates were treated with CAIs solutions at 3 different concentrations (1 mM, 100 μM, and 10 μM, made from the CAI stock solution via dilution with DMEM media) in either normoxic/hypoxic conditions. After 24 hours treatment period, the viability of cells was measured by using an MTT assay [219] (Figure 4.4).

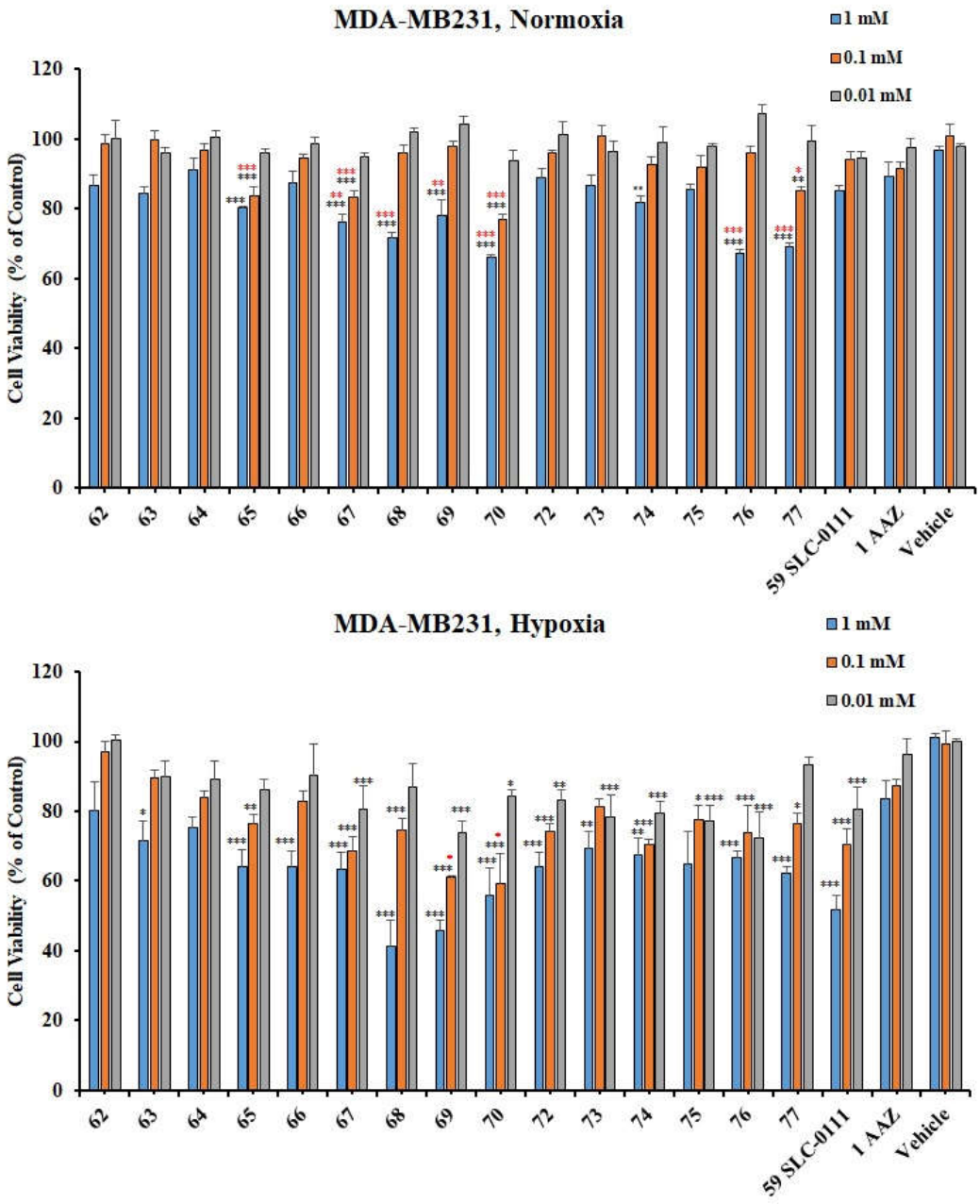

Figure 4.4 Effect of CAI **62-70** and **72-77**, acetazolamide **AAZ 1** and **59** (**SLC-0111)**, at different concentrations, on the viability of breast MDA-MB231 cancer cell line under normoxic (a) and hypoxic (b) conditions. P values were determined by one-way ANOVA, comparing the value with the corresponding value obtained for acetazolamide (**AAZ 1**, black stars) and for **SLC-0111 59** (red stars), considering *P < 0.05, **P < 0.01, ***P < 0.001. Only the statistically significant differences were shown.

Data from Figure 4.4 showed that all the inhibitors affected the MDA-MB 231 cancer cell viability in a concentration-dependent manner, with a greater impact observed in hypoxic conditions where CA IX and CA XII are overexpressed [74, 78, 92, 217, 218]. Under normoxic conditions, significant decreases in tumor cell viability were obtained with inhibitors **65**, **67**, **70** and **77** at both 1 mM and 0.1 mM concentration compared with acetazolamide **AAZ 1**, while inhibitors **68, 69, 74** and **76** showed significant tumor cell killing at 1 mM concentration only. None of these inhibitors were effective in killing tumor cells at low 0.01 mM concentration in normoxic conditions. Under normoxic conditions, the classical CAI acetazolamide **AAZ 1** was effective only at highest concentration of 1 mM, which decreased the cell viability to 89%. The reference CA IX inhibitor **59 SLC-0111** decreased the cell viability to 85% at 1 mM concentration, which was not significant compared to acetazolamide **AAZ 1**. A similar observation was reported by Andreucci et al. [220]. It was found that **59 SLC-0111** was efficient in killing A375-M6 melanoma cells at 0.1 mM concentration only at acidified conditions maintained at pH 6.7, while was ineffective in killing these cells at pH 7.4 at the same concentration [220]. However, CAIs **65**, **67**, **68**, **69**, **70**, **76** and **77** showed statistically significant cell killing compared with **SLC-0111 59** either or both 1 mM and 0.1 mM concentrations. Cell killing abilities of these CAIs **62-70** and **72-77** generally increased with the increases in the size of the tail moiety, with the highest cell killing observed with either aromatic or bulky adamantane tail groups. Benzenesulfonamide CAI **77**, bearing the adamantane tail group, proved to be the most efficient inhibitor under normoxic conditions, followed by corresponding 1,3,4-thiadiazole-2-sulfonamide CAI **70**, having

the same adamantane tail moiety. Inhibitors **70** and **77** decreased the cell viability to 66% and 62% respectively.

Under hypoxic conditions, all the ureido CAI **62-70** and **72-77** exhibited more pronounced tumor cell killing abilities compared to normoxic conditions, as expected in a concentration-dependent manner. Cell killing efficiency of these CAIs generally increased as the size of tail group increases. Again, the inhibitors having either aromatic or bulky tail group showed superior cell killing. CAIs **67, 69, 70, 72, 76** and the reference CA IX inhibitor **59 (SLC-0111)** displayed significant tumor cell killing at all three concentrations. CAIs **65, 68** and **77** were also found to significantly decrease the tumor cell viability at 1 mM and 0.1 mM concentrations. Other efficient CAIs in this in vitro MDA-MB 231 cell model were **63**, **66**, **73** and **75**, but in a less consistent manner. The 1,3,4-thiadiazole-2-sulfonamide CAIs **68** and **69,** having the 3-nitrophenyl and 4-fluoro phenyl tail group respectively, were found to be the most efficient inhibitors in reducing tumor cell viability. Inhibitor **69** displayed robust cell killing at all three concentrations and decreased the cell viabilities to 41% at 1 mM, 60% at 100 μM and 73% at 10 μM. Importantly, CAI **69** showed better cell killing ability for all three concentrations compared to its corresponding benzenesulfonamide analog, the reference CA IX CAI **SLC-0111 59**, which reduced cell viabilities to 51% at 1 mM, 70% at 100 μM and 80% at 10 μM. At 0.1 mM concentration, CAI **69** was significantly better in killing MDA-MB 231 cells compared to **SLC-0111 59**. These data along with the enzyme inhibition data again confirm the superiority of 1,3,4-thiadiazole-2-sulfonamide warhead over the benzenesulfonamide warhead in targeting the active sites of CA isozymes. As 1,3,4-thiadiazole-2-sulfonamide warhead can reliably orients the tail group of ureido CAIs into

the pocket 2 (P2), we expect similar binding of the tail group of CAI **69** into the hydrophobic pocket 2. Thus, CAI **69** showed significantly higher inhibition potency and selectivity against CA IX compared to **SLC-0111** which orients its tail group into pocket 1. An X-ray crystallographic study with CAI **69** can further clarify our hypothesis in designing this type CA IX selective inhibitors.

Conclusions

A series of ureido-sulfonamides **62-70** and **72-77** was designed employing the "tail approach' through the attachment of two different well-established carbonic anhydrase inhibitor "warheads", the 1,3,4-thiadiazole-2-sulfonamide and the benzenesulfonamide, with different aliphatic/aromatic tail moieties. These compounds were profiled for their ability to inhibit membrane-bound tumor-associated isozymes CA IX and CA XII, and off-target cytosolic CA I and CA II isoforms. A detailed structure-activity relationship study was carried out. We have identified moderate to highly selective and sub-nanomolar potent CA IX inhibitors together with several potent pan-inhibitors. These CAIs set were also assessed in vitro, in 2D tumor cellular models using MDA-MB 231 breast cancer cell line expressing CA IX and CA XII. We have successfully identified several potent CAIs that can significantly kill the tumor cells under both normoxic and hypoxic conditions. The most efficient CAI proved to be ureido-1,3,4-thiadiazole-2-sulfonamide sulfonamide **69**, which showed subnanomolar potency against purified CA IX and CA XII isozymes, and consistent and significant cancer cell killing at concentrations of 10-100 uM in MDA-MB 231 breast cancer cell line. Importantly, ureido-sulfonamide CAI **69** displayed 920-times and 11-times higher potency against CA IX and CA XII respectively, compared to its corresponding benzenesulfonamide analog CA IX inhibitor **SLC-0111 59**, which is currently in Phase I clinical trials as an antitumor/antimetastatic agent [212]. CAI **69** showed better selectivity profile for these membrane-bound tumor associated isozymes CA IX and CA XII versus off-target cytosolic isozyme CA I and CA II, compared with CAI **SLC-0111 59.** CAI **69** also exhibited statistically significant cell killing in MDA-MB 231 cell line compared to

SLC-0111. Thus, these potency, selectivity and in vitro cancer cell killing data is placing the new ureido-sulfonamide CAI **69** above **SLC-0111 59** as superior CA IX inhibitor.

Experimental Section

Materials and Methods

Materials: The following materials were used as received:

Acetazolamide, Ethyl isocyanate, n-propyl isocyanate, t-butyl isocyanate and hexyl isocyanate were from Sigma-Aldrich (St. Louis, MO), phenyl isocyanate and isopropyl isocyanate were from Alfa Aesar (Ward Hill, MA), 3-nitrophenyl isocyanate and 4-fluorophenyl isocyanate were from Alfa Aesar, (Heysham, England), 1-adamantyl isocyanate was from Acros (Livingston, NJ). Organic solvents (HPLC quality) were purchased from Fisher Scientific (Pittsburgh, PA), EMD (Gibbstown, NJ), and VWR International (West Chester, PA).

Techniques:

The microwave synthesis was performed into a CEM Discover Microwave (Matthews, NC) having Explorer PLS autosampler, as specified below.

The purity and the structure identity of the intermediary and final products were assessed by thin-layer chromatography (TLC), HPLC-MS, ^{1}H-, ^{13}C- and ^{19}F-NMR, high resolution mass spectrometry (HR-MS) and melting points. TLC was carried out on SiO_2-precoated aluminum plates (Alugram® SIL G/UV_{254} 20×20 cm with F254 indicator; layer thickness 0.20 nm; pore size 60 Å) from MACHEREY-NAGEL, (Bethlehem, PA). Flash

chromatography was performed using an Isco Combiflash RF (Teledyne Isco, Lincoln, NE), using Isco prepacked silica columns. The purity of compounds was also assessed via LC-MS, using an Agilent 1200 HPLC DAD-MS system (Santa Clara, CA) equipped with a G1315A DAD and a 6130 Quadrupole MS via a ZORBAX SB-C18 column eluted with H_2O (0.1% HCOOH)/MeCN (0.1% HCOOH) 95/5 to 0/100 linear gradient. NMR spectra were recorded at T = 300 K with a Bruker Avance III 400 Plus spectrometer equipped with a 5 mm indirect detection probe, operating at 400 MHz for ^{1}H NMR, at 100 MHz for ^{13}C NMR. Chemical shifts are reported as δ values, using tetramethylsilane (TMS) as internal standard for proton spectra and the solvent resonance for carbon. The melting points were determined via Thermolyne heating stage microscope (Dubuque, IA), equipped with an Olympus 5X objective, at heating/cooling rate of ~ 4 ºC/min and were uncorrected.

5-Amino-1,3,4-thiadiazole-2-sulfonamide was synthesized as previously described [214, 215].

General Procedure for the synthesis of Ureido Sulfonamides 62-70 and **72-77**

Thermal Reaction

A stirred solution of 5-amino-1,3,4-thiadiazole-2-sulfonamide or sulfanilamide (10 mmol) in 50 mL dry THF, cooled at 0ºC, was treated with alkyl or aryl isocyanate (10 mmol), under argon gas flow. Stirring was continued for 10 mins, then the ice bath was removed, and the reaction mixture was refluxed for overnight under continuous stirring. The next day, TLC revealed that all isocyanate was consumed, therefore the solvent was evaporated to dryness and the crude product was purified flash chromatography using

DCM/Methanol gradients. The pure fractions were grouped, solvent was evaporated to dryness and the pure compound was recrystallized from ethanol/water 1/1 (V/V).

Microwave Reaction

In a 10 mL microwave tube, 5-amino-1,3,4-thiadiazole-2-sulfonamide or sulfanilamide (2 mmol) was suspended in dry THF (3 mL) at 0ºC. Alkyl or aryl isocyanate (2 mmol) was added to this suspension in one batch, the tube was purged with argon, capped and stirred for 10 mins in an ice bath. Subsequently, the reaction mixture was transferred into a CEM Discover Microwave Synthesis System and irradiated with microwaves at 100 ºC for 30 mins. The microwave tube was cooled to 25 ºC, the content from the tube was transferred to a round bottom flask and the solvent was evaporated to dryness and the crude product was purified flash chromatography using DCM/Methanol gradients. The pure fractions were grouped, solvent was evaporated to dryness and the pure compound was recrystallized from ethanol/water 1/1 (v/v).

5-(3-ethylureido)-1,3,4-thiadiazole-2-sulfonamide 62

White crystals. mp 288-290°C (lit. 257-259°C)[216]. Yield 60%**.** ^{1}H-NMR (400 MHz, DMSO-d^{6}, δ, ppm): 11.38 (s, 1H), 8.21 (s, 2H), 6.76 (s, 1H), 3.22-3.16 (m, 2H), 1.10-1.05 (m, 3H). ^{13}C-NMR (100.6 MHz, DMSO-d^{6}, δ, ppm): 163.3, 153.1, 34.6, 15.0 (consisted with literature).[216] LC-MS (ESI) 252.0 (MH^{+}), t_R= 1.35 min, > 99% purity).

5-(3-propylureido)-1,3,4-thiadiazole-2-sulfonamide 63

White crystals. mp 245-247°C. Yield 80%**.** ^{1}H-NMR (400 MHz, DMSO-d^{6}, δ, ppm): 11.31 (s, 1H), 8.22 (s, 2H), 6.78 (s, 1H), 3.12 (q, J= 6.6 Hz, 2H), 1.47 (q, J= 7.2 Hz, 2H) 0.86 (t, J= 7.4, 3H). ^{13}C-NMR (100.6 MHz, DMSO-d^{6}, δ, ppm): 163.2, 153.2, 41.3, 22.5, 11.1. LC-MS (ESI) 266.0 (MH^{+}), t_R= 1.81 min, > 99% purity).

5-(3-isopropylureido)-1,3,4-thiadiazole-2-sulfonamide 64

Yellowish crystals. mp 285-287°C. Yield 35%**.** ^{1}H-NMR (400 MHz, DMSO-d^{6}, δ, ppm): 11.09 (s, 1H), 8.22 (s, 2H), 6.64 (s, 1H), 3.12 (q, J= 6.6 Hz, 2H), 1.47 (q, J= 7.2 Hz, 2H) 0.86 (t, J= 7.4, 3H). ^{13}C-NMR (100.6 MHz, DMSO-d^{6}, δ, ppm): 163.2, 153.2, 41.3, 22.5, 11.1. LC-MS (ESI) 266.0 (MH^{+}), t_R= 1.76 min, > 99% purity).

5-(3-(tert-butyl)ureido)-1,3,4-thiadiazole-2-sulfonamide 65

White crystals. Yield 45%**.** mp 187-189°C. ^{1}H-NMR (400 MHz, DMSO-d^{6}, δ, ppm): 10.86 (s, 1H), 8.21 (s, 2H), 6.59 (s, 1H), 1.32-1.30 (m, 9H). ^{13}C-NMR (100.6 MHz, DMSO-d^{6}, δ, ppm): 162.7, 157.0, 151.9, 50.4, 48.8, 29.3, 28.5**.** LC-MS (ESI) 280.0 (MH^{+}), t_R= 2.09 min, > 99% purity).

5-(3-cyclohexylureido)-1,3,4-thiadiazole-2-sulfonamide 66

White crystals. mp 241-243°. Yield 65%**.** ^{1}H-NMR (400 MHz, DMSO-d^{6}, δ, ppm): 11.04 (s, 1H), 8.23 (s, 2H), 6.70 (s, 1H), 3.54-3.52 (m, 1H), 1.82-1.79 (m, 2H), 1.68-1.64 (m, 2H), 1.56-1.53 (m, 1H), 1.36-1.17 (m, 5H). ^{13}C-NMR (100.6 MHz, DMSO-d^{6}, δ, ppm):

163.4, 163.0, 152.3, 48.5, 32.3, 25.0, 24.2**.** LC-MS (ESI) 307.0 (MH^+), t_R= 2.31 min, > 99% purity).

5-(3-phenylureido)-1,3,4-thiadiazole-2-sulfonamide 67

Off-white crystals. mp 282-284°C. (lit. 257-259°C)[216]. Yield 65% (Microwave heating) and 80% by conventional heating. ^{1}H-NMR (400 MHz, DMSO-d^6, δ, ppm): 11.44 (s, 1H), 9.18 (s, 1H), 8.31 (s, 2H), 7.51 (d, J= 7.9 Hz, 2H), 7.36 (t, J= 7.6 Hz, 2H), 7.09 (d, J= 7.4 Hz, 2H)**.** ^{13}C-NMR (100.6 MHz, DMSO-d^6, δ, ppm): 163.7, 162.7, 151.3, 137.9, 129.0, 123.4, 119.1. LC-MS (ESI) 301.0 (MH^+), t_R= 2.25 min, > 99% purity).

5-(3-(3-nitrophenyl)ureido)-1,3,4-thiadiazole-2-sulfonamide 68

Yellowish crystals. Yield 35%**.** mp 287-289°C. ^{1}H-NMR (400 MHz, DMSO-d^6, δ, ppm): 9.75 (s, 1H), 8.54 (s, 1H), 8.34 (s, 2H), 7.92 (dd, J= 8.2 Hz, 1.7 Hz, 1H), 7.85 (d, J= 8.2 Hz, 1H), 7.6 (d, J= 8.2 Hz, 1H). ^{13}C-NMR (100.6 MHz, DMSO-d^6, δ, ppm): 148.0, 140.6**,** 139.5, 130.2, 125.3, 124.6, 117.8, 113.2, 112.5. LC-MS (ESI) 346.0 (MH^+), t_R= 2.43 min, > 99% purity).

5-(3-(4-fluorophenyl)ureido)-1,3,4-thiadiazole-2-sulfonamide 69

White crystals. Yield 30%. mp 280-282°C. ^{1}H-NMR (400 MHz, DMSO-d^6, δ, ppm): 11.49 (s, 1H), 9.19 (s, 1H), 8.34-8.24 (m, 2H), 7.51 (brs, 2H), 7.21-7.17 (m, 2H). ^{13}C-NMR (100.6 MHz, DMSO-d^6, δ, ppm): 115.3, 121.1, 134.2, 151.1, 156.9, 159.3, 162.6, 163.5. LC-MS (ESI) 318.0 (MH^+), t_R= 2.31 min, > 99% purity).

5-(3-((3-adamantan-1-yl)ureido)-1,3,4-thiadiazole-2-sulfonamide 70

White crystals. Yield 20%. mp 238-240°C. ^{1}H-NMR (400 MHz, DMSO-d^{6}, δ, ppm): 10.84 (s, 1H), 8.21 (s, 2H), 6.48 (s, 1H), 2.03 (brs, 3H), 1.97-1.87 (m, 6H), 1.63 (s, 6H). ^{13}C-NMR (100.6 MHz, DMSO-d^{6}, δ, ppm): 163.3, 162.6, 151.5, 50.8, 41.1, 35.7, 28.8. LC-MS (ESI) 358.0 (MH^{+}), t_R= 2.79 min, > 99% purity).

4-(3-ethylureido)benzenesulfonamide 72

White crystals. mp 250-252°C. Yield 70%**.** ^{1}H-NMR (400 MHz, DMSO-d6, δ, ppm): 8.81 (brs, 1H), 7.73-7.53 (m, 4H), 7.22-7.09 (m, 2H), 6.24 (brs, 1H), 3.15-3.1 (m, 2H), 1.06-1.04 (m, 3H). ^{13}C-NMR (100.6 MHz, DMSO-d^{6}, δ, ppm): 154.7, 143.7, 135.9, 126.7, 116.7, 33.9, 15.3. LC-MS (ESI) 243.8 (MH^{+}), t_R= 1.19 min, > 99% purity).

4-(3-propylureido)benzenesulfonamide 73

White crystals. mp 246-247°C. Yield 80%**.** ^{1}H-NMR (400 MHz, DMSO-d^{6}, δ, ppm): 8.79 (brs, 1H), 7.68-7.64 (m, 2H), 7.55-7.14 (m, 2H), 7.14 (brs, 2H), 6.27 (brs, 1H), 3.06-3.03 (m, 2H), 1.46-1.42 (m, 2H), 0.89-0.834 (m, 3H). ^{13}C-NMR (100.6 MHz, DMSO-d^{6}, δ, ppm): 154.8, 143.7, 135.9, 126.7, 116.7, 40.8, 22.8, 11.3. LC-MS (ESI) 257.8 (MH^{+}), t_R= 1.72 min, > 99% purity).

4-(3-isopropylureido)benzenesulfonamide 74

White crystals. mp 238-239°C. Yield 75%**.** ^{1}H-NMR (400 MHz, DMSO-d^{6}, δ, ppm): 8.67 (s, 1H), 7.66 (d, J= 8.7 Hz, 2H), 7.51 (d, J= 8.7 Hz, 2H), 7.14 (s, 2H), 6.14 (d, J= 7.5 Hz, 1H), 3.80-3.72 (m, 1H), 1.11-1.09 (m, 6H). ^{13}C-NMR (100.6 MHz, DMSO-d^{6}, δ, ppm):

154.0, 143.6, 135.8, 126.9, 116.6, 40.9, 22.8, 22.6. LC-MS (ESI) 257.8 (MH^+), t_R= 1.67 min, > 99% purity).

4-(3-(tert-butyl)ureido)benzenesulfonamide 75

White crystals. mp 207-208°C. Yield 55%**.** ^{1}H-NMR (400 MHz, DMSO-d^6, δ, ppm): 8.60 (brs, 1H), 7.66-7.62 (m, 2H), 7.50-7.46 (m, 2H), 7.11 (brs, 2H), 6.10 (brs, 1H), 1.34-1.22 (m, 9H). ^{13}C-NMR (100.6 MHz, DMSO-d^6, δ, ppm): 153.8, 143.6, 135.7, 126.6, 116.4, 49.5, 28.8. LC-MS (ESI) 271.8 (MH^+), t_R= 2.09 min, > 99% purity).

4-(3-cyclohexylureido)benzenesulfonamide 76

White crystals. mp 248-249°C. Yield 90%**.** ^{1}H-NMR (400 MHz, DMSO-d^6, δ, ppm): 8.68 (s, 1H), 7.66 (d, J= 8.8 Hz, 2H), 7.51 (d, J= 8.8 Hz, 2H), 7.14 (s, 2H), 6.22 (d, J= 7.8 Hz, 1H), 3.48-3.46 (m, 1H), 1.82-1.52 (m, 5H), 1.35-1.13 (m, 5H). ^{13}C-NMR (100.6 MHz, DMSO-d^6, δ, ppm): 153.9, 143.6, 135.8, 126.6, 116.5, 47.6, 32.7, 25.1, 24.2. LC-MS (ESI) 298.8 (MH^+), t_R= 2.17 min, > 99% purity).

4-(3-((3s, 5s, 7s)-adamantan-1-yl)ureido)benzenesulfonamide 77

White crystals. mp 284-285°C. Yield 25%**.** ^{1}H-NMR (400 MHz, DMSO-d^6, δ, ppm): 8.63 (s, 1H), 7.65 (d, J= 8.0 Hz, 2H), 7.47 (d, J= 7.9 Hz, 2H), 7.13 (s, 2H), 6.01 (s, 1H), 2.03-1.89 (m, 9H), 1.63 (brs, 6H). ^{13}C-NMR (100.6 MHz, DMSO-d^6, δ, ppm): 153.8, 143.7, 135.7, 126.7, 116.5, 50.0, 41.5, 36.0, 28.9. LC-MS (ESI) 349.8 (MH^+), t_R= 2.84 min, > 99% purity).

CA inhibition assay

An Applied Photophysics stopped-flow instrument has been used for assaying the CA catalysed CO_2 hydration activity [173]. Phenol red (at a concentration of 0.2 mM) has been used as indicator, working at the absorbance maximum of 557 nm, with 20 mM Hepes (pH 7.5) as buffer, and 20 mM Na_2SO_4 (for maintaining constant the ionic strength), following the initial rates of the CA-catalyzed CO_2 hydration reaction for a period of 10-100 s. The CO_2 concentrations ranged from 1.7 to 17 mM for the determination of the kinetic parameters and inhibition constants. For each inhibitor at least six traces of the initial 5-10% of the reaction have been used for determining the initial velocity. The uncatalyzed rates were determined in the same manner and subtracted from the total observed rates. Stock solutions of inhibitor (0.1 mM) were prepared in distilled-deionized water and dilutions up to 0.01 nM were done thereafter with the assay buffer. Inhibitor and enzyme solutions were preincubated together for 15 min at room temperature prior to assay, in order to allow for the formation of the E-I complex. The inhibition constants were obtained by non-linear leastsquares methods using PRISM 6 and the Cheng-Prusoff equation, as reported earlier [202], and represent the mean from at least three different determinations. All CA isoforms were recombinant ones obtained in-house as reported earlier [17, 93, 207, 221], and their concentrations in the assay system were in the range of 7.8 – 10.6 nM.

Viability assays for determining the cytotoxicity of novel ureido CAIs in normoxic and hypoxic conditions

The breast MDA-MB-231 cancer cell line was used in this study. Cells were cultured at 37ºC, and 5% CO_2 in air using Dulbecco's Modified Eagle's medium (DMEM) media supplemented with 10% fetal bovine serum (FBS). When the cells were subconfluent in culture flasks, they were trypsinized with trypsin-EDTA, counted, and plated in 96 well plates at density of 20,000 cells/well with a final volume of 200 µL in each well. Then the cells were kept in normal conditions (37ºC, 5% CO_2 in air) and allowed to attach and to grow. Six 96 well plates were prepared. After 24 h growth in normal conditions three of the plates were placed in a hypoxic chamber, which was purged and filled with a hypoxia gas mixture (1% O_2, 5% CO_2 and 94% N_2) to induce hypoxia. After 1h the chamber was purged again with hypoxic gas mixture and placed back in the incubator. The closed hypoxia chamber with hypoxic plates was kept at the incubator at 37ºC for 48 h to induce the expression of CA IX isozyme. Other three plates were also kept for 48 h in the same incubator in normal conditions. After 48 h incubation period, both the normoxic and hypoxic plates were retrieved, media was aspirated from all plates and cells were treated with CAIs solutions in hydroxypropyl-β-cyclodextrin solution pre-dissolved in media at 3 different concentrations (1 mM, 100 µM, and 10 µM). Each experiment was done in quadruplicate. Eight wells, used as control for each plate, received only media. Hypoxic well plates were returned to hypoxic chamber, re-purged and filled with hypoxia gas mixture, then returned to the incubator. Normoxic plates were also returned to the incubator. After 24 h treatment, the normoxic and hypoxic plates were retrieved, media was aspirated, cells were washed once with

phosphate-buffered saline (PBS), which was subsequently removed. An MTT solution in media (120 μL, prepared from MTT 5 mg/mL concentration in PBS diluted 1:6 with the DMEM media) was added to each well and the plates were incubated for 4 h at 37ºC. The MTT solution was removed and 150 μL of DMSO was added to solubilize the blue formazan crystals, incubated at 37ºC for 10 min. Analysis of produced formazan was done spectrophotometrically using SpectraMax M2, measuring the absorbance at 570 nm, with a reference absorbance at 690 nm that was subtracted from readings. Data was reported as the average of three experiments. Statistical comparisons were performed by analysis of variance (ANOVA) with Dennett's multiple comparison test using GraphPad Prism 8, where $*P < 0.05$, $**P < 0.01$ and $***P < 0.001$.

CHAPTER 5

DEVELOPMENT AND BIOLOGICAL EVALUATION OF PEGYLATED BIS-SULFONAMIDES AS CARBONIC ANHYDRASE INHIBITORS

In this chapter, our goal was to design, synthesize, characterize and to evaluate the impact of the PEG linker length within a new series of PEGylated CAIs with different PEG backbone length, using the 1,3,4-thiadiazole-2-sulfonamide warhead and succinyl linker, on *in vitro* cell killing ability against CA IX expressing cancer cell lines and CA IX negative cell line.

Our working hypothesis is that the PEG backbone length will significantly influence the CA IX inhibition and *in vitro* cell killing ability of these bis-sulfonamides due to their different radius of gyration (i.e. measure of the size of the random coil shape that polymers adopt in solution or in the amorphous bulk state) and highly hydrated polymeric backbone, and an optimum PEG linker length is required for achieving significant cell killing.

Background and design approach

As mentioned in previous chapter, despite significant medicinal chemistry design efforts that have generated nanomolar and sub-nanomolar CA IX inhibitors, it is still difficult to generate CAIs that are highly selective for this isozyme due to the high sequence homology and active sites similarities between different CA isozymes [2, 13, 16, 58, 72, 222-224].

One of the frequently employed strategies to develop CA IX selective inhibitors is to make the inhibitors membrane-impermeant and thereby limit their access towards the intracellular CA isozymes. Different medicinal chemistry groups, including ours conjugated known CAI pharmacophores with charged groups [94-96, 214, 225], with sugar, or with polymeric moieties [226, 227] to make the inhibitors membrane-impermeant. Our group developed several series of membrane-impermeant CA inhibitors through the conjugation of primary aromatic and heterocyclic sulfonamides with positively charged pyridinium salts [94, 95, 214, 228]. Representative pyridinium sulfonamides such as **78**, **79** and **80** showed excellent selectivity against membrane-bound CA IV [94, 95, 214, 228] and also against tumor associated CA IX and CA XII [225, 229].

Another alternative design approach for generating membrane-impermeant CA IX selective inhibitors is the conjugation of known CA pharmacophores with water-soluble polymeric backbones such as dextran, aminoethyldextran and polyethylene glycol (PEG) [35, 226]. Three representative inhibitors such as **81**, **82** and **83** (Chart 5.1), developed in the late 80's and mid-90's, were impure and polydispersed, and showed unwanted side effects when administered in vivo. Interestingly, from the different polymeric backbones tested, polyethylene glycol (PEG) proved be the most efficient and biocompatible one. Polyethylene glycol conjugation (PEGylation) of drugs also provide several additional benefits such as improved drug solubility, increased stability and circulation time of the drug in the bloodstream, decreased drug immunogenicity, proteolysis and renal excretion, and optimized drug pharmacokinetics [230].

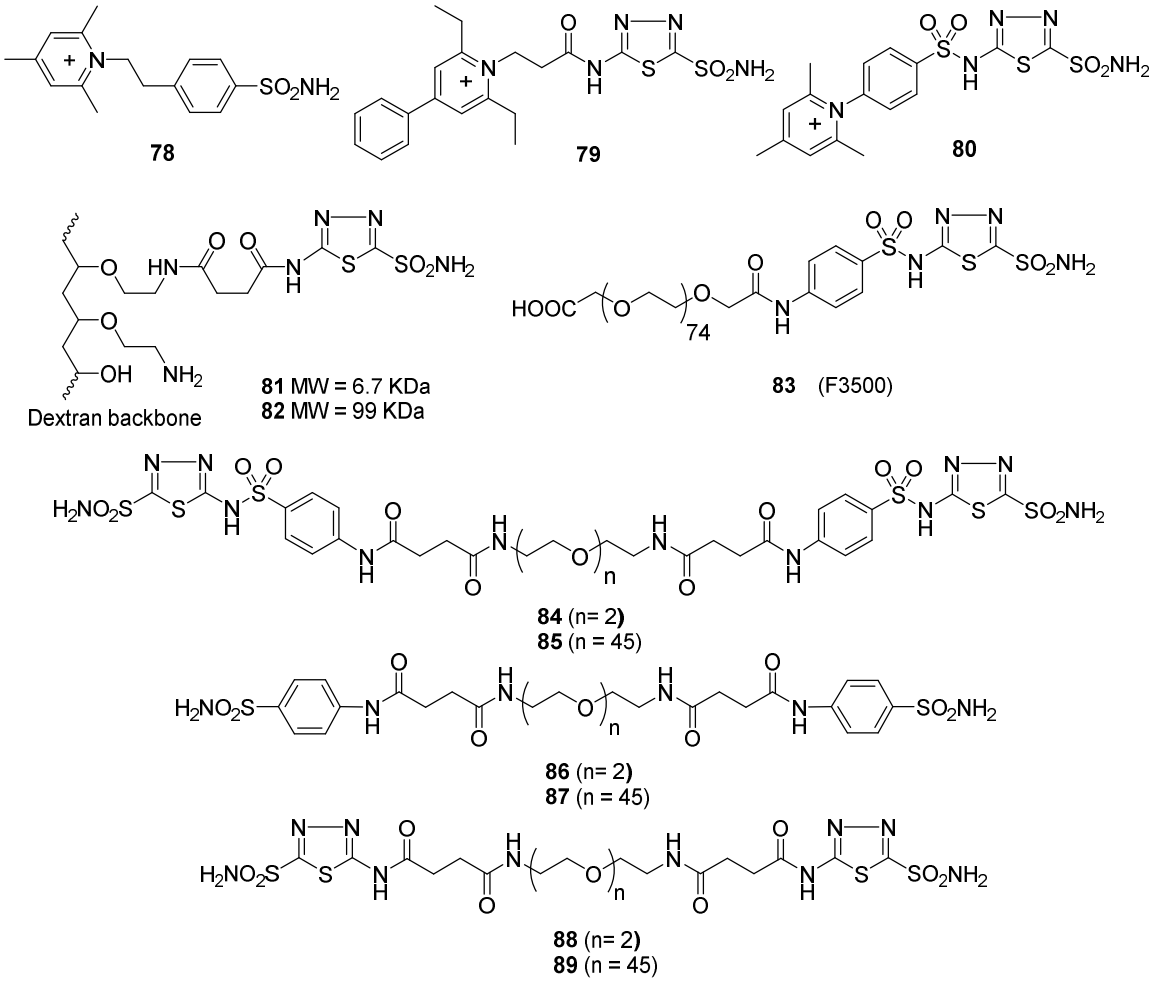

Chart 5.1 Representative CAIs with selectivity against membrane-bound CA isozymes

Building on these premises and taking into account that CA IX and XII are dimers in vivo [231], our group developed a series of bifunctional PEGylated CAIs **84-89** by attaching known CAI pharmacophores (aminobenzenesulfonamide, 5-amino-1,3,4-thiadiazole-2-sulfonamide, aminobenzolamide) on a PEG2000 polymeric backbone (PEG2K) and the corresponding oligoethyleneglycol analogs, having just three EG units (Chart 5.1) [92].

All the bifunctional PEGylated and oligoethyleneglycol analog CAIs **84-89** were tested for their ability to inhibit off-target cytosolic (CA I, II) and membrane-bound (CA IV, IX, XII, XIV) isozymes of carbonic anhydrase (Table 5.1) [92]. All these compounds **84-89** showed excellent inhibition profile against membrane-bound isozymes CA IV, IX, XII, XIV, with nanomolar potency of most representatives against these targets. As expected, these compounds **84-89** were found to be more potent against both tumor over-expressed isozymes CA IX and XII compared to CA CA XIV and CA IV, and much less potent against cytosolic isozyme CA I and CA II.

Importantly, the long PEG linker increased the selectivity of the bis-sulfonamides **85**, **87** and **89** for the membrane-bound isozymes versus the cytosolic ones (especially against CA II), as compared with their oligoethylene glycol congeners **84, 86** and **88**. Bis-sulfonamide **87** having benzenesulfonamide CAI warhead displayed the highest selectivity between membrane-bound isozymes and their cytosolic counterparts (Table 5.1), with bis-sulfonamide **89** bearing 1,3,4-thiadiazole-2-sulfonamide warhead showed moderate selectivity. Bis-sulfonamide **88** were identified as potent pan-inhibitors with nanomolar potency against all isozymes tested except CA I.

Table 5.1 Inhibition data of human CA isoforms hCA I, II, IV, IX, XII and XIV with derivatives **84-89** reported here and the standard sulfonamide inhibitor acetazolamide **AAZ 1** by a stopped flow CO_2 hydrase assay [92].

	K_I (nM)*					
Comp	**hCA I**	**hCA II**	**hCA IV**	**hCA IX**	**hCA XII**	**hCA XIV**
84	192	8.6	6.4	24.1	2.8	4.6
85	181	12.9	4.4	1.7	3.7	4.4
86	221	37.1	7.8	2.9	2.6	6.2
87	272	1764	9.5	4.8	3.2	7.3
88	180	8.7	5.0	9.6	5.9	4.6
89	225	66.6	5.8	2.5	5.4	6.8
1 AAZ	250	12	74	25	5.7	41

* Mean from 3 different assays, by a stopped flow technique. Monomeric (recombinant) human enzymes used in all cases.

CAIs **84-89** were also tested for *in vitro* cell viability in 2D cell models under normoxic and hypoxic conditions and in 3D (tumor spheroids) models of cancer namely colon carcinoma HT-29, the breast cancer MDA-MB 231, and the ovarian cancer SKOV3 cell models that express these CA isozymes [74, 78, 79, 82-84, 92, 217, 218, 221, 232-239]. PEGylated bis-sulfonamides **89**, bearing the classical 1,3,4-thiadiazole-2-sulfonamide "warhead", was found to be the most efficient inhibitor which displayed consistent and significant cancer cell killing at concentrations of 10-100 μM across all three cell lines in 2D cellular models under both normoxic and hypoxic conditions, as well as in tumor spheroid cellular models. This excellent potency against purified CA IX and CA XII isozymes, and consistent and significant cancer cell killing obtained with

PEGylated CAI **89**, probably due to the cooperative binding and bivalent association of this type of two-pronged inhibitor with the two neighboring active sites, as shown by Whitesides [240]. These results further fueled our group's growing interests toward developing CA IX selective inhibitors.

Inspired from these inhibition profile and *in vitro* cell killing ability of PEGylated CAI **89** bearing an 1,3,4-thiadiazole-2-sulfonamide warhead, we opted to investigate further the impact of the PEG linker length within a new series of PEGylated CAIs with different PEG backbone length, using the same 1,3,4-thiadiazole-2-sulfonamide warhead and succinyl linker, on CA IX inhibition and *in vitro* cell killing ability. Thus, our working hypothesis is that the PEG backbone length will significantly influence the CA IX inhibition and *in vitro* cell killing ability of these bis-sulfonamides due to the different radius of gyration (i.e. measure of the size of the random coil shape that polymers adopt in solution or in the amorphous bulk state) and highly hydrated polymeric backbone, and therefore an optimum PEG linker length is required for achieving significant warhead display, efficient CA IX inhibition and cell killing.

In order to test our working hypothesis, we have selected five different PEGylated bis-sulfonamides bearing PEG 1K, PEG 2K, PEG 3.4K, PEG 5K and PEG 20K polymeric backbones, which were synthesized via the procedure outlined below and were tested in vitro for their ability to kill cancer cells expressing CA IX.

Results and discussion

Synthesis of bis-sulfonamide CAIs

The new series of compounds **89** and **91-94** were synthesized following minor optimizations of a previously reported procedure (Scheme 5.1). Again, the starting 5-amino-1,3,4-thiadiazole-2-sulfonamide **61** was synthesized as previously described [214, 215]. First, the succinyl derivatives **90** was generated from the condensation of 5-amino-1,3,4-thiadiazole-2-sulfonamide **61** with succinic anhydride in acetonitrile at room temperature. The carboxy group of succinyl amido sulfonamide was subsequently activated with 2-chloro-4,6-dimethoxy-1,3,5-triazine (CDMT)/N-methylmorpholine (NMM)[92, 241] and was condensed with diamino polyethylene glycols with different PEG chain length to yield the bis-sulfonamides **89** and **91-94**. These compounds were purified by flash chromatography and characterized by standard analytical methods.

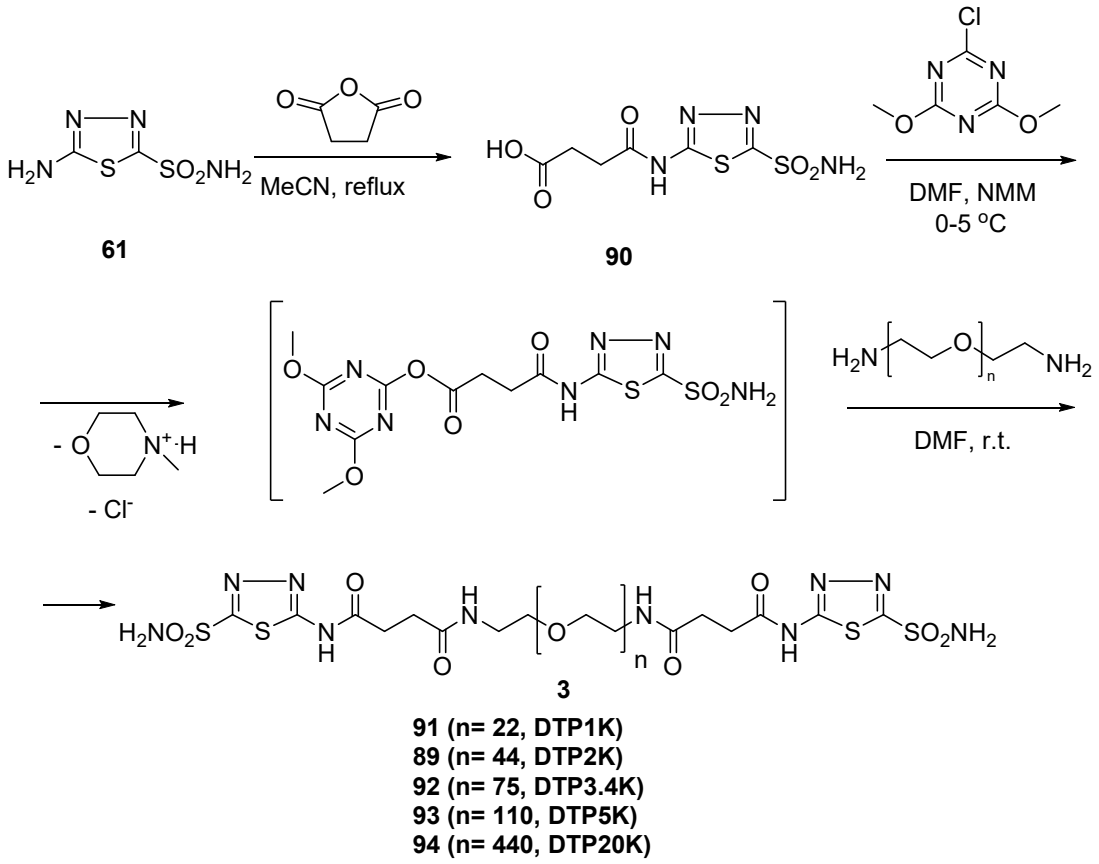

Scheme 5.1 Synthetic strategy for the generation of bis-sulfonamide CA inhibitors.

In vitro cell viabilities study

All of the PEGylated bis-sulfonamides **DTP2K 89** and **DTP1K 91-DTP20K 94** were tested in 2D and 3D (tumor spheroids) cancer cell models, either expressing CA IX (HT-29 colon cancer, MDA-MB 231 breast cancer, and SKOV-3 ovarian cancer) or CA IX negative cells (NCI-H23 lung cancer) [74, 78, 79, 82-84, 92, 217, 218, 221, 232-239]. The expression of CA IX under normoxic and hypoxic conditions was validated through western blotting (Figure 5.1a).

In the 2D cell viability assay, cells were grown subconfluent in petri dishes and then plated in 96 well plates in normal conditions (37ºC, 5% CO_2 in air). For each cell

line, half of the plates were incubated in normal (normoxic) conditions, while the other half were subjected to a hypoxic condition (1% O_2, 5% CO_2 and 94% N_2) to induce the expression of CA IX isozyme. Subsequently, the plates were treated with CAIs solutions in media for 24 h incubation time, at three different concentrations (1 mM, 100 μM, and 10 μM) in either normoxic/hypoxic conditions. Cell viability was measured using an MTT assay (Figure 5.1b, c) [219].

Data from Figure 3 showed that the ability of the new PEGylated CAIs to kill the tumor cells correlated well with CA IX expression. All PEGylated CAIs affected tumor cell viability in CA IX expressing cancer cell lines, with a greater effect observed under hypoxic conditions, where CA IX is overexpressed.

Under normoxic conditions the viability of the HT-29 cell line after treatment with bis-sulfonamides **DTP2K 89** and **DTP1K 91-DTP20K 94** was significantly reduced, with CAI having shorter PEG backbones being more efficient. Bis-sulfonamide **DTP1K 91** reduced the cell viability to around 45% and was the best inhibitor in these conditions for this cell line. The order of cell killing efficiency was **DTP1K 91** > **DTP2K 89** > **DTP3.4K 92** > **DTP5K 93**> **DTP20K 94** > **AAZ 1**. Breast cancer MDA-MB231 and ovarian cancer SKOV-3 cell line were less sensitive to bis-sulfonamide treatment under normoxic conditions, with **DTP1K 91** and **DTP2K 89** being again the most efficient, with an effect matching **AAZ 1**. Likewise, the viability of CA IX negative cell line NCI-H23 was not affected after treatment with these CAIs, implying a CA IX mediated cell killing for these inhibitors.

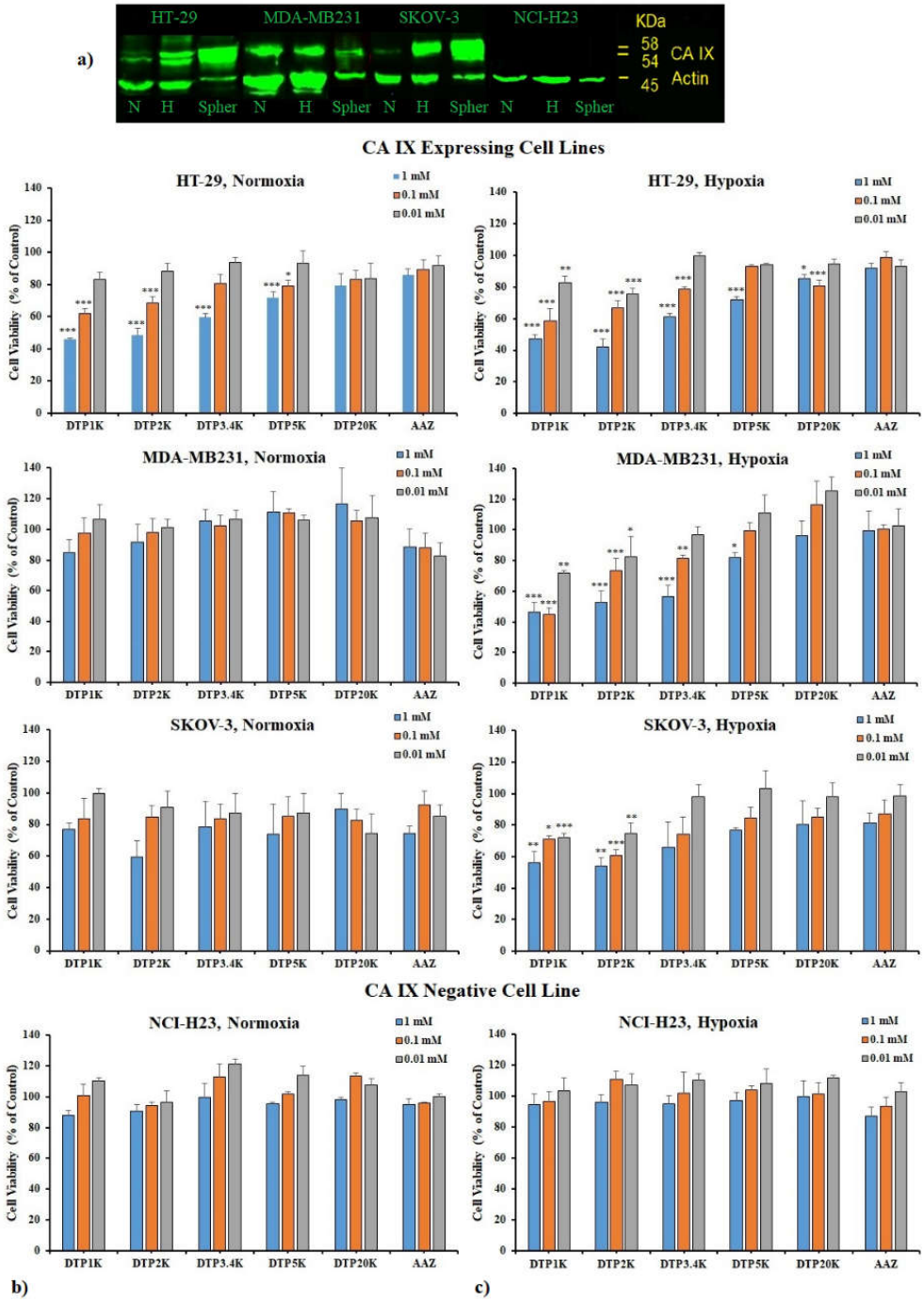

Figure 5.1 (a) Expression of CA IX target in 2D (normoxic/hypoxic) and 3D cancer cell cultures, and the effect of PEGylated CAIs **DTP2K 89** and **DTP1K 91-DTP20K 94** and acetazolamide **AAZ 1**, at different concentrations, on the viability of CA IX expressing cell lines (HT-29, MDA-MB231 and SKOV-3) and CA IX negative cell line (NCI-H23) under normoxic (b) and hypoxic (c) conditions. P values were determined by one-way ANOVA, comparing the value with the acetazolamide **1** (*P < 0.05, **P < 0.01, ***P < 0.001). Only the statistical significant differences were shown.

However, under hypoxic condition, all three CA IX expressing cell lines were affected by the CAI treatment in a concentration-dependent manner, as expected, with colon HT-29 and breast MDA-MB231 cancer cells being slightly more sensitive to CAI treatment than ovarian cancer cell line SKOV-3. All the PEGylated CAIs **DTP2K 89** and **DTP1K 91-DTP20K 94** showed significant tumor cell killing abilities. Cell killing efficiency decreased with the increase of PEG linker length. PEGylated CAIs **DTP1K 91, DTP2K 89** and **DTP3.4K 92,** bearing short and medium PEG backbones, were the most efficient in all three CA IX expressing cell models. The PEGylated bis-sulfonamide **DTP1K 91** was found to be the best inhibitor against all three cell lines under hypoxic conditions, followed by **DTP2K 89**, and **DTP3.4K 92.** Both **DTP1K 91** and **DTP2K 89** displayed robust cell killing, with cell viabilities as low as 30-40 % at 1 mM, 50 % at 100 μM and 70-80 % at 10 μM, being influenced by the cell type and presence of CA IX in large amounts due to hypoxia. On the other hand, inhibitors **DTP5K 93** and **DTP20K 94**, having long PEG linkers, were generally less efficient, even at high concentrations. Inhibitor **DTP5K 93** showed significant cell killing only at 1 mM concentration on HT-29 cell line and MDA-MB231 cell line under hypoxic conditions, with inhibitor **DTP20K 94** significantly reducing viability of HT-29 cell line only at 1 mM concentration.

These data infer that the length of PEG backbone plays an important role in tumor cell killing, with the PEG linker significantly affecting the availability of sulfonamide warhead group for binding into the active site of membrane bound CA IX isozyme. Considering that PEG backbone has a coiled structure, a longer PEG linker length might place the warhead towards the interior of the coiled backbone, decreasing its availability

to bind the CA IX active site and therefore decreasing the potency of the bis-sulfonamide in vitro.

All the PEGylated CAIs **DTP2K 89** and **DTP1K 91-DTP20K 94** showed superior cell killing profile than positive control **AAZ 1** used in this study, which was found to be less efficient toward tumor cell killings under both hypoxic and normoxic conditions. **AAZ 1** was efficient only at very high concentration, thus revealing the high impact of PEG backbone on the efficiency of cell killing.

Importantly, the CA IX negative cell line NCI-H23 did not respond to the treatment with these PEGylated CAIs, even under hypoxic conditions. These findings suggest a CA IX-medicated cell killing by the new PEGylated bis-sulfonamides.

After quantifying the relative amount of CA IX in tumor spheroids, we assessed their susceptibility to treatment with CAIs **DTP2K 89** and **DTP1K 91-DTP20K 94** at 1 mM, 100 μM and 10 μM concentration, for 24 h incubation time. Viability of the spheroids was assessed via a WST-1 assay [242] (Figure 5.2).

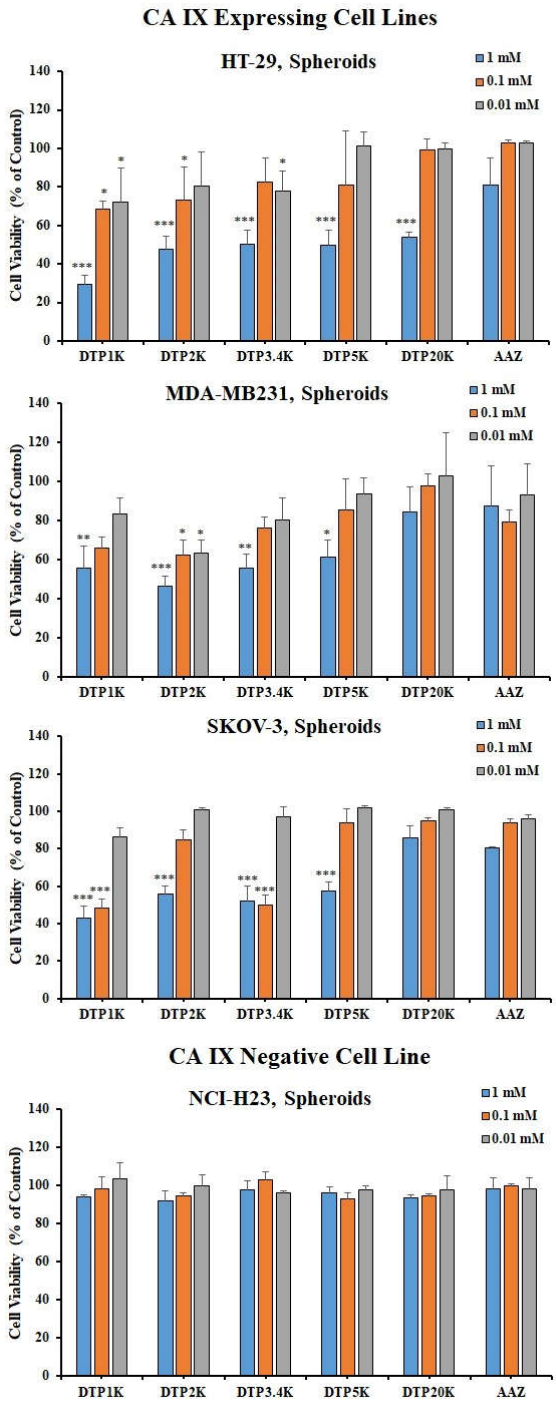

Figure 5.2 Effect of PEGylated CAI **DTP2K 89** and **DTP1K 91-DTP20K 94** and acetazolamide **AAZ 1**, at three different concentrations, on the viability of CA IX expressing HT-29, MDA-MB231 and SKOV-3, and CA IX negative NCI-H23 3D cell cultures (tumor spheroids). P values were determined by one-way ANOVA, comparing the value with the acetazolamide **1** (*P < 0.05, **P < 0.01, ***P < 0.001). Only the statistically significant differences were shown.

Cell viability data shown in Figure 5.2 correlated well with the level of CA IX expression in tumor spheroids (Figure 5.1a), similarly to the 2D cell cultures (Figure 5.1b and 5.1c). Tumor spheroids become hypoxic due to their 3D growth that limits the oxygen perfusion into the spheroid cores. Therefore, tumor spheroid model is closer to the in vitro conditions. The higher level of expression of CA IX in HT-29 and SKOV-3 tumor spheroids allows one to establish SAR for the new PEGylated CAIs even at low inhibitor concentrations of 100 μM and 10 μM. Among the three CA IX expressing cell lines, HT-29 and SKOV-3 tumor spheroids were found to be most sensitive to bis-sulfonamide CAIs treatment, in good correlation with CA IX expression level, with MDA-MB 231 cell line being slightly less affected. All the PEGylated CAIs impacted the viability of tumor spheroids for all three CA IX expressing 3D cell cultures, with cell killing efficiency decreasing with the increase of PEG linker length. At high concentration all CAIs were efficient in reducing cell viability. At lower concentrations the shorter ones were again more efficient. Thus, PEGylated bis-sulfonamide CAIs having shorter and medium PEG linker **DTP1K 91, DTP2K 89** and **DTP3.4K 92** were the most efficient CAIs in this assay. PEGylated CAI **DTP1K 91** at 1 mM, 100 μM and 100 μM concentrations, significantly decreased the cell viability to about 30%, 68%, and 72% in HT-29, 40%, 50%, and 86% in SKOV-3, and 55%, 70%, and 83% in MDA-MB231, whereas for **DTP2K 89** treatment at the respective concentration **,** cell viability decreased to about 50%, 75%, and 80% in HT-29, 55%, 85%, and 100% in SKOV-3, and 45%, 62%, and 64% in MDA-MB 231. High molecular weight PEGylated CAIs **DTP5K 93** and **DTP20K 94** were efficient in killing the cells only at higher concentration. At 1 mM concentration, CAI **DTP5K 93** decreased the cell viability to 49% in HT-29, 57% in

SKOV-3, and 61% in MDA-MB231 tumor spheroids, while PEGylated CAI **DTP20K 94** only significantly impacted the viability of HT-29 tumor spheroids, expressing the highest level of CA IX. Thus, length of PEG linker plays a significant role in killing tumor spheroid cells, with the short PEG 1K and 2K linkers being the most efficient for this type of CAIs. Again, all the new PEGylated CAIs exhibited better cell killing efficiency than positive control **AAZ 1**, which was found to reduce cell viability to about 80% (for 1 mM concentration) and was ineffective at lower concentrations.

Importantly, these PEGylated CAIs **DTP2K 89** and **DTP1K 91-DTP20K 94** did not affect the cell viability of CA IX negative NCI-H23 tumor spheroids, thus reconfirming a CA IX mediated cell killing of these inhibitors.

Thermal properties of polymeric CAIs

Differential Scanning Calorimetry (DSC) is a powerful method to assess the purity of polymers and polymer conjugates and to examine the thermal transitions of different polymeric materials [243, 244]. Important thermal transitions are glass transition temperature (T_g), crystallization temperature (T_c), and melting temperature (T_m) [244]. The knowledge about these thermal transitions is also important since these parameters dictate the formulation processes and the stability of polymer conjugates [243, 244]. When heat is applied to polymeric materials, the polymer molecules gained energy and they started to move around. At some point the heat energy is enough to change the amorphous rigid structure to a flexible structure. The polymer molecules move freely around each other. This transition point is called the glass transition temperature (T_g) [244]. If the temperature is increased further, at some point the polymer molecules will

acquire enough freedom of motion to spontaneously arrange themselves into a crystalline form. This is called as the crystallization temperature (T_c) [244]. This transition from amorphous solid to crystalline solid is an exothermic process and appeared as a peak in DSC signal. As the temperature increases further the polymer will eventually reach its melting temperature (T_m) and will exhibit an endothermic peak in the DSC curve. The ability to determine phase transition temperatures and associated enthalpies makes DSC a valuable tool in producing phase diagrams for various polymer and polymer conjugates [244].

DSC was used to analyze the thermal properties of the new PEGylated bis-sulfonamides **DTP2K 89** and **DTP1K 91-DTP20K 94** (Figure 5.3a, 5.3b). DSC thermograms of polyethylene glycol 1000 (PEG-1K-OH) and polyethylene glycol 1000 diamine (PEG-1K-NH2) were also generated for comparison. Briefly, DSC curves were obtained in the temperature range of -30°C and 170°C at a heating rate of 5°C/min for several heating and cooling cycles using DSC Q200 (TA Instruments, DE).

DSC thermograms from Figure 5.3a in the 1st cooling cycle and 2nd heating cycle respectively revealed that polyethylene glycol 1000 **(PEG-1K-OH)** has a sharp phase transition with a crystallization temperature T_c of 29.3°C and a melting temperature T_m of 39.18°C. The ~10°C supercooling reflects a relatively easy adoption of a crystalline structure due to the high mobility –OH small end group. Change of end functional group from –OH to –NH_2 in diamino PEG **(PEG-1K-NH2)** slightly affected the stability of the PEG backbone which presented a T_c at lower temperature (23.40°C). The T_m (37°C) was also lower than the one observed for **PEG-1K-OH**, revealing that amino groups slightly destabilize PEG backbone. The lower stability of **PEG-1K-NH_2** as compared with **PEG-**

1K-OH was also reflected by the lower enthalpy observed during crystallization/melting (~168 J/g for PEG-1K-NH_2 vs ~ 202 J/g for PEG-1K-OH).

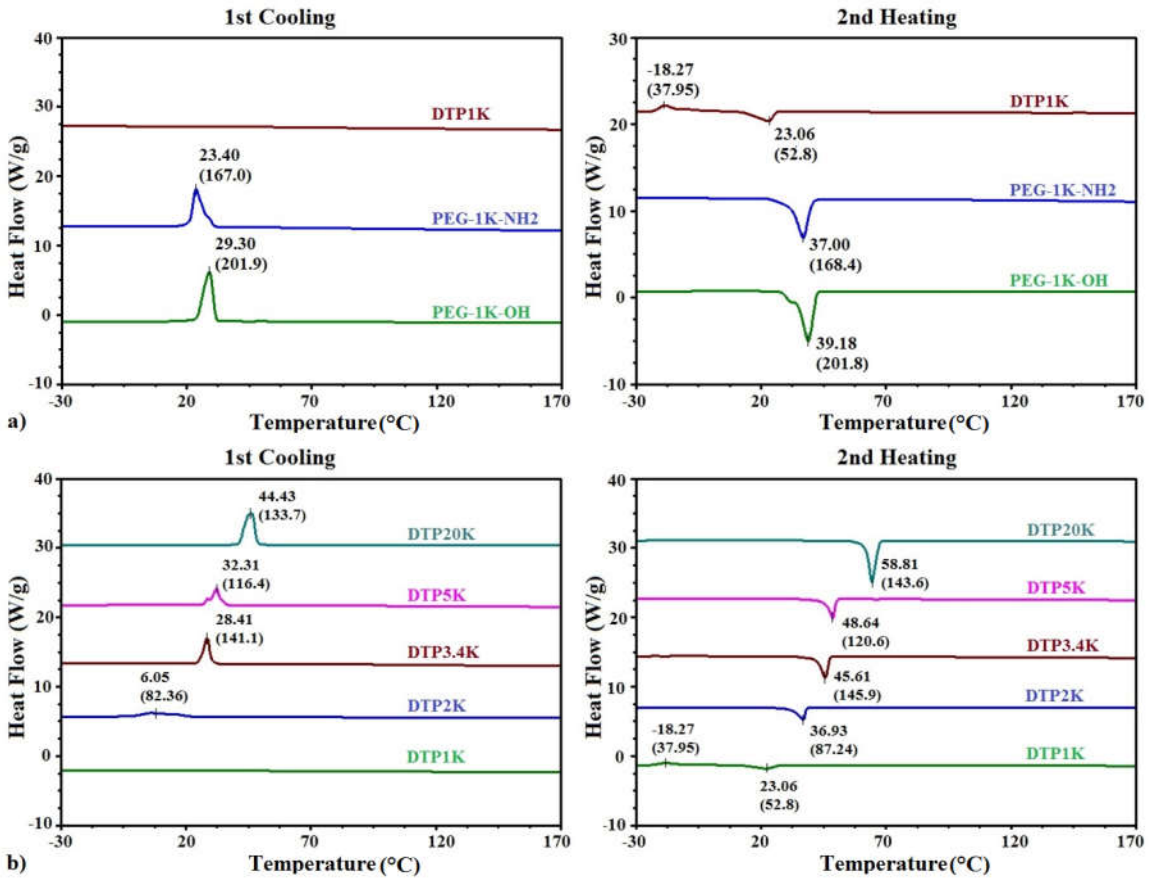

Figure 5.3 Comparative DSC thermograms of a**) PEG-1K-OH, PEG-1K-NH2** versus PEGylated bis-sulfonamide **DTP1K 91**, and of b) PEGylated bis-sulfonamides **DTP2K 89** and **DTP1K 91-DTP20K 94.**

The conjugation of warhead 2-sulfonamide-1,3,4-thiadiazole-5-(succinamido) on PEG significantly destabilized the PEG backbone. PEGylated bis-sulfonamide **DTP1K 91** did not show any phase transition in the first cooling cycle. Upon heating, the glassy material crystallizes at ~ -18°C and then melted around at 23°C. The enthalpy observed

upon meltings was about 1/3 of the corresponding thermal effect observed for PEG-1K-NH_2, reflecting the strong destabilizing effect of the bulky warhead on the (relatively short) (PEG backbone Figure 5.3). Elongation of the PEG backbone (Figure 5.3b) allowed a better organization of PEG linker upon cooling. **DTP2K 89** managed to crystallize upon cooling (with about 30°C supercooling). Longer PEG linkers (3.4K to 20K) raised the T_c and reduced the supercoolings monotonously, from ~17°C **(DTP3.4K 92)** to ~16.3°C **(DTP5K 93**) to ~14.4°C **(DTP20K 94).** It appears that once the linker length reached a critical length (~3.4K) the impact of the terminal warheads on the backbone is minimized. T_m increased monotonously from 36.93°C **(DTP3.4K 92)** to 58.81°C (**DTP20K 94**), as expected. Interestingly, the crystallization/meltings enthalpy did not follow a linear trend. **DTP3.4K 92** displayed the highest thermal effect (~142 J/g), followed by **DTP20K 94** (~140 J/g) and **DTP5K 93** having an intermediate value (~118 J/g). This particular trend probably reflects the different relative portion of the two warheads and the impact of PEG length and coilings towards their separation. We postulate that the two warheads are relatively well separated in **DTP3.4K 92** and **DTP20K 94** and can come closer to each other in **DTP5K 93**, thus hampering the crystallization and reducing the enthalpy associated with it.

Conclusions

A series bifunctional PEGylated CAIs **DTP2K 89** and **DTP1K 91-DTP20K 94** were generated through the attachment of CA warhead 1,3,4-thiadiazole-2-sulfonamide to PEG backbone having different lengths from 1K to 20K via a succinyl linker. These compounds were assessed in vitro for their ability to kill cancer cells in 2D and 3D (tumor spheroids) cancer cell models, either expressing CA IX (HT-29 colon cancer, MDA-MB 231 breast cancer, and SKOV-3 ovarian cancer) or CA IX negative cells (NCI-H23 lung cancer). A detailed structure activity relationship study was carried out within this series of PEGylated bis-sulfonamides **DTP2K 89** and **DTP1K 91-DTP20K 94**, bearing different PEG backbone length, in order to understand the impact of PEG linker length in killing these cancer cells. PEGylated CAIs **DTP1K 91, DTP2K 89** and **DTP3.4K 92,** bearing short and medium PEG backbones, were the most efficient CAIs in killing all three CA IX expressing tumor cells under both normoxic and hypoxic conditions, and in tumor spheroid models. We successfully identified the optimum PEG linker length for this type of bifunctional bis-sulfonamide CAIs. Thus, the most efficient PEGylated CAI was found to bis-sulfonamide **DTP1K 91**, which showed consistent and significant cancer cell killing at concentrations of 10−100 μM across different CA IX and XII expressing cancer cell lines. PEGylated CAIs **DTP2K 89** and **DTP1K 91-DTP20K 94** did not affect the cell viability of CA IX negative NCI-H23 tumor spheroids, thus revealing a CA IX mediated cell killing of these inhibitors.

Experimental section

Materials and methods

Materials

The following materials were used as received: succinic anhydride (TCI America, Portland, OR), N-methylmorpholine (TCI America, Portland, OR), 2-chloro-4,6-dimethoxy-1,3,5-triazine (Acros Organics, New Jersey, NJ), H_2N-PEG1000-NH_2, H_2N-PEG2000-NH_2, H_2N-PEG3400-NH_2, H_2N-PEG5000-NH_2 and H_2N-PEG20,000-NH_2 (Laysan Bio, Arab, AL). Other solvents (HPLC quality) were purchased from Fisher Scientific (Pittsburgh, PA), EMD (Gibbstown, NJ), and VWR International (West Chester, PA). Human colon adenocarcinoma cell line (HT-29), human ovary cancer cell line (SKOV-3-Luc), human breast cancer cell line (MDA-MB-231-Luc) and lung cancer cell line NCI-H23 were purchased from ATCC (Manassas, VA), Dulbecco's Modified Eagle's medium (DMEM), RPMI-1640, McCoy's 5A media were from Mediatech-Corning (Manassas, VA), fetal bovine serum (FBS) was from Fisher Scientific (Pittsburgh, PA), 3-(4,5-Dimethylthiazol-2-yl)-2,5-diphenyltetrazolium bromide (MTT), phosphate-buffered saline (PBS), dimethyl sulfoxide (DMSO) and water-soluble tetrazolium salt-1 (WST-1) were purchased from VWR International (West Chester, PA).

Techniques:

The purity and the structure identity of the intermediary and the final products were assessed by a combination of techniques that included thin-layer chromatography (TLC), HPLC-MS, ^{1}H-NMR, COSY, ^{13}C-NMR, high resolution mass spectrometry (HR-

MS), gel permeation chromatography (GPC) coupled with MALDI-TOF. TLC was carried out on SiO_2-precoated aluminum plates (silica gel with F254 indicator; layer thickness 200 μm; pore size 60 Å, from Sigma-Aldrich.

Melting points were determined using a Thermolyne heating stage microscope (Dubuque, IA), equipped with an Olympus 5X objective, at heating/cooling rate of ~ 4 ^oC/min and were uncorrected. The purity of compounds was assessed via LC-MS using an Agilent 1200 HPLC-DAD-MS system equipped with a G1315A DAD and a 6130 Quadrupole MS using a ZORBAX SB-C18 column, eluted with H_2O (0.1% HCOOH)/MeCN (0.1% HCOOH) 95/5 to 0/100 linear gradient. All compounds reported in the paper were > 98 % pure.

Analytical GPC was performed for the polymeric compounds using a Shimadzu prominence UFLC equipped with vacuum degasser, CC20AD pump, CBM 20A controller, CTO – 20 A column over, UV and RI detectors, under the control of EZ start software. Separation was performed with Phenomenex Phenogel columns (1 × Phenogel Guard column, 5 μm, linear, 50 × 7.8 mm + 1 × Phenogel 5 μm, 100 Å, 300 × 7.8 mm + 1 × Phenogel 5 μm, 500 Å, 300 × 7.8 mm) eluted with DMF, at 50°C, at a flow rate of 1 mL/min. Calibration was done with 10 PEG pure standards, with MW ranging from 200 to 50000. MALDI-TOF was performed on a Bruker Daltonix Autoflex TOF-TOF mass spectrometer, using α-cyano-4-hydroxycinnamic acid as matrix. Samples were dissolved in MeCN containing 0.1 % TFA at a concentration of 1 mg/mL. Equal volumes of sample and matrix (5 mg/mL in MeCN) were mixed and the solution was spotted on the MALDI plate. After drying, the plate was inserted into the instrument and the spectrum was determined, using a 20000V acceleration voltage and a variable bombardment time.

NMR spectra were recorded at ≈300 K with a Bruker Avance III 400 Plus spectrometer equipped with a 5 mm indirect detection probe, operating at 400 MHz for ^{1}H-NMR, at 100 MHz for ^{13}C-NMR. Chemical shifts are reported as δ values, using tetramethylsilane (TMS) as internal standard for proton spectra and the solvent resonance for carbon spectra. Assignments were made based on chemical shifts, signal intensity, COSY, HMQC, and HMBC sequences. For ^{1}H-NMR, data are reported as follows: chemical shift, multiplicity (s = singlet, d = doublet, t = triplet, sep = septet, m = multiplet), coupling constants J (Hz) and integration.

Synthesis of 4-oxo-4-((5-sulfamoyl-1,3,4-thiadiazol-2-yl)amino)butanoic acid 90 [92]

In a flame dried 20 mL reaction vial, 5-amino-1,3,4-thiadiazole-2-sulfonamide **61** (0.45 g, 2.5 mmol) was dissolved in 2 mL of DMF. Succinic anhydride (275 mg, 0.275 mmol) was added over it. The reaction was allowed to stir for 48 h and monitored by TLC and LC-MS. Once the reaction reached completion, it was evaporated to dryness by rotavap at 60˚C. A volume of 10 mL of water was added over the mix to dissolve all excess succinic anhydride, and the product precipitated. The precipitate was filtered and rinsed with methanol several times to remove water. The precipitate was 98% pure (LC-MS). Yield: 83%; mp. 232-236ºC; lit.[92] m.p. 232-236ºC. ^{1}H-NMR (400 MHz, DMSO-d^{6}, δ, ppm): 13.06 (br s, 1H, -NH), 12.27 (br s, 1H , NH), 8.32 (s, 2H, -SO_2NH_2), 2.76 (t, *J* = 6.5 Hz, 2H, CH_2COOH), 2.60 (t, *J* = 6.5 Hz, 2H, CH_2CONH) ; ^{13}C-NMR (100.6 MHz, DMSO-d^{6}, δ, ppm): 173.3 (CONH), 171.4 (COOH), 164.1 (C_5 TDA), 161.0 (C_2 TDA), 29.9 (-$\underline{C}H_2COOH$), 28.2 (-$\underline{C}H_2CONH$-); LC-MS: $C_6H_8N_4O_5S_2$, exact mass: 280.0; Found: 281.0 (MH^+).

General procedure for the preparation of bis-sulfonamides 89 and 91-94

In a flame dried 20 mL reaction vial, succinylamidosulfonamide **90** (0.536 g, 1.92 mmol) and 2-chloro-4,6-dimethoxy-1,3,5-triazine (CDMT, 0.37g, 2.11 mmol) were dissolved in 2 mL dry DMF. The reaction vial was cooled in an ice bath at 0˚C. After several minutes, N-methylmorpholine (NMM, 235 µL, 0.213 g, 2.11 mmol) was added and the reaction mixture was allowed to react at 0˚C for 45 min under nitrogen atmosphere. Then diamino PEG (H_2N-PEG-NH_2) (0.500 g, 0.250 mmol, dissolved in 1.5 mL dry DMF) was added dropwise to reaction mixture. The reaction was stirred at room temperature under nitrogen atmosphere for two days. The DMF was evaporated by rotavap, under high vacuum, and the crude compound was absorbed on SiO_2. Flash chromatography was performed with $CHCl_3$/MeOH gradients on a SiO_2 column. Useful fractions (determined by TLC, performed with DCM/MeOH (75/25 v/v), by NMR and by MALDI) were grouped and evaporated to dryness to yield relatively pure compound which was further purified by another run of flash chromatography. Finally, the pure compounds were dried under high vacuum for 24 h.

Bis-(5-Sulfamoyl-[1,3,4]thiadiazol-2-yl)-amidosuccinyl)-polyethyleneglycol1000diamide (DTP1K) 91

Yield: 75 %; ^{1}H-NMR (400 MHz, D_2O, δ, ppm): 3.65-3.52 (m, 88 H, 22 -OCH_2CH_2O-), 3.57-3.52 (m, 4H, -O$\underline{CH_2}CH_2NH$-), 3.31 (d, J = 7.1 Hz, 4H, -$OCH_2\underline{CH_2}NH$-), 2.87-2.79 (m, 4H, -CO$\underline{CH_2}CH_2CO$-), 2.66-2.60 (m, 4H, -$OCCH_2\underline{CH_2}CO$-). GPC: 96%+, t_R = 15.86 min.

Bis-(5-Sulfamoyl-[1,3,4]thiadiazol-2-yl)-amidosuccinyl)-polyethyleneglycol2000diamide (DTP2K) 89

Yield 56.7%; ^{1}H-NMR (D_2O, δ, ppm): 3.80-3.58 (m, 176 H, 44 OCH_2CH_2O), 3.55 (t, *J* = 5.8 Hz, 4H, -O$\underline{CH_2}CH_2NH$-), 3.33 (t, *J* = 5.4 Hz, 4H, -$OCH_2\underline{CH_2}NH$-), 2.87 (t, *J* = 6.6 Hz, 4H, -$COCH_2\underline{CH_2}CO$-), 2.63 (t, J = 6.6 Hz, 4H, -$OC\underline{CH_2}CH_2CO$-). GPC: 96%+, t_R = 15.38 min.

Bis-(5-Sulfamoyl-[1,3,4]thiadiazol-2-yl)-amidosuccinyl)-polyethyleneglycol3400diamide (DTP3.4K) 92

Yield: 55 %; 1H-NMR (D2O, δ, ppm): 3.81-3.58 (m, 299 H, 77 OCH2CH2O), 3.54-3.53 (m, 4H, -OCH2CH2NH-), 3.32 (t, J = 6.4 Hz, 4H, -OCH2CH2NH-), 2.85 (t, J = 6.6 Hz, 4H, -COCH2CH2CO-), 2.61 (t, J = 6.6 Hz, 4H, -OCCH2CH2CO-). GPC: 96%+, t_R = 14.57 min.

Bis-(5-Sulfamoyl-[1,3,4]thiadiazol-2-yl)-amidosuccinyl)-polyethyleneglycol5000diamide (DTP2K) 93

Yield: 60 %; 1H-NMR (D2O, δ, ppm): 3.82-3.58 (m, 440 H, 113 OCH2CH2O), 3.55-3.53 (m, 4H, -OCH2CH2NH-), 3.32 (t, J = 6.4 Hz, 4H, -OCH2CH2NH-), 2.86 (t, J = 6.4 Hz, 4H, -COCH2CH2CO-), 2.62 (t, J = 6.8 Hz, 4H, -OCCH2CH2CO-). GPC: 96%+, t_R = 14.003 min.

Bis-(5-Sulfamoyl-[1,3,4]thiadiazol-2-yl)-amidosuccinyl)-polyethyleneglycol20000diamide (DTP2K) 94

Yield: 55 %; 1H-NMR (D2O, δ, ppm): 3.80-3.57 (m, 1760 H, 440 OCH2CH2O), 3.45-3.43 (m, 4H, -OCH2CH2NH-), 3.31 (t, J = 4.8 Hz, 4H, -OCH2CH2NH-), 2.85 (t, J = 6.8 Hz, 4H, -COCH2CH2CO-), 2.61 (t, J = 6.6 Hz, 4H, -OCCH2CH2CO-). GPC: 96%+, t_R = 11.80 min.

Cytotoxicity evaluation in 2D cell cultures

Four cell lines namely HT-29, NCI-H23, MDA-MB-231 and SKOV3 were cultured at 37^0C and 5% CO_2 using RPMI-1640, Dulbecco's Modified Eagle's medium (DMEM) and McCoy's 5A Medium respectively supplemented with 10% fetal bovine serum. When the cells were sub-confluent in 75 cm^2 culture flasks, they were trypsinized with trypsin-EDTA, counted, and plated in 96-well plates at a density of 10^4 cells/well with a final volume of 200 µL in each well. Two plates were made for each cell line. After 24 h incubation in a 5% humidified incubator at 37°C, one plate from each cell line was placed in the hypoxia chamber and purged for 10 min with the hypoxia gas mixture (1% O_2, 5% CO_2, balance N_2). After 1h the chamber was purged again with hypoxic gas mixture and placed back in the incubator. After a 24 h incubation in the incubator at 37 °C, both the normoxic and hypoxic plates were retrieved, and media was removed from all wells. Cells were washed with 5 % sterile dextrose and treated with different solutions of different concentrations of CAI **DTP2K 89** and **DTP1K 91-DTP20K 94** in media, all pre-filtered through a 0.2 µm sterile nylon filter. Each assay was done at least in triplicate. After 24 h incubation time with CAIs, supernantant was discarded, cells were washed with phosphate-buffered saline (PBS) and, after removal of PBS, each well received 120 µL of MTT/media solution (prepared from 5 mg/mL MTT in sterile PBS,

added to media in the ratio 1:6). Plates were incubated 4 h at 37 ºC, MTT/media was aspirated off and 150 µL of DMSO was added to each well to dissolve formazan crystals. Plates were stored in the incubator for 5 min at 37 ºC and absorbance was read at 570 nm using the 630 nm wavelength as reference. Data was reported as the average of three experiments. Statistical comparisons were performed by analysis of variance (ANOVA) with Dennett's multiple comparison test using GraphPad Prism 8, where *P < 0.05, **P < 0.01 and ***P < 0.001.

Cytotoxicity evaluation in 3D cell cultures

Three cell lines, namely HT-29, NCI-H23, MDA-MB-231 and SKOV3, were cultured at 37^0C and at 5% CO_2 using RPMI-1640, Dulbecco's Modified Eagle's medium (DMEM) and McCoy's 5A medium respectively, supplemented with 10% fetal bovine serum. When the cells were about 75 % confluent in 75 cm^2 flasks they were trypsinized with trypsin-EDTA, counted, and plated in 96-well plates with round bottom at a density of 10^3 cells/well, in a final volume of 100 µL. After 7 days of incubation in a 5% CO_2 humidified incubator at 37 °C plates were treated with the same solutions/complexes of CAI presented above. Each assay was done at least in triplicate. After 24 h incubation, cells are treated with 10% WST-8 in media. The plate was stored in the incubator for 4 h and the plate was subsequently read for absorbance at 450 nm with a reference at 650 nm. Data was reported as the average of three experiments. Statistical comparisons were performed by analysis of variance (ANOVA) with Dennett's multiple comparison test using GraphPad Prism 8, where *P < 0.05, **P < 0.01 and ***P < 0.001.

CA IX profiling using western blotting

The HT-29, NCI-H23, MDA-MB231 and SKOV-3 cell lines were screened for the expression of carbonic anhydrase IX in 2D and 3D cell culture, under normoxic and hypoxic conditions. Cells were cultured in 60 mm petri dishes at a density of 10^6 cells under normoxic and hypoxic conditions. The hypoxic conditions were induced as described above, by placing the cells into a hypoxic chamber purged with hypoxia gas mixture containing 1% oxygen for 24 h. The chamber was placed in a 37°C incubator. For normoxic conditions cells were kept in regular incubator for 24 h. The next day, all cells were harvested, pelleted and washed with phosphate buffer saline (PBS). Cells were then lysed with RIPA buffer containing protease inhibitors and lysates were collected and stored at -20°C. Total protein concentration was determined using bicinchoninic acid method (BCA). Cells were also cultured in rounded bottom 96 well plates at a density of 1000 cells/well and were placed in the incubator for 1-2 week to grow into tumor spheroids. After the spheroids were fully developed, they were harvested and lysed as mentioned previously. Western Blot analysis was performed as described.[19] Briefly, cell lysate samples were loaded onto 10% SDS-PAGE precast gels (Bio-rad, 456-8034) and separation was done at 150 V for 2 h. Gels were transblotted onto nitrocellulose membranes for 30 min and membranes were blocked using blocking buffer followed by incubation with a specific primary mouse monoclonal antibody for CA IX (M75, Bioscience Slovakia) at 4°C overnight. After washing, membranes were incubated with anti-mouse IgG IRDye800CW secondary antibody (Rockland) for 1 h at room temperature. Finally, membranes were detected using an Odyssey image system (Li-Cor, Lincoln NE). Beta actin was used as a control and was detected using a mouse

monoclonal beta actin antibody (Genetex) binding followed by detection with the same IgG IRDye800CW secondary antibody.

Determination of thermal properties by DSC

DSC thermograms were recorded using a Q200 Differential Scanning Calorimeter (TA instrument, New Castle, DE). Each sample was prepared by placing 3-5 mg of compound in a Tzero sample pan. The sample pan was then closed with Tzero lid and placed onto the sample cell. DSC curves were obtained in the temperature range of -30°C and 170°C at a heating rate of 5°C/min for several heating and cooling cycles. Data was processed using the Universal Analysis 2000 software package provided with the DSC machine.

CHAPTER 6

NEW MULTI-LIGAND TARGETED NANOPLATFORMS FOR DOXORUBICIN DELIVERY: LIGAND DESIGN, SYNTHESIS AND CHARACTERIZATION

In this chapter our goal was to design, synthesize and characterize CA inhibitor conjugates and doxorubicin conjugates required towards the development and optimization of a gold nanoplatform targeting carbonic anhydrase IX (CA IX) epitope, which is overexpressed in many hypoxic tumor cells versus normal tissues.

Targeting of the gold nanoplatform was achieved through Au-compatible oligo and polyethylene glycol-conjugated carbonic anhydrase inhibitor ligands (CAI), while loading of doxorubicin (Dox) was achieved using Au-compatible doxorubicin conjugates bearing either an amide or a pH sensitive hydrazone linker. This gold nanoplatform was intended to selectively deliver chemotherapeutic drug doxorubicin to hypoxic tumors overexpressing CA IX in a controlled release fashion.

Our working hypothesis was that the PEGylated 1,3,4-thiadiazole sulfonamide can be engineered for anchoring onto gold nanoparticle surface, with simultaneous decoration with doxorubicin conjugates towards targeting CA IX to enhance the selective delivery of doxorubin into the CA IX overexpressing hypoxic tumors. This nanoplatform was expected to increase the therapeutic activity of the drug while minimizing the hypoxia induced chemoresistance and the systemic side effects associated with IV administration of free drug, doxorubicin.

Background and design approach

As discussed in the Introduction chapter (Chapter 3), CA IX is over-expressed in many tumor cells such as breast [78], colorectal [79], ovarian [82], bladder [84], head and neck [85], cervical, brain [88], pancreatic [89] and renal cancer [90], while its normal expression in the human body is limited to the epithelium of stomach, duodenum and upper small intestine. This makes CA IX a particularly appealing epitope to target by anticancer delivery systems [2, 75]. Importantly, CA IX is a dimeric membrane-bound CA isozyme which works in tandem with cytosolic isozymes, especially CA II, to facilitate the efficient transport of glycolytic protons from cytoplasm to exterior of the cell [2, 72, 75]. Thus, it makes the extracellular pH slightly acidic (pH = 6.8) [2, 72]. Acidification of external milieu protonates the basic chemotherapeutic drugs and prevents them from accessing the hypoxic tumor, contributing to tumor resistance to chemotherapy [245]. Therefore, inhibition of CA IX was explored for the detection, imaging and the treatment of hypoxic solid tumors [2, 92].

Focusing on the delivery platform, over the last decade, gold nanoparticles (Au NPs) have emerged as a solid and versatile multi-functional nanotechnology platform for different medical purposes which include detection, imaging and delivery of cancer chemotherapeutic agents [120, 121]. A combination of physical, chemical, optical and electronic properties along with a biocompatibility unique from other delivery nanotechnologies made Au NPs one of the most employed DDSs for delivery of chemotherapeutic agents having low solubility and poor pharmacokinetics. Moreover, gold nanoparticles can be synthesized in large scale quite reliably in a variety of shapes and sizes and owing to their large surface area can be functionalized with multiple

ligands simultaneously to achieve the desired nanoDDS, with the opportunity to further optimize the binding affinity for a particular disease type or stage [121, 123]. Au NPs functionalized with multiple ligands can simultanously engage multiple adjacent receptor or enzyme sites, with increasing selectivity in their uptake through multivalent binding [246].

Building on these premises and following the success of small MW sulfonamide CAIs and PEGylated sulfonamide CAIs towards potent and selective inhibition of CA IX [92], we decided to further explore the possibility of using CA IX as a targeting epitope for the development of a gold nanoparticle based drug delivery system. We decided to translate the oligoEG- and PEGylated CAI conjugates into efficient targeting ligands for gold nanoparticle decoration along with chemotherapeutic agent doxorubicin (Dox), in a novel multi-ligand gold nanoplatform designed to selectively release the drug intracellularly, in order to enhance the selective tumor drug uptake and killing.

We initiated our project with the design of CA IX targeting ligands for the efficient surface decoration of gold nanoparticles. The design approach for CA IX targeting ligands is shown in Chart 6.1. A CA IX targeting ligand possess the CA inhibitor warhead, attached to a gold anchoring moiety through either a short EG or long PEG linker (Chart 6.1). As CAI warhead, we have selected the succinyl derivative **90** bearing 2-amino-1,3,4-thiadiazol-5-sulfonamide warhead that proved to be an efficient CAI pharmacophore in many CA inhibition studies [57, 58, 72, 92], which binds to the catalytically active Zn ion with high affinity within the active site of CA.

On the other hand, Au NPs are often decorated with surface molecules (ligands) that stabilize them against coalescence. An efficient ligand exchange can be performed

with the particle's capping material to further increase the stability of the functionalized particles in physiological environments and to add targeting. Studies revealed that biocompatible polymers such as PEG and oligoethylene glycol can be commonly employed to minimize the non-specific adsorption of other biomaterial on the gold nanoparticle surface and to enhance the particle stability in high-ionic strength environments such as in physiological fluids [247]. These polymers were also found to decrease immunogenic responses and minimize the recognition of the AuNPs by macrophages and the reticuloendothelial system (RES) [121, 247]. PEGylation was found to increase circulatory half-life of gold nanoparticles as long as ~51 hours [247]. Therefore, we decided to employ a short oligoethylene glycol and long polyethyleneglycol 2000 (PEG 2000) onto the surface of our Au NPs on which to attach CAI warheads. In terms of warhead, we opted for the 2-amino-1,3,4-thiadiazole-2-sulfonamide warhead, connected to the oligo/polyethylene glycol moieties via a succinyl linker. These type of conjugates were proved recently to have nanomolar potency against CA IX and to be able to efficiently kill the hypoxic CA IX-expressing tumor cells in a very recent comprehensive study from our team [92].

From the various method of gold nanoparticles synthesis, we decided to employ the classical Turkevitch method, where a solution of tetrachloroauric acid ($HAuCl_4$) is reduced with sodium citrate to yield colloidal gold nanoparticles that are stabilized electrostatically by a layer of citrate ions [248].

A large variety of linkers are available for anchoring of biomolecules/drugs onto gold nanoparticles. The most employed functional groups for covalent attachment of gold nanoparticles with different biomolecules and biopolymers are thiols/thiolates, dithiols,

carboxylates and amines. Gold-sulfur bonds are fairly robust (~40 kcal mol^{-1}) [249], and quite stronger, compared to both gold-nitrogen bonds (~8 kcal mol^{-1}) [250] and gold-carboxylates associations (~2 kcal mol^{-1}) [250]. Thus, citrate capped gold nanoparticles are easily functionalized with thiol or dithiol derivatives through surface ligand exchange. For these reasons, we have decided to explore several thiol/dithiol containing gold anchoring linkers such as lipoic acid, thioglycolic acid and 3,3'-dithiodipropinic acid (Chart 6.1).

From these three linkers, we have started with a lipoic acid (LA) anchor, which contains a 1,2-dithiacyclopentane moiety that can readily attach to gold surface through its sulfur atoms and that was used extensively in anchoring various materials on Au surface, including CA inhibitors and activators [125, 126, 251].

We designed two targeting ligands **103** and **104**, in which succinylated 2-amino-1,3,4-thiadiazole-2-sulfonamide CAI warhead was conjugated to lipoic acid (LA) gold anchoring moiety. We used either a short linker having 3 ethylene glycol (EG) units or a long linker, having 45 EG units respectively, to connect the LA gold anchoring unit to the CAI warhead (Chart 6.1). It was expected that the linkers would contribute differently to the stabilization of the Au nanoparticles post-decoration with ligands **103** and **104** [252-254]. A non-targeting ligand **105** was also designed where mPEG 2000 was only conjugated with lipoic acid, to be used as inert control (non-targeting) surface ligand.

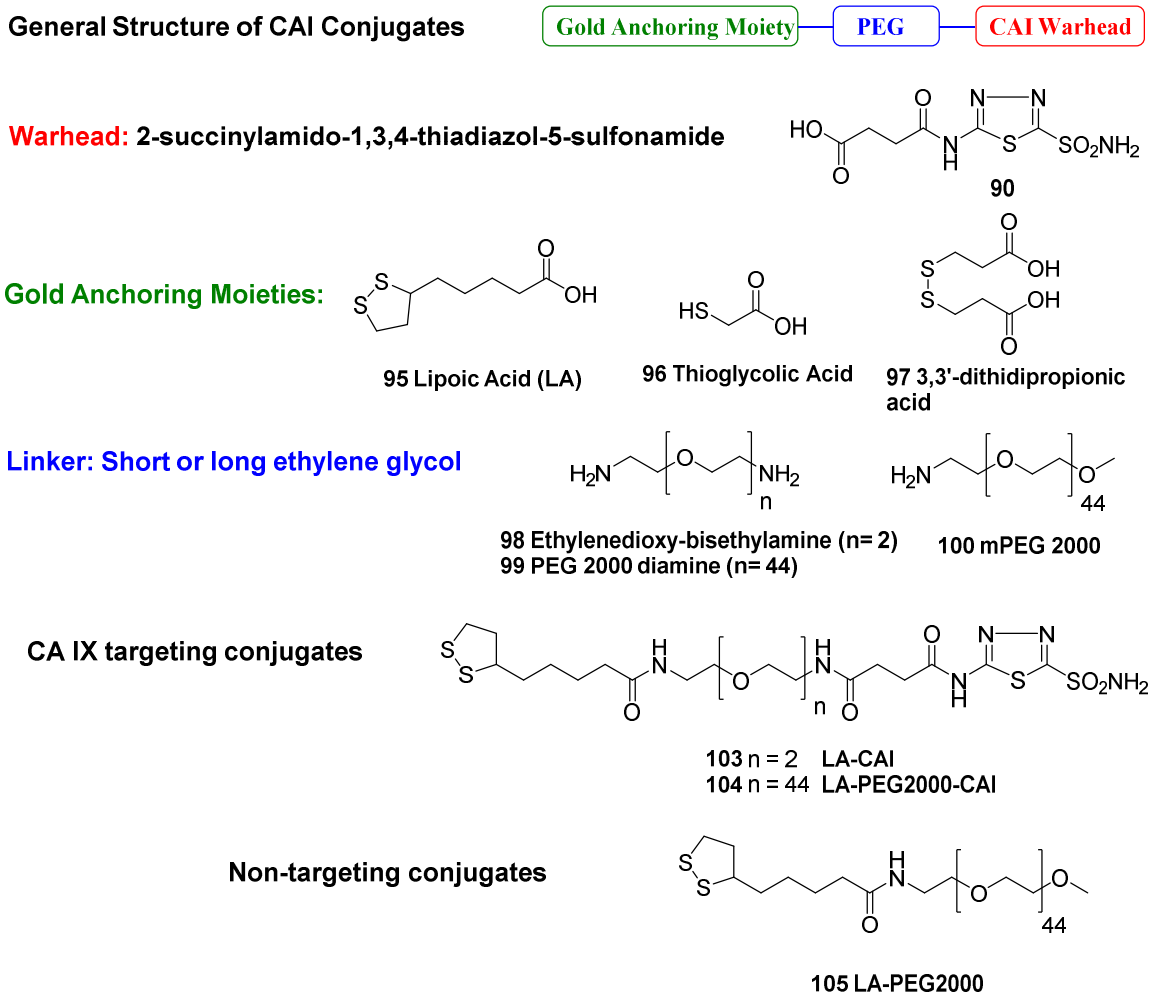

Chart 6.1 Design elements of the CAI conjugates, and designed targeting conjugates and non-targeting conjugates

Results and Discussion

Synthesis of carbonic anhydrase inhibitor-ligands

A convergent strategy was chosen for the synthesis of both CAI conjugates. Thus, the synthesis of both compounds started from succinyl derivative **90**, readily available through the condensation of 2-amino-1,3,4-thiadiazole-5-sulfonamide **61** with succinic

anhydride [92]. Briefly, the carboxylic acid moiety of succinyl aminosulfonamide **90** was activated with 2-chloro-4,6-dimethoxy-1,3,5-triazine (CDMT)/N-methylmorpholine (NMM) and reacted with 1,8-diamino-3,6-dioxahexane **98** or with $H_2NPEG_{2k}NH_2$ **99**, in DMF, at low temperature (Scheme 6.1).

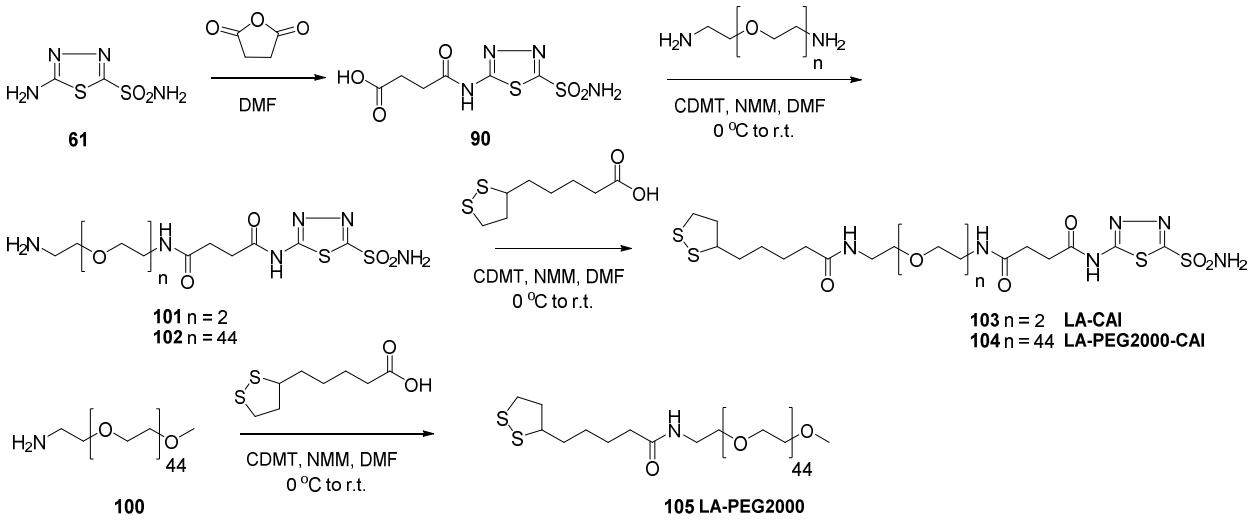

Scheme 6.1 Synthesis of CA inhibitor ligands **103** and **104**, bearing the 2-succinylamido-1,3,4,-thiadiazole-5-sulfonamide pharmacophore attached to lipoic acid anchoring moieties via either a short or long ethylene glycol linker. An amino-PEG lipoic acid conjugate **105** (without the CAI pharmacophore) was also synthesized to be used in control experiments.

The mono-substituted products **101** and **102** were purified from disubstituted side-products via flash chromatography and were subsequently reacted with CDMT/NMM activated lipoic acid in DMF to generate the final CAI ligands **103** and **104** in pure form, which were characterized by standard techniques. A lipoic acid-PEG2000 conjugate (LA-PEG2000) **105**, devoid of the CAI warhead, was also synthesized as an inert conjugate to

be used in control formulations via a similar synthetic strategy involving the activation of lipoic acid with CDMT/NMM and subsequent reaction with H_2N-PEG2000OCH_3 **100** in DMF (Scheme 6.1).

Au NPs synthesis and decoration with thiol-containing ligands

Synthesis of gold nanoparticles, functionalization, determination of cellular uptake of functionalized gold nanoparticles and cytotoxicity studies were done by Dr. Ahmed M. Shabana. Briefly, gold nanoparticles were synthesized by Turkevich method through the reduction of $HAuCl_4$ with citrate at high temperature and were fully characterized [255, 256]. For functionalization, 100 µL of synthesized citrate capped gold nanoparticles were treated with predetermined volume (30 µL) of stock solutions (0.02 M) of different ligands such as lipoic acid (LA), lipoic acid-CAI (LA-CAI), lipoic acid-PEG2000 (LA-PEG2000) and lipoic acid-PEG2000-CAI (LA-PEG2000-CAI) [257, 258]. After treatment, all the samples were sonicated for 5 min then allowed to sit in the dark for 24 h. All the samples were subsequently filtered through 0.22 µm membrane filter and centrifuged at 10000 rpm for 15 min in order to remove excess ligand. The resulted functionalized Au NPs were resuspend in DI water and cleaning was repeated one more time, leaving the Au NPs into a final volume of 100 µL DI water. The concentration of the functionalized Au NPs was determined via ICP-OES using a calibration curve made with standards of known gold concentration. The presence of CAI ligands on the surface of functionalized Au NPs was confirmed by 4-nitrophenylacetate assay [16, 57], revealed the efficient inhibition of CA with the CAI-decorated Au NPs. Au NPs that do not have the CA targeting ligands on their surface did not show any CA inhibition [257, 258].

The uptake of the CAI-decorated Au NPs was studied on HT-29 cancer cell lines that significantly overexpress CA IX under hypoxic conditions compare to normoxic conditions [92, 259], by quantitatively using ICP-OES technique as well as qualitatively through silver staining of Au NPs internalized by tumor cells. These cellular uptake studies revealed that gold nanoparticles functionalized with lipoic acid (Au NPs-LA) were uptaken by HT-29 cells non-specifically under both normoxic and hypoxic conditions [257, 258]. Introduction of PEG on PEGylated Au NPs (Au NPs-LA-PEG2000) was found to significantly diminish the cellular uptake in both normoxic and hypoxic conditions due to the steric stabilization of PEG2000, which reduces non-specific uptake and interactions with any proteins and receptors [260].

Importantly, introduction of CAI ligands on the surface of PEGylated Au NPs (Au NPs-LA-PEG2000-CAI), triggered selective uptake and internalization by HT-29 cells, proportionally with the expression of CA IX epitope. Thus AuNPs-LA-PEG2000-CAI displayed significantly higher cell uptake under hypoxic conditions, where CA IX is over-expressed, as compared to normoxic conditions [141, 261]. The AuNPs-LA-PEG2000-CAI were clearly more selective for CA IX-expressing, hypoxic HT-29 cells than the particles functionalized with short chain ethylene glycol ligands AuNPs-LA-CAI. This difference in cellular uptake further emphasized the importance of using the long PEG spacer for eliminating non-specific uptake and optimum interaction with CA IX target.

After confirming the cellular uptake of Au NPs, we determined the cytotoxicity of all the functionalized gold nanoparticle formulatuions on the same HT-29 colon cancer cell line following a 24 h treatment period under normoxic or hypoxic conditions [257,

258]. Naked Au NPs did not show any significant toxicity under normoxic conditions, irrespective of the type of Au NPs or their concentration. Under hypoxic conditions, only Au NPs decorated with PEG2000-CAI ligands (Au NPs-LA-PEG2000-CAI) were found to kill HT-29 cells in a statistically significant manner but only at the highest concentration of 100 μM, in perfect match with the previous published study with CAI-decorated Au NPs platforms [141]. We postulate that this is due to the efficient inhibition of the overexpressed CA IX by the CAI targeting moiety of these Au NPs, similarly to our CA polymeric inhibitors from which our targeting ligands derived [92]. These findings prompted us to our CAI decorated PEGylated gold nanoplatform (Au NPs-LA-PEG2000-CAI) as a platform for the delivery of doxorubicin, by combining the excellent CA IX targeting capabilities of Au NPs-LA-PEG2000-CAI with the high toxicity of doxorubicin. Therefore, we initiated a synthetic program to identify the most efficient ways to load doxorubicin on the Au NPs-LA-PEG2000-CAI nanocarriers.

Design, synthesis of doxorubicin conjugates, and loading of them on Au nanoplatform

We designed a series of doxorubicin conjugates based on general structure shown in Chart 6.2. In this design, we conjugated the doxorubicin with different gold nanoparticle anchoring ligands such as lipoic acid (LA) or 3,3'-dithiodipropionic acid (DTDP), dithiodipropionic acid hydrazide, thioglycolic acid and thioglycolic acid hydrazide via either amide linker or hydrolysable hydrazine linker.

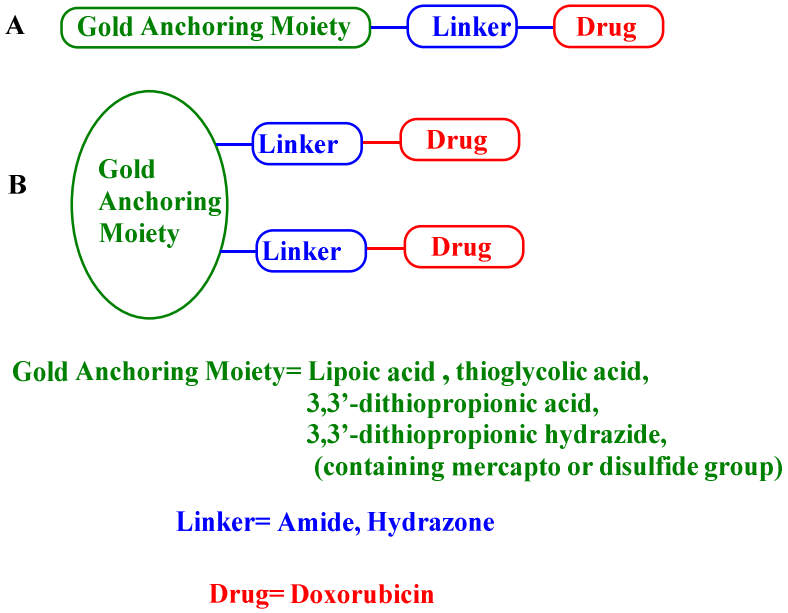

Chart 6.2 Cartoon depicting the main design elements of the doxorubicin conjugates

We started our investigations by synthesizing conjugates in which the drug was attached through a stable amide (AM) linker. We first synthesized the DOX-lipoic acid amide conjugate (Dox-AM-LA) **107** through the coupling of doxorubicin with lipoic acid (Scheme 6.2). Briefly, the carboxylic groups of the lipoic acid **95** was activated with 2-chloro-4,6-dimethoxy-1,3,5-triazine (CDMT)/N-methylmorpholine (NMM) and subsequently reacted with doxorubicin in dry DMF, at room temperature to yield the Dox-AM-LA **107** conjugate. The reaction was quenched with 10% citric acid solution and the useful crude conjugate were extracted with DCM, and finally purified with flash chromatography. With this conjugate in hand, we proceeded towards assessing different strategies to maximize the loading of doxorubicin conjugates on Au NPs, while preserving their physicochemical properties and colloidal stability.

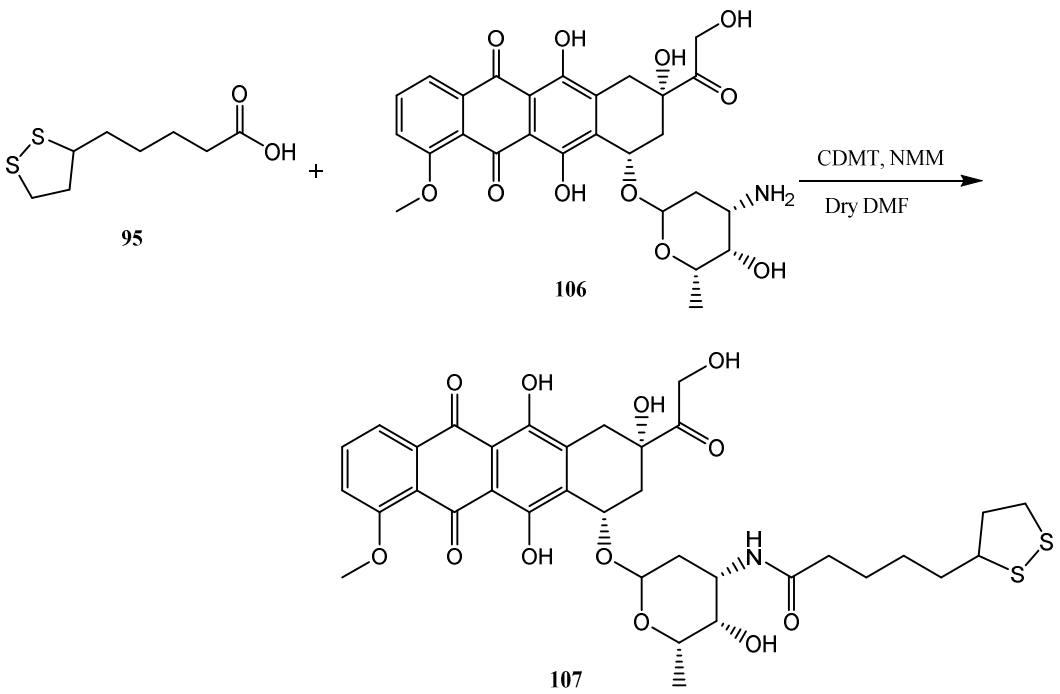

Scheme 6.2 Synthesis of DOX-lipoic acid amide conjugate (Dox-AM-LA)

To our surprise, conjugate LA-AM-Dox proved to have a poor water solubility and failed to generate stable gold nanoparticles. Threfore we replaced the LA anchoring group with the dithiodipropionic (DTDP) acid gold-binding moiety, synthesizing the doxorubicin-dithiodipropionic acid amide conjugate (Dox-AM-DTDP) **108**, according to Scheme 6.3, through the CDMT and NMM based amide coupling of dithiodipropionic acid and doxorubicin. The pure conjugate was characterized by standard analytical methods and utilized for subsequent studies.

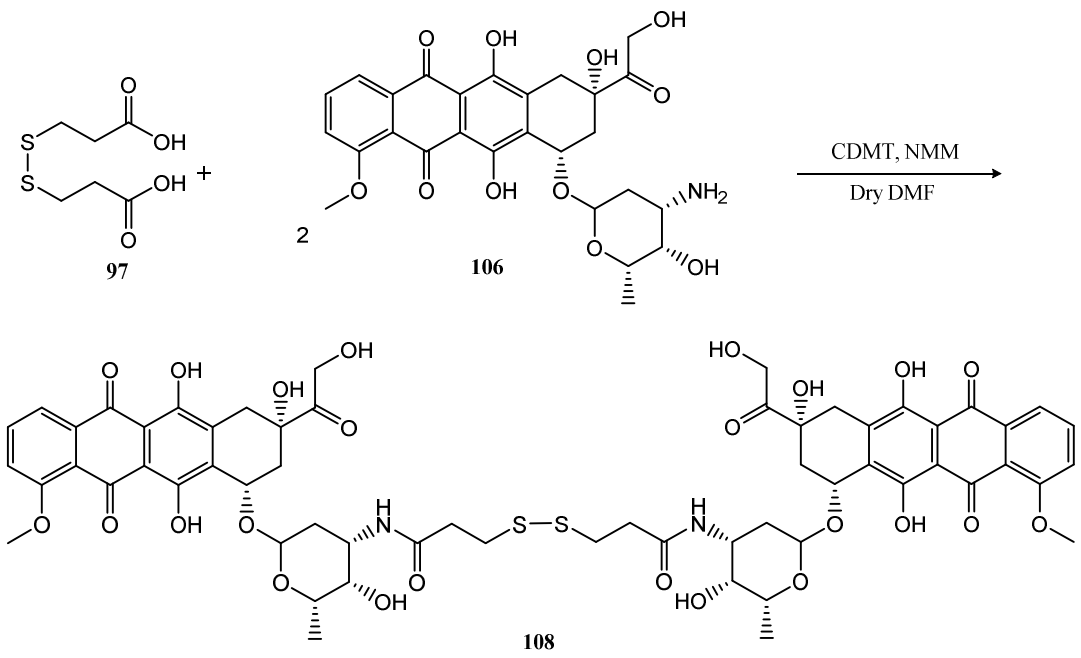

Scheme 6.3 Synthesis of Doxorubicin-dithiodipropionic acid amide conjugate (Dox-AM-DTDP)

This time the solubility of DTDP-doxorubicin amide conjugate (DTDP-AM-Dox) in water/ethanol mixtures was found to be quite good and we were successful in generating gold nanoparticles Dox-AM-DTDP @ Au NPs-LA-PEG2000 (non-targeted) and Dox-AM-DTDP @ Au NPs-LA-PEG2000-CAI (CAI-targeted) after an optimization study [257, 258] .

We have also designed similar ligands containing a pH-sensitive hydrazone linker, which was used successfully by other groups for the similar delivery purposes [135, 262, 263]. The hydrazone linker was opted to be generated either in situ, by reacting Au NPs pre-decorated with hydrazide-containing ligands with excess Dox in solution, or was pre-synthesized and subsequently added onto Au NPs. We have employed the high solubility dithiodipropionic acid (DTDP) as Au anchoring ligand, as

optimized in the previous section. Two DTDP ligands were made for this purpose, DTDP-hydrazide (DTDP-HZD) **110** and the Dox hydrazone conjugate with DTDP (DTDP-HZN-Dox) **111**, following the reactions depicted in Scheme 6.4. The starting 3,3'-dithiodipropinic acid **97** was esterified with ethanol in presence of toluenesulfonic acid and the resulted bis- diethyl ester **109** was subsequently treated with excess hydrazine hydrate to produce DTDP-hydrazide (DTDP-HZD). Condensation of DTDP-hydrazide (DTDP-HZD) **110** with doxorubicin hydrochloride **106** yielded Dox hydrazone conjugate (DTDP-HZN-Dox) **111** (Scheme 6.4).

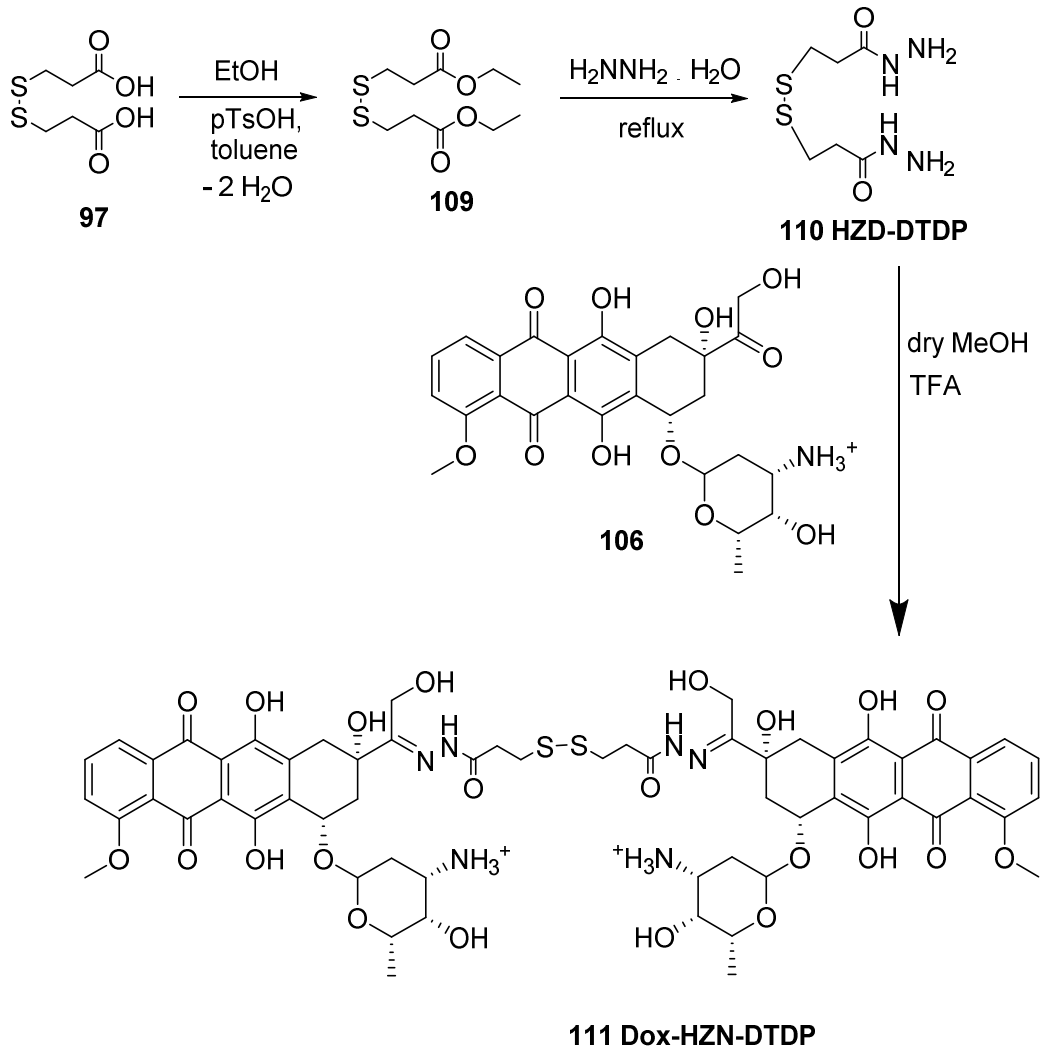

Scheme 6.4 Synthesis of dithiodipropionic acid hydrazide (HZD-DTDP) and doxorubicin dithiodipropionic acid hydrazone conjugate (Dox-HZN-DTDP)

Both ligands were installed on Au NPs together with the PEGylated ones using an optimized simultaneous ligand exchange strategy pre-optimized by A. Shabana [257, 258]. After successful validation of Dox loading onto the surface of PEGylated Au NPs, we observed that the anchoring of Dox onto Au NPs results in quenching of Dox fluorescence signal [129, 262]. However, when the hydrazone linker is cleaved (at pH <

5.5) and Dox is released, the fluorescence signal is retrieved and intensifies as more drug is being released.

We have validated the pH dependent cleavage of the hydrazone linker and the subsequent release of Dox, through the incubation of targeted formulation Dox-HZN-DTDP @ Au NPs-LA-PEG2000-CAI **(THZN)** and non-targeted formulation Dox-HZN-DTDP @ Au NPs-LA-PEG2000 **(NTHZN)** in phosphate buffer saline (PBS) at either pH 5.5 or pH 7.4, over a time period of 24 h. We revealed that the fluorescence intensity of Dox was found to increase quite rapidly with time for both NTHZN and THZN at pH 5.5, while at pH 7.4, no significant increase in fluorescence intensity was observed for both formulations over the entire period of 24 h [257, 258].

Dr. Ahmed Shabana re-assessed the cytotoxic effects of the new doxorubicin loaded Au NPs, having the Dox conjugated to the Au anchoring moiety either via an amide group (Dox-AM-DTDP) or via a hydrazone group (Dox-HZN-DTDP) on the same HT-29 cell model expressing CA IX, under normoxic and hypoxic conditions [257, 258].

The Dox loaded formulations bearing the drug linked via an amide group did not show any additional cytotoxic effects to their non-targeted or CA IX targeted platforms. On the other hand, the Dox formulations bearing the pH labile hydrazone group showed an improved cytotoxicity compared with their unloaded delivery platforms under both normoxic and hypoxic conditions. This was due to the fast cleavage of acid sensitive hydrazone linker in the late endosome following the uptake of the nanoparticles, thus liberating free Dox in large amounts, which killed the cells in a significant manner. Interestingly, the toxicity of the **(NTHZN)** was reduced under hypoxic conditions versus normoxic ones, similarly to the free Dox ($P < 0.05$). Most importantly, the CA IX

targeted **(THZN)** formulations showed superior cytotoxic effects as compared to **NTHZN** formulations. We postulate that this is due to the contribution of CA IX in facilitating the uptake and the internalization of the nanoparticles.

Conclusions

We designed, synthesized and characterized compatible CAI- and Dox- ligands for dual functionalization of gold nanoparticles. We were successful in decorating AuNPs efficiently after several optimization steps, with both good targeting ligand density and optimum drug loading, while preserving colloidal stability of the gold nanoplatform.

Our optimized, CA IX targeted Dox-HZN-DTDP @ Au NPs-LA-PEG2000-CAI (THZN) nanoplatform bearing the pH-sensitive hydrazone doxorubicin conjugate, was found to be very efficient towards killing HT-29 tumor cells especially under hypoxic conditions, reducing the hypoxia-induced chemoresistance, and displaying a better tumor penetration and intratumoral doxorubicin delivery as compared to free Doxorubicin. These findings revealed the potentiating role of CA IX as a targeting epitome, overexpressed in hypoxia, to enhance the selective uptake of the targeted gold nanoformulations. Thus, recommend our CA IX-targeted gold nanoplatform as a compelling nanosystem technology to enhance the selective delivery of basic chemotherapeutic agents, reduce hypoxia-induced chemoresistance and to maximize tumor killing, with the promise to improve the therapy of solid hypoxic tumors.

Experimental Section

Materials and methods

Materials

The following materials were used as received: succinic anhydride (TCI America, Portland, OR), 2,2`-(ethylenedioxy)-diethylamine (Fluka, St Louis, MO), N-methylmorpholine (TCI America, Portland, OR), 2-chloro-4,6-dimethoxy-1,3,5-triazine (Acros Organics, New Jersey, NJ), H_2N-PEG2000-NH_2 and H_2N-PEG2000-OCH_3 (Laysan Bio, Arab, AL). Other solvents (HPLC quality) were purchased from Fisher Scientific (Pittsburgh, PA), EMD (Gibbstown, NJ), and VWR International (West Chester, PA). Sodium citrate dihydrate, was from Sigma-Aldrich, $HAuCl_4$ trihydrate was from LabChem Inc, Hydrochloric acid 37% and nitric acid 68% were from BDH chemicals, lipoic acid from Alfa Aesar, thiazolyl blue tetrazolium bromide (MTT) from Affymetrix, hydrazine hydrate from Acros Organics, RIPA lysis buffer and NaOH were purchased from Amresco, doxorubicin hydrochloride from TRC Canada, dithiodipropionic acid from Aldrich.

Techniques: Same techniques were employed as described in Chapter 5.

Preparation of CAI ligands

4-oxo-4-((5-sulfamoyl-1,3,4-thiadiazol-2-yl)amino)butanoic acid 90 [92]

In a flame dried 20-mL reaction vial, TDA-NH_2 **61** (0.45 g, 2.5 mmol) was dissolved in 2 mL of DMF. Succinic anhydride (275 mg, 0.275 mmol) was added over it in small portions and the reaction mixture was stirred for 4 days at 25^{o}C. After the

reaction reached completion, DMF was removed by rotavap, then 10 mL of water was added over the mix to dissolve all excess succinic anhydride, and the product precipitated. The precipitate was filtered and rinsed with methanol to remove water. The precipitate was 98% pure (LC-MS). Yield: 83%; mp. 232-236^{o}C; lit.[92] m.p. 232-236^{o}C. ^{1}H-NMR (400 MHz, DMSO-d^{6}, δ, ppm): 13.06 (br s, 1H, -NH), 12.27 (br s, 1H , NH), 8.32 (s, 2H, -SO_2NH_2), 2.76 (t, *J* = 6.5 Hz, 2H, CH_2COOH), 2.60 (t, *J* = 6.5 Hz, 2H, CH_2CONH) ; ^{13}C-NMR (100.6 MHz, DMSO-d^{6}, δ, ppm): 173.3 (CONH), 171.4 (COOH), 164.1 (C_5 TDA), 161.0 (C_2 TDA), 29.9 (-$\underline{C}H_2COOH$), 28.2 (-$\underline{C}H_2CONH$-); LC-MS: $C_6H_8N_4O_5S_2$, exact mass: 280.0; Found: 281.0 (MH^+).

N1-(2-(2-(2-aminoethoxy)ethoxy)ethyl)-N4-(5-sulfamoyl-1,3,4-thiadiazol-2-yl)succinamide 101

In a flame dried 20 mL reaction vial, the succinyl derivative **90** (0.536 g, 1.92 mmol) and 2-chloro-4,6-dimethoxy-1,3,5-triazine (CDMT, 0.37g, 2.11 mmol) were dissolved in 2 mL DMF. The flask was cooled in an ice bath at 0˚C, N-methylmorpholine (NMM, 235 µL, 0.213 g, 2.11 mmol) was added and the reaction mixture was allowed to react at 0˚C for 45 min under nitrogen atmosphere. Ethylenedioxy-bisethylamine **98** (0.312 g, 2.11 mmol, dissolved in 1.5 mL dry DMF) was added to reaction mix in one aliquot. The reaction mixture was stirred at room temperature for two days. The DMF was evaporated via rotavap, under vacuum, and the crude product was absorbed on silica. Flash chromatography was performed with DCM/MeOH gradients, on SiO_2 column. Useful fractions (determined by TLC, performed with DCM/ methanol (80/20 v/v), by

NMR and by LCMS) were grouped and evaporated to dryness to yield 180 mg of crude amine **101**, which was used without further purification in the next step.

Amino-PEG2000-(5-sulfamoyl-1,3,4-thiadiazol-2-yl)succinamide 102

In a flame dried 20 mL reaction vial, the succinyl derivative **90** (0.084 g, 0.3 mmol) and 2-chloro-4,6-dimethoxy-1,3,5-triazine (0.053 g,0.3 mmol) was dissolved in 3 mL DMF. The flask was cooled with an ice bath at 0˚C and N-methylmorpholine (35 μL, 0.031 g, 0.3 mmol) was added. The mix was kept at 0˚C for 45 min under nitrogen, then treated with H_2N-PEG_{2K}-NH_2 **99** (0.500 g, 0.250 mmol, dissolved in 1.5 mL dry DMF). The reaction was subsequently stirred at room temperature for two days. The DMF was evaporated via rotavap under high vacuum, and the crude compound was absorbed on SiO_2. Flash chromatography was performed with $CHCl_3$/MeOH gradients on a SiO_2 column. Useful pure fractions (determined by TLC, performed with DCM/MeOH (75/25 v/v), by NMR and by MALDI) were grouped and evaporated to dryness to yield 327 mg of crude compound, which was used without further purification in the next step.
Yield: 66 %; ^{1}H-NMR (400 MHz, D_2O, δ, ppm): 3.80-3.58 (m, 176 H, 44 -OCH_2CH_2O-), 3.53 (t, J = 5.8 Hz, 4H, -O$\underline{CH_2}CH_2NH$-), 3.31 (t, J = 5.4 Hz, 4H, -$OCH_2\underline{CH_2}NH$-), 2.83 (t, J = 6.6 Hz, 4H, -CO$\underline{CH_2}CH_2CO$-), 2.60 (t, J = 6.6 Hz, 4H, -$OCCH_2\underline{CH_2}CO$-).

N1-(2-(2-(2-(5-(1,2-dithiolan-3-yl)pentanamido)ethoxy)ethoxy)ethyl)-N4-(5-sulfamoyl-1,3,4-thiadiazol-2-yl)succinamide 103

In a flame dried 20 mL reaction vial, lipoic acid **95** (25 mg, 0.145 mmol) and 2-chloro-4,6-dimethoxy-1,3,5-triazine (21 mg, 0.145 mmol) were dissolved in 1 mL DMF.

The flask was cooled in an ice bath at 0˚C and N-methylmorpholine (15 µL, 13 mg, 0.145 mmol) was added. The reaction mixture was kept at 0˚C for 45 minutes under nitrogen, and was subsequently treated with compound **101** (49 mg, 0.12 mmol, dissolved in 1mL dry DMF). The reaction mixture was then stirred at room temperature for two days. The DMF was evaporated via rotavap, under high vacuum, and the crude product was absorbed on silica. Flash chromatography was performed with chloroform and methanol gradients using a 12g Silica column. Useful pure fractions (determined by TLC, performed with DCM/MeOH (80/20), by NMR and by LCMS) were grouped and evaporated to dryness to yield 20 mg of pure compound.

Yield: 27%; ^{1}H-NMR (400 MHz, DMSO-d^{6}, δ, ppm): 11.16 (s, 2H, -CONH-), 8.29 (s, 1H, -SO_2NH_2), 7.99 (t, J = 5.27 Hz, 1H, -CONH-), 7.83 (t, J = 6.08 Hz, -CONH-), 3.55 (m, 4H, 2-NHCH$_2$<u>CH$_2$</u>O-), 3.5 (s, 4H, 2-O<u>CH$_2$CH$_2$</u>O-), 3.39 (t, 4H, 2-NH<u>CH$_2$</u>CH$_2$O-), 3.18 (m, 2H, -S<u>CH$_2$</u>CH$_2$- and 1H, -SCH$_2$<u>CH$_2$</u>-), 2.73 (t, J = 6.8 Hz, 4H, -CO<u>CH$_2$</u>CH$_2$CO-), 2.5 (t, J = 6.8 Hz, 4H, -OCCH$_2$<u>CH$_2$</u>CO-), 2.39 (m, 1H, -S<u>CH</u>CH$_2$-), 2.06 (t, 2H, J = 6.6 Hz, -SCHCH$_2$CH$_2$CH$_2$<u>CH$_2$</u>CO-), 1.84 (m, 1H, -SCH$_2$<u>CH$_2$</u>-), 1.64 (m, 1H, -SCHCH$_2$CH$_2$<u>CH$_2$</u>CH$_2$CO-), 1.51(m, 2H, -SCH<u>CH$_2$</u>CH$_2$CH$_2$CH$_2$CO- and 1H, -SCHCH$_2$CH$_2$<u>CH$_2$</u>CH$_2$CO-), 1.33 (m, 2H, -SCHCH$_2$<u>CH$_2$</u>CH$_2$CH$_2$CO-). LC-MS: $C_{20}H_{34}N_6O_7S_4$, exact mass: 598.14; Found: 599.2 (MH^+); HRMS: $C_{20}H_{34}N_6O_7S_4$, exact mass: 598.1372; found 598.1376.

Lipoylamido-PEG2000-(5-sulfamoyl-1,3,4-thiadiazol-2-yl)succinamide 104

In a flame dried 20 mL reaction vial, lipoic acid **95** (5.12 mg, 0.0251 mmol) and 2-chloro-4,6-dimethoxy-1,3,5-triazine (4.41 mg, 0.0251 mmol) were dissolved in 1 mL DMF. The flask was cooled in an ice bath at 0˚C, then N-methylmorpholine (2.5 µL, 2.25 mg, 0.0251 mmol) was added. The mix was kept at 0˚C for 45 min under nitrogen, then treated with the crude monoconjugate **102** (51.8 mg, 0.023 mmol, dissolved in 1 mL dry DMF). The reaction was subsequently stirred at room temperature for two days. The DMF was evaporated via rotavap, under high vacuum, and the crude product was absorbed on silica. Flash chromatography was performed with $CHCl_3$/MeOH gradients on a SiO_2 column. Useful fractions (determined by TLC, performed with DCM/MeOH (80/20), by NMR and by MALDI) were grouped and evaporated to dryness to yield 21 mg of pure product.

Yield: 37.5%; ^{1}H-NMR (400 MHz, D_2O, δ, ppm): 3.62 (s, 176 H, 44 -OCH_2CH_2O-), 3.32 (m, 2H, -S$\underline{CH_2}CH_2$- and 1H, -$SCH_2\underline{CH_2}$-), 2.88 (t, J = 6.6 Hz, 4H, -CO$\underline{CH_2}CH_2CO$-), 2.62 (t, J = 6.6 Hz, 4H, -$OCCH_2\underline{CH_2}CO$-), 2.44 (m, 1H, -S$\underline{CH}CH_2$-), 2.19 (t, 2H, J = 6.6 Hz, -$SCHCH_2CH_2CH_2\underline{CH_2}CO$-), 1.66 (m, 1H, -$SCHCH_2CH_2\underline{CH_2}CH_2CO$-), 1.55(m, 2H, -S$CH\underline{CH_2}CH_2CH_2CH_2CO$- and 1H, -$SCHCH_2CH_2\underline{CH_2}CH_2CO$-), 1.34 (m, 2H, -$SCHCH_2\underline{CH_2}CH_2CH_2CH_2CO$-). GPC: 96%+, t_R = 15.13 min, PDI = 1.18; MALDI-TOF: $C_{106}H_{206}N_6O_{50}S_4$, exact mass: 2491.3; Found: 2447.4.

Lipoylamido-PEG2000-OMe 105

In a flame dried 20 ml reaction vial, lipoic acid **95** (28.3 mg, 0.1375 mmol) and 2-chloro-4,6-dimethoxy-1,3,5-triazine (24.1mg, 0.1375 mmol) were dissolved in 1 ml

DMF. The flask was cooled in a water-ice bath to 0˚C and N-methylmorpholine (15.3 µL, 13.9 mg, 0.1375 mmol) was added. The homogeneous mixture was allowed to react at 0˚C for 45 min under nitrogen and was subsequently treated dropwise with $CH_3OPEG_{2K}NH_2$ **100** (250 mg, 0.125 mmol) dissolved in 1 mL dry DMF. The reaction was allowed to warm at room temperature and was stirred under inert atmosphere for 2 days. The solvent was evaporated under reduced pressure and the residue was subjected to flash chromatography on SiO_2 using $CHCl_3$/MeOH gradients. Pure fractions (determined by TLC, performed with DCM/MeOH (80/20), by NMR and by MALDI) were grouped and evaporated to dryness to yield 164 mg (63%) conjugate as colorless sticky compound.

^{1}H-NMR (400 MHz, D_2O, δ, ppm): 3.62 (s, 176 H, 44 -OCH_2CH_2O-), 3.32 (m, 2H, -$S\underline{CH_2}CH_2$- and 1H, -$SCH_2\underline{CH_2}$-), 3.29 (s, 3H, CH_3O-), 2.44 (m, 1H, -$S\underline{CH}CH_2$-), 2.19 (t, 2H, J = 6.6 Hz, -$SCHCH_2CH_2CH_2\underline{CH_2}CO$-), 1.66 (m, 1H, -$SCHCH_2CH_2\underline{CH_2}CH_2CO$-), 1.55 (m, 2H, -$SCH\underline{CH_2}CH_2CH_2CH_2CO$- and 1H, -$SCHCH_2CH_2\underline{CH_2}CH_2CO$-), 1.34 (m, 2H, -$SCHCH_2\underline{CH_2}CH_2CH_2CO$-). GPC: 96%+, t_R = 15.21 min, PDI = 1.15; MALDI-TOF: $C_{101}H_{201}NO_{47}S_2$, exact mass: 2244.3; Found: 2288.4.

Synthesis of DOX-lipoic acid amide conjugate (Dox-AM-LA) 107

In a flame dried 20 mL reaction vial, lipoic acid **95** (17 mg, 0.0825 mmol) and 2-Chloro-4,6-dimethoxy-1,3,5-triazine (15 mg, 0.0825 mmol) were dissolved in 2 mL DMF. The flask was coled in ice bath at 0°C and N-methylmorpholine (9.2 µL, 8.5 mg, 0.0825 mmol) was added dropwise. The reaction mixture was stirred at 0°C for 45 min under nitrogen and subsequently treated with a solution of Doxorubicin hydrochloride

106 (43 mg, 0.0725 mmol) and N-methylmorpholine (9.2 µL, 8.5 mg, 0.0825 mmol) dissolved in 2 mL DMF. Stirring was continued for two days at 25°C, then the reaction was quenched with 10% citric acid solution (15 mL) and the useful product was extracted with DCM (5 times X 15 mL). The DCM layer was dried on anhydrous Na_2SO_4 and evaporated to dryness to yield the crude product. The crude conjugate was adsorbed onto silicagel and flash chromatography was performed with DCM/MeOH gradients. Useful fractions (determined by TLC, in DCM: MeOH (95:5), by LCMS and NMR) were grouped and evaporated to dryness to yield the purified product (35 mg, yield 66%).

Dox-AM-LA conjugate. Red amorphous solid, ^{1}H-NMR (400 MHz, DMSO-d^6, δ, ppm): 14.01 (s, 1H, 6-OH), 13.25 (s, 1H, 11-OH), 7.89 (dd, J = 6, 2.4 Hz, 2H, H2, H3), 7.62 (dd, J = 6, 3.6 Hz, 1H, H1), 7.49 (d, J = 7.6 Hz, 1H, 3'-NH), 5.43 (br s, 1H, 14-OH), 5.22 (td, J= 19.7, 3 Hz, 4'-OH), 4.92 (t, J= 4.8 Hz, 1H, H7), 4.84 (t, J= 6 Hz, 1H, H4', 4.72 (d, J = 6 Hz, 1H, H1'), 4.58 (d, J= 6 Hz, 2H, H14), 4.18-4.15 (m, 1H, H5'), 4.09 (q, J=5.3 Hz, 1H, H3'), 3.97 (s, 3H, OCH_3), 3.58-3.51 (m, 1H, H6'), 3.23-3.11 (m, 2H, H5'), 2.95 (d, 1H, H10), 2.89 (brs, 1H, H10), 2.40-2.32 (m, 1H, H8"), 2.18-2.03 (m, 4H, H8, H2"), 1.86-1.79 (m, 1H, H8"), 1.65-1.59 (m, 1H, H7"), 1.56-1.42 (m, 4H, H3", H2'), 1.30-1.23 (m, 4H, H4", H7", H9), 1.13 (d, J = 6.5 Hz, 3H, H6'). ^{13}C-NMR (100.6 MHz, DMSO-d^6, δ, ppm): 213.7, 186.5, 186.4, 171.3, 160.7, 156.1, 154.5, 136.2, 135.5, 134.6, 134.0, 120.0, 119.7, 118.9, 110.7, 110.6, 100.4, 74.9, 69.9, 68.1, 66.7, 63.6, 56.5, 56.0, 48.6, 44.8, 38.0, 36.6, 35.1, 34.1, 32.1, 29.8, 29.0, 28.2, 25.0, 17.0 LC-MS (>97%): $C_{35}H_{41}NO_{12}S_2$, exact mass: 731.2; Found: 732.2 (MH^+); HRMS: $C_{35}H_{41}NO_{12}S_2$, exact mass: 731.2070; found 731.2076.

Synthesis of Doxorubicin-dithiodipropionic acid amide conjugate (Dox-AM-DTDP) 108

In a flame dried 20 mL reaction vial, 3,3'-dithiodipropionic acid **97** (4.5 mg, 0.0201 mmol) and 2-chloro-4,6-dimethoxy-1,3,5-triazine (7.5 mg, 0.04125 mmol) were dissolved in 2 mL DMF. The flask cooled at 0 ^{o}C with an ice bath and N-methylmorpholine (4.7 μL, 4.25 mg, 0.04125 mmol) was added dropwise. The reaction mixture was stirred at 0°C for 45 min under nitrogen and was subsequently treated with a solution obtained by dissolving Doxorubicin hydrochloride **106** (23 mg, 0.04125 mmol) and N-methylmorpholine (4.7 μL, 4.25 mg, 0.04125 mmol) in 2 mL DMF. Stirring was continued for two days at 25^{o}C. The reaction was quenched through dilution with 10% citric acid solution (15 mL) and extracted with DCM (5 times x 15 mL). The DCM layer was dried on anhydrous Na_2SO_4, then evaporated to dryness to yield the crude product. The crude conjugate was absorbed onto SiO_2 and flash chromatography was performed with DCM/MeOH gradients. Useful fractions (determined by TLC, in DCM: MeOH (95:5), by LCMS and NMR) were grouped and evaporated to dryness to yield the purified product (17 mg, yield 67 %).

Dox-AM-DTDP. Red amorphous solid. ^{1}H-NMR (400 MHz, DMSO-d^{6}, δ, ppm): 14.02 (brs, 2H, 6-OH), 13.25 (brs, 2H, 11-OH), 7.90 (br d, J = 6, 2.4 Hz, 4H, H2, H3), 7.72 (br d, J = 6, 3.6 Hz, 2H, H1), 7.64 (br t, J = 7.6 Hz, 1H, 3'-NH), 5.45 (brs, 2H, 14-OH), 5.22 (brs, 3H), 5.09-4.80 (m, 3H), 4.62-4.52 (m, 5H), 2.97 (d, 5H), 2.89-2.81 (m, 14H), 262-2.54 (m, 9H), 2.22-2.09 (m, 4H), 1.87-1.75 (m, 2H), 1.44-1.41 (m, 2H), 1.23 (brs, 2H), 1.12 (d, J = 6.5 Hz, 6H, H6′). ^{13}C-NMR (100.6 MHz, DMSO-d^{6}, δ, ppm): 213.7, 186.5, 186.5, 172.6, 169.3, 160.8, 156.1, 154.5, 136.2, 135.5, 134.7, 134.1, 120.0,

119.7, 119.0, 110.8, 110.6, 100.3, 74.9, 69.9, 68.0, 66.7, 63.6, 56.6, 45.0, 40.1, 36.7, 34.9, 34.0, 33.6, 33.1, 33.0, 32.1, 29.7, 17.0. LC-MS (>96%): $C_{60}H_{64}N_2O_{24}S_2$, exact mass: 1260.3; Found: 631.2 ($MH_2^{/2+}$); MALDI-TOF: $C_{60}H_{64}N_2O_{24}S_2$, exact mass: 1260.3; Found 1260.3.

Dithiodipropionic acid hydrazide (HZD-DTDP) and Dox-dithiodipropionic hydrazone conjugate (Dox-HZN-DTDP)– adapted from reference [264]

In a flame dried 50 mL round bottom flask, 3,3'-dithiodipropionic acid **97** (5 g, 23.8 mmol) was suspended in ethanol (11.05 g, 240 mmol) and p-toluenesulfonic acid (0.2 g, 1.05 mmol) was added slowly. Then toluene (30 mL) was added over it. The reaction mixture was refluxed for 24 h using a Dean–Stark trap, then it was evaporated to dryness to yield crude ethyl dithiodipropionate **109** followed by washing with $NaHCO_3$ solution and water to pH 7-8. Evaporation to dryness, followed by crystallization from cold ethanol yielded the pure product.

Ethyl dithiodipropionate 109. ^{1}H-NMR (400 MHz, DMSO-d^6, δ, ppm): 4.16-4.01 (m, 4H), 2.98-2.85 (m, 4H), 2.76-2.63 (m, 4H), 1.26-1.17 (m, 6H). ^{13}C-NMR (100.6 MHz, DMSO-d^6, δ, ppm): 171.0, 60.1, 33.4, 32.6, 13.0.

In the subsequent reaction, ethyl dithiodipropionate **109** (4 g, 15 mmol) was dissolved in ethanol (20 mL) in a 50 mL round bottom flask and hydrazine hydrate (4.8 g, 96 mmol) was added dropwise, under stirring. The reaction mixture was refluxed overnight at 90°C, then cooled at room temperature and bulk solvent evaporated under

vacuum. The obtained crude HZD-DTDP **110** was recrystallized from (5% v/v) ethanol–water solution three times to yield pure HZD-DTDP.

Dithiodipropionic acid hydrazide (HZD-DTDP) 110 Yield: 60%, mp 128–129°C. Lit. mp 131-132°C. ^{1}H-NMR (400 MHz, DMSO-d^{6}, δ, ppm): 9.1 (s, -NH), 4.2 (s, -NH_2), 2.89 (t, J= 7.2 Hz, -SCH_2CH_2), 2.41 (t, J= 7.2 Hz, -SCH_2CH_2). ^{13}C-NMR (100.6 MHz, DMSO-d^{6}, δ, ppm): 169.4, 33.5, 33.2. LC-MS (>99%): $C_6H_{14}N_4O_2S_2$, exact mass: 238.1; Found: 239.2 (MH^+).

Subsequently, in a flame dried 20 mL reaction vial, doxorubicin hydrochloride **106** (25 mg, 0.0431 mmol) was dissolved in dry MeOH (5 mL) and treated dropwise, under stirring with a solution obtained by dissolving dithiodipropionic hydrazide **110** (5 mg, 0.201 mmol) in dry methanol (3 mL). Trifluoroacetic acid (10 µL) was subsequently added and the reaction mixture was stirred under inert atmosphere for 2 days. Evaporation of solvent yielded the product **111** in pure form, as assessed by TLC and LC-MS.

Dox-HZN-DTDP 111. Red solid, ^{1}H-NMR (400 MHz, DMSO-d^{6}, δ, ppm): 13.93 (brs, 2H, 6-OH), 13.12 (brs, 2H, 11-OH), 10.40 (s, 2H, 1”-NH) 7.64-7.62 (m, 2H, H1), 7.61-7.58 (m, 4H, H2, H3), 5.25 (brs, 2H, 14-OH), 5.17 (s, 2H, 4’-OH), 4.92 (brs, 2H, H7), 4.72 (brs, 1H, H1’), 4.51 (s, 2H, H4’), 4.46-4.37 (m, 4H, H14), 4.14-4.12 (m, 2H, H5’), 4.09-4.07 (m, 2H, H3’), 4.04-4.02 (m, 2H, 9-OH), 3.92 (s, 3H, OCH_3), 3.88 (s, 3H, OCH_3), 2.92-2.87 (m, 4H, H10), 2.72 (brs, 4H, H3”), 2.22-2.18 (m, 4H, H8, H2”), 1.57-1.55 (m, 4H, H2’), 1.46-1.44 (m, 4H, 3”-NH_2), 0.81 (d, J = 6.5 Hz, 6H, H6’). LC-MS (>98%): $C_{60}H_{70}N_6O_{22}S_2^{2+}$, exact mass: 1290.4; Found: 645.2 (M+/2).

CHAPTER 7

SUMMARY AND FUTURE STUDIES

We employed multiple drug design approaches towards the development of CA modulators (activators and inhibitors), and translated the CA inhibitors for the development of CA IX targeted gold nanoplatform. We have successfully generated potent and selective CAAs for specific CA isozymes, with good fluorescence properties. These CAAs can be used as biomolecular tools for investigating the role of CA isozymes in brain, and can be translated for memory and learning enhancement studies *in vivo*. On the other side, we developed several series of potent and selective CA IX inhibitors, both small molecular weight and large molecular weight PEGylated compounds, that can efficiently kill the CA-expressing tumor cells. The generated CA inhibitors have demonstrated the therapeutic potential of being used as carbonic anhydrase IX inhibitors for treatment of hypoxic tumors.

For CAA project, the X-ray study of the pyridinium histamine derivatives provides valuable insights into the binding of the CAAs within the CA active site. The generated novel bis-imidazole CAAs proved to be nanomolar potent for several brain related isozymes. This study will be again supplemented with X-ray crystallography studies on CA adducts with several potent representative CAAs. Finding from X-ray crystallography studies will be subsequently utilized to develop another series CAAs in order to further improve the potency and selectivity.

From Small MW CAI project, ureido 1,3,4-thiadiazole sulfonamides proved to be potent and selective inhibitors of CA IX and CA XII, with good MDA-MB 231 tumor cell killing revealed from our in vitro toxicity assays. These novel ureido

sulfonamides will be profiled for ADME (absorption, distribution, metabolism, elimination), and will be translated to in vivo testing, in animal models of breast cancer.

To further improve the design, X-ray crystal structures will be obtained on CA adducts with the best inhibitors and a new series of ureido thiadiazole sulfonamides will also be developed.

For PEGylated bis-sulfonamide CAI project, the present study reveals the impact of PEG linker length for tumor cell killing for this design of PEGylated bis-sulfonamide CAI. These insights will be employed towards developing new series of PEGylated CAIs and gold nanoplatforms decorated with PEGylated CAIs with improved efficiency towards the selective delivery of cancer chemotherapeutics via targeting CA IX.

BIBLIOGRAPHY

1. Parkkila, S., *An overview of the distribution and function of carbonic anhydrase in mammals*, in *The Carbonic Anhydrases: New Horizons*, W.R. Chegwidden, N.D. Carter, and Y.H. Edwards, Editors. 2000, Birkhäuser Basel: Basel. p. 79-93.
2. Supuran, C.T., *Carbonic anhydrases: novel therapeutic applications for inhibitors and activators.* Nat Rev Drug Discov, 2008. **7**(2): p. 168-81.
3. Maren, T.H., *The Kinetics of HCO3− Synthesis Related to Fluid Secretion, pH Control, and CO2 Elimination.* Annual Review of Physiology, 1988. **50**(1): p. 695-717.
4. Supuran, C.T., *Carbonic anhydrase inhibitors and activators for novel therapeutic applications.* Future Medicinal Chemistry, 2011. **3**(9): p. 1165-1180.
5. Sun, M.-K. and D.L. Alkon, *Pharmacological Enhancement of Synaptic Efficacy, Spatial Learning, and Memory through Carbonic Anhydrase Activation in Rats.* Journal of Pharmacology and Experimental Therapeutics, 2001. **297**(3): p. 961-967.
6. Supuran, C.T. and A. Scozzafava, *Carbonic anhydrase inhibitors and their therapeutic potential.* Expert Opinion on Therapeutic Patents, 2000. **10**(5): p. 575-600.
7. Xiang, Q., et al., *Kinetics of the reversible reaction of CO2(aq) and HCO3(-) with sarcosine salt in aqueous solution.* J Phys Chem A, 2012. **116**(42): p. 10276-84.
8. Keilin, D. and T. Mann, *Carbonic anhydrase. Purification and nature of the enzyme.* Biochem J, 1940. **34**(8-9): p. 1163-76.

9. Van Slyke, D.D. and J.A. Hawkins, *Studies of gas and electrolyte equilibria in blood: xvi. The evolution of carbon dioxide from blood and buffer solutions.* Journal of Biological Chemistry, 1930. **87**(2): p. 265-279.

10. Meldrum, N.U. and F.J. Roughton, *Carbonic anhydrase. Its preparation and properties.* J Physiol, 1933. **80**(2): p. 113-42.

11. Bradfield, J.R., *Plant carbonic anhydrase.* Nature, 1947. **159**(4040): p. 467.

12. Smith, K.S., et al., *Carbonic anhydrase is an ancient enzyme widespread in prokaryotes.* Proc Natl Acad Sci U S A, 1999. **96**(26): p. 15184-9.

13. Krishnamurthy, V.M., et al., *Carbonic anhydrase as a model for biophysical and physical-organic studies of proteins and protein-ligand binding.* Chem Rev, 2008. **108**(3): p. 946-1051.

14. Supuran, C.T. and C. Capasso, *The η-class carbonic anhydrases as drug targets for antimalarial agents.* Expert Opinion on Therapeutic Targets, 2015. **19**(4): p. 551-563.

15. Ozensoy Guler, O., C. Capasso, and C.T. Supuran, *A magnificent enzyme superfamily: carbonic anhydrases, their purification and characterization.* Journal of Enzyme Inhibition and Medicinal Chemistry, 2016. **31**(5): p. 689-694.

16. Alterio, V., et al., *Multiple binding modes of inhibitors to carbonic anhydrases: how to design specific drugs targeting 15 different isoforms?* Chem Rev, 2012. **112**(8): p. 4421-68.

17. Draghici, B., et al., *Ethylene bis-imidazoles are highly potent and selective activators for isozymes VA and VII of carbonic anhydrase, with a potential nootropic effect.* Chemical Communications, 2014. **50**(45): p. 5980-5983.

18. Supuran, C.T., *Carbonic anhydrases: from biomedical applications of the inhibitors and activators to biotechnological use for CO(2) capture.* J Enzyme Inhib Med Chem, 2013. **28**(2): p. 229-30.

19. Supuran, C.T., *Structure-based drug discovery of carbonic anhydrase inhibitors.* J Enzyme Inhib Med Chem, 2012. **27**(6): p. 759-72.

20. Truppo, E., et al., *Carbonic anhydrase VII is S-glutathionylated without loss of catalytic activity and affinity for sulfonamide inhibitors.* Bioorg Med Chem Lett, 2012. **22**(4): p. 1560-4.

21. Imtaiyaz Hassan, M., et al., *Structure, function and applications of carbonic anhydrase isozymes.* Bioorganic & Medicinal Chemistry, 2013. **21**(6): p. 1570-1582.

22. Supuran, C.T., J.Y. Winum, and B. Wang, *Drug Design of Zinc-Enzyme Inhibitors: Functional, Structural, and Disease Applications*. 2009: Wiley.

23. Ferry, J.G., *The γ class of carbonic anhydrases.* Biochimica et Biophysica Acta (BBA) - Proteins and Proteomics, 2010. **1804**(2): p. 374-381.

24. Xu, Y., et al., *Structure and metal exchange in the cadmium carbonic anhydrase of marine diatoms.* Nature, 2008. **452**: p. 56.

25. Lane, T.W., et al., *A cadmium enzyme from a marine diatom.* Nature, 2005. **435**: p. 42.

26. Alterio, V., et al., *Structural and inhibition insights into carbonic anhydrase CDCA1 from the marine diatom Thalassiosira weissflogii.* Biochimie, 2012. **94**(5): p. 1232-41.

27. So, A.K.C., et al., *A Novel Evolutionary Lineage of Carbonic Anhydrase (ε Class) Is a Component of the Carboxysome Shell.* Journal of Bacteriology, 2004. **186**(3): p. 623-630.

28. Tripp, B.C., K. Smith, and J.G. Ferry, *Carbonic Anhydrase: New Insights for an Ancient Enzyme.* Journal of Biological Chemistry, 2001. **276**(52): p. 48615-48618.

29. Sawaya, M.R., et al., *The Structure of β-Carbonic Anhydrase from the Carboxysomal Shell Reveals a Distinct Subclass with One Active Site for the Price of Two.* Journal of Biological Chemistry, 2006. **281**(11): p. 7546-7555.

30. Nair, S.K. and D.W. Christianson, *Unexpected pH-dependent conformation of His-64, the proton shuttle of carbonic anhydrase II.* Journal of the American Chemical Society, 1991. **113**(25): p. 9455-9458.

31. Silverman, D.N. and S. Lindskog, *The catalytic mechanism of carbonic anhydrase: implications of a rate-limiting protolysis of water.* Accounts of Chemical Research, 1988. **21**(1): p. 30-36.

32. De Simone, G., A. Scozzafava, and C.T. Supuran, *Which carbonic anhydrases are targeted by the antiepileptic sulfonamides and sulfamates?* Chem Biol Drug Des, 2009. **74**(3): p. 317-21.

33. Maren, T.H., *Carbonic anhydrase: chemistry, physiology, and inhibition.* Physiol Rev, 1967. **47**(4): p. 595-781.

34. Vogh, B.P., *The relation of choroid plexus carbonic anhydrase activity to cerebrospinal fluid formation: study of three inhibitors in cat with extrapolation to man.* J Pharmacol Exp Ther, 1980. **213**(2): p. 321-31.

35. Maren, T.H., et al., *Renal and cerebrospinal fluid formation pharmacology of a high molecular weight carbonic anhydrase inhibitor.* J Pharmacol Exp Ther, 1997. **280**(1): p. 98-104.

36. Parkkila, S., *An overview of the distribution and function of carbonic anhydrase in mammals.* Exs, 2000(90): p. 79-93.

37. Tong, C.K., et al., *Interstitial carbonic anhydrase (CA) activity in brain is attributable to membrane-bound CA type IV.* J Neurosci, 2000. **20**(22): p. 8247-53.

38. Shah, G.N., et al., *Carbonic anhydrase IV and XIV knockout mice: roles of the respective carbonic anhydrases in buffering the extracellular space in brain.* Proc Natl Acad Sci U S A, 2005. **102**(46): p. 16771-6.

39. Sly, W.S., et al., *Carbonic anhydrase II deficiency identified as the primary defect in the autosomal recessive syndrome of osteopetrosis with renal tubular acidosis and cerebral calcification.* Proceedings of the National Academy of Sciences of the United States of America, 1983. **80**(9): p. 2752-2756.

40. Sly, W.S. and P.Y. Hu, *Human Carbonic Anhydrases and Carbonic Anhydrase Deficiencies.* Annual Review of Biochemistry, 1995. **64**(1): p. 375-401.

41. Meier-Ruge, W., P. Iwangoff, and K. Reichlmeier, *Neurochemical enzyme changes in Alzheimer's and Pick's disease.* Archives of Gerontology and Geriatrics, 1984. **3**(2): p. 161-165.

42. McCarthy, K.D. and D.J. Reed, T*he effect of acetazolamide and furosemide on cerebrospinal fluid production and choroid plexus carbonic anhydrase activity.*

Journal of Pharmacology and Experimental Therapeutics, 1974. **189**(1): p. 194-201.

43. Sultana, R., et al., *Redox proteomics identification of oxidized proteins in Alzheimer's disease hippocampus and cerebellum: An approach to understand pathological and biochemical alterations in AD.* Neurobiology of Aging. **27**(11): p. 1564-1576.

44. Sultana, R., M. Perluigi, and D.A. Butterfield, *Oxidatively modified proteins in Alzheimer's disease (AD), mild cognitive impairment and animal models of AD: role of Abeta in pathogenesis.* Acta neuropathologica, 2009. **118**(1): p. 131.

45. Sultana, R., et al., *Identification of nitrated proteins in Alzheimer's disease brain using a redox proteomics approach.* Neurobiology of Disease, 2006. **22**(1): p. 76-87.

46. Tang, Y.-P., et al., *Genetic enhancement of learning and memory in mice.* Nature, 1999. **401**: p. 63.

47. Wu, M., et al., *Cholinergic Excitation of Septohippocampal GABA But Not Cholinergic Neurons: Implications for Learning and Memory.* The Journal of Neuroscience, 2000. **20**(10): p. 3900-3908.

48. Sun, M.-K. and D.L. Alkon, *Carbonic anhydrase gating of attention: memory therapy and enhancement.* Trends in Pharmacological Sciences. **23**(2): p. 83-89.

49. Sun, M.-K., D. Dahl, and D.L. Alkon, *Heterosynaptic Transformation of GABAergic Gating in the Hippocampus and Effects of Carbonic Anhydrase Inhibition.* Journal of Pharmacology and Experimental Therapeutics, 2001. **296**(3): p. 811-817.

50. Ferris, K.E., R.D. Clark, and E.L. Coates, *Topical Inhibition of Nasal Carbonic Anhydrase Affects the CO2 Detection Threshold in Rats.* Chemical Senses, 2007. **32**(3): p. 263-271.

51. Hipkiss, A.R., *Could carnosine or related structures suppress Alzheimer's disease?* J Alzheimers Dis, 2007. **11**(2): p. 229-40.

52. Sugrue, M.F., *Pharmacological and ocular hypotensive properties of topical carbonic anhydrase inhibitors.* Progress in Retinal and Eye Research, 2000. **19**(1): p. 87-112.

53. Swenson, E.R., *Carbonic Anhydrase Inhibitors and High Altitude Illnesses*, in *Carbonic Anhydrase: Mechanism, Regulation, Links to Disease, and Industrial Applications*, S.C. Frost and R. McKenna, Editors. 2014, Springer Netherlands: Dordrecht. p. 361-386.

54. Supuran, C.T., *The history and rationale of using carbonic anhydrase inhibitors in the treatment of peptic ulcers. In memoriam Ioan Puşcaş (1932–2015) AU - Buzás, György M.* Journal of Enzyme Inhibition and Medicinal Chemistry, 2016. **31**(4): p. 527-533.

55. Supuran, C.T., *Structure-based drug discovery of carbonic anhydrase inhibitors.* Journal of Enzyme Inhibition and Medicinal Chemistry, 2012. **27**(6): p. 759-772.

56. Faught, E., *Topiramate in the treatment of partial and generalized epilepsy.* Neuropsychiatric disease and treatment, 2007. **3**(6): p. 811-821.

57. Supuran, C.T., *Carbonic anhydrases: novel therapeutic applications for inhibitors and activators.* Nature Reviews Drug Discovery, 2008. **7**: p. 168-181.

58. Akocak, S. and M.A. Ilies, *Next-generation primary sulfonamide carbonic anhydrase inhibitors*, in *Targeting carbonic anhydrases*, C.T. Supuran and C. Capasso, Editors. 2014, Future Science: London. p. 35-51.

59. Siegel, R.L., K.D. Miller, and A. Jemal, *Cancer Statistics, 2017.* CA Cancer J Clin, 2017. **67**(1): p. 7-30.

60. Hanahan, D. and R.A. Weinberg, *The hallmarks of cancer.* Cell, 2000. **100**(1): p. 57-70.

61. Kinzler, K.W. and B. Vogelstein, *Cancer-susceptibility genes. Gatekeepers and caretakers.* Nature, 1997. **386**(6627): p. 761, 763.

62. Hanahan, D. and R.A. Weinberg, *Hallmarks of Cancer: The Next Generation.* Cell, 2011. **144**(5): p. 646-674.

63. Chaffer, C.L. and R.A. Weinberg, *How Does Multistep Tumorigenesis Really Proceed?* Cancer Discovery, 2015. **5**(1): p. 22-24.

64. Vander Heiden, M.G., L.C. Cantley, and C.B. Thompson, *Understanding the Warburg Effect: The Metabolic Requirements of Cell Proliferation.* Science, 2009. **324**(5930): p. 1029-1033.

65. McDonald, P.C., S.C. Chafe, and S. Dedhar, *Overcoming Hypoxia-Mediated Tumor Progression: Combinatorial Approaches Targeting pH Regulation, Angiogenesis and Immune Dysfunction.* Frontiers in Cell and Developmental Biology, 2016. **4**: p. 27.

66. Parks, S.K., J. Chiche, and J. Pouyssegur, *pH control mechanisms of tumor survival and growth.* Journal of Cellular Physiology, 2011. **226**(2): p. 299-308.

67. Bruick, R.K. and S.L. McKnight, *A conserved family of prolyl-4-hydroxylases that modify HIF.* Science, 2001. **294**(5545): p. 1337-40.

68. Maxwell, P.H., et al., *The tumour suppressor protein VHL targets hypoxia-inducible factors for oxygen-dependent proteolysis.* Nature, 1999. **399**(6733): p. 271-5.

69. Semenza, G.L., *Targeting HIF-1 for cancer therapy.* Nat Rev Cancer, 2003. **3**(10): p. 721-32.

70. Eales, K.L., K.E. Hollinshead, and D.A. Tennant, *Hypoxia and metabolic adaptation of cancer cells.* Oncogenesis, 2016. **5**: p. e190.

71. Alterio, V., et al., *Crystal structure of the catalytic domain of the tumor-associated human carbonic anhydrase IX.* Proc Natl Acad Sci U S A, 2009. **106**(38): p. 16233-8.

72. Neri, D. and C.T. Supuran, *Interfering with pH regulation in tumours as a therapeutic strategy.* Nat Rev Drug Discov, 2011. **10**(10): p. 767-77.

73. Gillies, R.J. and R.A. Gatenby, *Metabolism and Its Sequelae in Cancer Evolution and Therapy.* Cancer Journal, 2015. **21**(2): p. 88-96.

74. Tafreshi, N.K., et al., *Carbonic anhydrase IX as an imaging and therapeutic target for tumors and metastases.* Subcell Biochem, 2014. **75**: p. 221-54.

75. Svastova, E., et al., *Hypoxia activates the capacity of tumor-associated carbonic anhydrase IX to acidify extracellular pH.* FEBS Lett, 2004. **577**(3): p. 439-45.

76. Austin, R.P., et al., *The influence of nonspecific microsomal binding on apparent intrinsic clearance, and its prediction from physicochemical properties.* Drug Metab Dispos, 2002. **30**(12): p. 1497-503.

77. Dave, K., et al., *Pyridinium derivatives of histamine are potent activators of cytosolic carbonic anhydrase isoforms I, II and VII.* Org Biomol Chem, 2011. **9**(8): p. 2790-800.

78. Chen, C.L., et al., *Hypoxia and metabolic phenotypes during breast carcinogenesis: expression of HIF-1alpha, GLUT1, and CAIX.* Virchows Arch, 2010. **457**(1): p. 53-61.

79. Saarnio, J., et al., *Immunohistochemical study of colorectal tumors for expression of a novel transmembrane carbonic anhydrase, MN/CA IX, with potential value as a marker of cell proliferation.* Am J Pathol, 1998. **153**(1): p. 279-85.

80. Ennaceur, A., *One-trial object recognition in rats and mice: methodological and theoretical issues.* Behav Brain Res, 2010. **215**(2): p. 244-54.

81. Arque, G., et al., *Impaired spatial learning strategies and novel object recognition in mice haploinsufficient for the dual specificity tyrosine-regulated kinase-1A (Dyrk1A).* PLoS One, 2008. **3**(7): p. e2575.

82. Choschzick, M., et al., *Overexpression of carbonic anhydrase IX (CAIX) is an independent unfavorable prognostic marker in endometrioid ovarian cancer.* Virchows Arch, 2011. **459**(2): p. 193-200.

83. Hynninen, P., et al., *Expression of transmembrane carbonic anhydrases IX and XII in ovarian tumours.* Histopathology, 2006. **49**(6): p. 594-602.

84. Hussain, S.A., et al., *Carbonic anhydrase IX, a marker of hypoxia: correlation with clinical outcome in transitional cell carcinoma of the bladder.* Oncol Rep, 2004. **11**(5): p. 1005-10.

85. Koukourakis, M.I., et al., *Endogenous markers of two separate hypoxia response pathways (hypoxia inducible factor 2 alpha and carbonic anhydrase 9) are associated with radiotherapy failure in head and neck cancer patients recruited in the CHART randomized trial.* J Clin Oncol, 2006. **24**(5): p. 727-35.

86. Barker, P.L., P.L. Gendler, and H. Rapoport, *Acylation of dibasic compounds containing amino amidine and aminoguanidine functions.* Journal of Organic Chemistry, 1981. **46**(12): p. 2455-2465.

87. Ganti, V., E.A. Walker, and S. Nagar, *Pharmacokinetic application of a bio-analytical LC-MS method developed for 5-fluorouracil and methotrexate in mouse plasma, brain and urine.* Biomed Chromatogr, 2013. **27**(8): p. 994-1002.

88. Bisen-Hersh, E.B., P.N. Hineline, and E.A. Walker, *Effects of early chemotherapeutic treatment on learning in adolescent mice: implications for cognitive impairment and remediation in childhood cancer survivors.* Clin Cancer Res, 2013. **19**(11): p. 3008-18.

89. Dave, K., et al., *An inhibitor-like binding mode of a carbonic anhydrase activator within the active site of isoform II.* Bioorg Med Chem Lett, 2011. **21**(9): p. 2764-8.

90. Garthwaite, G., et al., *Signaling from blood vessels to CNS axons through nitric oxide.* J Neurosci, 2006. **26**(29): p. 7730-40.

91. Pastorekova, S. and J. Pastorek, *Cancer-related carbonic anhydrase isozymes and their inhibition.* Carbonic Anhydrase, 2004: p. 255-281.

92. Akocak, S., et al., *PEGylated Bis-Sulfonamide Carbonic Anhydrase Inhibitors Can Efficiently Control the Growth of Several Carbonic Anhydrase IX-Expressing Carcinomas.* J Med Chem, 2016. **59**(10): p. 5077-88.

93. Ilies, M.A., et al., *Carbonic anhydrase inhibitors. Inhibition of tumor-associated isozyme IX by halogenosulfanilamide and halogenophenylaminobenzolamide derivatives.* J Med Chem, 2003. **46**(11): p. 2187-96.

94. Supuran, C.T., et al., *Carbonic anhydrase inhibitors - Part 53 - Synthesis of substituted-pyridinium derivatives of aromatic sulfonamides: The first non-polymeric membrane-impermeable inhibitors with selectivity for isozyme IV.* European Journal of Medicinal Chemistry, 1998. **33**(7-8): p. 577-594.

95. Scozzafava, A., et al., *Carbonic anhydrase inhibitors: synthesis of membrane-impermeant low molecular weight sulfonamides possessing in vivo selectivity for the membrane-bound versus cytosolic isozymes.* J Med Chem, 2000. **43**(2): p. 292-300.

96. Supuran, C.T., et al., *Carbonic anhydrase inhibitors: synthesis of sulfonamides incorporating 2,4,6-trisubstituted-pyridinium-ethylcarboxamido moieties possessing membrane-impermeability and in vivo selectivity for the membrane-bound (CA IV) versus the cytosolic (CA I and CA II) isozymes.* J Enzyme Inhib, 2000. **15**(4): p. 381-401.

97. Pastorekova, S., J. Kopacek, and J. Pastorek, *Carbonic anhydrase inhibitors and the management of cancer.* Curr Top Med Chem, 2007. **7**(9): p. 865-78.

98. Casanovas, O., *Cancer: Limitations of therapies exposed.* Nature, 2012. **484**(7392): p. 44-6.

99. Doane, T.L. and C. Burda, *The unique role of nanoparticles in nanomedicine: imaging, drug delivery and therapy.* Chem Soc Rev, 2012. **41**(7): p. 2885-911.

100. Wang, L., *Synthetic methods of CuS nanoparticles and their applications for imaging and cancer therapy.* RSC Advances, 2016. **6**(86): p. 82596-82615.

101. Brigger, I., C. Dubernet, and P. Couvreur, *Nanoparticles in cancer therapy and diagnosis.* Adv Drug Deliv Rev, 2002. **54**(5): p. 631-51.

102. Cabral, H., N. Nishiyama, and K. Kataoka, *Supramolecular nanodevices: from design validation to theranostic nanomedicine.* Acc Chem Res, 2011. **44**(10): p. 999-1008.

103. Zhang, H., D. Yee, and C. Wang, *Quantum dots for cancer diagnosis and therapy: biological and clinical perspectives.* Nanomedicine (Lond), 2008. **3**(1): p. 83-91.

104. Cordeiro, M., et al., *Gold Nanoparticles for Diagnostics: Advances towards Points of Care.* Diagnostics (Basel), 2016. **6**(4).

105. Liu, G., et al., *Applications and potential toxicity of magnetic iron oxide nanoparticles.* Small, 2013. **9**(9-10): p. 1533-45.

106. Bae, Y.H. and K. Park, *Targeted drug delivery to tumors: myths, reality and possibility.* J Control Release, 2011. **153**(3): p. 198-205.

107. Pattni, B.S., V.V. Chupin, and V.P. Torchilin, *New Developments in Liposomal Drug Delivery.* Chem Rev, 2015. **115**(19): p. 10938-66.

108. Yuan, F., et al., *Vascular permeability in a human tumor xenograft: molecular size dependence and cutoff size.* Cancer Res, 1995. **55**(17): p. 3752-6.

109. Maruyama, K., et al., *Prolonged circulation time in vivo of large unilamellar liposomes composed of distearoyl phosphatidylcholine and cholesterol containing amphipathic poly(ethylene glycol).* Biochim Biophys Acta, 1992. **1128**(1): p. 44-9.

110. Garcia, A.A., et al., *A phase II study of Doxil (liposomal doxorubicin): lack of activity in poor prognosis soft tissue sarcomas.* Ann Oncol, 1998. **9**(10): p. 1131-3.

111. Allen, T.M., *Ligand-targeted therapeutics in anticancer therapy.* Nat Rev Cancer, 2002. **2**(10): p. 750-63.

112. Meissner, J.M., et al., *Novel antisense therapeutics delivery systems: In vitro and in vivo studies of liposomes targeted with anti-CD20 antibody.* J Control Release, 2015. **220**(Pt A): p. 515-28.

113. Dai, W., et al., *Peptide PHSCNK as an integrin alpha5beta1 antagonist targets stealth liposomes to integrin-overexpressing melanoma.* Nanomedicine, 2012. **8**(7): p. 1152-61.

114. Sriraman, S.K., et al., *Enhanced Cytotoxicity of Folic Acid-Targeted Liposomes Co-Loaded with C6 Ceramide and Doxorubicin: In Vitro Evaluation on HeLa, A2780-ADR, and H69-AR Cells.* Mol Pharm, 2016. **13**(2): p. 428-37.

115. Kirpotin, D., et al., *Sterically stabilized anti-HER2 immunoliposomes: design and targeting to human breast cancer cells in vitro.* Biochemistry, 1997. **36**(1): p. 66-75.

116. Zhao, S., et al., *Doxorubicin hydrochloride-oleic acid conjugate loaded nanostructured lipid carriers for tumor specific drug release.* Colloids Surf B Biointerfaces, 2016. **145**: p. 95-103.

117. Egusquiaguirre, S.P., et al., *Nanoparticle delivery systems for cancer therapy: advances in clinical and preclinical research.* Clin Transl Oncol, 2012. **14**(2): p. 83-93.

118. Torchilin, V.P., *Recent advances with liposomes as pharmaceutical carriers.* Nat Rev Drug Discov, 2005. **4**(2): p. 145-60.

119. Yeh, Y.C., B. Creran, and V.M. Rotello, *Gold nanoparticles: preparation, properties, and applications in bionanotechnology.* Nanoscale, 2012. **4**(6): p. 1871-80.

120. Sperling, R.A., et al., *Biological applications of gold nanoparticles.* Chem Soc Rev, 2008. **37**(9): p. 1896-908.

121. Dreaden, E.C., et al., *The golden age: gold nanoparticles for biomedicine.* Chem Soc Rev, 2012. **41**(7): p. 2740-79.

122. Saha, K., et al., *Gold nanoparticles in chemical and biological sensing.* Chem Rev, 2012. **112**(5): p. 2739-79.

123. Giljohann, D.A., et al., *Gold nanoparticles for biology and medicine.* Angew Chem Int Ed Engl, 2010. **49**(19): p. 3280-94.

124. Huang, X. and M.A. El-Sayed, *Gold nanoparticles: Optical properties and implementations in cancer diagnosis and photothermal therapy.* Journal of Advanced Research, 2010. **1**(1): p. 13-28.

125. Stiti, M., et al., *Carbonic anhydrase inhibitor coated gold nanoparticles selectively inhibit the tumor-associated isoform IX over the cytosolic isozymes I and II.* J Am Chem Soc, 2008. **130**(48): p. 16130-1.

126. Saada, M.C., et al., *Carbonic anhydrase activators: gold nanoparticles coated with derivatized histamine, histidine, and carnosine show enhanced activatory effects on several mammalian isoforms.* Journal of Medicinal Chemistry, 2011. **54**(5): p. 1170-7.

127. Ghosh, P., et al., *Gold nanoparticles in delivery applications.* Adv Drug Deliv Rev, 2008. **60**(11): p. 1307-15.

128. Dhar, S., et al., *Polyvalent Oligonucleotide Gold Nanoparticle Conjugates as Delivery Vehicles for Platinum(IV) Warheads.* Journal of the American Chemical Society, 2009. **131**(41): p. 14652-+.

129. Kang, B., et al., *Exploiting the Nanoparticle Plasmon Effect: Observing Drug Delivery Dynamics in Single Cells via Raman/Fluorescence Imaging Spectroscopy.* Acs Nano, 2013. **7**(8): p. 7420-7427.

130. Rosi, N.L., et al., *Oligonucleotide-modified gold nanoparticles for intracellular gene regulation.* Science, 2006. **312**(5776): p. 1027-30.

131. Kizewski, A. and M.A. Ilies, *Efficient and synergetic DNA delivery with pyridinium amphiphiles-gold nanoparticle composite systems having different packing parameters.* Chem Commun (Camb), 2016. **52**(1): p. 60-3.

132. Grzelczak, M., et al., *Shape control in gold nanoparticle synthesis.* Chemical Society Reviews, 2008. **37**(9): p. 1783-1791.

133. Cygan, M.T., et al., *Insertion, conductivity, and structures of conjugated organic oligomers in self-assembled alkanethiol monolayers on Au{111}.* Journal of the American Chemical Society, 1998. **120**(12): p. 2721-2732.

134. Popovtzer, R., et al., *Targeted gold nanoparticles enable molecular CT imaging of cancer.* Nano Lett, 2008. **8**(12): p. 4593-6.

135. Morshed, R.A., et al., *Cell-Penetrating Peptide-Modified Gold Nanoparticles for the Delivery of Doxorubicin to Brain Metastatic Breast Cancer.* Mol Pharm, 2016. **13**(6): p. 1843-54.

136. Minotti, G., et al., *Anthracyclines: molecular advances and pharmacologic developments in antitumor activity and cardiotoxicity.* Pharmacol Rev, 2004. **56**(2): p. 185-229.

137. Duggan, S.T. and G.M. Keating, *Pegylated liposomal doxorubicin: a review of its use in metastatic breast cancer, ovarian cancer, multiple myeloma and AIDS-related Kaposi's sarcoma.* Drugs, 2011. **71**(18): p. 2531-58.

138. Barenholz, Y., *Doxil(R)--the first FDA-approved nano-drug: lessons learned.* J Control Release, 2012. **160**(2): p. 117-34.

139. Tacar, O., P. Sriamornsak, and C.R. Dass, *Doxorubicin: an update on anticancer molecular action, toxicity and novel drug delivery systems.* J Pharm Pharmacol, 2013. **65**(2): p. 157-70.

140. Lotem, M., et al., *Skin toxic effects of polyethylene glycol-coated liposomal doxorubicin.* Arch Dermatol, 2000. **136**(12): p. 1475-80.

141. Ratto, F., et al., *Plasmonic Particles that Hit Hypoxic Cells.* Advanced Functional Materials, 2015. **25**(2): p. 316-323.

142. Gieling, R.G., et al., *Inhibition of carbonic anhydrase activity modifies the toxicity of doxorubicin and melphalan in tumour cells in vitro.* J Enzyme Inhib Med Chem, 2013. **28**(2): p. 360-9.

143. van Kuijk, S.J., et al., *The Sulfamate Small Molecule CAIX Inhibitor S4 Modulates Doxorubicin Efficacy.* PLoS One, 2016. **11**(8): p. e0161040.

144. Supuran, C.T. and A. Scozzafava, *Activation of carbonic anhydrase isozymes*, in *The Carbonic Anhydrases: New Horizons*, W.R. Chegwidden, N.D. Carter, and Y.H. Edwards, Editors. 2000, Birkhäuser Basel: Basel. p. 197-219.

145. Ho, C. and J.M. Sturtevant, *Activation of bovine carbonic anhydrase by ethlyenediamine tetraacetic acid.* Biochemical and Biophysical Research Communications, 1960. **3**(1): p. 20-23.

146. Ilies, M.A., et al., *Carbonic anhydrase activators. Part 17. Synthesis and activation study of a series of 1-(1,2,4-triazole-(1H)-3-yl)-2,4,6-trisubstituted-pyridinium salts against isozymes I, II and IV.* European Journal of Medicinal Chemistry, 1997. **32**(11): p. 911-918.

147. Silverman, D.N., C. Tu, and G.C. Wynns, *Proton transfer between hemoglobin and the carbonic anhydrase active site.* J Biol Chem, 1978. **253**(8): p. 2563-7.

148. Silverman, D.N., L. Backman, and C. Tu, *Role of hemoglobin in proton transfer to the active site of carbonic anhydrase.* J Biol Chem, 1979. **254**(8): p. 2588-91.

149. Paranawithana, S.R., et al., *Enhancement of the catalytic activity of carbonic anhydrase III by phosphates.* J Biol Chem, 1990. **265**(36): p. 22270-4.

150. Parkes, J.L. and P.S. Coleman, *Enhancement of carbonic anhydrase activity by erythrocyte membranes.* Arch Biochem Biophys, 1989. **275**(2): p. 459-68.

151. Briganti, F., A. Scozzafava, and C.T. Supuran, *Carbonic Anhydrase Activators. Part 191 Spectroscopic and Kinetic Investigations for the Interaction of Isozymes I and II With Primary Amines.* Metal-Based Drugs, 1997. **4**(4): p. 221-227.

152. Briganti, F., et al., *Carbonic anhydrase activators: X-ray crystallographic and spectroscopic investigations for the interaction of isozymes I and II with histamine.* Biochemistry, 1997. **36**(34): p. 10384-92.

153. Temperini, C., et al., *Carbonic anhydrase activators. Activation of isozymes I, II, IV, VA, VII, and XIV with l- and d-histidine and crystallographic analysis of their adducts with isoform II: engineering proton-transfer processes within the active site of an enzyme.* Chemistry - An European Journal, 2006. **12**(27): p. 7057-66.

154. Temperini, C., et al., *Carbonic anhydrase activators: Kinetic and X-ray crystallographic study for the interaction of d- and l-tryptophan with the mammalian isoforms I–XIV.* Bioorganic & Medicinal Chemistry, 2008. **16**(18): p. 8373-8378.

155. Temperini, C., et al., *Carbonic Anhydrase Activators. Activation of Isoforms I, II, IV, VA, VII, and XIV with l- and d-Phenylalanine and Crystallographic Analysis of Their Adducts with Isozyme II: Stereospecific Recognition within the Active Site of an Enzyme and Its Consequences for the Drug Design.* Journal of Medicinal Chemistry, 2006. **49**(10): p. 3019-3027.

156. Ilies, M., et al., *Carbonic Anhydrase Activators: Design of High Affinity Isozymes I, II, and IV Activators, Incorporating Tri-/Tetrasubstituted-pyridinium-azole Moieties.* Journal of Medicinal Chemistry, 2002. **45**(2): p. 504-510.

157. Draghici, B., et al., *Ethylene bis-imidazoles are highly potent and selective activators for isozymes VA and VII of carbonic anhydrase, with a potential nootropic effect.* Chem Commun (Camb), 2014. **50**(45): p. 5980-3.

158. Vullo, D., et al., *Carbonic anhydrase activators: Activation of the human isoforms VII (cytosolic) and XIV (transmembrane) with amino acids and amines.* Bioorganic & Medicinal Chemistry Letters, 2007. **17**(15): p. 4107-4112.

159. Supuran, C.T., et al., *Carbonic anhydrase activators. VII. Isozyme II activation by bisazolyl-methanes, -ethanes and related azoles.* Biol Pharm Bull, 1993. **16**(12): p. 1236-9.

160. Supuran, C.T., et al., *Carbonic anhydrase activators. XV. A kinetic study of the interaction of bovine isozyme II with pyrazoles, bis- and tris-azolyl-methanes.* Biol Pharm Bull, 1996. **19**(11): p. 1417-22.

161. Ilies, M., et al., *Carbonic anhydrase activators: design of high affinity isozymes I, II, and IV activators, incorporating tri-/tetrasubstituted-pyridinium-azole moieties.* J Med Chem, 2002. **45**(2): p. 504-10.

162. Temperini, C., et al., *Carbonic anhydrase activators: X-ray crystal structure of the adduct of human isozyme II with L-histidine as a platform for the design of stronger activators.* Bioorg Med Chem Lett, 2005. **15**(23): p. 5136-41.

163. Temperini, C., A. Scozzafava, and C.T. Supuran, *Carbonic anhydrase activators: the first X-ray crystallographic study of an adduct of isoform I.* Bioorg Med Chem Lett, 2006. **16**(19): p. 5152-6.

164. Duda, D., et al., *Structural and kinetic analysis of the chemical rescue of the proton transfer function of carbonic anhydrase II.* Biochemistry, 2001. **40**(6): p. 1741-8.

165. Elder, I., et al., *Proton transfer from exogenous donors in catalysis by human carbonic anhydrase II.* Arch Biochem Biophys, 2005. **437**(1): p. 106-14.

166. Aggarwal, M., et al., *Structural insight into activity enhancement and inhibition of H64A carbonic anhydrase II by imidazoles.* IUCrJ, 2014. **1**: p. 129-135.

167. Scozzafava, A. and C.T. Supuran, *Carbonic anhydrase activators: high affinity isozymes I, II, and IV activators, incorporating a beta-alanyl-histidine scaffold.* J Med Chem, 2002. **45**(2): p. 284-91.

168. Earnhardt, J.N., et al., *Introduction of Histidine Analogs Leads to Enhanced Proton Transfer in Carbonic Anhydrase V.* Archives of Biochemistry and Biophysics, 1999. **361**(2): p. 264-270.

169. Scozzafava, A., et al., *Carbonic anhydrase inhibitors. A general approach for the preparation of water-soluble sulfonamides incorporating polyamino-polycarboxylate tails and of their metal complexes possessing long-lasting, topical intraocular pressure-lowering properties.* J Med Chem, 2002. **45**(7): p. 1466-76.

170. Christianson, D.W. and C.A. Fierke, *Carbonic Anhydrase: Evolution of the Zinc Binding Site by Nature and by Design.* Accounts of Chemical Research, 1996. **29**(7): p. 331-339.

171. Supuran, C.T. and A. Scozzafava, *Activation of carbonic anhydrase isozymes.* Exs, 2000(90): p. 197-219.

172. Supuran, C.T. and A. Scozzafava, *Carbonic anhydrase activators: amino acyl/dipeptidyl histamine derivatives bind with high affinity to isozymes I, II and IV and act as efficient activators.* Bioorg Med Chem, 1999. **7**(12): p. 2915-23.

173. Khalifah, R.G., *The Carbon Dioxide Hydration Activity of Carbonic Anhydrase: I. Stop-flow kinetic studies on the native human isoenzymes b and c.* Journal of Biological Chemistry, 1971. **246**(8): p. 2561-2573.

174. Leschke, C., J. Altman, and W. Schunack, *Bis[1h-Imidazol-4(5)-Yl]Ethane and Bis(1-Tritylimidazol-4-Yl)Alkanes.* Synthesis-Stuttgart, 1993(2): p. 197-198.

175. Leschke, C., et al., *Synthesis and histamine H1 receptor agonist activity of a series of 2-phenylhistamines, 2-heteroarylhistamines, and analogues.* J Med Chem, 1995. **38**(8): p. 1287-94.

176. Miller, B., J. Altman, and W. Beck, *Bis[1H-imidazol-4(5)-yl]alkanes and 1,2,9,10- and 1,2,11,12-Tetraaminoalkane Tetrahydrochlorides.* Synthesis, 1997. **1997**(03): p. 347-350.

177. Sasaki, H. and T. Kitagawa, S*ynthesis and conformational properties of diimidazolo[3²]metacyclophane and homologs.* Chemical & pharmaceutical bulletin, 1988. **36**(4): p. 1593-1596.

178. Mézière, C., et al., *Mixed-Valence, Layered, Cation Radical Salts of the Ethane-Bridged Dimeric Tetrathiafulvalene [(EDT-TTF−CH2−)2•+][X-][THF]0.5, X- = fecl4-, gacl4.* Chemistry of Materials, 2000. **12**(8): p. 2250-2256.

179. Barker, P.L., P.L. Gendler, and H. Rapoport, *Acylation of dibasic compounds containing amino amidine and aminoguanidine functions.* The Journal of Organic Chemistry, 1981. **46**(12): p. 2455-2465.

180. Kazmierski, W.M., et al., *Novel Spiroketal Pyrrolidine GSK2336805 Potently Inhibits Key Hepatitis C Virus Genotype 1b Mutants: From Lead to Clinical Compound.* Journal of Medicinal Chemistry, 2014. **57**(5): p. 2058-2073.

181. Tan, J., et al., *Suzuki-Miyaura Cross-Coupling Reactions of Unprotected Haloimidazoles.* The Journal of Organic Chemistry, 2014. **79**(18): p. 8871-8876.

182. Chen, J., et al., *Discovery of Novel 2-Aryl-4-benzoyl-imidazoles Targeting the Colchicines Binding Site in Tubulin As Potential Anticancer Agents.* Journal of Medicinal Chemistry, 2010. **53**(20): p. 7414-7427.

183. Voss, M.E., et al., *A simple and convenient one-pot method for the preparation of heteroaryl-2-imidazoles from nitriles.* Tetrahedron, 2008. **64**(4): p. 645-651.

184. Kauffman, J.M., et al., *Electronic absorption and emission spectral data and fluorescence quantum yields of bridgedp-oligophenylenes, bi- to deciphenyls, and related furans and carbazoles.* Journal of Fluorescence, 1995. **5**(3): p. 295-305.

185. Lavis, L.D. and R.T. Raines, *Bright ideas for chemical biology.* ACS chemical biology, 2008. **3**(3): p. 142-155.

186. Suzuki, K., et al., *Reevaluation of absolute luminescence quantum yields of standard solutions using a spectrometer with an integrating sphere and a back-thinned CCD detector.* Phys Chem Chem Phys, 2009. **11**(42): p. 9850-60.

187. Brouwer, A.M., *Standards for photoluminescence quantum yield measurements in solution (IUPAC Technical Report).* Pure and Applied Chemistry, 2011. **83**(12).

188. Williams, A.T.R., S.A. Winfield, and J.N. Miller, *Relative fluorescence quantum yields using a computer-controlled luminescence spectrometer.* Analyst, 1983. **108**(1290): p. 1067-1071.

189. Schumann, J., A. Kanitz, and H. Hartmann, *Synthesis and Characterization of Some Heterocyclic Analogues of N,N'-Perarylated Phenylene-1,4-diamines and Benzidines as a New Class of Hole Transport Materials.* Synthesis, 2002. **2002**(09): p. 1268-1276.

190. Wang, H.B., J.A. Wisner, and M.C. Jennings, *Anion receptors containing thiazine-1,1-dioxide heterocycles as hydrogen bond donors.* Beilstein J Org Chem, 2010. **6**: p. 50.

191. Hon, Y.-S., Y.-C. Wong, and K.-J. Wu, *A convenient and versatile method for the preparation of α-hydroxymethyl ketone derivatives from the corresponding allyl silyl ethers or allyl carboxylates.* J. Chin. Chem. Soc. (Taipei, Taiwan), 2008. **55**(4): p. 896-914.

192. Bogdan, N., et al., *New [4.4]Cyclophane Diketals, Monoketones, and Diketones: Design, Synthesis, and Structural Analysis.* European Journal of Organic Chemistry, 2007. **2007**(28): p. 4674-4687.

193. Ruggli, P. and K. Knecht, *Über m-Phenylen-di-glykol. (53. Mitteilung über Stickstoff-Heterocyclen).* Helvetica Chimica Acta, 1944. **27**(1): p. 1108-1115.

194. Schubert, H., H.J. Lorenz, and R. Fischer, *Diimidazole, III. Synthese von Aromatisch überbrückten 4(5),4'(5')-Diimidazolen.* Journal für Praktische Chemie, 1963. **22**(3-4): p. 140-152.

195. Sawa, N., *Synthesis of imidazoles by catalytic dehydrogenation of imidazolines.* Nippon Kagaku Zasshi, 1968. **89**(9): p. 868-72.

196. Tanaka, K., T. Nagatsuka, and M. Doi, *Electrophotographic toner*. 1995, Canon Kk, Japan . p. 25 pp.

197. Breslow, R., et al., *Synthesis of some polyimidazole ligands related to zinc enzymes.* Journal of the American Chemical Society, 1983. **105**(16): p. 5337-5342.

198. Baldwin, J.J., *Substituierte imidazole*. 1975, Google Patents.

199. Baldwin, J.J., et al., *2-Pyridylimidazoles as inhibitors of xanthine oxidase.* Journal of Medicinal Chemistry, 1977. **20**(9): p. 1189-1193.

200. Takagi, K., et al., *Synthesis and Optical Properties of Imidazole- and Benzimidazole-Based Fused π-Conjugated Compounds: Influence of Substituent, Counteranion, and π-Conjugated System.* The Journal of Organic Chemistry, 2015. **80**(14): p. 7172-7183.

201. Supuran, C.T. and A. Scozzafava, *Carbonic anhydrase activators: amino acyl/dipeptidyl histamine derivatives bind with high affinity to isozymes I, II and IV and act as efficient activators.* Bioorganic & Medicinal Chemistry, 1999. **7**(12): p. 2915-2923.

202. Casini, A., et al., *Carbonic Anhydrase Inhibitors: Water-Soluble 4-Sulfamoylphenylthioureas as Topical Intraocular Pressure-Lowering Agents with Long-Lasting Effects.* Journal of Medicinal Chemistry, 2000. **43**(25): p. 4884-4892.

203. Scozzafava, A., et al., *Carbonic Anhydrase Inhibitors. A General Approach for the Preparation of Water-Soluble Sulfonamides Incorporating Polyamino−Polycarboxylate Tails and of Their Metal Complexes Possessing Long-Lasting, Topical Intraocular Pressure-Lowering Properties.* Journal of Medicinal Chemistry, 2002. **45**(7): p. 1466-1476.

204. Güzel-Akdemir, Ö., et al., *Structural study of the location of the phenyl tail of benzene sulfonamides and the effect on human carbonic anhydrase inhibition.* Bioorganic & Medicinal Chemistry, 2013. **21**(21): p. 6674-6680.

205. Ilies, M.A., et al., *Carbonic Anhydrase Inhibitors. Inhibition of Tumor-Associated Isozyme IX by Halogenosulfanilamide and Halogenophenylaminobenzolamide Derivatives.* Journal of Medicinal Chemistry, 2003. **46**(11): p. 2187-2196.

206. Menchise, V., et al., *Carbonic anhydrase inhibitors: X-ray crystallographic studies for the binding of 5-amino-1,3,4-thiadiazole-2-sulfonamide and 5-(4-amino-3-chloro-5-fluorophenylsulfonamido)-1,3,4-thiadiazole-2-sulfonamide to human isoform II.* Bioorganic & Medicinal Chemistry Letters, 2006. **16**(24): p. 6204-6208.

207. Ilies, M.A., et al., *Carbonic anhydrase inhibitors: aromatic and heterocyclic sulfonamides incorporating adamantyl moieties with strong anticonvulsant activity.* Bioorganic & Medicinal Chemistry, 2004. **12**(10): p. 2717-2726.

208. Pacchiano, F., et al., *Ureido-Substituted Benzenesulfonamides Potently Inhibit Carbonic Anhydrase IX and Show Antimetastatic Activity in a Model of Breast Cancer Metastasis.* Journal of Medicinal Chemistry, 2011. **54**(6): p. 1896-1902.

209. Biswas, S., R. McKenna, and C.T. Supuran, *Effect of incorporating a thiophene tail in the scaffold of acetazolamide on the inhibition of human carbonic anhydrase isoforms I, II, IX and XII.* Bioorganic & Medicinal Chemistry Letters, 2013. **23**(20): p. 5646-5649.

210. Biswas, S., et al., *Structural effect of phenyl ring compared to thiadiazole based adamantyl-sulfonamides on carbonic anhydrase inhibition.* Bioorganic & Medicinal Chemistry, 2013. **21**(8): p. 2314-2318.

211. Avvaru, B.S., et al., *Carbonic anhydrase inhibitors. The X-ray crystal structure of human isoform II in adduct with an adamantyl analogue of acetazolamide resides in a less utilized binding pocket than most hydrophobic inhibitors.* Bioorganic & Medicinal Chemistry Letters, 2010. **20**(15): p. 4376-4381.

212. ClinicalTrials.gov. *Safety Study of SLC-0111 in Subjects With Advanced Solid Tumours*. 2014; Available from: https://clinicaltrials.gov/ct2/show/NCT02215850.

213. Pacchiano, F., et al., *Selective hydrophobic pocket binding observed within the carbonic anhydrase II active site accommodate different 4-substituted-ureido-benzenesulfonamides and correlate to inhibitor potency.* Chemical Communications, 2010. **46**(44): p. 8371-8373.

214. Supuran, C.T., M.A. Ilies, and A. Scozzafava, *Carbonic anhydrase inhibitors — Part 29 1: Interaction of isozymes I, II and IV with benzolamide-like derivatives.* European Journal of Medicinal Chemistry, 1998. **33**(9): p. 739-751.

215. Jitianu, A., et al., S*ynthesis and carbonic anhydrase inhibitory activity of 5-benzoylamido- and 5-(3-nitrobenzoylamido)- 1,3,4-thiadiazole-2-sulfonamide and their metal complexes*, in *Main Group Metal Chemistry*. 1997. p. 151.

216. Katritzky, A.R., et al., *Synthesis and physicochemical properties of thiadiazolo[3,2-a]pyrimidinesulfonamides and thiadiazolo[3,2-*

a]triazinesulfonamides as candidates for topically effective carbonic anhydrase inhibitors. Journal of Medicinal Chemistry, 1987. **30**(11): p. 2058-2062.

217. Tafreshi, N.K., et al., *Evaluation of CAIX and CAXII Expression in Breast Cancer at Varied O2 Levels: CAIX is the Superior Surrogate Imaging Biomarker of Tumor Hypoxia.* Molecular imaging and biology : MIB : the official publication of the Academy of Molecular Imaging, 2016. **18**(2): p. 219-231.

218. Wykoff, C.C., et al., *Hypoxia-inducible Expression of Tumor-associated Carbonic Anhydrases.* Cancer Research, 2000. **60**(24): p. 7075-7083.

219. Al-Ahmady, Z.S., O. Chaloin, and K. Kostarelos, *Monoclonal antibody-targeted, temperature-sensitive liposomes: In vivo tumor chemotherapeutics in combination with mild hyperthermia.* Journal of Controlled Release, 2014. **196**: p. 332-343.

220. Andreucci, E., et al., *Carbonic anhydrase IX inhibition affects viability of cancer cells adapted to extracellular acidosis.* Journal of Molecular Medicine, 2017. **95**(12): p. 1341-1353.

221. Hussain, S.A., et al., *Hypoxia-regulated carbonic anhydrase IX expression is associated with poor survival in patients with invasive breast cancer.* British journal of cancer, 2007. **96**(1): p. 104-109.

222. Supuran, C.T., *How many carbonic anhydrase inhibition mechanisms exist?* J Enzyme Inhib Med Chem, 2016. **31**(3): p. 345-60.

223. Supuran, C.T., *Carbonic anhydrase inhibitors.* Bioorganic & Medicinal Chemistry Letters, 2010. **20**(12): p. 3467-3474.

224. Supuran, C.T. and J.-Y. Winum, *Carbonic anhydrase IX inhibitors in cancer therapy: an update.* Future Medicinal Chemistry, 2015. **7**(11): p. 1407-1414.

225. Casey, J.R., et al., *Carbonic Anhydrase Inhibitors. Design of Selective, Membrane-Impermeant Inhibitors Targeting the Human Tumor-Associated Isozyme IX.* Journal of Medicinal Chemistry, 2004. **47**(9): p. 2337-2347.

226. Tinker, J.P., R. Coulson, and I.M. Weiner, *Dextran-bound inhibitors of carbonic anhydrase.* Journal of Pharmacology and Experimental Therapeutics, 1981. **218**(3): p. 600-607.

227. Maren, T.H., et al., *Renal and Cerebrospinal Fluid Formation Pharmacology of a High Molecular Weight Carbonic Anhydrase Inhibitor.* Journal of Pharmacology and Experimental Therapeutics, 1997. **280**(1): p. 98-104.

228. Supuran, C.T., et al., *Carbonic Anhydrase Inhibitors: Synthesis of Sulfonamides Incorporating 2, 4, 6–Trisubstituted-Pyridinium-Ethylcarboxamido Moieties Possessing Membrane-Impermeability and in Vivo Selectivity for the Membrane-Bound (CA IV) Versus the Cytosolic (CA I and CA II) Isozymes.* Journal of Enzyme Inhibition, 2000. **15**(4): p. 381-401.

229. Winum, J.-Y., et al., *Carbonic anhydrase inhibitors: N-(p-sulfamoylphenyl)-α-d-glycopyranosylamines as topically acting antiglaucoma agents in hypertensive rabbits.* Bioorganic & Medicinal Chemistry Letters, 2004. **14**(1): p. 225-229.

230. Veronese, F.M. and A. Mero, *The impact of PEGylation on biological therapies.* BioDrugs, 2008. **22**(5): p. 315-29.

231. Whittington, D.A., et al., *Crystal structure of the dimeric extracellular domain of human carbonic anhydrase XII, a bitopic membrane protein overexpressed in certain cancer tumor cells.* Proc Natl Acad Sci U S A, 2001. **98**(17): p. 9545-50.

232. Dubois, L., et al., *Imaging the hypoxia surrogate marker CA IX requires expression and catalytic activity for binding fluorescent sulfonamide inhibitors.* Radiotherapy and Oncology, 2007. **83**(3): p. 367-373.

233. Ahlskog, J.K.J., et al., *Human monoclonal antibodies targeting carbonic anhydrase IX for the molecular imaging of hypoxic regions in solid tumours.* British journal of cancer, 2009. **101**(4): p. 645-657.

234. Carlin, S., et al., *Molecular targeting of carbonic anhydrase IX in mice with hypoxic HT29 colorectal tumor xenografts.* PloS one, 2010. **5**(5): p. e10857-e10857.

235. Koukourakis, M.I., et al., *Endogenous Markers of Two Separate Hypoxia Response Pathways (hypoxia inducible factor 2 alpha and carbonic anhydrase 9) Are Associated With Radiotherapy Failure in Head and Neck Cancer Patients Recruited in the CHART Randomized Trial.* Journal of Clinical Oncology, 2006. **24**(5): p. 727-735.

236. Loncaster, J.A., et al., *Carbonic Anhydrase (CA IX) Expression, a Potential New Intrinsic Marker of Hypoxia: Correlations with Tumor Oxygen Measurements and Prognosis in Locally Advanced Carcinoma of the Cervix.* Cancer Research, 2001. **61**(17): p. 6394-6399.

237. Noordhuis, M.G., et al., *Prognostic Cell Biological Markers in Cervical Cancer Patients Primarily Treated With (Chemo)radiation: A Systematic Review.* International Journal of Radiation Oncology • Biology • Physics, 2011. **79**(2): p. 325-334.

238. Järvelä, S., et al., *Carbonic anhydrase IX in oligodendroglial brain tumors.* BMC Cancer, 2008. **8**(1): p. 1.

239. Chrastina, A., et al., *Biodistribution and pharmacokinetics of 125I-labeled monoclonal antibody M75 specific for carbonic anhydrase IX, an intrinsic marker of hypoxia, in nude mice xenografted with human colorectal carcinoma.* International Journal of Cancer, 2003. **105**(6): p. 873-881.

240. Mack, E.T., et al., *Dependence of Avidity on Linker Length for a Bivalent Ligand-Bivalent Receptor Model System.* Journal of the American Chemical Society, 2012. **134**(1): p. 333-345.

241. Kamiński, Z.J., P. Paneth, and J. Rudziński, *A Study on the Activation of Carboxylic Acids by Means of 2-Chloro-4,6-dimethoxy-1,3,5-triazine and 2-Chloro-4,6-diphenoxy-1,3,5-triazine.* The Journal of Organic Chemistry, 1998. **63**(13): p. 4248-4255.

242. Akocak, S., et al., *PEGylated Bis-Sulfonamide Carbonic Anhydrase Inhibitors Can Efficiently Control the Growth of Several Carbonic Anhydrase IX-Expressing Carcinomas.* Journal of Medicinal Chemistry, 2016. **59**(10): p. 5077-5088.

243. Chiu, M.H. and E.J. Prenner, *Differential scanning calorimetry: An invaluable tool for a detailed thermodynamic characterization of macromolecules and their interactions.* Journal of pharmacy & bioallied sciences, 2011. **3**(1): p. 39-59.

244. Menczel, J.D., et al., *Differential Scanning Calorimetry (DSC)*, in *Thermal Analysis of Polymers*, J.D. Menczel and R.B. Prime, Editors. 2008.

245. Wojtkowiak, J.W., et al., *Drug resistance and cellular adaptation to tumor acidic pH microenvironment.* Mol Pharm, 2011. **8**(6): p. 2032-8.

246. Jiang, W., et al., *Nanoparticle-mediated cellular response is size-dependent.* Nature Nanotechnology, 2008. **3**: p. 145.

247. Dreaden, E.C., et al., *Size matters: gold nanoparticles in targeted cancer drug delivery.* Therapeutic delivery, 2012. **3**(4): p. 457-478.

248. Kimling, J., et al., *Turkevich method for gold nanoparticle synthesis revisited.* J Phys Chem B, 2006. **110**(32): p. 15700-7.

249. Ulman, A., *Formation and Structure of Self-Assembled Monolayers.* Chemical Reviews, 1996. **96**(4): p. 1533-1554.

250. Tarazona-Vasquez, F. and P.B. Balbuena, *Complexation of the Lowest Generation Poly(amidoamine)-NH2 Dendrimers with Metal Ions, Metal Atoms, and Cu(II) Hydrates: An ab Initio Study.* The Journal of Physical Chemistry B, 2004. **108**(41): p. 15992-16001.

251. Nair, L.V., et al., *Fluorescence Imaging Assisted Photodynamic Therapy Using Photosensitizer-Linked Gold Quantum Clusters.* Acs Nano, 2015. **9**(6): p. 5825-32.

252. Pelaz, B., et al., *Surface Functionalization of Nanoparticles with Polyethylene Glycol: Effects on Protein Adsorption and Cellular Uptake.* ACS Nano, 2015. **9**(7): p. 6996-7008.

253. Tirosh, O., et al., *Hydration of polyethylene glycol-grafted liposomes.* Biophys J, 1998. **74**(3): p. 1371-9.

254. Shiraishi, K., et al., *Determination of polymeric micelles' structural characteristics, and effect of the characteristics on pharmacokinetic behaviors.* J Control Release, 2015. **203**: p. 77-84.

255. Turkevich, J., P.C. Stevenson, and J. Hillier, *A study of the nucleation and growth processes in the synthesis of colloidal gold.* Discussions of the Faraday Society, 1951. **11**(0): p. 55-75.

256. Link, S. and M.A. El-Sayed, *Size and Temperature Dependence of the Plasmon Absorption of Colloidal Gold Nanoparticles.* The Journal of Physical Chemistry B, 1999. **103**(21): p. 4212-4217.

257. Shabana, A.M., *Development and biological evaluation of drug delivery nanosystems targeting hypoxic tumors*, in *Pharmaceutical Sciences*. 2018, Temple University.

258. Shabana, A.M., et al., *pH-Sensitive Multiligand Gold Nanoplatform Targeting Carbonic Anhydrase IX Enhances the Delivery of Doxorubicin to Hypoxic Tumor Spheroids and Overcomes the Hypoxia-Induced Chemoresistance.* ACS applied materials & interfaces, 2018. **10**(21): p. 17792-17808.

259. Lv, P.C., et al., *Evaluation of a Carbonic Anhydrase IX-Targeted Near-Infrared Dye for Fluorescence-Guided Surgery of Hypoxic Tumors.* Mol Pharm, 2016. **13**(5): p. 1618-25.

260. Soenen, S.J., et al., *The Cellular Interactions of PEGylated Gold Nanoparticles: Effect of PEGylation on Cellular Uptake and Cytotoxicity.* Particle & Particle Systems Characterization, 2014. **31**(7): p. 794-800.

261. Petrul, H.M., et al., *Therapeutic mechanism and efficacy of the antibody-drug conjugate BAY 79-4620 targeting human carbonic anhydrase 9.* Mol Cancer Ther, 2012. **11**(2): p. 340-9.

262. Wang, F., et al., *Doxorubicin-tethered responsive gold nanoparticles facilitate intracellular drug delivery for overcoming multidrug resistance in cancer cells.* ACS Nano, 2011. **5**(5): p. 3679-92.

263. Xiao, Y., et al., *Gold Nanorods Conjugated with Doxorubicin and cRGD for Combined Anticancer Drug Delivery and PET Imaging.* Theranostics, 2012. **2**(8): p. 757-68.

264. Cui, N., et al., *Preparation, characterization, and biocompatibility evaluation of poly(Nvarepsilon-acryloyl-L-lysine)/hyaluronic acid interpenetrating network hydrogels.* Carbohydr Polym, 2016. **136**: p. 1017-26.